UNIVERSITÀ DEGLI STUDI DI TRIESTE

Università Ca'Foscari Venezia

UNIVERSITÀ DEGLI STUDI DI TRIESTE

UNIVERSITÀ CÀ FOSCARI VENEZIA

XXXVI CICLO DEL DOTTORATO DI RICERCA IN CHIMICA

COMBINED SUPRA- & NANO-ARCHITECTURES FOR FUNCTIONAL MATERIALS

Settore scientifico-disciplinare: CHIM/06

DOTTORANDO
SIMONE ADORINNI

COORDINATORE
PROF. ENZO ALESSIO

SUPERVISORE DI TESI
PROF. SILVIA MARCHESAN

ANNO ACCADEMICO 2022/2023

TABLE OF CONTENTS

Abstract

The technological advances over the last years are driving research towards alternative ways to produce materials with reduced cost and enhanced properties. These newly synthesised materials with various potential applications are referred to as functional materials. In particular, smart materials change their properties in response to a certain stimulus (*e.g.*, chemical, physical or mechanical), thus enabling new potential applications. In literature, there is a wide variety of functional materials, such as carbon nanomaterials, soft materials (*i.e*. gels, liquid crystals, ionic liquids), and, generally, supramolecular materials. The possibility of fine-tuning the properties of different materials by combing them together is very attractive. This approach can lead to novel composites or even hybrids, which display new properties, thus extending the range of possible applications.

This Ph.D. thesis focuses on the synthesis of innovative functional materials based on supramolecular peptide gels or carbon nanotubes (CNTs) combined with metal organic cages (MOCs). In particular, **Chapter 2** describes the synthesis on new MOCs having pendant peptides as peripherical ligands. The peptides chosen for this purpose were heterochiral tripeptides PABA-L-Phe-D-Xaa-L-Phe-NH_2 (Xaa = Ala, Val, Leu, Ile) derivatised at the N-terminus with a *p*-amino benzoyl unit and amidated at the C-terminus. All four peptides were able to gel on their own. The peptides were self-assembled with different aldehydes and metal ions to obtain different MOCs. The gelling ability of the MOCs was studied and it was rationalized both from a theoretical (Molecular Dynamics) and experimental point of view (UV Resonance Raman Spectroscopy).

Chapter 3 investigates the self-assembly of MOCs containing pendant peptides based on another type of interaction. In this case the tripeptides contain sulfur on their sidechains. The gelation of these MOCs was induced by the formation of coordinative bond between the sulfur unit and other metals ions (*i.e.*, Ag^{+}, Zn^{2+}, Hg^{2+}). This gelation in the presence of heavy metals holds promise for the removal of toxic metal ions from the environment.

Chapter 4 describes the first example of functionalisation of CNTs with MOCs. The affinity of the MOC for different CNT types was studied through thermogravimetric analysis (TGA). The MOC employed in this study was able to transfer between aqueous and organic solvents by counter-anion exchange. The MOC binding onto

the CNTs enabled their phase transfer as well, upon ion exchange. This phenomenon was exploited to test CNT sorting by phase extraction depending on their diameter.

In conclusion, this work identified new ways to combine supramolecular materials with nanostructures, offering new designs to hierarchically co-assemble tripeptides, aldehydes, and metal ions into gelling MOCs, as well as providing the first example of MOC binding onto CNTs to transfer them across phases for sorting. Further developments in these areas could enable advances in separation, sensing or catalysis.

Riassunto della tesi

L'enorme sviluppo tecnologico degli ultimi anni ha guidato la ricerca verso strade alternative per la produzione di materiali a basso costo e con proprietà sempre migliori. Questi nuovi materiali con diverse potenziali applicazioni sono comunemente denominati materiali funzionali. In particolare, questi materiali *smart* sono in grado di cambiare le loro proprietà in risposta a diversi stimoli (ad esempio chimici, fisici o meccanici). In letteratura è riportata una grande varietà di questi materiali, come i materiali carboniosi, i materiali "*soft*" (ad esempio gel, cristalli liquidi, liquidi ionici), o in generale materiali supramoleculari. La possibilità di regolare in modo fine le loro proprietà, grazie alla combinazione di diversi materiali, è estremamente attrattiva. Questo approccio può portare a nuove materiali compositi o ibridi, con nuove proprietà in modo da estendere la gamma delle diverse possibili applicazioni.

In questo progetto di dottorato si sono sintetizzati diversi materiali funzionali a base di gel di peptidi supramolecolari o nanotubi di carbonio (CNTs), combinati con delle gabbie supramoleculari (MOCs). Nel **Capitolo 2**, in particolare, viene descritta la sintesi di nuove gabbie aventi dei peptidi come leganti periferici. I peptidi scelti per questo scopo sono tripeptidi eterochirali PABA-L-Phe-D-Xaa-L-Phe-NH_2 (Xaa = Ala, Val, Leu, Ile) derivatizzati al N-terminale con un gruppo p-amino benzoico e amidati al C-terminale. Tutti i peptidi sono in grado di assemblare in acetonitrile a diverse concentrazioni. L'assemblaggio dei peptidi, con diverse aldeidi e ioni metallici ha portato alla formazione di diverse gabbie supramoleculari. L'abilità di formare gel delle gabbie è stata studiata e razionalizzata sia da un punto di vista teorico (Dinamica Molecolare) che sperimentale (Spettroscopia UV Raman Risonante). Il **Capitolo 3** si focalizza sullo studio dell'auto-assemblaggio di gabbie simili a quelle del precedente capitolo, ma il cui auto-assemblaggio si basa un altro tipo di interazione. I peptidi utilizzati contengono degli atomi di zolfo sulle catene laterali degli amino acidi. La capacità delle gabbie di gelare è indotta dalla formazione di un legame di coordinazione tra lo zolfo e altri ioni metallici (Ag^+, Zn^{2+}, Hg^{2+}), aggiunti in soluzione. La capacità di formare gel in presenza di metalli pesanti può essere estremamente promettente per la rimozione di metalli tossici dall'ambiente.

Nel Capitolo 4 viene riportato il primo esempio di funzionalizzazione di CNTs con le MOCs. Si è inizialmente studiata l'affinità delle MOC verso diverse tipologie di CNTs mediante analisi termogravimetrica. La gabbia

utilizzata nello studio ha inoltre la capacità di passare da un solvente acquoso ad uno organico grazie al cambio di contro ione. Questa abilità è stata utilizzata per testare la separazione di CNTs con diversi diametri mediante estrazione di fase. Ulteriori sviluppi in quest'area potrebbero portare ad enormi avanzamenti nel campo della separazione, della sensoristica e della catalisi.

CHAPTER 1

Introduction

1. Introduction

1.1. Gels

Materials play a key role in everyday life, so much that they define historical periods of human development.[1] Nowadays, soft materials are emerging as innovative materials for different applications from biology and medicine to soft robotics and electronics devises.[1] Gels are intriguing type of soft materials, characterised by "a non-fluid colloidal network or polymer network that is expanded throughout its whole volume by a fluid".[2] In 1974, Flory proposed a comprehensive definition, for which a gel must be characterised by the two properties.[3] It must have a continuous structure, able to encapsulate solvents, with macroscopic dimensions that stay constant for the duration of the experimental measure. The second requirement is that a gel should behave like a solid.[3] Gels can be grouped in various ways, for instance based on their source (natural or synthetic), the medium, and their constitution (***Figure 1.1***). In terms of the latter parameters, there are two types of gels, the macromolecular, the first to be discovered and studied, and the low-molecular-weight gelators (LMWG), which are formed thanks to the self-assembly of small molecules (*i.e.*, bis(ureas), amide, nucleobases derivates, amino acid derivatives, fatty acids, steroids, porphyrins, etc.). LMWG have emerged in the last years as promising materials in different fields. The LMWG are physical gels because their particles or fibres are held together through weak, non-covalent interactions. On the other hand, the macromolecular matrix could be both physical and chemical, the latter one being the case for the gels networks that are covalently cross-linked.

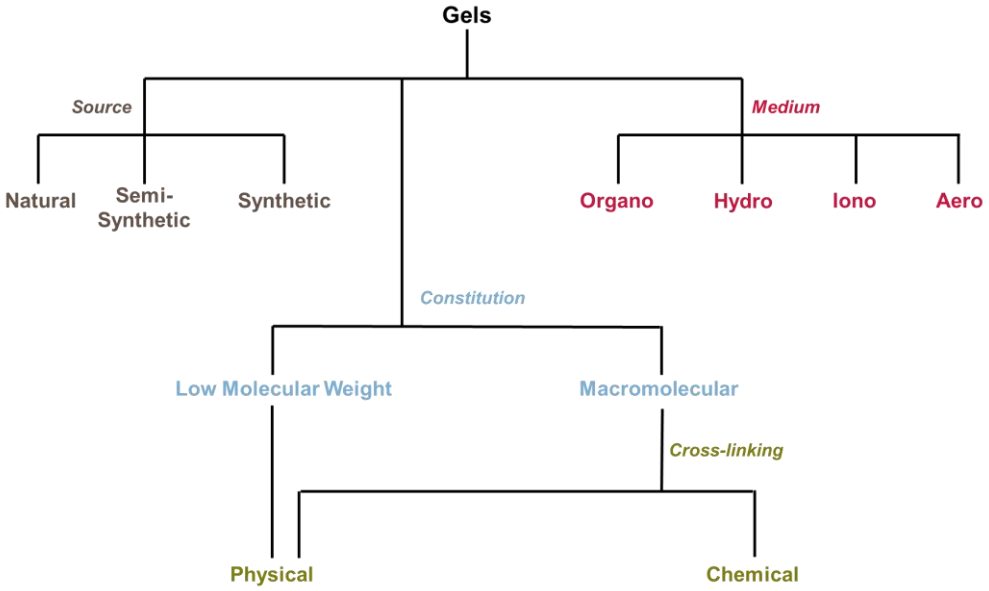

Figure 1.1: *Gel classification based on their source, medium, and constitution.*

1.1.1. Chemical gels

Chemical gels are intriguing materials thanks to their great mechanical strength and irreversibility, deriving from the strong chemical bonds (250-500 kJ/mol). The first generation of hydrogels to have been developed belongs to this category. One of the most famous example is poly(2-hydroxyethylmethacrylate) (pHEMA) hydrogel, which arose from the free-radical copolymerization of HEMA with 2,3-dihydroxypropylmethacrylate (DHPM), using ethylene dimethacrylate (DME) as crosslinking agent and 2,2′-azobisisobutyronitrile (AIBN) as redox initiator.[4] pHEMA-base hydrogels have found widespread biomedical applications from controlled drug release[5-7] to blood-based compatible materials.[8, 9] Moreover, they have been used as bulk space fillers in reconstructive surgery,[10, 11] but its main application still remains as raw materials for contact lenses.[12, 13] In particular, contact lenses made by pHEMA can be loaded with several drugs for ocular drug delivery.[14, 15] Figure 1.2 reports an example of contact lenses based on co-polymerization of 92% of HEMA and 8% of other monomers (*i.e.*, EGD, GMA, and NVP).[16] This work presented a way to increase drug loading thanks to the addition of lipophilic organic molecules, such as vitamin E or vitamin A.[16] Apolar vitamins gave rise to hydrophobic aggregates within the hydrogel matrix. This hydrophobic environment enhanced the drug loading thanks to the interaction between drug and vitamin aggregates.[16]

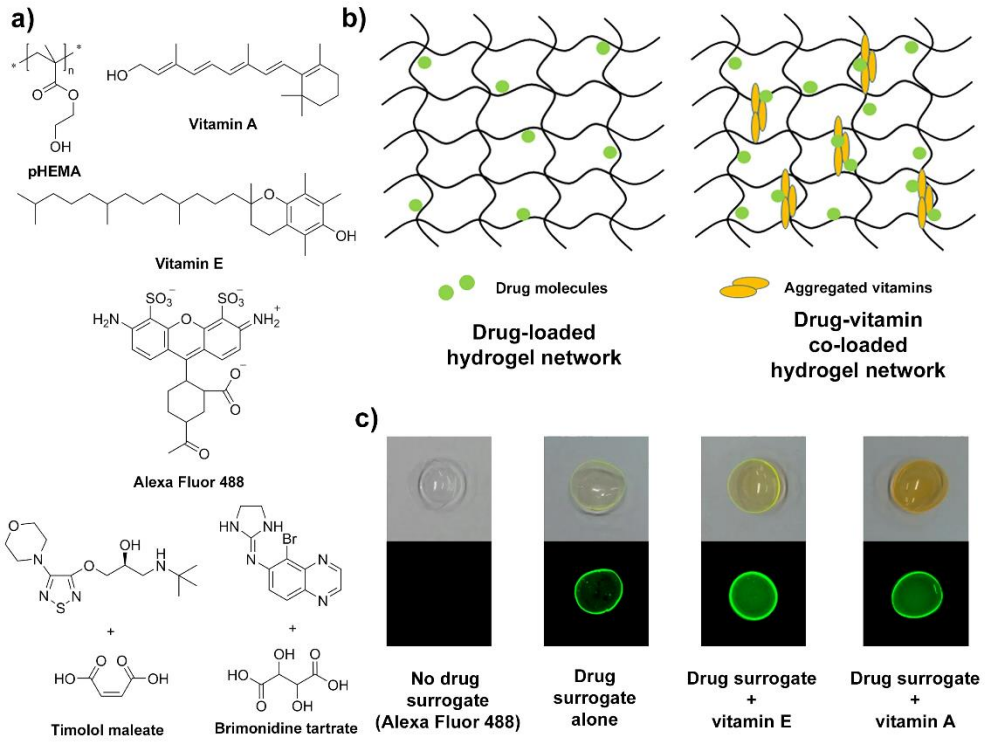

Figure 1.2: *Contact lenses based on HEMA copolymer.* ***a)*** *Chemical structures of pHEMA, vitamins and drugs used in the study;* ***b)*** *Schemes depicting the hydrogel matrix loaded with drug alone or with the vitamin too;* ***c)*** *White-light (top panels) and fluorescence (bottom panels) images of contact lenses, from left to right: without or with a drug amalog (Alexa Fluor 488), alone, or with either vitamin E or vitamin A. Reproduced with permission from Ref[16], copyright ©2016, Springer Nature.*

Furthermore, pHEMA is an excellent example to describe one of most popular approaches to form chemical gels, consisting of hydrophilic-monomer polymerization in the presence of a crosslinker. One of the main concerns for biomedical uses of this first approach is the possible presence of residual crosslinking agents that could yield adverse effects. [17] In this context, the possibility to induce the cross-linking by a high-energy radiation is an attractive option. For instance, since 1960, the ability of poly(vinyl acetate) (PVA) to gel water by irradiation with gamma or electron beam was known.[18, 19] The irradiations generate free radicals due to homolytic scission of C-H bond. In addition, the radiolysis of water generates molecules and radicals with different levels of chemical reactivity (***Figure 1.3***).

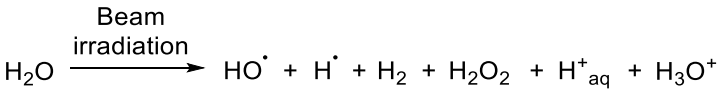

Figure 1.3: *Products of water's radiolysis.*

H• and HO• react with the macromolecular chain generating macroradicals, which produce the interconnected polymer networks through inter and intramolecular free radical recombination. Many hydrogels with common polymers (*i.e.* poly (ethylene glycol), poly (acrylic acid), poly (vinyl alcohol), *etc.*) were prepared with this methodology, which can also be performed in mild conditions, including physiological pH and room temperature under inert atmosphere. Generally, these polymer hydrogels showed poor mechanical properties,[20] which could be reinforced either by annealing and consequent introduction of crystallites in the polymeric network or by using a blend of natural polymers. In particular, the latter solution allows to optimize the blend performance, whilst not altering the individual polymer properties. The advantages of these systems include the absence of chemical contamination rendering them very suitable for biomedical use, as well as to sterilize biomedical devices [21] and remove water pollutants.[22]

Another approach involves the use of polymers with complementary functional groups, offering a great tunability of the gel properties, including kinetic and mechanical stability. [23] Different types of chemistry were employed to this end, spanning from the classical reaction of aldehydes with alcohols, thiols, amines, and hydrazide, to Michael additions, Passerini and Ugi condensations, and even to click chemistry reactions, or to native chemical ligation (***Figure 1.4***). In particular, click chemistry reactions are very popular, thanks to the possibility of using physiological conditions with fast kinetics.

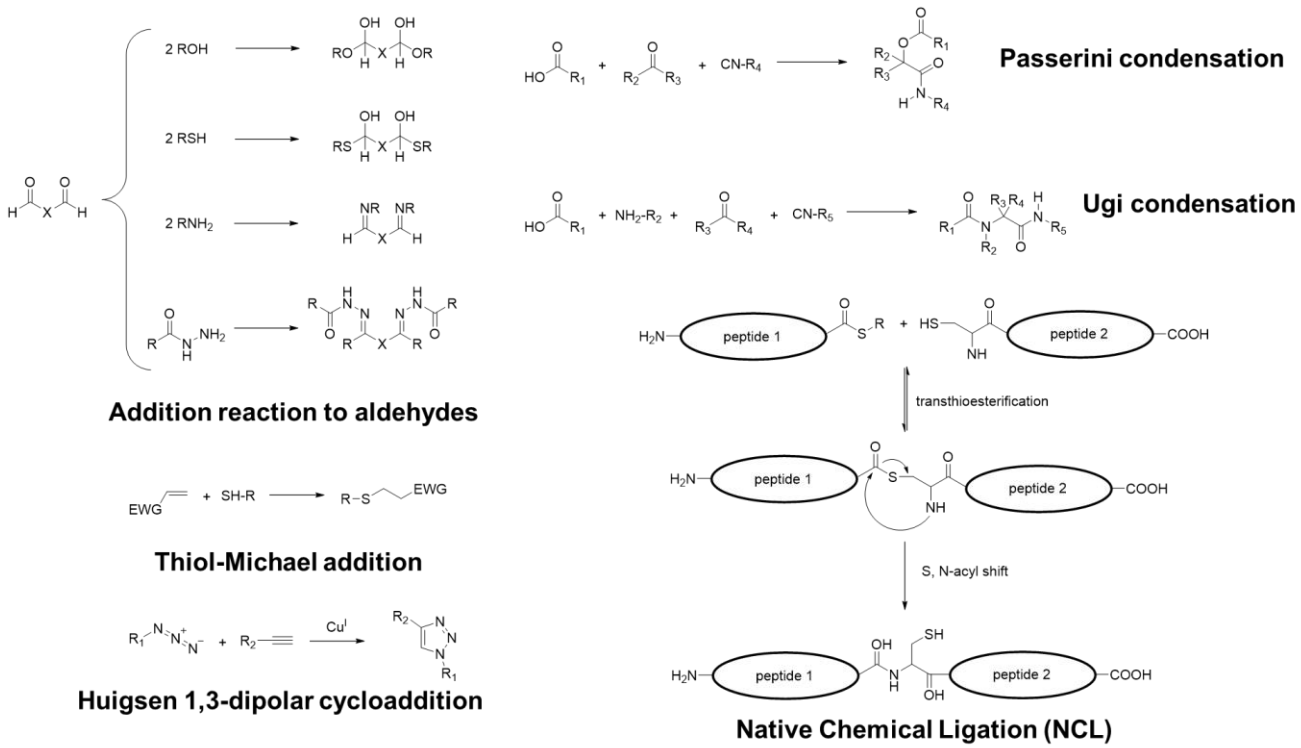

Figure 1.4: *General chemical reaction used to cross-link polymers for gel formation.*

Different approaches can also be combined together. For instance, Caruso and co-workers, in 2012, described an example of a one-pot reaction, where a photo "click" copper(I)-catalysed azide-alkyne cycloaddition was combined with a radical polymerization to yield micropatterned PEG hydrogels.[24] To this end, the surface of a silicon wafer that acted as solid support for the hydrogel, was firstly functionalised with azides thanks to plasma polymerization, and then the so-obtained "clickable" surface was reacted with a 4-armed alkyne-functionalised PEG. The formation of Cu(I), required to catalyse the "click" reaction, was achieved thanks to the photogeneration of radicals by Irgacure 2959 (4-(2-hydroxyethoxy)phenyl-(2-hydroxy-2-propyl)ketone) that was used as photoinitiator under UV-light irradiation. At the same time, the photoinitiator radicals abstracted labile PEG α-hydrogen to generate radicals that induced PEG radical polymerisation.

1.1.2. Physical gels

Physical gels have been gaining a growing popularity during recent years, thanks to their ability to respond to changes in their local physical-chemical conditions, such as pH, temperature, mechanical stimulation, light irradiation, and also presence of other molecules. This type of gelation is determined by cooperative, yet

individually weak, forces, mainly H-bonding and hydrophobic interactions that can be easily broken and reformed (***Table 1.1***).

Interaction	Interaction strength (kJ mol^{-1})
ion-ion	> 190
ion-dipole	40-120
dipole-dipole	5-40
hydrogen bonding	15-40 (strong) 5-15 (moderate) < 5 (weak)
π-π interactions	10-15 (face to face) 15-20 (edge to face)
van der Waals forces	< 5
hydrophobic effects	varied 5-40

Table 1.1: *Weak interactions and their strength in kJ mol^{-1}.*

One of the environmentally responsive systems that are most studied include temperature-sensitive hydrogels. One of the main advantages is that they can be used so that they form *in situ*, for instance following a local injection in a non-invasive way. Thermoresponsive hydrogels can be categorised base on the temperature that induces gelation that can be considered lower critical solution temperature (LCST) and upper critical solution temperature (UCST).[25] The first ones are generally based on polymers with both hydrophobic and hydrophilic groups, with the most common being the poly(N-isopropylalcrimide) (pNIPAAm).[26] LCST hydrogels undergo shrinking at temperature values that are above the critical one, whilst they become highly viscous liquids at lower temperature values. In contrast, UCST gels are mainly composed of hydrophilic groups, such as poly(acrylic acid-co-acrylamide), and gel at temperature values that are below the critical one. [26] In 2017, Chen and co-workers developed a thermally responsive actuator based on bilayers composed of 1) PNIPAM and P(AA-co-Aam) as LCST gelator, and 2) UCST hydrogels, respectively (***Figure 1.5a***).[27] Upon heating, the PNIPAM-based gel swell, and the P(AA-co-AAm) hydrogel shrunk generating a water flow from the former to the latter. This aqueous self-circulation enabled the hydrogel to bend, thus yielding a soft gripper that can grasp, transport, and release cargos in air (***Figure 1.5b***).[27]

Yamaguchi and Harada developed a fascinating hydrogel actuator that is based on host-guest interactions between an α-cyclodextrin (α-CD) and polyacrylamide functionalised with an azobenzene moiety (***Figure 1.5c***).[28] The photoisomerization of the azo moiety altered the cross-linking density and the macromolecular chains' length, generating the reversible swell-shrink behaviour of the hydrogel. ***Figure 1.5d*** shows that after irradiation with UV-light (λ = 365 nm), the hydrogel bent in the opposite direction relative to that of light irradiation. Subsequent irradiation with visible light (λ = 430 nm) restored the hydrogel to its initial state. These stimuli-responsive expansion-contraction properties mimicked those of muscle fibrils.[28]

In 2021, Stupp and co-workers reported an example of physical gel based on ionic interaction used as 3D-printing ink.[29] They synthetised a cation and anionic version of an amphiphilic peptide, that cross-linked in presence of anions ($_{e.g.}$ SO_4^{2-}) or cations (Ca^{2+}), respectively (***Figure 1.5e***). pH and salt concentration played a key role in ink viscosity. In particular, enhancing the hierarchical interactions among assemblies in highly viscous inks led to greater alignment of the filaments at the nanoscale, so that a higher printing speed was possible (***Figure 1.5f***).[29]

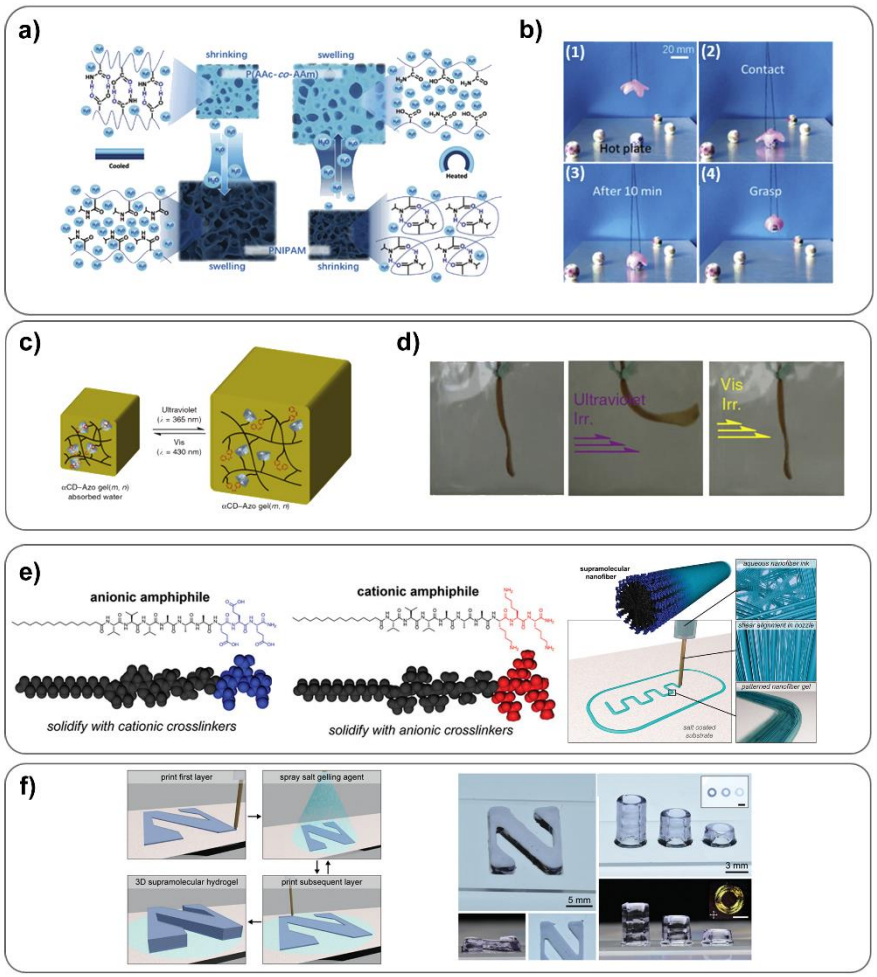

Figure 1.5: *Examples of physical gels envisaged for various uses.* ***a)*** *Working mechanisms of a thermo-responsive actuator that consists of a bilayer composed of PNIPAM and of P(AA-co-AAm) hydrogels;* ***b)*** *Soft gripper with a bilayered structure that works in air;* ***c)*** *Working mechanisms of an optically responsive actuator that uses azo-functionalised polymers and α-CD;* ***d)*** *Hydrogel deformation by ultraviolet irradiation and restoration to its initial state by visible (Vis) light irradiation;* ***e)*** *Extrusion printing liquid crystalline supramolecular polymer hydrogels;* ***f)*** *3D-printing multilayer hydrogel constructs from liquid crystalline supramolecular polymer inks.* ***a)-d)*** *Reproduced with permission from*[25]*, Copyright © 2020 The Authors. Published by Elsevier Ltd.;* ***e)-f)*** *Reproduced with permission from Ref*[29]*, Copyright © 2021, John Wiley and Sons.*

1.1.3. Low molecular weight gelators (LMWG) based on peptides

Gels based on LMWG are emerging as an attractive group of materials. These gels arise from the self-assembly of small molecules into fibres, which can entangle into a matrix that immobilises a solvent. The self-assembly process of these gels is based on the formation of molecular aggregates that can entangle mainly towards one direction forming fibrils. Thus, LMWG are commonly compounds that form relatively strong interactions such as hydrogen bonds or π-stacks in one direction, while forming only weaker ones (*e.g.* van der Waals) in the other.

Among small molecules, peptides are gaining widespread popularity as building blocks for supramolecular nanostructures. Small peptides have a low cost and can be easily synthesised through different strategies, which range from liquid- and solid-phase synthesis, to biocatalysis and biotechnology. These benefits make peptides accessible not only to synthetic chemists, but also to biologists and materials scientists. Another key advantage of peptides is the wide range of functional groups that can be displayed on the amino acidic sidechains. The choice is not restricted only to 20 proteinogenic amino acids, but can include their D-enantiomers, and other non-canonical or non-natural amino acids.

One of the key interactions for peptide self-assembly is the π-π stacking between aromatic groups on the sidechain or at the N-terminus of the peptide sequence. The dipeptide Phe-Phe is a minimalistic and powerful motif towards the formation of nanoscopic fibers.[30] However, the Phe-Phe motif alone is not able to yield stable gels, unless it is cyclized to the corresponding 2,5-piperazinedione. Another approach to induce gelation consists of adding an aromatic moiety at the N-terminus, such as naphthalene, anthracene or benzyloxy groups. The 9-fluorenylmethoxycarbonyl moiety (Fmoc) is one of the most commonly used, because of its wide commercial availability on amino acids, since it serves as protective group during peptide synthesis. Another way to prompt gelation is the alternation of hydrophobic L- and D-amino acids, to yield an amphiphilic β conformation in sequences as short as three residues.[31] In this way, the hydrophobic sidechains and the hydrophilic backbone groups will be displayed on opposite sides of the peptide molecule in this way.

Peptide LMWG have been used for a wide range of applications. One example is their use in organocatalysis to mimic the active site of enzymes, especially aldolase[32] and hydrolase,[33, 34] but also in photocatalysis (***Figure 1.6a***).[35] Furthermore, hydrogels made of short peptides can also template the controlled formation of gold nanoparticles (AuNPs) through a green redox process, whereby stereochemistry of the peptide sequence is important to yield a gel matrix that efficiently stabilises AuNPs that are embedded in the matrix and do not aggregate (***Figure 1.6b***).[36] These hydrogels were also applied in the biomedical area, for example the eight stereoisomers of Pro-Phe-Phe were tested *in vitro* to hinder the Alzheimer's disease-associated Aβ(1–42) peptide fibrillation thanks to Pro that acts as a breaker of β-stacks, which are the key units forming the amyloid fibrils (***Figure 1.6c***).[37] Another emerging application area is the development of the next-generation of antimicrobial peptides (AMPs). In this context, different hydrogels with antimicrobial activity were developed using tripeptides,[38] or even simply a functionalised amino acid[39] (***Figure 1.6c***) or cyclic dipeptides

(diketopiperazines).[40] These supramolecular hydrogels offer also the possibility for co-assembly with drugs. Marchesan and co-workers reported a hydrogel based on the tripeptide D-Leu-L-Phe-L-Phe that co-assembled with antibiotics, such as ciprofloxacin,[41] but also anti-inflammatory drugs, such as naproxen and ketoprofen (***Figure 1.6c***),[42] or antineoplastics, such as 5-fluorouracil (5-FU).[43]

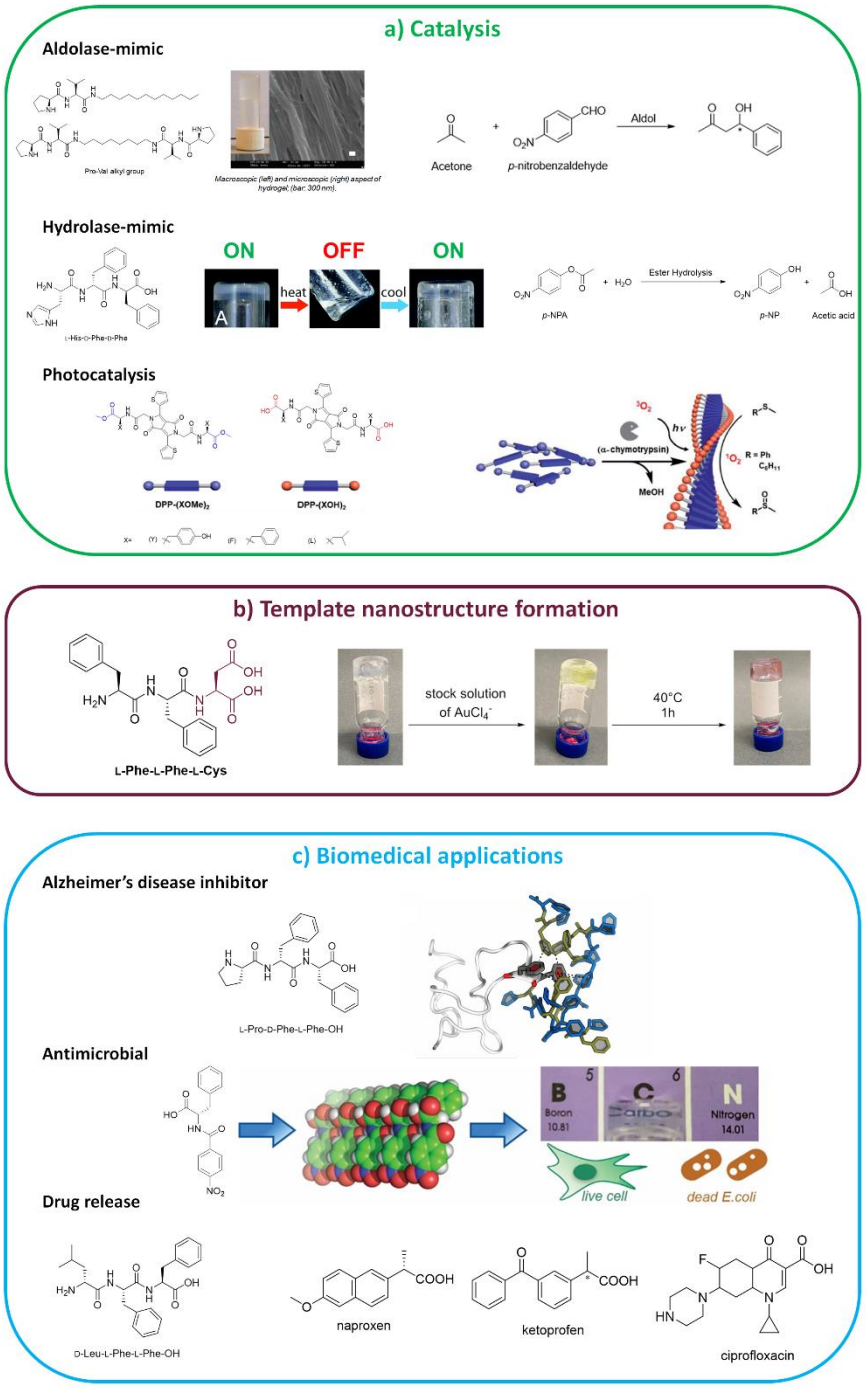

Figure 1.6: *Applications of LMWG peptide's gels.* ***a)*** *organocatalysis[32, 33] and photocatalysis[35];* ***b)*** *template AuNPs formation;[36]* ***c)*** *Biomedical applications as inhibitor for Alzheimer's disease,[37] antimicrobial activity[39] or drug release.[42]*

1.2. Carbon nanomaterials (CNMs)*

*Partly reproduced and adapted from Adorinni, S. et al., *Appl. Sc.* **2021**, *11* (6), 2490. [44]

The family of carbon nanomaterials (CNMs) (***Figure 1.7***) comprises many different members that generally share the common feature of being composed of carbon atoms, covalently bound in a sp^2 hexagonal lattice, although exceptions exist.[45] The two-dimensional (2D)-sheet of graphene (G) can be considered as a universal building block, which, depending on how it is folded, can give rise to 0D fullerenes,[46] 1D single-wall[47] or multi-wall[48] carbon nanotubes (CNTs), or 2D-graphene-based materials (GBM).[49] Other nanostructures comprise nano-onions (CNOs),[50] nanohorns (CNHs),[51] nanocones, and nanodiscs.[52] Nanodiamonds (NDs) differ for they contain a large portion of sp^3 carbon atoms.[53] More recently, carbon dots have drawn increasing attention.[54] Furthermore, CNMs can be assembled together in superstructures[55] and 3D-materials.[56]

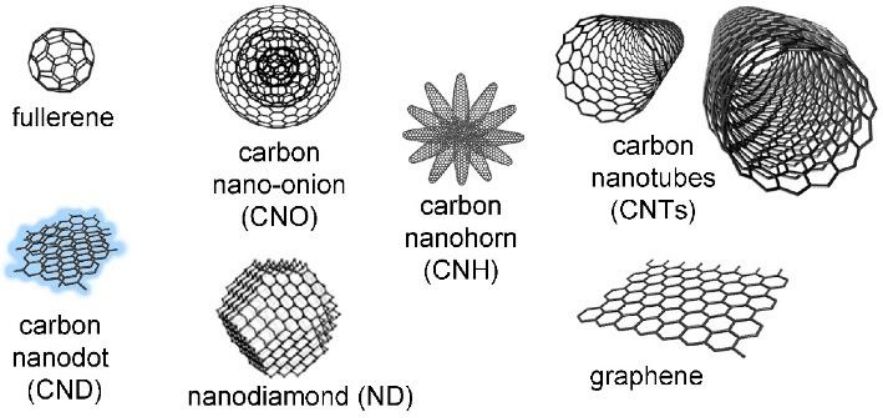

Figure 1.7: *Family of carbon nanomaterials (CNMs). CNO is reproduced with permission from Ref.[44], copyright ©1995, Elsevier.*

Each of these components has its own unique properties related to the specific morphology, size, and reactivity. They generally feature very interesting electronic conductivity, high mechanical strength, low density, as well as the ability to undergo chemical functionalization to further tune their properties as needed for the intended application. It is thus not surprising that many reviews already exist on their clinical applications[57] in biomedicine[58-60] and, above all, on their potential use in oncology,[61] such as innovative components in cancer theranostic[62] and cancer therapy,[63] thanks to their ability to target the tumor micro-environment.[64] Indeed, the

possibility to use them not only as vehicles for drug delivery,[65] but also for innovative imaging[66] and biosensing,[67] makes them ideal candidates for innovative theranostics.[68, 69]

1.2.1. Carbon nanotubes (CNTs)

CNTs can be considered as sheets of graphene rolled up in a tube, and comprise mainly single-walled CNTs (SWCNTs) or multi-walled CNTs (MWCNTs), depending on the number of sheets that compose their walls. Similar to the other nanostructures, they have been noted as promising materials to innovate in the biochemical field. However, their morphological similarity to asbestos fibers has posed many barriers for their applications, despite the fact that functionalization can alleviate their toxicity, as recently reviewed.[70] In 2019, CNTs have been added to the ChemSec SIN (Substitute It Now) list, in light of the studies on their toxicity and resistance to biodegradation.[71] This prompted a strong response from the academic community active on CNT research that feared further obstacles to innovation, in which it was noted that toxicity was related to a specific type of CNT, and this class of nanomaterials is very diverse, as the biocompatibility profiles depend on a plethora of factors, which include functionalization and route of administration.[71-73]

Indeed, CNTs have shown a unique ability to boost the activity of conductive cells,[74] demonstrating an unmissable opportunity to regenerate the cardiac[75] and nerve tissues.[76] Furthermore, their high mechanical resilience and low mass density is promising for orthopaedic applications.[77] CNT-coated surfaces effectively stimulated osteogenic differentiation of mesenchymal stem cells, which adhered and spread, with numerous visible focal adhesion and actin stress fibers.[78] Besides tissue engineering,[79] CNTs have also been proposed to attain antimicrobial and anti-adhesive surfaces for medical applications.[80] Their bioconjugation can serve a variety of innovative applications that span from tissue engineering, to sensing and wearable electronics,[81] and, in general, to prepare innovative biomedical electrodes.[82] Their biodegradation is possible, depending also on experimental conditions, route of degradation, and CNT functionalization.[83]

1.2.2. Functionalisation of CNTs

The functionalisation of CNTs is an excellent way to decrease the attractive van der Waals forces that keep them together, in favour of interactions between CNTs and the solvent, to increase their reactivity. There are different ways to functionalize CNTs (***Figure 1.8***) that can be classified mainly in two categories, *i.e.*, exohedral, when the functionalisation occurs on the surface of the CNTs, or endohedral, if it occurs inside the walls.[84] In this chapter the focus will be on the former type of functionalisation, which can be further subdivided in covalent and non-covalent functionalisation.

The covalent functionalisation can be performed by directly attaching functional groups onto the CNT surface. One of the most common reactions was the fluorination of CNTs, performed by treatment with molecular fluorine at a temperature between 150 and 600 °C. The success of the reaction can be easily detectable by infrared (IR) spectroscopy, thanks to the diagnostic C-F valence vibration at 1220-1250 cm^{-1}.[85] Another advantage was the possibility to replace the fluorine atoms with alkyl groups, using Grignard or organolithium reagents.[86] Another useful reaction is the hydrogenation, which allowed to obtain CNTs with a stoichiometry of $C_{11}H$ and stable up to 400 °C.[87] Also, cycloadditions were very common reactions performed on CNTs.[48] In particular, the 1,3-dipolar cycloaddition of azomethine ylides developed by Prato and co-workers led to SWCNTs and MWCNTs highly soluble in water as well as organic solvents such as chloroform, acetone, methanol.[88] Moreover, the pyrrolidine rings can be substituted with different chemical functionalities in order to synthesise materials with a wide range of applications. Nowadays, the Tour reaction is possibly the most widely used to functionalise CNTs. J. M. Tour described the direct treatment of CNTs with aryl diazonium tetrafluoroborate salts and *in situ* generation of the diazonium with an alkyl nitrite.[89, 90] Another common approach to achieve covalent functionalisation is the chemical oxidation of CNTs to introduce -COOH and -OH groups on the surface. After that, these groups can be further derivatised, often by amidation or esterification. Carboxylic groups are generally activated using either $SOCl_2$, obtaining the correspondent acyl chloride, or the most common coupling agents, such as EDC and NHS, which allowed to perform the reaction also in water.

Alternatively, the non-covalent functionalisation offers the great opportunity to adsorb molecules with different functionalities onto the CNT surface, without perturbing their π system. The first practical example was the

surfactant functionalisation, which allowed to disperse the CNTs in water. Different types of surfactants, both ionic and non-ionic, have been used, and their action mechanism was because of the hydrophobic part was oriented towards the CNTs' surface, whereas the polar moiety interacted with the solvent.[84] Generally, the non-covalent functionalisation occurred through π-π interactions, electrostatic interactions, and CH-π interactions. Therefore, compounds with aromatic moieties were the preferred choice to functionalise CNTs. In literature, there are many extensive reviews on this topic with different applications of the functionalised material ranging from biosensing,[91] tissue engineering,[92] drug delivery[93] to heterogeneous catalysis[94, 95] and energy storage.[96]

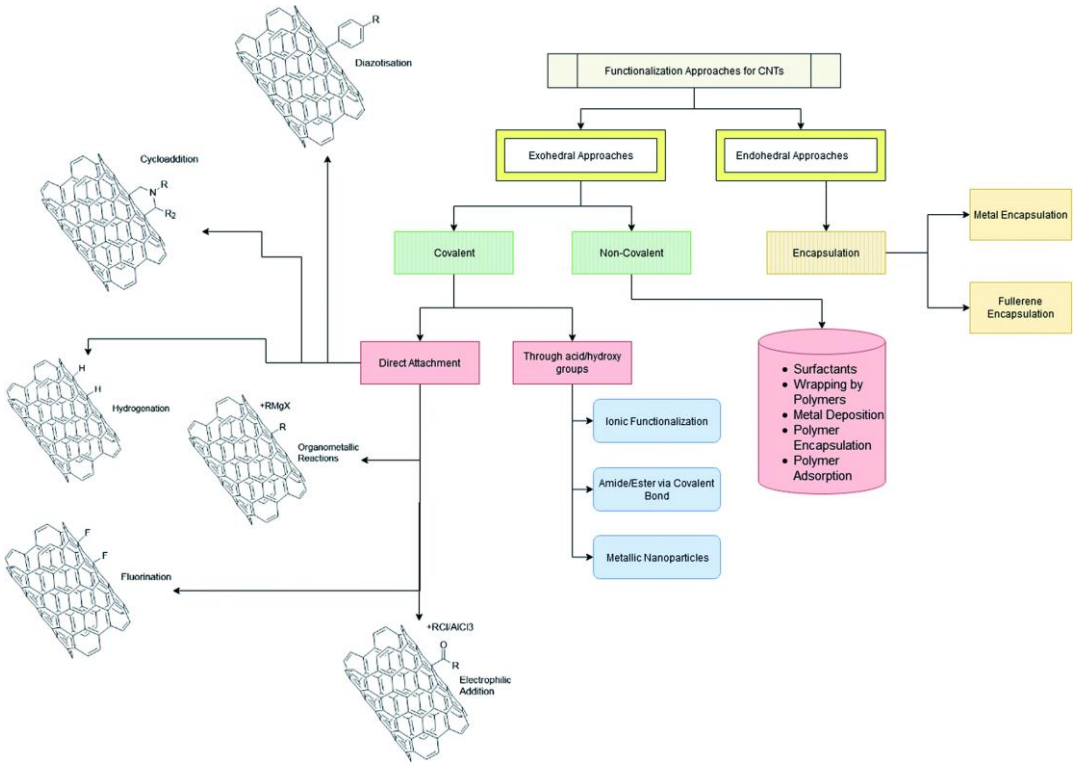

Figure 1.8: *Functionalisation approaches for CNTs. Reproduced with permission from Ref[84], copyright ©2021, Royal Society of Chemistry.*

Clearly the non-covalent functionalisation is the easiest approach to derivatise CNTs, but suffers from limited stability, in the sense that, depending on the conditions, the molecules adsorbed onto the CNTs can also detach. Another approach was thus developed to derivatise CNTs without perturbing their π system and also providing higher stability of the final product. This new type of derivatisation is possible on SWCNTs and takes inspiration from mechanically interlocked molecules (MIMs).[97] These new mechanically interlocked derivatives of carbon nanotubes (MINTs) can be described as rotaxane-like species where SWCNTs act as

threads (***Figure 1.9***).[97] The main challenge relative to their synthesis regards the absence of directional supramolecular interactions, which generally drive the MIMs' synthesis, and as a consequence it was based on exploiting dispersion forces. In 2014, Perèz and co-workers reported the synthesis of MINTs through a "clipping reaction" that involved a ring-closing metathesis (RCM).[98] They used a U-shaped molecule containing two π-extended tetrathiafulvene (exTTF) derivatives, which interacted with high affinity with the CNTs, and alkene-terminated alkyl chains, for the RCM. A similar approach was developed by von Delius and co-workers, in this case the ring closure was based on the formation of disulfide bonds between thiols groups at the termini of the macrocycles.[99] Miki, Ohe, and co-workers[100] and Gonzalez-Rodriguez and co-workers[101] reported a completely different strategy, where in first instance the macrocycle was synthesised, and then there was the fitting of the SWCNTs inside macrocycle's cavity. Also metal-ligand[102] and hydrogen bonding interactions[101] can be used for this purpose.

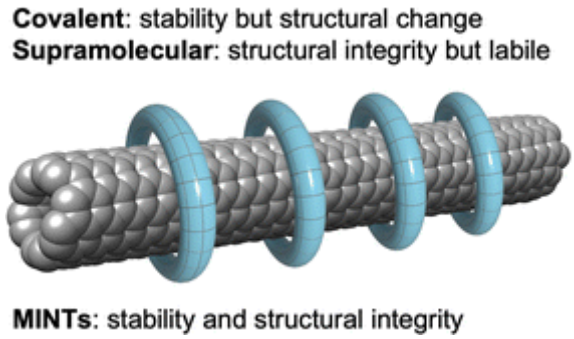

Figure 1.9: *General structure of MINTs. Reproduced with permission from Ref[97], Copyright ©2022, Royal society of Chemistry.*

1.2.3. Composite CNTs and their applications

Functionalised CNTs have been widely used additives for advanced nanocomposites. An interesting way to increase the processibility of CNTs is their incorporation inside gel matrices. Armaroli and co-workers reported an example of CNT's influence on a gel nanostructure.[103] The squaraine derivative assembled, after sonication, forming an entangled fibrous structure that led to gelation. The addition of small amounts of SWCNTs, at gelator concentrations lower than the minimum gelling concentration (mgc), resulted in the formation of nanotapes.[103] CNTs were also employed to reinforce gels. Marchesan and co-workers studied the effects of three oxidized nanocarbons (CNTs, graphene, CNHs) on the self-assembly of a hydrogelator tripeptide (L-Leu-

D-Phe-D-Phe) (***Figure 1.10a***).[104] Supramolecular hydrogels were obtained for all the CNMs, although those with MWCNTs displayed the best properties. TEM images revealed an excellent coating of the CNTs' surface by the peptide, which acted as dispersant for CNTs in basic aqueous media (***Figure 1.10b***). Once the hydrogel was formed, TEM micrographs showed an excellent interaction between CNTs and peptide fibers, which had similar nanomorphology (***Figure 1.10c-d***). In terms of rheological properties, the hydrogel with CNTs resulted stiffer, and it also presented a self-healing behaviour, after an applied stress of 250 Pa (***Figure 1.10e***).[104] The self-healing property was particularly interesting, but from that work it was unclear if it was due solely to the similar morphology of CNTs and peptide fibers, or also to the fact that the peptide coated very well the CNT surface, thus enabling a high level of interaction between CNTs and peptide fibers. To shed light on these aspects, the following steps of this work focussed on composite hydrogels containing the free L-Leu-D-Phe-D-Phe tripeptide and either CNTs or CNHs that were previously functionalised with the same peptide grafted on their surface. In this way, CNHs could better interact with peptide fibers, but still did not lead to self-healable nanocomposites, demonstrating that the self-healing property was due to the anisotropic morphology of CNTs.[105]

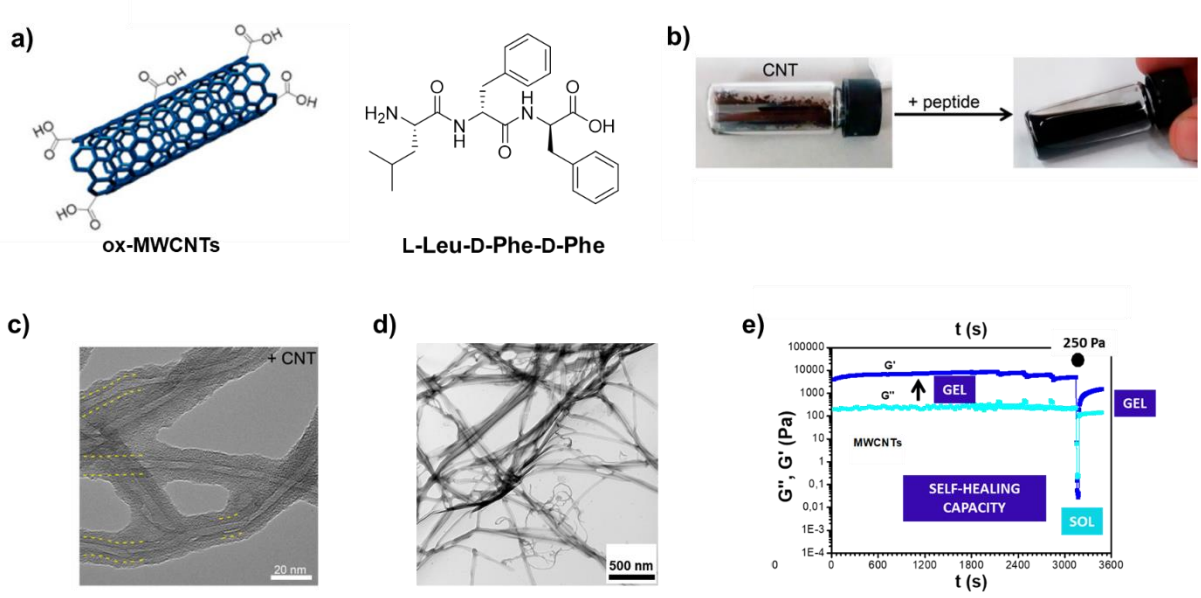

Figure 1.10: *Nanocomposite based on ox-MWCNTs and gelator tripeptide L-Leu-D-Phe-D-Phe.* ***a)*** *ox-MWCNTs and L-Leu-D-Phe-D-Phe structures;* ***b)*** *Peptide acts as dispersant for ox-CNTs in basic aqueous media;* ***c)*** *TEM images of ox-MWCNTs and L-Leu-D-Phe-D-Phe in basic aqueous buffer, scalebar 20 nm; d) TEM images of hydrogel of ox-MWCNTs and L-Leu-D-Phe-D-Phe at neutral pH, scalebar 500 nm. Reproduced with permission from Ref[104], Copyright © 2018 American Chemical Society.*

CNTs were also extensively used to reinforce polymer nanocomposites.[106] In particular, in the last years, the incorporation of CNTs in natural rubber has become popular. Nowadays, researchers are focussing on addressing some challenges on these hybrid systems, such as finding the best approaches to modify CNTs or improve their mixing in the rubber matrices.[107] For example, Mensah and Gao developed a slurry blending method that stabilised thermal conductivity and improved tensile strength.[106]

1.3 Metal organic cages (MOCs)

The examples of self-assembling systems shown in the previous Section **1.1** are generally based on weak, non-covalent interactions (*i.e.* hydrogen-bonding, π-π, van der Waals, electrostatic interactions). The limit of these interactions concerns the inability to completely control their directionality, a key aspect for the construction of more complex two- (2D) and three-dimensional architectures (3D). The use of highly directional and predictable metal-ligand coordination sphere represents the preferential route to synthesise molecules of desired dimensions and geometries with fine control. Metal-ligand bonds display intermediate energies (*i.e.*, 15-50 kcal/mol), relative to the strong, organic covalent bonds (60-120 kcal/mol) and the weak interactions (0.5-10 kcal/mol). They help the self-assembly process by introducing rigidity and reversibility. The latter property provides a way for the system to self-correct leading to a product that is thermodynamically more stable than the starting materials or the intermediates.[108]

1.3.1. General design of MOCs

Recently, we have witnessed an exponential growth of synthetic strategies based on metal-ligand coordination to achieve complex topologies (***Figure 1.11***).[108] These strategies have produced various and diverse sets of 2D and 3D molecular architectures. From a mechanistic point of view, the first four approaches rely on thermodynamic control, since the desired product lies at the thermodynamic minimum. The weak link approach concerns both kinetic and thermodynamic control.[108]

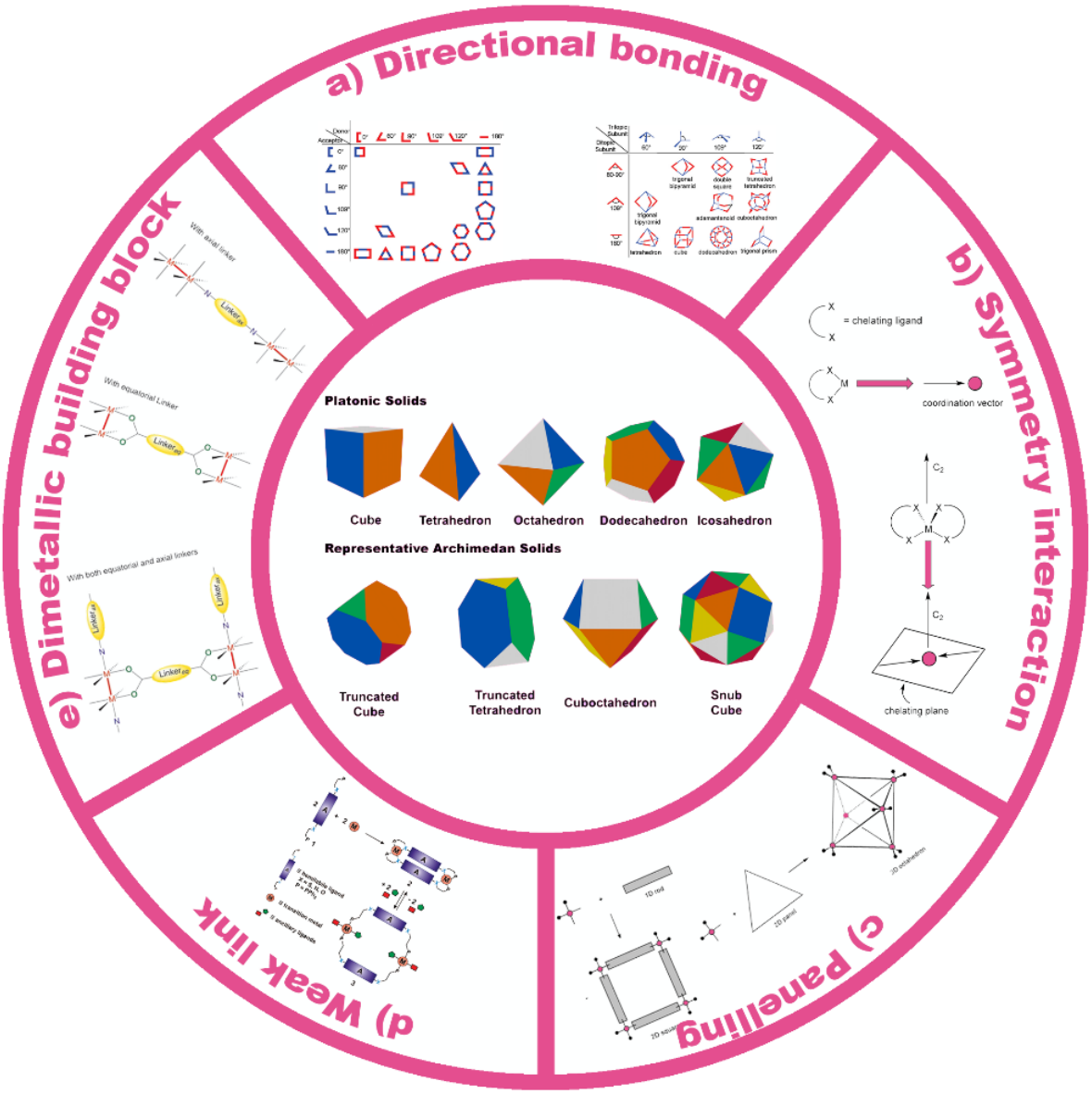

Figure 1.11: *Different approaches to design metal organic cages (MOCs). Reproduced with permission from Ref[108], Copyright © 2011 American Chemical Society.*

The directional bonding approach (***Figure 11.1a***) is a general strategy introduced by Fujita[109, 110] and Stang[111] in the early 1990s that provides high yields. The transition metals, thanks to their coordination sites with specific geometries, serve as acceptor subunits. These can be bound together via donor building blocks, which constitute the rigid frame of the final assembly (***Figure 1.11a***). The first requirements regard the donor subunits, which must be rigid and multidentate, or at least bidentate, and with pre-defined bite angles. The acceptors must have at least two coordination sites not capped. The building blocks are also divided into two types: linear units (L) with two-fold symmetry that display reactive sites that are oriented at 180° relative to

each other, and angular units (A) that contain reactive sites with other desirable angles and that may display either two-fold or higher symmetry axes. The second requirement is the appropriate stoichiometric ratio among the different subunits to achieve the desired geometry.

The second method consists of the symmetry interaction approach (***Figure 1.11b***), and it has been rationalised by Raymond and collaborators. The cages' design was explained based on the geometric relationship between the ligand and the metal taking symmetry into consideration. A coordinate vector directed towards the metal describes the interaction with the ligand (***Figure 1.11b***). Chelating ligands are illustrated based on the chelate plane, which is an orthogonal plane to the major axis of symmetry of the complex. This approach is convenient, because the angle between chelate planes can effectively describe any coordination complex cluster. This approach is also advantageous, since it offers a direct measure to compare and relate any high-symmetry cluster.[112, 113]

The panelling approach (***Figure 1.11c***), pioneered by Fujita and co-workers, is based on reducing the polyhedral to molecular components.[114, 115] For examples, regular polygons (*i.e.*, triangles, squares, etc.) make up Platonic solids when they are arranged in space matching edges and vertices to create the geometric solid.[116] Similarly shaped MOCs can thus be built using panels that display regular and polygonal morphology (*i.e.*, triangles, squares, etc.), so that their assembly with *cis*-protected square-planar coordination metals can yield many 3D geometries, depending on how they are combined together (***Figure 1.11c).*** The special attention to the geometry of square-planar metals highlights the observation that non-distorted 90° bond angles cannot be obtained by the hybridization of exclusively organic building blocks.[109]

The weak-link approach (WLA) (***Figure 1.11d***), pioneered by Mirkin is characterised by the metal centre being available for further reactions without causing the disassembly of the MOC.[117] In this approach, hemilabile bidentate ligands coordinate the transition metals, so that one of the metal-ligand bonds is weaker than the other. The ligands are generally phosphinoalkyl ether, tioethers or amine groups that can incorporate several functionalities, such as fluorophores, redox-active or catalytic groups. The transition metals introduced a further source of tailorability, adding an additional control over the macrocyclic properties, such as the level of stability to air and water, the overall charge, the shape of the MOC cavity, and the reactivity towards small molecules. Finally, the choice of the ancillary ligands provides a way to modulate the size and morphology of the MOC inner cavity.

The last approach is based on dimetallic building blocks (***Figure 1.11e***), and it was extensively studied by Cotton. It requires the use of paddlewheel or lantern frameworks as basic structural units.[118] The key choice in synthesis for large arrays with dimetal units is the type of nonlinking (protective) ligands, generally substituted, to give convenient solubility properties. For equatorial and axial linkers, the mostly used are polycarboxylate ions and polyamines or dinitriles, respectively. Depending on the dimetallic unit and the linkers used, it is possible to join the units in different ways, for example face-to-face using an axial linker, or end-to-end through an equatorial linker, or even a combination of both types of linkers can be possible.

1.3.2. Biomolecular cages

Since its discovery, supramolecular chemistry has been inspired by biological systems and processes, for the mimicry of their structures or functions.[119] In particular, the works of Fischer[120] on the "lock and key" model for enzymatic catalysis and of Ehrlich[121-124] on antibodies introduced the idea of the selective receptor-substrate binding. These studies opened the way to the research on interactions that direct the assembly of natural molecules, enabling molecular sensing and recognition events, and eventually leading to the so-called host-guest chemistry concept which marked the advent of supramolecular chemistry.

From this point of view, the combination of biomolecules and synthetic supramolecular architectures is the next logical step to enable a finer mimicry of natural systems. One of the most intriguing research areas in this field regards the synthesis of biomolecular nanocages following a bottom-up approach based on self-assembly of biomolecules, such as proteins or DNA. The nanocages obtained with this approach are characterised by high solubility in water, and highly efficient cellular uptake with minimal toxicity. These key features make them excellent carriers for biomedical applications.

DNA is an attractive template to generate supramolecular structures. The nucleobase pairing guarantees the possibility to create 1D, 2D and 3D DNA structures with high control and used for encapsulation and delivery. In this context, in the last years DNA nanotechnology has become an intriguing research area and metalated DNA three-dimensional cages are an attractive class of new materials, thanks to their good programmability and responsiveness. Since the discovery in 1991 of the first discrete 3D structure, different approaches have been developed.[125] The first one is based on a set of single-strand and cyclic DNA building blocks decorated

with aromatic rigid units at their vertices (***Figure 1.12a***).[126] Following this approach Sleiman and co-workers constructed a series of triangular, square, pentagonal and hexagonal prisms (***Figure 1.12b***).[126] Polyhedra with higher complexity, such as tetrahedra, dodecahedra, icosahedra, and a buckyball was instead synthesised by a hierarchical approach (***Figure 1.12c***). This latter approach relies on the association of identical symmetrical DNA three-point-star or five-point star tiles. Other 3D was based on DNA origami, that can extend using several approaches. A general one constated of rolling sheets of DNA helices to create multi-layered structures with enough rigidity to have 3D discrete structures.[127] The cross-section of these multi-layers can fall into two distinct lattices, *i.e.*, honeycomb or a square lattice. The first one was used to obtain objects that are more rigid per unit mass. The second one enabled construction of flatter surfaces, finer grade cavities, and denser objects.[127] The second approach was based on the wrapping of the scaffold strand around the entire structure, tetrahedral cages with inside closed by faces were designed following this synthetic strategy.[128] A double-helical DNA was bent to follow the rounded contours of a target object to make a DNA-urn (***Figure 1.12d***).[129] A third strategy, proposed by Kjems and co-workers, allowed to obtain a DNA box with a controllable lid. In this case, the strand was assembled into eight-connected origami square sheets describing the face of the cube (***Figure 1.12e***).[130] This approach was based on using concentric rings of DNA. Finally, Hogberg and co-workers in 2015 developed a method to create wireframed 3D structures. The approach based on reducing the structure into a triangulated 3D mesh and using an algorithm to trace the contour of the desired structure allowed to produce exotic and complex 3D structures (***Figure 1.12f***).

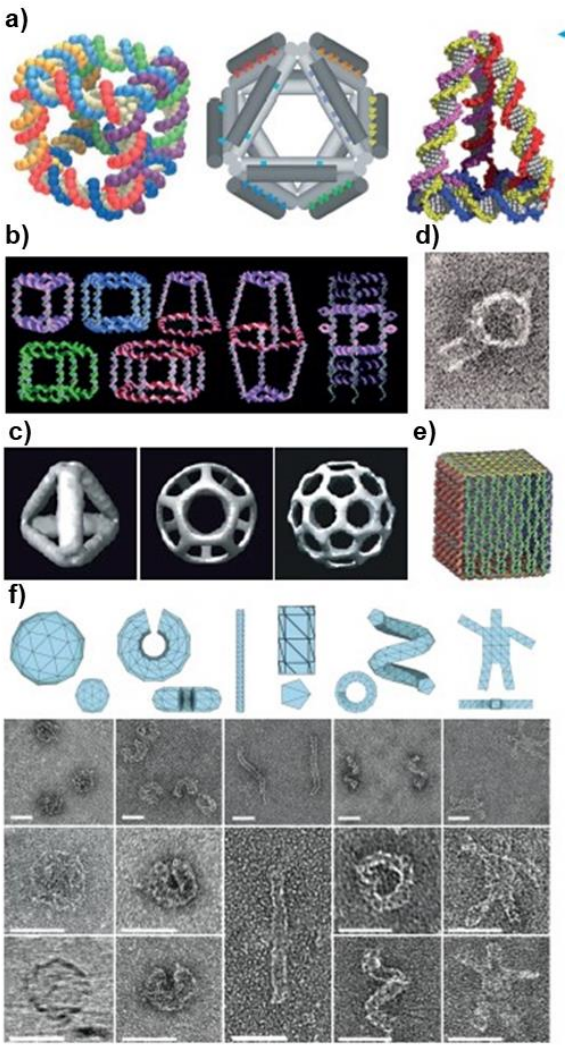

Figure 1.12: *Three-dimensional structures from DNA.* ***a)*** *The left panel shows a DNA cube constructed from connected three-arm junctions. The middle panel shows an octahedron constructed from a long DNA strand and five connecting strands. The right panel shows a tetrahedron constructed from four DNA single strands;* ***b)*** *A face-centred approach to build prismatic cages;* ***c)*** *Cryo-electron microscopy images of polyhedra assembled from DNA crossover tiles;* ***d)*** *Electron microscopy of a DNA 'urn' assembled by stacked concentric circles in an origami design;* ***e)*** *DNA origami sheets connected into a cube;* ***f)*** *Wireframe DNA origami structures, scale bars are 50nm. Reproduced with permission from Ref*[131]*, Copyright © 2017, Macmillan Publishers Limited.*

The synthesis of coordination structures from biomolecules was extremely challenging. Fujita and co-workers in 2018 reported the first example of synthetic β-barrel tertiary structures through metal directed self-assembly leading to folding of the peptide-based ligand.[132] The octapeptide FVFVXPGP was functionalised with two pyridyl metal-binding sites, so as to be able to form both a β-strand and a loop through self-assembly with different zinc (II) salts (ZnI_2, $ZnCl_2$ or $ZnBr_2$). The association created a pore bearing barrel made of three Zn_2L_2 macrocycles (***Figure 1.13***).

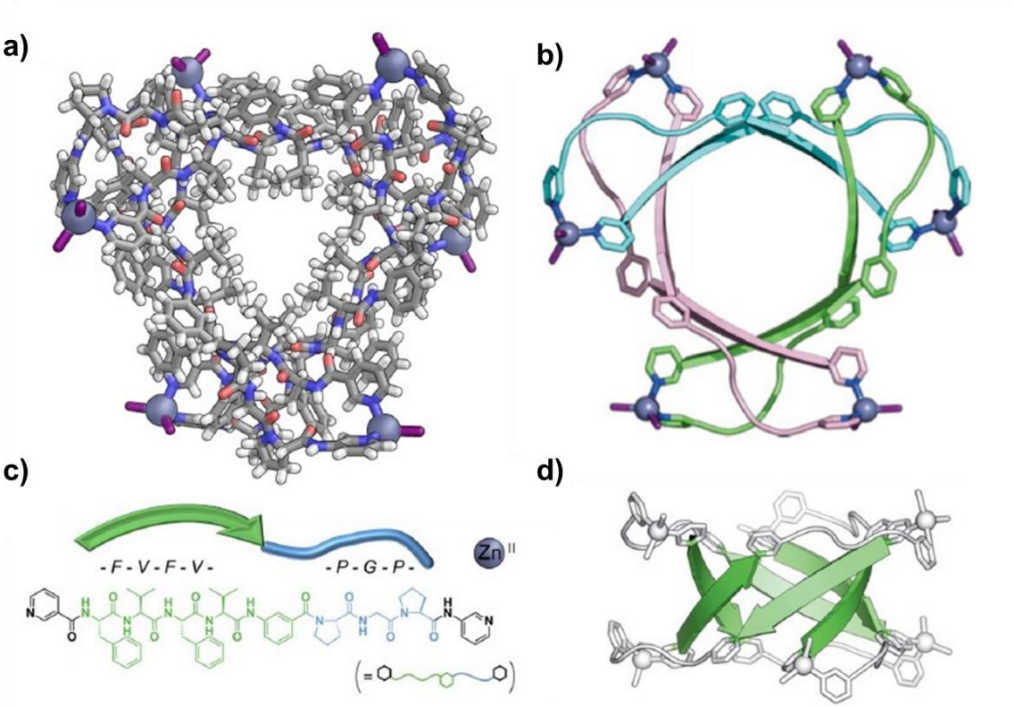

Figure 1.13: a) *Crystal structure of β-barrel made from three macrocyclic $Zn^{II}_2L_2$ units;* ***b)*** *The cartoon representation with each $Zn^{II}_2L_2$ unit in a different colour;* ***c)*** *Structure of the components used: octapeptide highlighting the barrel forming sequence (green arrow, F-V-F-V) and the loop forming sequence (blue string, P-G-P) and Zn^{II} (purple sphere);* ***d)*** *Side view of Fujita structures with β-strands highlighted in green. Reproduced with permission from Ref[132], Copyright © 2018, American Chemical Society.*

The challenges in the synthesis of biomolecular cages were overcome by developing nanoarchitectures where the core framework of the cage was maintained, and it was tagged with some biomolecules. This strategy allowed to improve biocompatibility, whilst preserving the main properties of the cage. Fujita reported in a pioneering work a hollow $Pd_{12}L_{24}$ capsule with peptides through amide coupling.[133] A similar strategy was used to functionalise the outside of a cage with different polysaccharides.[134, 135]

1.3.3. Porous materials based on gels and cages*

*Partly reproduced from Jahović, I., Zou, Y.-Q., Adorinni, S., *et al.* Matter **2021**, 4 (7), 2123.[136]

Soft materials have found use in many areas such as medicine, robotics, and battery research. These advances are the result of the properties of gels stemming from both their solid- and liquid-like features. However, fine-tuning of these properties and an onset of new applications can be envisaged if gels are coupled to metal-organic cages (MOCs), discrete three-dimensional structures containing well-defined cavities.

MOCs make good linkers within gels because the rules governing their formation are relatively well understood. These rules can be inferred from the coordination chemistry of their metal-ion vertices, together with the lengths and geometries of the multiply-binding, *i.e.* multitopic, organic ligands that link these metal ions together.[137-139] The host-guest chemistry of these cages can then be probed and rationalized, particularly for compact, isotropic guests that fit well within relatively spherical cavities.

Gels containing cages possess well-defined cavities stemming from the cages, in addition to the mesoscopic pores of the gel, which contain entrained solvent. However, embedding cages into porous materials might not only endow gels with features characteristic of the cages, but it could also lead to the development of new properties that have not been observed in soft materials before. Therefore, new functions could be programmed into the resulting materials. Research in this area has resulted in the design of self-healing porous polymers, as well as materials that show promise as systems for targeted drug delivery. However, further work is required to enable precise control and design of the structures of such systems so as to obtain hierarchical structures from a bottom-up approach.

Smart gels containing MOCs have found broad applications. For instance, they can be used for selective guest encapsulation. A polymeric hydrogel was reported to encapsulate fluorobenzene efficiently, as determined during guest binding studies.[140]This gel featured two distinct internal phases — the mesopores within the hydrogel and the inner cavities of the cages — which show selective guest uptake properties and differential release profiles.

As shown in ***Figure 1.14A***, guest release experiments were conducted using gels loaded with two similar molecules, benzene and anisole. Due to the size difference between the two molecules, benzene was found to occupy both the cage cavities and gel pores, while anisole was located only in the gel pores. Because anisole was too large for the cage cavity, it was released more rapidly than benzene from the gel into an adjacent aqueous phase. Interestingly, furan could serve as a competing guest and therefore it induced the release of benzene from the gel into the aqueous phase.

Some MOC-based gels also showed remarkable self-healing properties. A photoswitchable gels prepared by Johnson and coworkers exhibited self-healing behaviour. More specifically, the *o*-gel showed self-healing properties and the *c*-gel did not due to its slower exchange kinetics.[141] The difference between these two gels opened a new avenue for using a single material in applications that require both strength and self-healing,

albeit not both at once. In another example, Haino and co-workers constructed a self-healing gel from a polymer-attached metal organic cage with encapsulated polyester guest (***Figure 1.14B***).[142] At the concentration of 45 mM, the gel could heal itself within 10 minutes. The development of novel luminescent materials based on MOCs is an attractive area of research in materials science, as such materials can report, using light, upon their environment or the identity of a guest. For instance, Johnson's gel containing $Pd^{II}_{12}L_{24}$ cage gave rise to blue fluorescence under the irradiation of long-wavelength UV light when replacing the crosslinker with its pyrene containing variant (***Figure 1.14C***). The gel based on $Pd^{II}_{2}L_{4}$ cages and pillar[5]arenes fabricated by Huang and coworkers was found to be able to uptake and release certain drug molecules. The MOC gel could selectively encapsulate the drug molecule emodin and the dye methylene blue in its cage cavities and the pores of the gels, respectively. Upon heating and shaking, gel-sol transition took place, and methylene blue was first released from the gel into the aqueous phase (***Figure 1.14D***). Subsequently, treatment of the resulting mixture with excess acid led to the destruction of the MOC and the release of emodin. The property of gels to release different cargoes in a controlled manner may find applications in biology, including drug delivery.

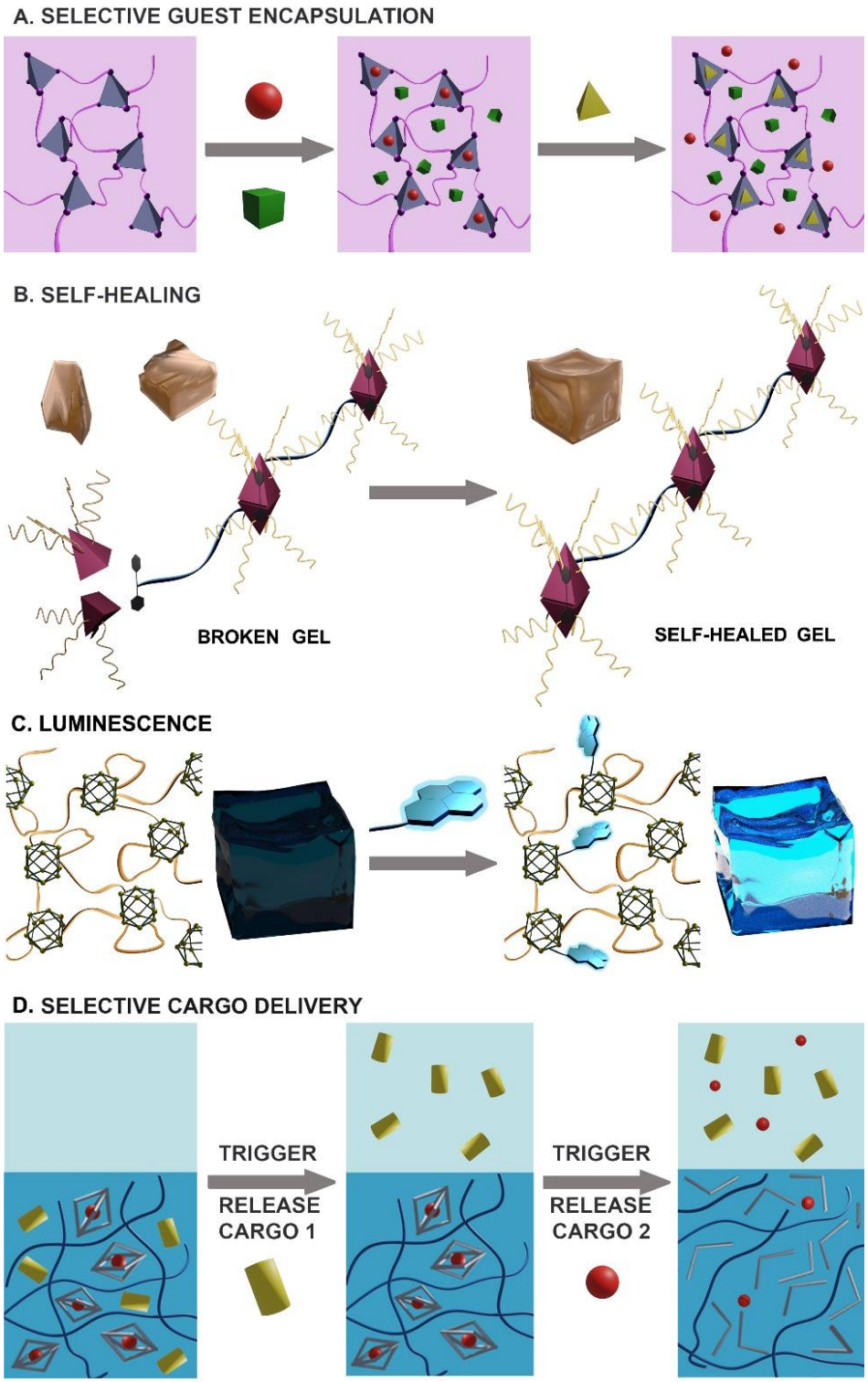

Figure 1.14: *Examples of MOC-gel applications.* ***(A)*** *Multiple-guest-selective capture (red ball, benzene; green cube, anisole; yellow tetrahedron, furan);* ***(B)*** *Supramolecular graft polymer and properties of self-healing;*[142] ***(C)*** *Luminescence arising from cross-linker substitution by a pyrene-containing analog;*[143] ***(D)*** *Selective cargo delivery.*

Besides guest encapsulation, self-healing, liquid crystals, luminescent materials and drug release, MOC-based gels were also used in catalysis. Recently, Johnson and co-workers synthesized an elegant $Cu^{II}_{24}L_{24}$-crosslinked polyMOC *c*-gel and successfully applied it to the copper-catalyzed alkyne-azide cycloaddition (CuAAC)

"click" reaction.[144] PolyMOC *c*-gel was fabricated from a 4-arm PEG star polymer functionalized with *m*-BDC (BDC = benzenedicarboxylate), an *m*-BDC derivatized coumarin-based ligand, benzophenone, $Cu^{II}(OAc)_2$, and ethyl-4–(dimethylamino)benzoate (EDMAB) (***Figure 1.15A***). The authors found this polyMOC *c*-gel could be reversibly switched between Cu^{II}, Cu^{I} and Cu^{0} states through photoreduction or air oxidation (***Figure 1.15B***). Upon irradiation with UV light, the *c*-gel disassembled into a green transparent liquid within 2 hours, and the photoexcited coumarin moiety reduced Cu^{II} to Cu^{I}. Further irradiation led to a brown liquid resulting from the formation of Cu^{0} nanoparticles. Interestingly, the polyMOC *c*-gel could be regenerated either from the Cu^{I} or Cu^{0} solution upon exposure to ambient air. To demonstrate the potential utility of the polyMOC *c*-gel, the authors showed that the "click" reaction between benzyl azide and tetrakis(prop-2-ynyloxymethyl)-methane proceeded smoothly in the presence of a catalytic amount of polyMOC *c*-gel upon UV irradiation, and the desired triazole product was isolated in 85% yield (***Figure 1.15C***).

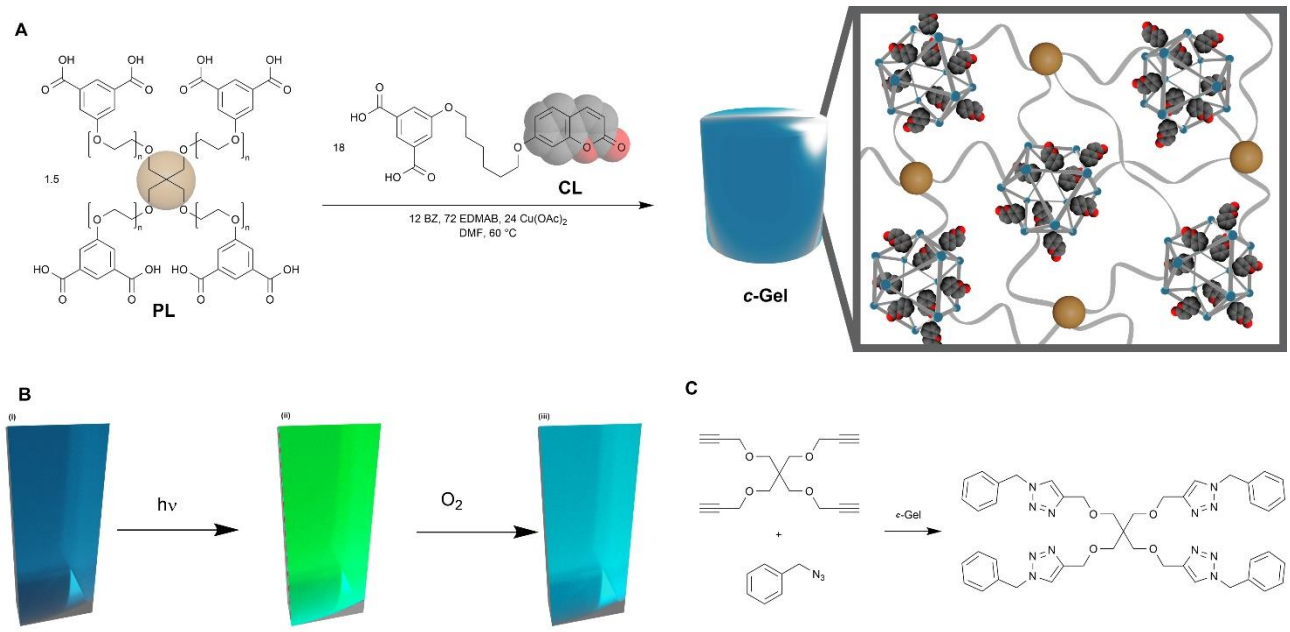

Figure 1.15: (A) *Synthesis of $Cu_{24}L_{24}$-cross-linked polyMOC c-gels from m-BDC-functionalized PEG star polymers (**PL**) and coumarin functionalized m-BDC (**CL**). DMF, dimethylformamide; EDMAB, ethyl-4-(dimethylamino)benzoate;* ***(B)*** *Images of c-gels (synthesized from 2 kDa a,w-azide-terminated PEG and tetrakis-alkyne) after annealing (i), after irradiation with UV light to induce the copper catalyzed alkyne-azide cycloaddition reaction (ii), and after reoxidation (iii);* ***(C)*** *PolyMOC c-gels catalyzed the alkyne-azide cycloaddition "click" reaction.*

1.4 Conclusion and outlook

*Partly reproduced from Jahović, I., Zou, Y.-Q., Adorinni, S., et al. Matter **2021**, 4 (7), 2123.[136]

Given the above discussion, further investigation and development of novel and already-existing applications of MOC-based gels are warranted. There is great potential for building upon the current applications, but also for devising new ones that could not previously be imagined. The field has already resulted in the fabrication of gels with tuneable mechanical properties. As a next step, we envisage systems consisting of arrays of cages which could change their architectural frameworks within the soft matter matrix. This would enable further fine-tuning of properties of both the cage micropores and gel mesopores, which could lead to the advent of attractive applications such as catalytic cascades or chemical separations. Finally, we suspect the future will bring further development of characterization methods for MOC-based gels, which will guide rational design and fabrication of these materials.

1.5 Outline and general aims of the thesis

As described in the sections above, there is a growing interest in the incorporation of MOCs into macroscopic gels to attain soft matter with addressable dual porosities that could yield smart materials with wide potential for applications. Furthermore, the interaction between MOCs and CNTs has not been explored thus far, and could lead to potentially interesting new ways to functionalise them. In general, the combination of nanotechnology with supramolecular chemistry, as well as the use of orthogonal supramolecular chemistries, are fertile areas for innovation and will be explored in this thesis.

In particular, **Chapter 2** describes the combination of minimalistic peptide self-assembly with MOCs to enable the hierarchical assembly of gelling MOCs with pendant peptides, so that, starting from very simple building blocks, macroscopic yet nanostructured gels with dual porosity can be attained.

Chapter 3 focusses on a similar approach, whereby self-assembling peptides decorate MOCs as peripheral ligands, but gelation is triggered by the addition of a second metal that coordinates the peptides' functional groups. This type of approach could be interesting to entrap heavy metals, which are used to trigger gelation.

Chapter 4 investigates the combination of MOCs with CNTs. In particular, the binding of different MOCs to CNTs is studied, as well their ability to transport CNTs across phases by changing their counterion. Finally, this strategy is tested for the phase-separation of CNTs based on their differing diameter.

Finally, **Chapter 5** will summarise the key findings of the thesis and identify further opportunities to bring forward the research in this exciting area.

1.6 Bibliography

(1) Amabilino, D. B.; Smith, D. K.; Steed, J. W. Supramolecular materials. *Chem. Soc. Rev.* **2017**, *46* (9), 2404-2420.

(2) Alemán, J. V.; Chadwick, A. V.; He, J.; Hess, M.; Horie, K.; Jones, R. G.; Kratochvíl, P.; Meisel, I.; Mita, I.; Moad, G.; et al. Definitions of terms relating to the structure and processing of sols, gels, networks, and inorganic-organic hybrid materials (IUPAC Recommendations 2007). *Pure Appl. Chem.* **2007**, *79* (10), 1801-1829.

(3) Flory, P. J. Introductory lecture. *Faraday Discuss.* **1974**, *57* (0), 7-18.

(4) Macret, M.; Hild, G. Hydroxyalkyl methacrylates: hydrogel formation based on the radical copolymerization of 2-hydroxyethylmethacrylate and 2,3-dihydroxypropylmethacrylate. *Polymer* **1982**, *23* (5), 748-753.

(5) Roorda, W.; De Vries, M.; De Leede, L.; De Boer, A.; Breimer, D.; Junginger, H. Zero-order release of oxprenolol-HCl, a new approach. *J. Control. Release.* **1988**, *7* (1), 45-52.

(6) Yean, L.; Bunel, C.; Vairon, J. P. Reversible immobilization of drugs on a hydrogel matrix, 2. Diffusion of free chloramphenicol from poly (2-hydroxyethyl methacrylate) hydrogels. *Die Makromolekulare Chemie: Macromolecular Chemistry and Physics* **1990**, *191* (5), 1119-1129.

(7) Andrade-Vivero, P.; Fernandez-Gabriel, E.; Alvarez-Lorenzo, C.; Concheiro, A. Improving the loading and release of NSAIDs from pHEMA hydrogels by copolymerization with functionalized monomers. *J Pharm Sci.* **2007**, *96* (4), 802-813.

(8) Brynda, E.; Cepalova, N.; Štol, M. Equilibrium adsorption of human serum albumin and human fibrinogen on hydrophobic and hydrophilic surfaces. *J. Biomed. Mater. Res.* **1984**, *18* (6), 685-693.

(9) Tanzawa, H.; Mori, Y.; Harumiya, N.; Miyama, H.; Hori, M.; Ohshima, N.; Idezuki, Y. Preparation and evaluation of a new athrombogenic heparinized hydrophilic polymer for use in cardiovascular system. *ASAIO J.* **1973**, *19* (1), 188-194.

(10) Calnan, J.; Pflug, J.; Chhabra, A.; Raghupati, N. Clinical and experimental studies of polyhydroxyethylmethacrylate gel ("hydron") for reconstructive surgery. *Br J Surg* **1971**, *24*, 113-124.

(11) Voldřrich, Z.; Tománek, Z.; Vacík, J.; Kopečcek, J. Long-term experience with poly (glycol monomethacrylate) gel in plastic operations of the nose. *J. Biomed. Mater. Res.* **1975**, *9* (6), 675-685.

(12) Wichterle, O.; Lim, D. Hydrophilic gels for biological use. *Nature* **1960**, *185* (4706), 117-118.
(13) Nicolson, P. C.; Vogt, J. Soft contact lens polymers: an evolution. *Biomaterials* **2001**, *22* (24), 3273-3283.
(14) Xinming, L.; Yingde, C.; Lloyd, A. W.; Mikhalovsky, S. V.; Sandeman, S. R.; Howel, C. A.; Liewen, L. Polymeric hydrogels for novel contact lens-based ophthalmic drug delivery systems: A review. *Contact Lens Anterior Eye* **2008**, *31* (2), 57-64.
(15) Carvalho, I.; Marques, C.; Oliveira, R.; Coelho, P.; Costa, P.; Ferreira, D. Sustained drug release by contact lenses for glaucoma treatment—A review. *J. Control. Release.* **2015**, *202*, 76-82.
(16) Lee, D.; Cho, S.; Park, H. S.; Kwon, I. Ocular Drug Delivery through pHEMA-Hydrogel Contact Lenses Co-Loaded with Lipophilic Vitamins. *Sci. Rep.***2016**, *6* (1), 34194.
(17) Gough, J. E.; Scotchford, C. A.; Downes, S. Cytotoxicity of glutaraldehyde crosslinked collagen/poly (vinyl alcohol) films is by the mechanism of apoptosis. *J. Biomed. Mater. Res.: An Official Journal of The Society for Biomaterials, The Japanese Society for Biomaterials, and The Australian Society for Biomaterials and the Korean Society for Biomaterials* **2002**, *61* (1), 121-130.
(18) Ikada, Y.; Mita, T.; Horii, F.; Sakurada, I.; Hatada, M. Preparation of hydrogels by radiation technique. *Radiat. Phys. Chem. (1977)* **1977**, *9* (4-6), 633-645.
(19) Danno, A. Gel formation of aqueous solution of polyvinyl alcohol irradiated by gamma rays from cobalt-60. *J. Phys. Soc. Japan***1958**, *13* (7), 722-727.
(20) Hafezi Moghaddam, R.; Dadfarnia, S.; Shabani, A. M. H.; Amraei, R.; Hafezi Moghaddam, Z. Doxycycline drug delivery using hydrogels of O-carboxymethyl chitosan conjugated with caffeic acid and its composite with polyacrylamide synthesized by electron beam irradiation. *Int. J. Biol. Macromol.* **2020**, *154*, 962-973.
(21) Juby, K. A.; Dwivedi, C.; Kumar, M.; Kota, S.; Misra, H. S.; Bajaj, P. N. Silver nanoparticle-loaded PVA/gum acacia hydrogel: Synthesis, characterization and antibacterial study. *Carbohydr. Polym.* **2012**, *89* (3), 906-913.
(22) Gad, Y. Preparation and characterization of poly (2-acrylamido-2-methylpropane-sulfonic acid)/Chitosan hydrogel using gamma irradiation and its application in wastewater treatment. *Radiat. Phys. Chem.* **2008**, *77* (9), 1101-1107.
(23) Hennink, W. E.; van Nostrum, C. F. Novel crosslinking methods to design hydrogels. *Adv. Drug Deliv. Rev.* **2012**, *64*, 223-236.
(24) Chen, R. T.; Marchesan, S.; Evans, R. A.; Styan, K. E.; Such, G. K.; Postma, A.; McLean, K. M.; Muir, B. W.; Caruso, F. Photoinitiated Alkyne–Azide Click and Radical Cross-Linking Reactions for the Patterning of PEG Hydrogels. *Biomacromolecules* **2012**, *13* (3), 889-895.
(25) Lee, Y.; Song, W. J.; Sun, J. Y. Hydrogel soft robotics. *Mater. Today Phys.* **2020**, *15*, 100258.
(26) Buwalda, S. J.; Boere, K. W. M.; Dijkstra, P. J.; Feijen, J.; Vermonden, T.; Hennink, W. E. Hydrogels in a historical perspective: From simple networks to smart materials. *J. Control. Release.* **2014**, *190*, 254-273.

(27) Zheng, J.; Xiao, P.; Le, X.; Lu, W.; Théato, P.; Ma, C.; Du, B.; Zhang, J.; Huang, Y.; Chen, T. Mimosa inspired bilayer hydrogel actuator functioning in multi-environments. *J. Mater. Chem. C* **2018**, *6* (6), 1320-1327.

(28) Takashima, Y.; Hatanaka, S.; Otsubo, M.; Nakahata, M.; Kakuta, T.; Hashidzume, A.; Yamaguchi, H.; Harada, A. Expansion–contraction of photoresponsive artificial muscle regulated by host–guest interactions. *Nat. Commun.* **2012**, *3* (1), 1270.

(29) Sather, N. A.; Sai, H.; Sasselli, I. R.; Sato, K.; Ji, W.; Synatschke, C. V.; Zambrotta, R. T.; Edelbrock, J. F.; Kohlmeyer, R. R.; Hardin, J. O.; et al. 3D Printing of Supramolecular Polymer Hydrogels with Hierarchical Structure. *Small* **2021**, *17* (5), 2005743.

(30) Reches, M.; Gazit, E. Casting Metal Nanowires Within Discrete Self-Assembled Peptide Nanotubes. *Science* **2003**, *300* (5619), 625-627.

(31) Garcia, A. M.; Iglesias, D.; Parisi, E.; Styan, K. E.; Waddington, L. J.; Deganutti, C.; De Zorzi, R.; Grassi, M.; Melchionna, M.; Vargiu, A. V. Chirality effects on peptide self-assembly unraveled from molecules to materials. *Chem* **2018**, *4* (8), 1862-1876.

(32) Zozulia, O.; Dolan, M. A.; Korendovych, I. V. Catalytic peptide assemblies. *Chem. Soc. Rev.* **2018**, *47* (10), 3621-3639.

(33) Garcia, A. M.; Kurbasic, M.; Kralj, S.; Melchionna, M.; Marchesan, S. A biocatalytic and thermoreversible hydrogel from a histidine-containing tripeptide. *ChemComm* **2017**, *53* (58), 8110-8113,

(34) Kurbasic, M.; Garcia, A. M.; Viada, S.; Marchesan, S. Heterochiral tetrapeptide self-assembly into hydrogel biomaterials for hydrolase mimicry. *J. Pept. Sci.* **2022**, *28* (1), e3304.

(35) Biswas, S.; Kumar, M.; Levine, A. M.; Jimenez, I.; Ulijn, R. V.; Braunschweig, A. B. Visible-light photooxidation in water by 1O2-generating supramolecular hydrogels. *Chem. Sci.* **2020**, *11* (16), 4239-4245,

(36) Adorinni, S.; Gentile, S.; Bellotto, O.; Kralj, S.; Parisi, E.; Cringoli, M.; Deganutti, C.; Malloci, G.; Piccirilli, F.; Pengo, P. Peptide stereochemistry effects from pKa-shift to gold nanoparticle templating in a supramolecular hydrogel. **2023**.

(37) Garcia, A. M.; Melchionna, M.; Bellotto, O.; Kralj, S.; Semeraro, S.; Parisi, E.; Iglesias, D.; D'Andrea, P.; De Zorzi, R.; Vargiu, A. V.; et al. Nanoscale Assembly of Functional Peptides with Divergent Programming Elements. *ACS Nano* **2021**, *15* (2), 3015-3025.

(38) Kurbasic, M. SELF-ASSEMBLY DEI PEPTIDI ETEROCHIRALI IN IDROGEL ANTIMICROBICI. **2020**.

(39) Garcia, A. M.; Lavendomme, R.; Kralj, S.; Kurbasic, M.; Bellotto, O.; Cringoli, M. C.; Semeraro, S.; Bandiera, A.; De Zorzi, R.; Marchesan, S. Self-Assembly of an Amino Acid Derivative into an Antimicrobial Hydrogel Biomaterial. *Chem. Eur. J.* **2020**, *26* (8), 1880-1886.

(40) Rosetti, B.; Scarel, E.; Colomina-Alfaro, L.; Adorinni, S.; Pierri, G.; Bellotto, O.; Mamprin, K.; Polentarutti, M.; Bandiera, A.; Tedesco, C.; et al. Self-Assembly of Homo- and Hetero-Chiral Cyclodipeptides into Supramolecular Polymers towards Antimicrobial Gels. *Polymers* **2022**, *14* (21), 4554.

(41) Marchesan, S.; Qu, Y.; Waddington, L. J.; Easton, C. D.; Glattauer, V.; Lithgow, T. J.; McLean, K. M.; Forsythe, J. S.; Hartley, P. G. Self-assembly of ciprofloxacin and a tripeptide into an antimicrobial nanostructured hydrogel. *Biomaterials* **2013**, *34* (14), 3678-3687.

(42) Kurbasic, M.; Romano, C. D.; Garcia, A. M.; Kralj, S.; Marchesan, S. Assembly of a Tripeptide and Anti-Inflammatory Drugs into Supramolecular Hydrogels for Sustained Release. *Gels* **2017**, *3* (3), 29.

(43) Parisi, E.; Garcia, A. M.; Marson, D.; Posocco, P.; Marchesan, S. Supramolecular Tripeptide Hydrogel Assembly with 5-Fluorouracil. *Gels* **2019**, *5* (1), 5.

(44) Adorinni, S.; Cringoli, M. C.; Perathoner, S.; Fornasiero, P.; Marchesan, S. Green Approaches to Carbon Nanostructure-Based Biomaterials. *Appl. Sci.* **2021**, *11* (6), 2490.

(45) Georgakilas, V.; Perman, J. A.; Tucek, J.; Zboril, R. Broad family of carbon nanoallotropes: classification, chemistry, and applications of fullerenes, carbon dots, nanotubes, graphene, nanodiamonds, and combined superstructures. *Chem. Rev.* **2015**, *115* (11), 4744-4822.

(46) Mchedlov-Petrossyan, N. O. Fullerenes in liquid media: an unsettling intrusion into the solution chemistry. *Chem. Rev.* **2013**, *113* (7), 5149-5193.

(47) Yang, F.; Wang, M.; Zhang, D.; Yang, J.; Zheng, M.; Li, Y. Chirality pure carbon nanotubes: Growth, sorting, and characterization. *Chem. Rev.* **2020**, *120* (5), 2693-2758.

(48) Tasis, D.; Tagmatarchis, N.; Bianco, A.; Prato, M. Chemistry of carbon nanotubes. *Chem. Rev.* **2006**, *106* (3), 1105-1136.

(49) Fadeel, B.; Bussy, C.; Merino, S.; Vázquez, E.; Flahaut, E.; Mouchet, F.; Evariste, L.; Gauthier, L.; Koivisto, A. J.; Vogel, U. Safety assessment of graphene-based materials: focus on human health and the environment. *ACS nano* **2018**, *12* (11), 10582-10620.

(50) Giordani, S.; Camisasca, A.; Maffeis, V. Carbon nano-onions: A valuable class of carbon nanomaterials in biomedicine. *Curr. Med. Chem.***2019**, *26* (38), 6915-6929.

(51) Karousis, N.; Suarez-Martinez, I.; Ewels, C. P.; Tagmatarchis, N. Structure, properties, functionalization, and applications of carbon nanohorns. *Chem. Rev.* **2016**, *116* (8), 4850-4883.

(52) Lin, C.-T.; Lee, C.-Y.; Chiu, H.-T.; Chin, T.-S. Graphene structure in carbon nanocones and nanodiscs. *Langmuir* **2007**, *23* (26), 12806-12810.

(53) Basso, L.; Cazzanelli, M.; Orlandi, M.; Miotello, A. Nanodiamonds: Synthesis and application in sensing, catalysis, and the possible connection with some processes occurring in space. *Appl. Sci.* **2020**, *10* (12), 4094.

(54) Liu, J.; Li, R.; Yang, B. Carbon dots: A new type of carbon-based nanomaterial with wide applications. *ACS Cent. Sci.* **2020**, *6* (12), 2179-2195.

(55) Li, Z.; Liu, Z.; Sun, H.; Gao, C. Superstructured assembly of nanocarbons: fullerenes, nanotubes, and graphene. *Chem. Rev.* **2015**, *115* (15), 7046-7117.

(56) Sun, Z.; Fang, S.; Hu, Y. H. 3D graphene materials: from understanding to design and synthesis control. *Chem. Rev.* **2020**, *120* (18), 10336-10453.

(57) Loh, K. P.; Ho, D.; Chiu, G. N. C.; Leong, D. T.; Pastorin, G.; Chow, E. K. H. Clinical applications of carbon nanomaterials in diagnostics and therapy.Adv. Mater. **2018**, *30* (47), 1802368.

(58) Plonska-Brzezinska, M. E. Carbon nanomaterials: Perspective of their applications in biomedicine. *Curr. Med. Chem.***2019**, *26* (38), 6832-6833.
(59) Gupta, T. K.; Budarapu, P. R.; Chappidi, S. R.; YB, S. S.; Paggi, M.; Bordas, S. P. Advances in carbon based nanomaterials for bio-medical applications. *Curr. Med. Chem.***2019**, *26* (38), 6851-6877.
(60) Teradal, N. L.; Jelinek, R. Carbon nanomaterials in biological studies and biomedicine. *Adv. Healthc. Mater.* **2017**, *6* (17), 1700574.
(61) Mehra, N. K.; Jain, A. K.; Nahar, M. Carbon nanomaterials in oncology: An expanding horizon. *Drug Discov. Today* **2018**, *23* (5), 1016-1025.
(62) Augustine, S.; Singh, J.; Srivastava, M.; Sharma, M.; Das, A.; Malhotra, B. D. Recent advances in carbon based nanosystems for cancer theranostics. *Biomater Sci.***2017**, *5* (5), 901-952.
(63) Hosnedlova, B.; Kepinska, M.; Fernandez, C.; Peng, Q.; Ruttkay-Nedecky, B.; Milnerowicz, H.; Kizek, R. Carbon nanomaterials for targeted cancer therapy drugs: A critical review. *Chem Rec* **2019**, *19* (2-3), 502-522.
(64) Saleem, J.; Wang, L.; Chen, C. Carbon-based nanomaterials for cancer therapy via targeting tumor microenvironment. *Adv. Healthc. Mater.* **2018**, *7* (20), 1800525.
(65) Zhao, Q.; Lin, Y.; Han, N.; Li, X.; Geng, H.; Wang, X.; Cui, Y.; Wang, S. Mesoporous carbon nanomaterials in drug delivery and biomedical application. *Drug Del.* **2017**, *24* (2), 94-107.
(66) Bartelmess, J.; Quinn, S.; Giordani, S. Carbon nanomaterials: multi-functional agents for biomedical fluorescence and Raman imaging. *Chem. Soc. Rev.* **2015**, *44* (14), 4672-4698.
(67) Sainio, S.; Leppänen, E.; Mynttinen, E.; Palomäki, T.; Wester, N.; Etula, J.; Isoaho, N.; Peltola, E.; Koehne, J.; Meyyappan, M. Integrating carbon nanomaterials with metals for bio-sensing applications. *Mol. Neurobiol.* **2020**, *57*, 179-190.
(68) Kim, M.; Jang, J.; Cha, C. Carbon nanomaterials as versatile platforms for theranostic applications. *Drug Discov. Today* **2017**, *22* (9), 1430-1437.
(69) Mishra, V.; Patil, A.; Thakur, S.; Kesharwani, P. Carbon dots: emerging theranostic nanoarchitectures. *Drug Discov. Today* **2018**, *23* (6), 1219-1232.
(70) Marchesan, S.; Kostarelos, K.; Bianco, A.; Prato, M. The winding road for carbon nanotubes in nanomedicine. *Mater. Today* **2015**, *18* (1), 12-19.
(71) Hansen, S. F.; Lennquist, A. Carbon nanotubes added to the SIN List as a nanomaterial of Very High Concern. *Nat. Nanotechnol.* **2020**, *15* (1), 3-4.
(72) Heller, D. A.; Jena, P. V.; Pasquali, M.; Kostarelos, K.; Delogu, L. G.; Meidl, R. E.; Rotkin, S. V.; Scheinberg, D. A.; Schwartz, R. E.; Terrones, M. Banning carbon nanotubes would be scientifically unjustified and damaging to innovation. *Nat. Nanotechnol.* **2020**, *15* (3), 164-166.
(73) Aoki, K.; Saito, N. Biocompatibility and carcinogenicity of carbon nanotubes as biomaterials. *Nanomaterials* **2020**, *10* (2), 264.
(74) Marchesan, S.; Bosi, S.; Alshatwi, A.; Prato, M. Carbon nanotubes for organ regeneration: An electrifying performance. *Nano Today* **2016**, *11* (4), 398-401.

(75) Paez-Mayorga, J.; Hernández-Vargas, G.; Ruiz-Esparza, G.; Iqbal, H.; Wang, X.; Zhang, Y.; Parra-Saldivar, R.; Khademhosseini, A. Bioreactors for Cardiac Tissue Engineering, Adv. Healthc. Mater. 8 (2019) 1701504.

(76) Marchesan, S.; Ballerini, L.; Prato, M. Nanomaterials for stimulating nerve growth. *Science* **2017**, *356* (6342), 1010-1011.

(77) Aoki, K.; Ogihara, N.; Tanaka, M.; Haniu, H.; Saito, N. Carbon nanotube-based biomaterials for orthopaedic applications. *J Mater Chem B.* **2020**, *8* (40), 9227-9238.

(78) Mori, H.; Ogura, Y.; Enomoto, K.; Hara, M.; Maurstad, G.; Stokke, B. T.; Kitamura, S. Dense carbon-nanotube coating scaffolds stimulate osteogenic differentiation of mesenchymal stem cells. *PLoS One* **2020**, *15* (1), e0225589.

(79) Lekshmi, G.; Sana, S. S.; Nguyen, V.-H.; Nguyen, T. H. C.; Nguyen, C. C.; Le, Q. V.; Peng, W. Recent progress in carbon nanotube polymer composites in tissue engineering and regeneration. *Int. J. Mol. Sci.***2020**, *21* (17), 6440.

(80) Teixeira-Santos, R.; Gomes, M.; Gomes, L. C.; Mergulhao, F. J. Antimicrobial and anti-adhesive properties of carbon nanotube-based surfaces for medical applications: A systematic review. *Iscience* **2021**, *24* (1).

(81) Anaya-Plaza, E.; Shaukat, A.; Lehtonen, I.; Kostiainen, M. A. Biomolecule-Directed Carbon Nanotube Self-Assembly. *Adv. Healthc. Mater.* **2021**, *10* (1), 2001162.

(82) Deshmukh, M. A.; Jeon, J.-Y.; Ha, T.-J. Carbon nanotubes: An effective platform for biomedical electronics. *Biosens. Bioelectron.* **2020**, *150*, 111919.

(83) Chen, M.; Qin, X.; Zeng, G. Biodegradation of carbon nanotubes, graphene, and their derivatives. *Trends Biotechnol.* **2017**, *35* (9), 836-846.

(84) Dubey, R.; Dutta, D.; Sarkar, A.; Chattopadhyay, P. Functionalized carbon nanotubes: synthesis, properties and applications in water purification, drug delivery, and material and biomedical sciences. *Nanoscale Advances* **2021**, *3* (20), 5722-5744.

(85) Mickelson, E. T.; Huffman, C. B.; Rinzler, A. G.; Smalley, R. E.; Hauge, R. H.; Margrave, J. L. Fluorination of single-wall carbon nanotubes. *Chem. Phys. Lett.* **1998**, *296* (1), 188-194.

(86) Khabashesku, V. N.; Billups, W. E.; Margrave, J. L. Fluorination of Single-Wall Carbon Nanotubes and Subsequent Derivatization Reactions. *Acc. Chem. Res.* **2002**, *35* (12), 1087-1095.

(87) Pinkerton, F. E.; Wicke, B. G.; Olk, C. H.; Tibbetts, G. G.; Meisner, G. P.; Meyer, M. S.; Herbst, J. F. Thermogravimetric Measurement of Hydrogen Absorption in Alkali-Modified Carbon Materials. *J. Phys. Chem. B* **2000**, *104* (40), 9460-9467.

(88) Tagmatarchis, N.; Prato, M. Functionalization of carbon nanotubes via 1,3-dipolar cycloadditions. *J. Mater. Chem.* **2004**, *14* (4), 437-439.

(89) Bahr, J. L.; Yang, J.; Kosynkin, D. V.; Bronikowski, M. J.; Smalley, R. E.; Tour, J. M. Functionalization of Carbon Nanotubes by Electrochemical Reduction of Aryl Diazonium Salts: A Bucky Paper Electrode. *J. Am. Chem. Soc.* **2001**, *123* (27), 6536-6542.

(90) Bahr, J. L.; Tour, J. M. Highly Functionalized Carbon Nanotubes Using in Situ Generated Diazonium Compounds. *Chem. Mater.* **2001**, *13* (11), 3823-3824.
(91) Wang, J. Carbon-nanotube based electrochemical biosensors: A review. *Electroanalysis: An International Journal Devoted to Fundamental and Practical Aspects of Electroanalysis* **2005**, *17* (1), 7-14.
(92) Harrison, B. S.; Atala, A. Carbon nanotube applications for tissue engineering. *Biomaterials* **2007**, *28* (2), 344-353.
(93) Bianco, A.; Kostarelos, K.; Prato, M. Applications of carbon nanotubes in drug delivery. *Curr Opin Chem Biol* **2005**, *9* (6), 674-679.
(94) Yan, Y.; Miao, J.; Yang, Z.; Xiao, F.-X.; Yang, H. B.; Liu, B.; Yang, Y. Carbon nanotube catalysts: recent advances in synthesis, characterization and applications. *Chem. Soc. Rev.* **2015**, *44* (10), 3295-3346.
(95) Su, D. S.; Perathoner, S.; Centi, G. Nanocarbons for the development of advanced catalysts. *Chem. Rev.* **2013**, *113* (8), 5782-5816.
(96) Zhang, Q.; Huang, J. Q.; Qian, W. Z.; Zhang, Y. Y.; Wei, F. The road for nanomaterials industry: A review of carbon nanotube production, post-treatment, and bulk applications for composites and energy storage. *Small* **2013**, *9* (8), 1237-1265.
(97) López-Moreno, A.; Villalva, J.; Pérez, E. M. Mechanically interlocked derivatives of carbon nanotubes: synthesis and potential applications. *Chem. Soc. Rev.* **2022**, *51* (23), 9433-9444.
(98) de Juan, A.; Pouillon, Y.; Ruiz-González, L.; Torres-Pardo, A.; Casado, S.; Martín, N.; Rubio, Á.; Pérez, E. M. Mechanically Interlocked Single-Wall Carbon Nanotubes. *Angew. Chem. Int. Ed.***2014**, *53* (21), 5394-5400.
(99) Balakrishna, B.; Menon, A.; Cao, K.; Gsänger, S.; Beil, S. B.; Villalva, J.; Shyshov, O.; Martin, O.; Hirsch, A.; Meyer, B.; et al. Dynamic Covalent Formation of Concave Disulfide Macrocycles Mechanically Interlocked with Single-Walled Carbon Nanotubes. *Angew. Chem. Int. Ed.***2020**, *59* (42), 18774-18785.
(100) Miki, K.; Saiki, K.; Umeyama, T.; Baek, J.; Noda, T.; Imahori, H.; Sato, Y.; Suenaga, K.; Ohe, K. Unique Tube–Ring Interactions: Complexation of Single-Walled Carbon Nanotubes with Cycloparaphenyleneacetylenes. *Small* **2018**, *14* (26), 1800720.
(101) Chamorro, R.; de Juan-Fernández, L.; Nieto-Ortega, B.; Mayoral, M. J.; Casado, S.; Ruiz-González, L.; Pérez, E. M.; González-Rodríguez, D. Reversible dispersion and release of carbon nanotubes via cooperative clamping interactions with hydrogen-bonded nanorings. *Chem. Sci.* **2018**, *9* (17), 4176-4184.
(102) Cheng, G.; Hayashi, T.; Miyake, Y.; Sato, T.; Tabata, H.; Katayama, M.; Komatsu, N. Interlocking of Single-Walled Carbon Nanotubes with Metal-Tethered Tetragonal Nanobrackets to Enrich a Few Hundredths of a Nanometer Range in Their Diameters. *ACS Nano* **2022**, *16* (8), 12500-12510.
(103) Malicka, J. M.; Sandeep, A.; Monti, F.; Bandini, E.; Gazzano, M.; Ranjith, C.; Praveen, V. K.; Ajayaghosh, A.; Armaroli, N. Ultrasound Stimulated Nucleation and Growth of a Dye Assembly into Extended Gel Nanostructures. *Chem. Eur. J.* **2013**, *19* (39), 12991-13001.

(104) Iglesias, D.; Melle-Franco, M.; Kurbasic, M.; Melchionna, M.; Abrami, M.; Grassi, M.; Prato, M.; Marchesan, S. Oxidized Nanocarbons-Tripeptide Supramolecular Hydrogels: Shape Matters! *ACS Nano* **2018**, *12* (6), 5530-5538.

(105) Rozhin, P.; Adorinni, S.; Iglesias, D.; Mackiol, T.; Kralj, S.; Bisetto, M.; Abrami, M.; Grassi, M.; Bevilacqua, M.; Fornasiero, P.; et al. Nanocomposite Hydrogels with Self-Assembling Peptide-Functionalized Carbon Nanostructures. *Chem. Eur. J. n/a* (n/a), e202301708.

(106) Abubakre, O. K.; Medupin, R. O.; Akintunde, I. B.; Jimoh, O. T.; Abdulkareem, A. S.; Muriana, R. A.; James, J. A.; Ukoba, K. O.; Jen, T.-C.; Yoro, K. O. Carbon nanotube-reinforced polymer nanocomposites for sustainable biomedical applications: A review. *J SCI-ADV MATER DEV* **2023**, *8* (2), 100557.

(107) Mensah, B.; Kim, H. G.; Lee, J.-H.; Arepalli, S.; Nah, C. Carbon nanotube-reinforced elastomeric nanocomposites: a review. *Int. J. Smart Nano Mater.* **2015**, *6* (4), 211-238.

(108) Chakrabarty, R.; Mukherjee, P. S.; Stang, P. J. Supramolecular Coordination: Self-Assembly of Finite Two- and Three-Dimensional Ensembles. *Chem. Rev.* **2011**, *111* (11), 6810-6918.

(109) Fujita, M.; Yazaki, J.; Ogura, K. Preparation of a macrocyclic polynuclear complex,[(en) Pd (4, 4'-bpy)] 4 (NO3) 8 (en= ethylenediamine, bpy= bipyridine), which recognizes an organic molecule in aqueous media. *J. Am. Chem. Soc.* **1990**, *112* (14), 5645-5647.

(110) Makoto, F.; Jun, Y.; Katsuyuki, O. Spectroscopic Observation of Self-Assembly of a Macrocyclic Tetranuclear Complex Composed of Pt2+ and 4,4′-Bipyridine. *Chem. Lett.* **1991**, *20* (6), 1031-1032.

(111) Stang, P. J.; Cao, D. H. Transition metal based cationic molecular boxes. Self-assembly of macrocyclic platinum (II) and palladium (II) tetranuclear complexes. *J. Am. Chem. Soc.* **1994**, *116* (11), 4981-4982.

(112) Caulder, D. L.; Raymond, K. N. Supermolecules by Design. *Acc. Chem. Res.* **1999**, *32* (11), 975-982.

(113) L. Caulder, D.; N. Raymond, K. The rational design of high symmetry coordination clusters†. *J. Chem. Soc., Dalton trans.* **1999**, (8), 1185-1200.

(114) Fujita, M.; Umemoto, K.; Yoshizawa, M.; Fujita, N.; Kusukawa, T.; Biradha, K. Molecular paneling coordination. *ChemComm* **2001**, (6), 509-518.

(115) Fujita, M.; Tominaga, M.; Hori, A.; Therrien, B. Coordination Assemblies from a Pd(II)-Cornered Square Complex. *Acc. Chem. Res.* **2005**, *38* (4), 369-378.

(116) MacGillivray, L. R.; Atwood, J. L. Structural Classification and General Principles for the Design of Spherical Molecular Hosts. *Angew. Chem. Int. Ed.***1999**, *38* (8), 1018-1033.

(117) Gianneschi, N. C.; Masar, M. S.; Mirkin, C. A. Development of a Coordination Chemistry-Based Approach for Functional Supramolecular Structures. *Acc. Chem. Res.* **2005**, *38* (11), 825-837.

(118) Cotton, F. A.; Lin, C.; Murillo, C. A. The use of dimetal building blocks in convergent syntheses of large arrays. *Proc. Natl. Acad. Sci. U.S.A.* **2002**, *99* (8), 4810-4813.

(119) Cram, D. J. The Design of Molecular Hosts, Guests, and Their Complexes (Nobel Lecture). *Angew. Chem. Int. Ed.in English* **1988**, *27* (8), 1009-1020.

(120) Fischer, E. The influence of configuration on enzyme activity. *Dtsch. Chem. Ges* **1894**, *27*, 2984-2993.

(121) Ehrlich, P. Experimentelle untersuchungen über immunität. I. Ueber ricin. *DMW-Deutsche Medizinische Wochenschrift* **1891**, *17* (32), 976-979.

(122) Ehrlich, P. Experimentelle untersuchungen über immunität. II. Ueber abrin. *DMW-Deutsche Medizinische Wochenschrift* **1891**, *17* (44), 1218-1219.

(123) Ehrlich, P. Die seitenkettentheorie und ihre gegner. *Münchner Med Wochenschr* **1901**, *52*, 2123-2124.

(124) Ehrlich, P. Die schutzstoffe des blutes. *DMW-Deutsche Medizinische Wochenschrift* **1901**, *27* (52), 913-916.

(125) Chen, J.; Seeman, N. C. Synthesis from DNA of a molecule with the connectivity of a cube. *Nature* **1991**, *350* (6319), 631-633.

(126) Aldaye, F. A.; Sleiman, H. F. Modular Access to Structurally Switchable 3D Discrete DNA Assemblies. *J. Am. Chem. Soc.* **2007**, *129* (44), 13376-13377.

(127) Shih, W. M.; Lin, C. Knitting complex weaves with DNA origami. *Curr. Opin. Struct.* **2010**, *20* (3), 276-282.

(128) Ke, Y.; Sharma, J.; Liu, M.; Jahn, K.; Liu, Y.; Yan, H. Scaffolded DNA Origami of a DNA Tetrahedron Molecular Container. *Nano Lett.***2009**, *9* (6), 2445-2447.

(129) Han, D.; Pal, S.; Nangreave, J.; Deng, Z.; Liu, Y.; Yan, H. DNA Origami with Complex Curvatures in Three-Dimensional Space. *Science* **2011**, *332* (6027), 342-346. DOI: doi:10.1126/science.1202998.

(130) Andersen, E. S.; Dong, M.; Nielsen, M. M.; Jahn, K.; Subramani, R.; Mamdouh, W.; Golas, M. M.; Sander, B.; Stark, H.; Oliveira, C. L. P.; et al. Self-assembly of a nanoscale DNA box with a controllable lid. *Nature* **2009**, *459* (7243), 73-76.

(131) Seeman, N. C.; Sleiman, H. F. DNA nanotechnology. *Nat. Rev. Mater.* **2017**, *3* (1), 17068.

(132) Yamagami, M.; Sawada, T.; Fujita, M. Synthetic β-Barrel by Metal-Induced Folding and Assembly. *J. Am. Chem. Soc.* **2018**, *140* (28), 8644-8647.

(133) Suzuki, K.; Kawano, M.; Sato, S.; Fujita, M. Endohedral Peptide Lining of a Self-Assembled Molecular Sphere To Generate Chirality-Confined Hollows. *J. Am. Chem. Soc.* **2007**, *129* (35), 10652-10653.

(134) Kamiya, N.; Tominaga, M.; Sato, S.; Fujita, M. Saccharide-Coated M12L24 Molecular Spheres That Form Aggregates by Multi-interaction with Proteins. *J. Am. Chem. Soc.* **2007**, *129* (13), 3816-3817.

(135) Yan, G.; Yamaguchi, T.; Suzuki, T.; Yanaka, S.; Sato, S.; Fujita, M.; Kato, K. Hyper-Assembly of Self-Assembled Glycoclusters Mediated by Specific Carbohydrate–Carbohydrate Interactions. *Chem Asian J* **2017**, *12* (9), 968-972.

(136) Jahović, I.; Zou, Y.-Q.; Adorinni, S.; Nitschke, J. R.; Marchesan, S. Cages meet gels: Smart materials with dual porosity. *Matter* **2021**, *4* (7), 2123-2140.

(137) Yoshizawa, M.; Klosterman, J. K.; Fujita, M. Functional molecular flasks: new properties and reactions within discrete, self-assembled hosts. *Angew. Chem. Int. Ed.***2009**, *48* (19), 3418-3438.

(138) Cook, T. R.; Zheng, Y.-R.; Stang, P. J. Metal–organic frameworks and self-assembled supramolecular coordination complexes: comparing and contrasting the design, synthesis, and functionality of metal–organic materials. *Chem. Rev.* **2013**, *113* (1), 734-777.

(139) Brown, C. J.; Toste, F. D.; Bergman, R. G.; Raymond, K. N. Supramolecular catalysis in metal–ligand cluster hosts. *Chem. Rev.* **2015**, *115* (9), 3012-3035.

(140) Foster, J. A.; Parker, R. M.; Belenguer, A. M.; Kishi, N.; Sutton, S.; Abell, C.; Nitschke, J. R. Differentially addressable cavities within metal–organic cage-cross-linked polymeric hydrogels. *J. Am. Chem. Soc.* **2015**, *137* (30), 9722-9729.

(141) Gu, Y.; Alt, E. A.; Wang, H.; Li, X.; Willard, A. P.; Johnson, J. A. Photoswitching topology in polymer networks with metal–organic cages as crosslinks. *Nature* **2018**, *560* (7716), 65-69.

(142) Nitta, N.; Takatsuka, M.; Kihara, S. i.; Hirao, T.; Haino, T. Self-Healing Supramolecular Materials Constructed by Copolymerization via Molecular Recognition of Cavitand-Based Coordination Capsules. *Angew. Chem. Int. Ed.***2020**, *59* (38), 16690-16697.

(143) Zhukhovitskiy, A. V.; Zhong, M.; Keeler, E. G.; Michaelis, V. K.; Sun, J. E.; Hore, M. J.; Pochan, D. J.; Griffin, R. G.; Willard, A. P.; Johnson, J. A. Highly branched and loop-rich gels via formation of metal–organic cages linked by polymers. *Nat. Chem.* **2016**, *8* (1), 33-41.

(144) Oldenhuis, N. J.; Qin, K. P.; Wang, S.; Ye, H. Z.; Alt, E. A.; Willard, A. P.; Van Voorhis, T.; Craig, S. L.; Johnson, J. A. Photoswitchable Sol–Gel Transitions and Catalysis Mediated by Polymer Networks with Coumarin-Decorated Cu24L24 Metal–Organic Cages as Junctions. *Angew. Chem. Int. Ed.***2020**, *59* (7), 2784-2792.

CHAPTER 2

Gelation of MOCs

with pendant peptides

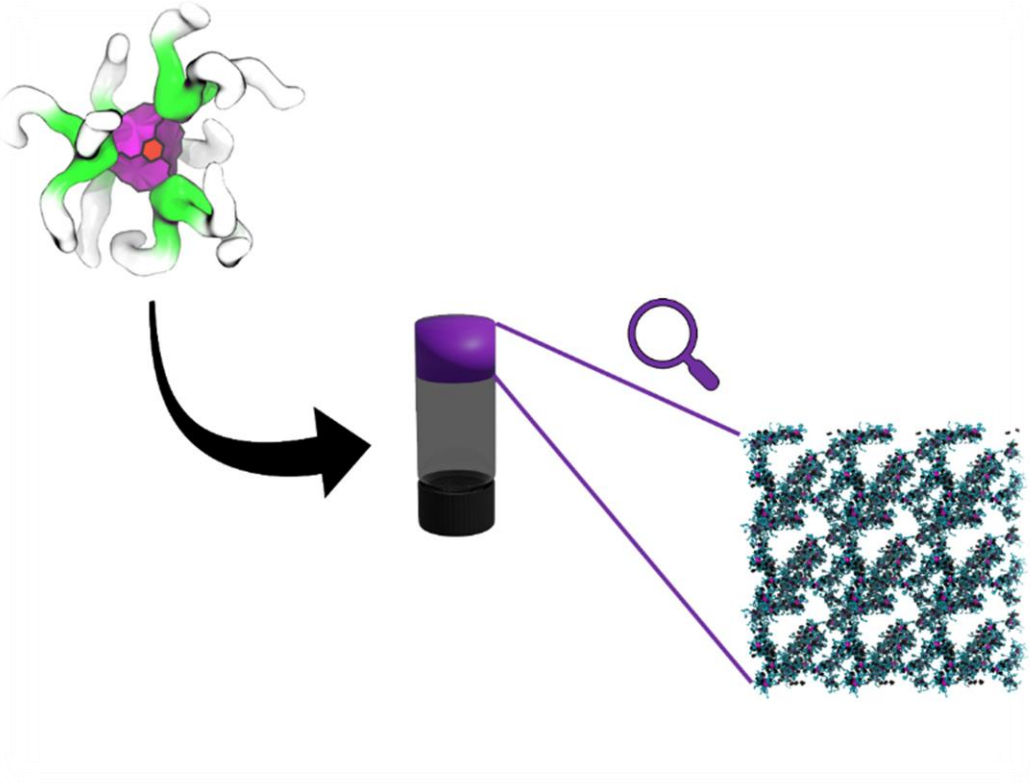

2.1. Introduction

The design of novel materials having dual porosity is an intriguing research field, as discussed in **Section 1.3.3**, thanks to the novel properties and the different possible applications of these systems.[1] In this context, the combination of two different orthogonal supramolecular systems is a very exciting area. The first study in this direction was published by the groups of Prof. Marchesan and Prof. Nitschke.[2] A self-assembling tripeptide PABA-FaF-NH_2, able to gel acetonitrile (CH_3CN), was combined with two distinct (MOCs), each one displaying the selective binding of different guests in CH_3CN (***Figure 2.1***). The immobilization of the cages enabled the formation of different gel layers, each one with a different MOC. In this manner, when a mixture of guests diffused through the gel, they were selectively captured in the corresponding host layer, thus the guests were separated. Furthermore, the gels increased the MOCs' stability against acid-mediated hydrolysis.

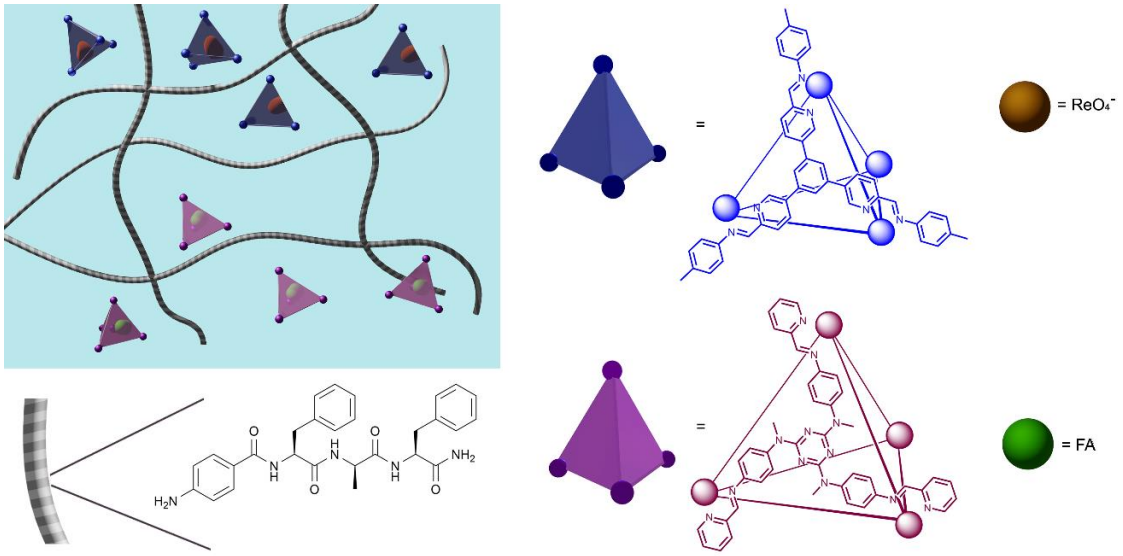

Figure 2.1: *Physical gel based on a self-assembling tripeptide that embeds two MOCs soluble in the same solvent (acetonitrile) and allows for their physical separation in different layers (i.e., top and bottom of the gel) (FA: fluoroadamantane).*[2] *Reproduced with permission from Ref.*[1]*, Copyright © 2021 Elsevier Inc.*

2.2. Self-assembling peptide-based iron cage

The following step of the previous work is the bioconjugation of peptides onto coordination cages in order to study their self-assembly. The Ph.D. thesis of Dr. Marion Kieffer reported the first example of a cage having

a low-molecular weight peptide as peripherical ligand able to gel CH_3CN.[3] The iron tetrahedral cage obtained by the condensation of picolinaldehyde and the previously reported peptide, PABA-FaF-NH_2, (***Figure 2.2A***) was able to gel at 5 mM in CH_3CN after 1 hour as confirmed by the tube inversion test (***Figure 2.2B***).[3] The ^{1}H-NMR spectrum showed the presence of two sets of signals, assigned to the two possible diastereomers (***Figure 2.2C***). This difference in intensity of these signals was attributed to chiral induction exerted on the cage by chiral peptide as confirmed by circular dichroism (***Figure 2.2D***).[3]

Furthermore, the possible reversibility of the sol-gel transition was studied using an external trigger as a photoacid generator (**PAG**), the (E)-3-(2-(2-Hydroxystyryl)-3,3-dimethyl-3H-indol-1-ium-1-yl)propane-1-sulfonate, **MEH**. In the thesis work, it has been studied, for the first time, the conversion from merocyanine form (**MEH**) to spiropyran one (**SP**) in CH_3CN, through NMR and UV-Vis spectroscopies analysis. This study showed the conversion of MEH to SP after irradiation for 5 min with a blue LED ($\lambda \sim 470$ nm) and a drop of $pH_{CH3CN/H2O}$ of 3.2 units, which was sufficient to impact the gelation (***Figure 2.2E***).

The gel of the iron cage, assembled in presence of PAG, was destroyed after irradiation with blue light for 10 min and it was recovered after being placed in the dark for 1 h (***Figure 2.2F***). Four total cycles were performed, giving the same outcome each time and confirming the reversibility of the self-assembly process in the presence of an external trigger. Interestingly, the cage was not disassembled during the cycles, thus giving the opportunity to selectively open the pores of the gel whilst preserving those of the MOCs.[3]

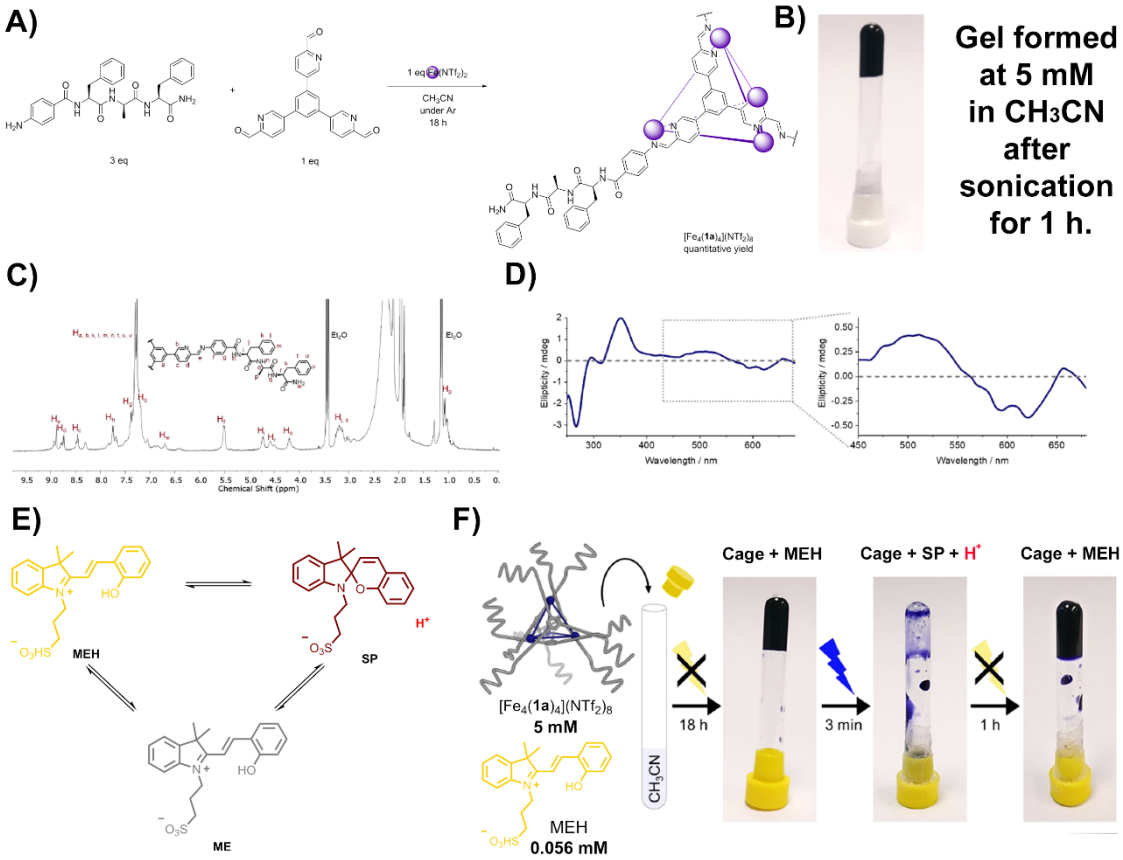

Figure 2.2: *A) Synthesis of the iron cage [Fe4(**1a**)4](NTf2)8; B) Tube inversion test of the gel; C) ^{1}H-NMR of cage [Fe4(**1a**)4](NTf2)8; D) Circular dichroism of cage [Fe4(**1a**)4](NTf2)8; E) two forms of the PAG, the open ring form in darkness (**MEH**) and the closed ring form one exposed to visible light (**SP**); F) Gel-sol-gel transition of a solution of (5 mM) and the PAG (0.056 mM) in CH3CN in the absence of light , after irradiation with blue light for 3 min and after being placed in the dark again for 1 h. Reproduced with permission from Ref*[3].

2.3. Aim of the work

The aim of this project is the synthesis and the self-assembly studies of new cages based on different peptides, aldehydes and metal ions, to study the generality of the approach described above. The rational design of the peptides' library is inspired by a recent work published by Marchesan and co-workers in which a series of L-Phe-D-Xaa-L-Phe tripeptides, where D-Xaa is an aliphatic D-amino acid, have shown their ability to self-assembly to form hydrogels (***Figure 2.3***).[4] In this case the peptide scaffold was preserved, but all the peptides have been derivatised to amides at the C-terminus to avoid the coordination with the metal centre, and to *p*-amino benzoyl amides at the N-terminus to form the imine bond necessary for the cage synthesis.

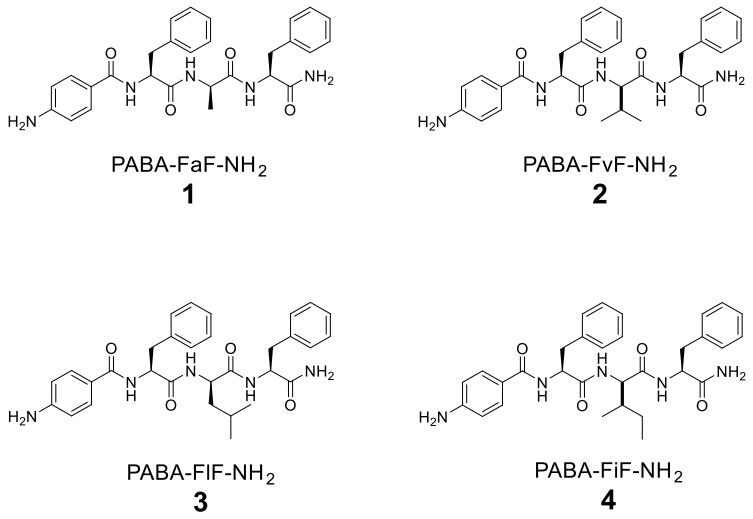

Figure 2.3: *Peptides' library.*

The aldehydes chosen are all previously reported by the Nitschke group (**Figure 2.4**). Aldehyde **a** is the one used for the synthesis of the *parent* cage, and it guarantees a good rigidity in comparison to **b** where the ether bond increases the flexibility of the resulting cage. The bisaldehyde **c** on the other side keeps the tetrahedral geometry changing the position of the ligands on the edges of the tetrahedra instead of the faces. Triazatruxene-based aldehyde **d** can be oriented either clockwise (C) or anticlockwise (A), these two possible diastereoisomeric configurations are added to the two possible optical isomers deriving from the octahedral coordination geometry, Δ_4 and Λ_4.[5] The use of this aldehyde contributes to increase the complexity of the structures and to study more in detail the effects of the use of enantiopure peripherical ligand. Finally, aldehyde **e** guarantees the possibility to study a new geometry, forming a cubic cage. The two divalent metal salts chosen for this study are $Fe(Ntf_2)_2$ and $Zn(Ntf_2)_2$.

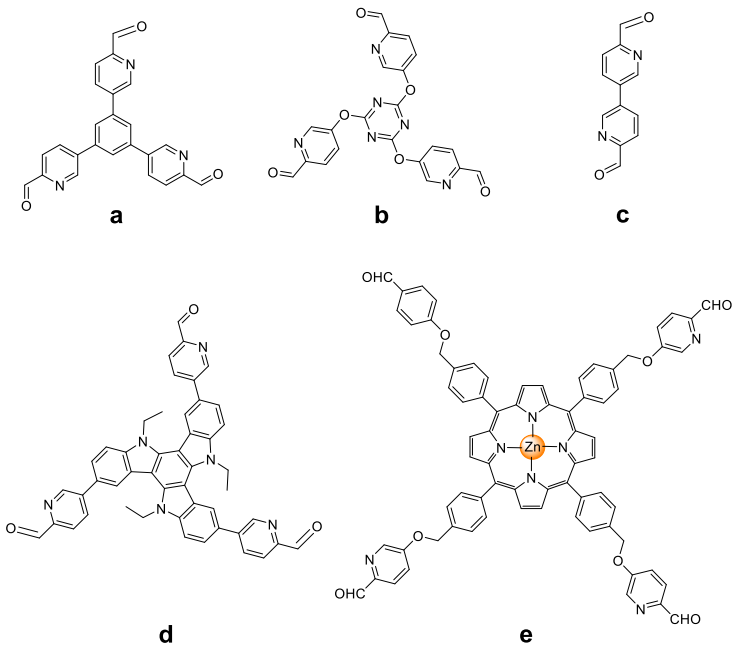

Figure 2.4: *Aldehydes' library.*

2.4. Result and discussion

2.4.1. Synthesis and molecular characterisation of 4-amino benzoic acid (PABA)-derivatised peptide

The peptides were synthesised by Fmoc-based Solid-Phase Peptide Synthesis (SPPS) using 2-chlorotrityl chloride resin as solid support. The resin consisted of polystyrene beads crosslinked with 1% divinylbenzene (DVB) that guarantees the solvation and the sweeling in aprotic solvents as dimethylformamide (DMF) and dichloromethane (DCM). The 1% of cross-linking with DVB allows a resin swelling of 4 to 6 times its original volume in DCM. The mesh size of 100-200 mesh size (75 to 150 microns) offers a good balance of reaction kinetics versus reliability. The peptide synthesis occurs by coupling the carboxyl group of the incoming amino acid to the N-terminus of the growing peptide chain. This synthetic pathway reduces the racemization related to the formation of 5(4H)-oxazolone. The first step of the SPPS is the swelling of the resin to increase the volume of resin which corresponds to a good accessibility to the coupling sites and its activation with $SOCl_2$. The second step is the loading of the C-terminus amino acid, followed by the coupling reaction and Fmoc-deprotection, alternatingly. The final step is the peptide cleavage from the support with a mixture of

trifluoroacetic acid (TFA)-DCM with triisopropylsilane (TIPS) and water as scavenger. This approach was successfully used to achieve the desired compounds as described in ***Figure 2.5***. The crude product was then purified by reverse-phase HPLC.

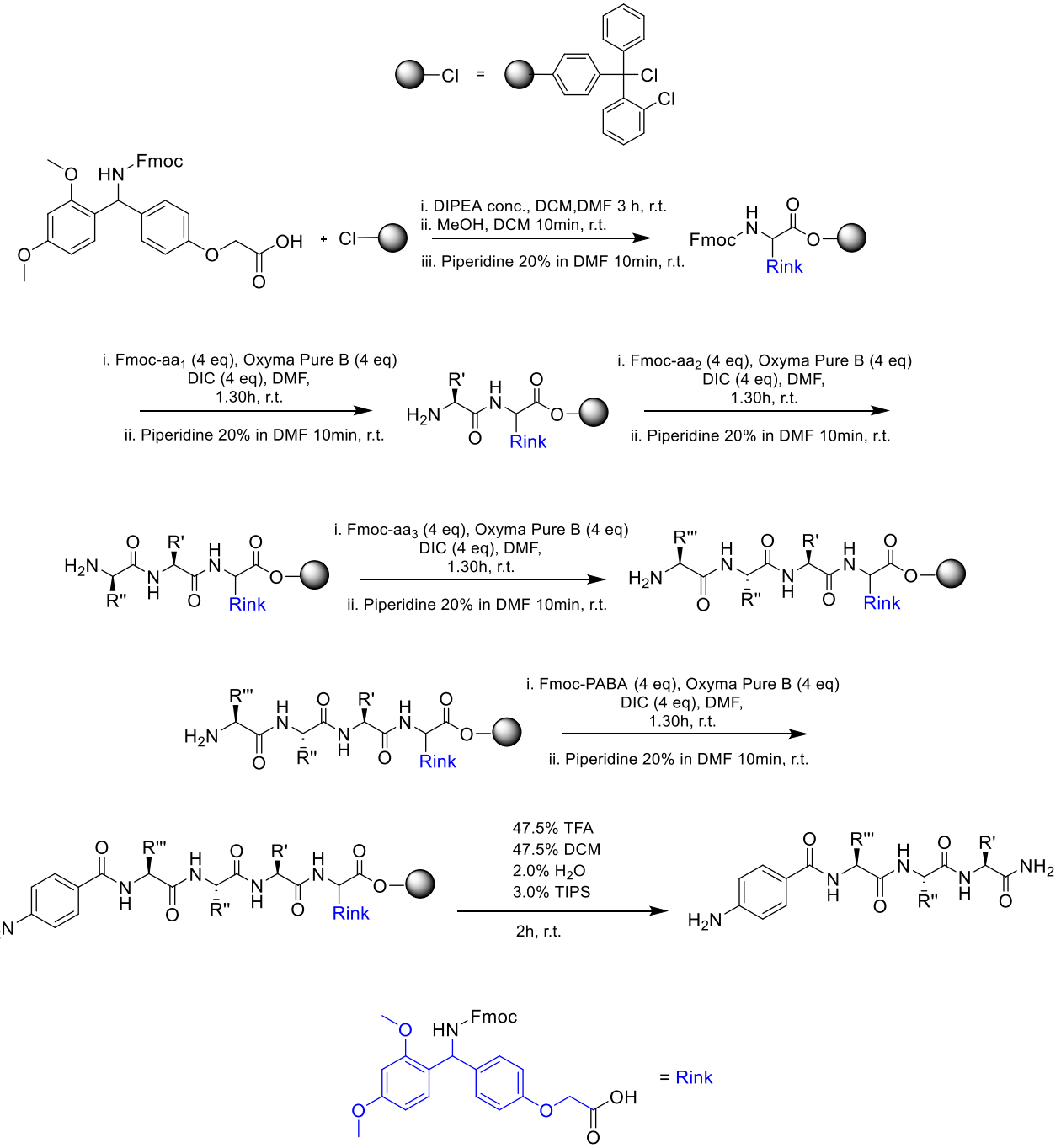

Figure 2.5: *Generical SPPS scheme.*

All the peptides were fully characterised by LC-MS and NMR spectroscopy. Here it was reported the characterisation of **1**, as example, all the other spectra are reported in **Experimental part 2.6.1**.

The ^{1}H NMR (***Figure 2.6***) spectrum confirmed the purity of the compound and showed typical signals of peptides in DMSO-d_6, at chemical shifts higher than 8 ppm the amide protons, the α-protons in the range between 4.0 and 4.8 ppm, and the aliphatic protons in the range between 0 and 3 ppm. ^{1}H-^{1}H-COSY NMR (***Figure 2.7***) showed the correlation between the doublet, integrating for six protons, at 0.49 ppm relative to valine methyl protons (H_o) and the valine methine proton signal (H_n) at 1.72-1.76 ppm. The correlation peak between this last signal and the doublet of doublet at 4.09 ppm allowed to assign it to the α-proton of the valine (H_r). The valine amide signal was finally assigned to the doublet at 7.97 ppm (H_l). The ^{1}H-^{1}H-COSY NMR (***Figure 2.7***) showed also the cross-peaks among the amide, α- and β-protons signals of the two phenylalanine and the correlation peak of the protons of the p-aminobenzoic unit. The correct assignment of these signals has been made using heteronuclear 2D-NMR analysis, ^{1}H,^{13}C-HSQC (***Figure 2.9***) and ^{1}H,^{13}C-HMBC NMR (***Figure 2.10***).

The cross peak in ^{1}H,^{13}C-HMBC NMR (***Figure 2.10***) between the signal at 7.55 ppm and the carbonyl quaternary carbon at 166.3 ppm indicated that the doublet was relative to the PABA-moiety protons H_d. The doublet at 6.58 was consequently assigned to protons H_c. The peak at 166.3 ppm (C_f) also displayed a cross peak with the amide signal at 8.14 ppm assigned to H_h. This allowed to fully assign all the remaining signals. The signal at 173.1 ppm was relative to the carboxylic carbon of C-terminus phenylalanine as confirmed by the cross-peak with the proton signal of the C-terminus amide at 7.39 (H_v). At the end, the two cross-peaks between the amide signal at H_q and the carbon signal at 170.6 ppm and the cross-peak between the amide signal H_l and the carbon one at 171.9 ppm, allowed to assign them to C_p and C_k, respectively.

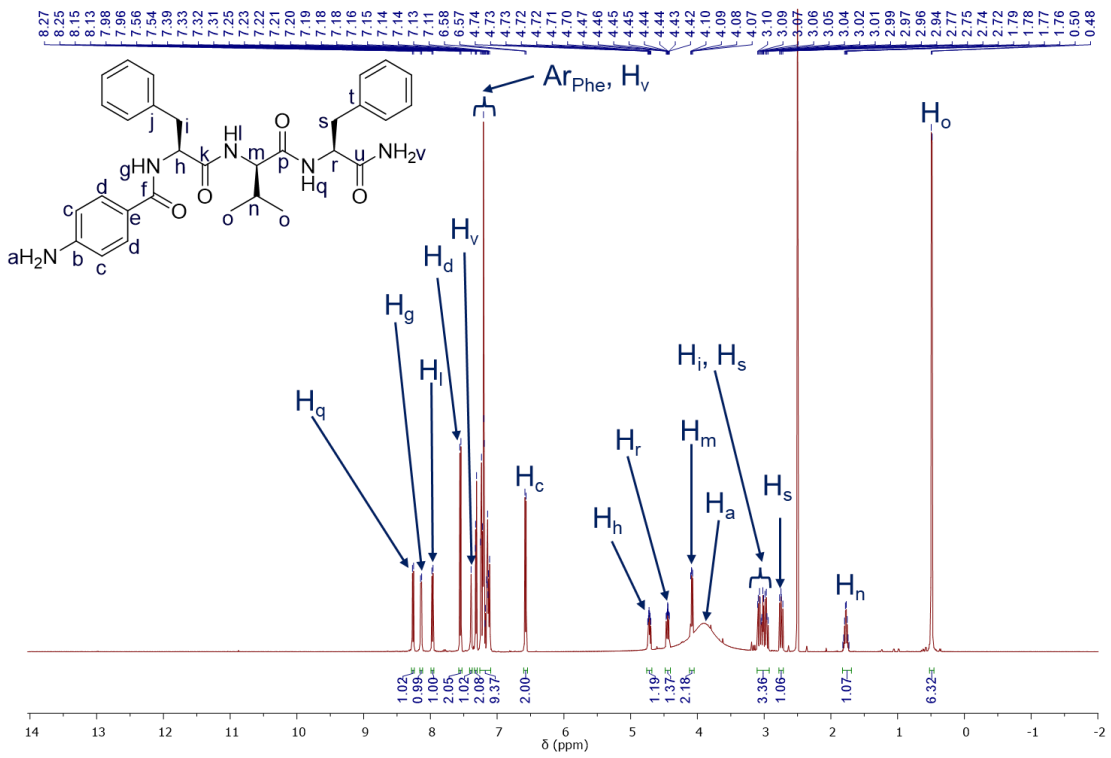

Figure 2.6: *^{1}H-NMR spectrum (DMSO-d$_6$, T = 298 K) of peptide **2**.*

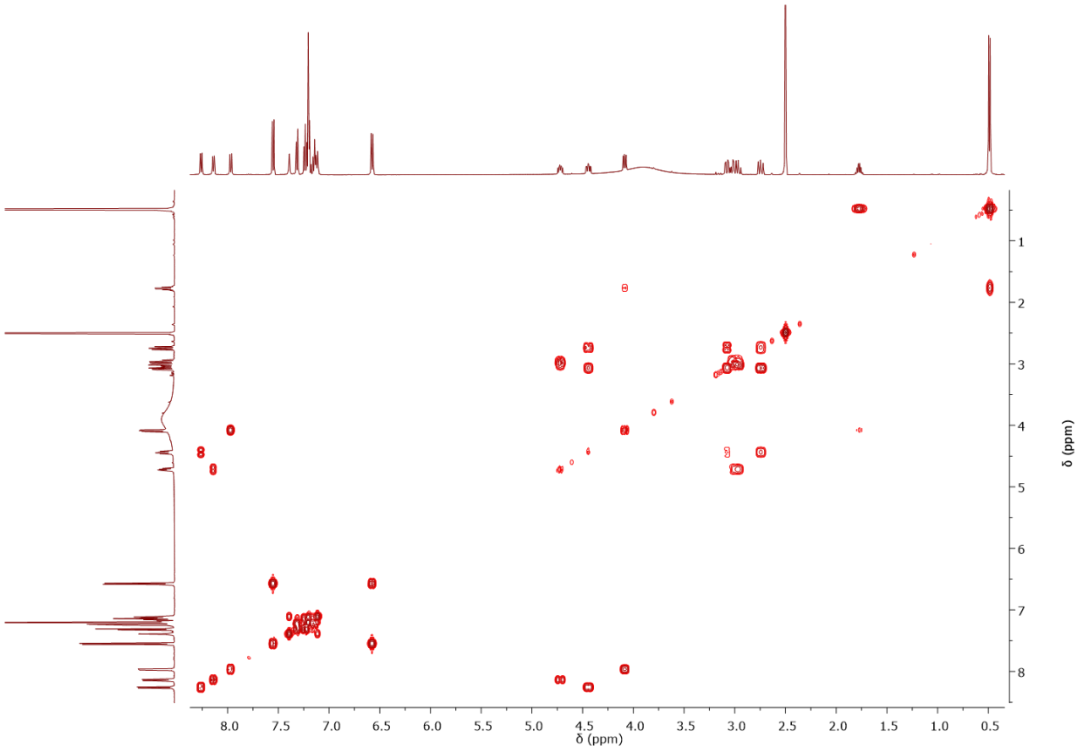

Figure 2.7: *^{1}H,^{1}H-COSY spectrum (DMSO-d$_6$, T = 298 K) of peptide **2**.*

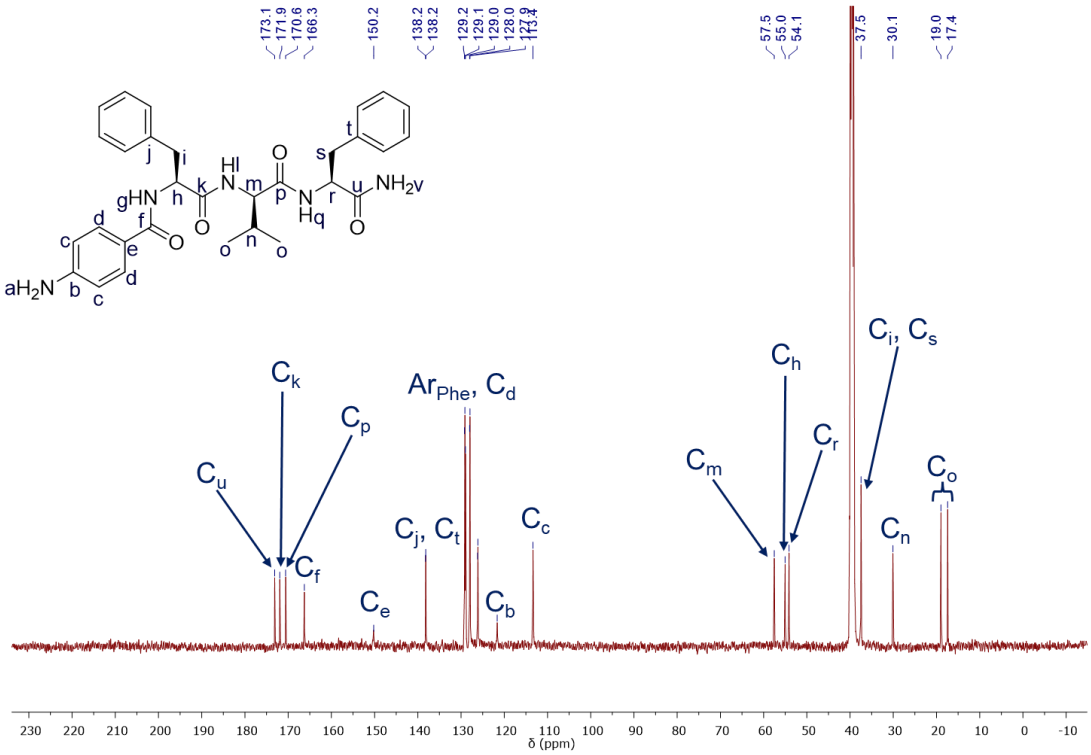

Figure 2.8: *^{13}C-NMR spectrum (DMSO-d$_6$, T = 298 K) of peptide* ***2****.*

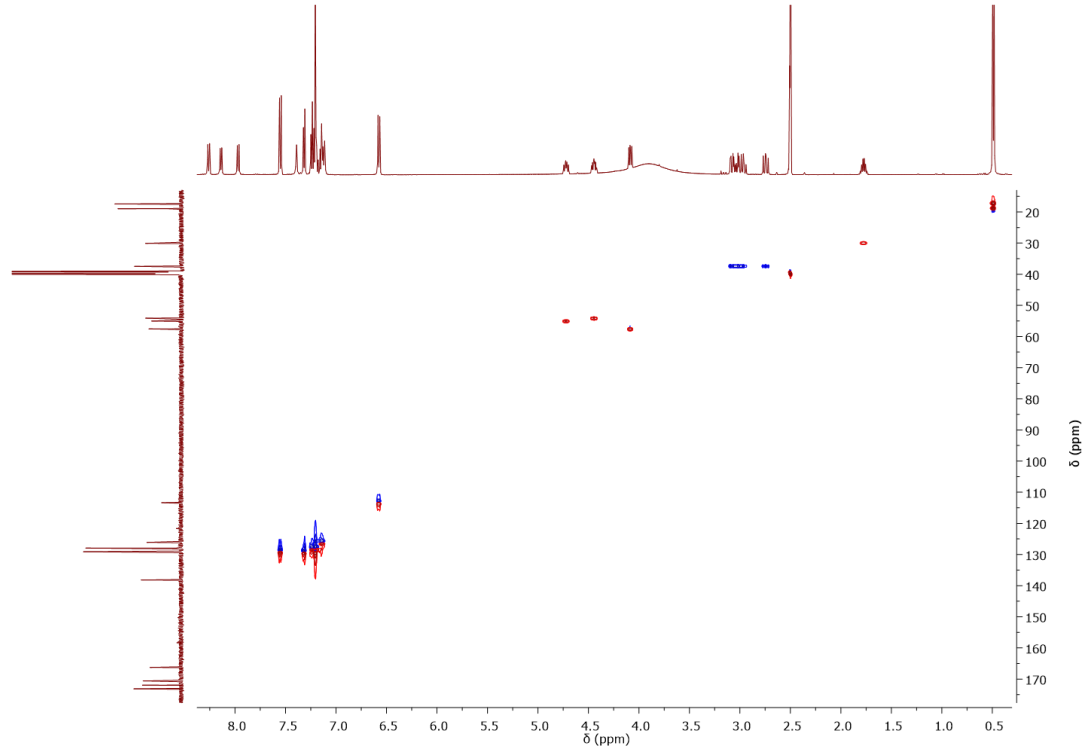

Figure 2.9: *^{1}H, ^{13}C-HSQC spectrum (DMSO-d$_6$, T = 298 K) of peptide* ***2****.*

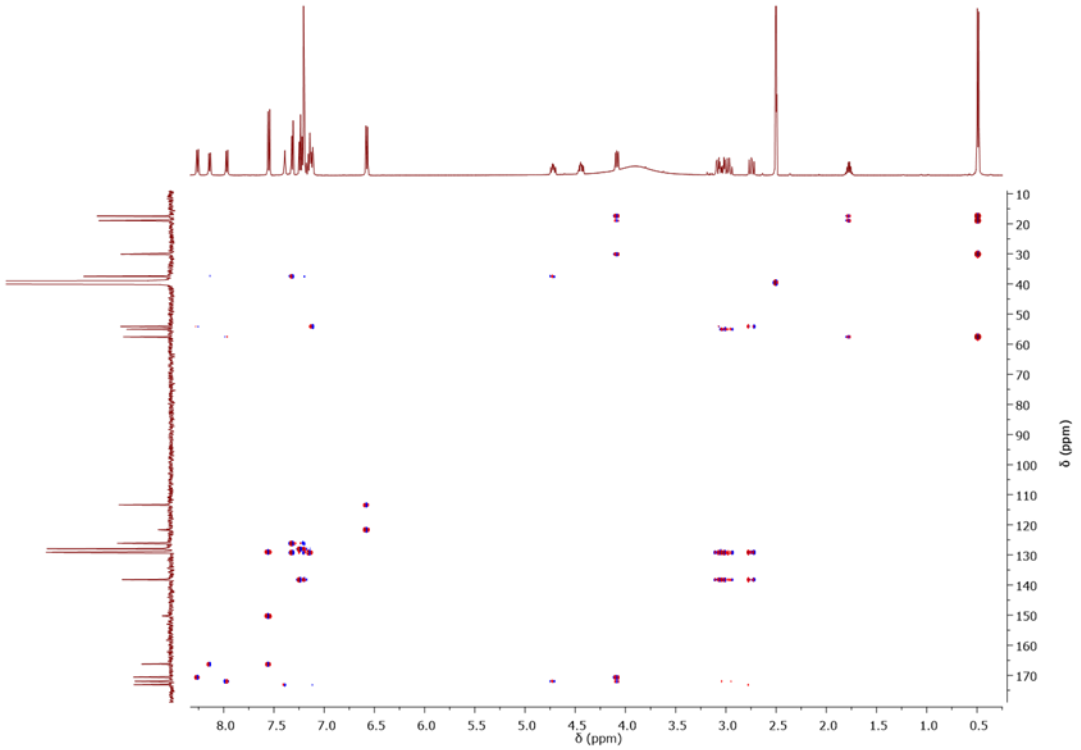

Figure 2.10: *$^{1}H,^{13}C$-HMBC spectrum (DMSO-d_6, T = 298 K) of peptide* ***2****.*

2.4.2. Self-assembly behaviour of PABA-based peptides

The supramolecular behaviour of these peptides was studied following the same protocol, previously reported in literature for parent peptide **1**.[2] This procedure consisted in dissolving the peptide in acetonitrile by heating at 50 °C, followed by cooling down the solution to room temperature. It was, also, observed that sonication induced a faster gelation, thanks to the cleaving of locked weak intramolecular interactions and forming 3D networks based on intermolecular interactions.[6, 7] The gelation process, typically, start with nucleation of the molecule, followed by self-assembling into one dimensional structure and by anisotropic growing that lead to fiber formation. Their entanglement gives rise to a 3D network able to entrap the solvent.

All the peptides in this work rapidly formed supramolecular organogels and their minimum gelling concentration (mgc) is reported in ***Table 2.1***. The mgc depends not only on the peptide hydrophobicity (as measured by logP and HPLC retention times reported in ***Table 2.1***), but also by the stereoconfiguration and the branching of the alkyl sidechain. This is particularly evident for the peptides **3** and **4**, having similar logP values and retention time (***Table 2.1***), while they differ for the constitutional isomer of the aliphatic sidechain, the *iso*-butyl and the *sec*-butyl group for the leucine and the isoleucine, respectively. The mgc for the first one

is way higher (40 mM) than the mgc for the second one (10 mM), suggesting a positive effect of β-branching in inducing the gelation.

Compound	t_r	logP	mgc
p-aminobenzoyl-L-Phe-D-Ala-L-Phe-NH_2 (1)[a]	16.0	1.52	30 mM
p-aminobenzoyl-L-Phe-D-Val-L-Phe-NH_2 (2)	17.8	2.40	30 mM
p-aminobenzoyl-L-Phe-D-Leu-L-Phe-NH_2 (3)	18.6	2.75	40 mM
p-aminobenzoyl-L-Phe-D-Ile-L-Phe-NH_2 (4)	18.7	2.82	15 mM

Table 2.1: *HPLC t_r, logP and minimum gelling concentration (m.g.c.) of peptides.*
a) self-assembly studies yet reported in literature.[2]

The gelation was assessed using a qualitative method called tube inversion test, that is based on the capacity of a gel to resist to gravity (***Figure 2.11***). This test, although not accurate, gives the opportunity to rapidly screen the possible gelation conditions of a peptide.

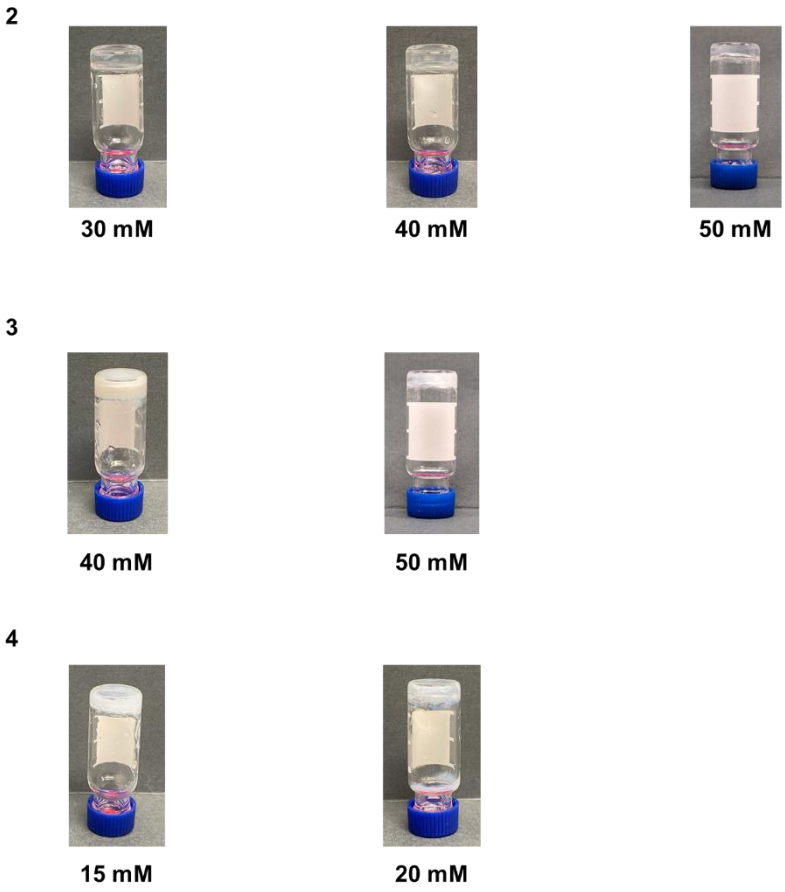

Figure 2.11: *Tube inversion tests of peptides gels studied at different concentrations.*

The organogel nature of all the peptides have been confirmed by oscillatory rheology. Oscillatory rheology is a technique to study the flow and the deformation of matter. The world rheology, in fact, derives from the combination of two Greek words, ῥέω- (rhéō-) "flow" and -λογῑα (logia) "study of". The materials can be divided into three main categories related to the value of the Deborah number, D_e. De is defined as the ratio between the relaxation time (τ) and the observation time (t). τ could be defined as the time needed for a deformation to occur under an applied stress. Materials with values of De >> 1 are defined as solid-like, liquid-like materials are the ones with De << 1 and finally materials with a value ~ 1 are defined as viscoelastic, and the gels belong to latter category. The properties of viscoelastic materials can be studied through oscillations tests. These analyses are based on deformation with intensity that changes sinusoidally during the time. The oscillatory deformation applied, and the material response can be described using two different equations **(2.1)** and **(2.2)**, respectively:

$$\varepsilon = \varepsilon_0 \sin(\omega t) \ (\mathbf{2.1})$$

$$\sigma = \ \sigma_0 \sin(\omega t + \delta) \ (\mathbf{2.2})$$

Equation 2.1 describes the applied stimuli, the deformation ε, while **equation 2.2** the strain, σ. The difference between the two curves, the phase angle (δ), is the parameter measured. It is a value that is characteristic of the type of material studied (***Figure 2.12***).

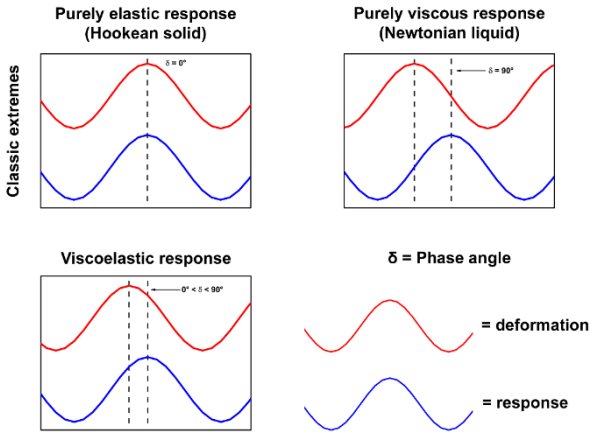

Figure 2.12: *Material responses. $\delta = 0°$ elastic response; $\delta = 90°$ viscous response; $0° < \delta < 90°$ viscoelastic response.*

The complex shear modulus measured for the viscoelastic material can be described as combination of a material with δ = 0°, elastic component, and a material with δ = 90°, viscous component (**Equation 2.3**).

$$\sigma = \ \varepsilon_0 G' \sin(\omega t) + \ \varepsilon_0 G"cos(\omega t) \ (\mathbf{2.3})$$

The G' is the component in phase and it is called storage or elastic modulus, white G'' is the out of phase component, called loss or viscous modulus. A material can be defined a gel when G' is higher than G'', when G' > 10 G'' the gel is defined strong.

The classic rheological analyses are oscillation tests where the intensity and the phase angle of the response to certain stimuli are measured. The two main stimuli that can be applied to characterise the material are the stress or the strain and the frequency. In the stress sweep test, stimuli with increasing intensity are applied to the material to determine the linear viscoelastic regime, wherein performed the other analyses, and the strength of

the gel. In the frequency sweep test, a frequency, varying over the time, is applied and information about the viscoelasticity of the material and the stability of the material are obtained.

Regarding the mechanical properties, peptide **2** showed a good stability in all the concentrations range, as confirmed by the fact that the elastic modulus (G') was ten time higher than the viscous one (G'') (***Figure 2.13***, ***Table 2.2)***. On contrary, peptide **3**, at the same concentrations, displayed lower stability in comparison with **2** (***Figure 2.14***). This mechanical behaviour can be explained in terms of morphology of the samples. Peptide **2** formed entangled thin nanoscopic fibrils (***Figure 2.16-18***), while **3** bigger fibers (***Figure 2.19***), that prevent the formation of a stable 3D-network able to keep the solvent inside the gel mesh.

Finally, peptide **4**, formed gel at lower concentrations than the previous two peptides. This is related to the higher hydrophobicity of the sequence and the different branching of the sidechain. In this case, as for peptide **2**, it was observed the positive effect of β-branching on the resistance against an applied stress (***Figure 2.15***, ***Table 2.2***).

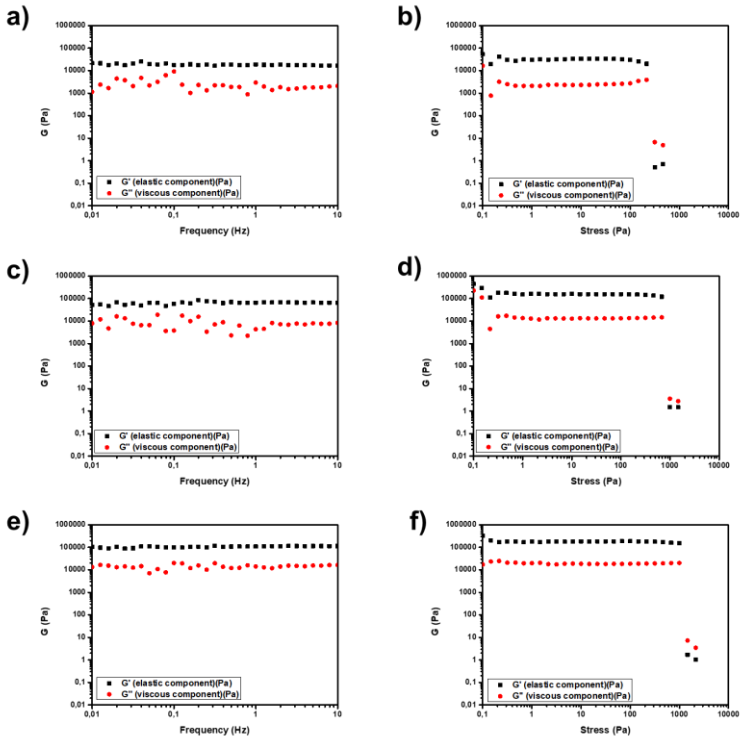

Figure 2.13: *Frequency and stress sweep tests of **2** at different concentrations. a), c), e) frequency sweep tests at 30, 40 and 50 mM, respectively. b), d), f) stress sweep tests at 30, 40 and 50 mM, respectively.*

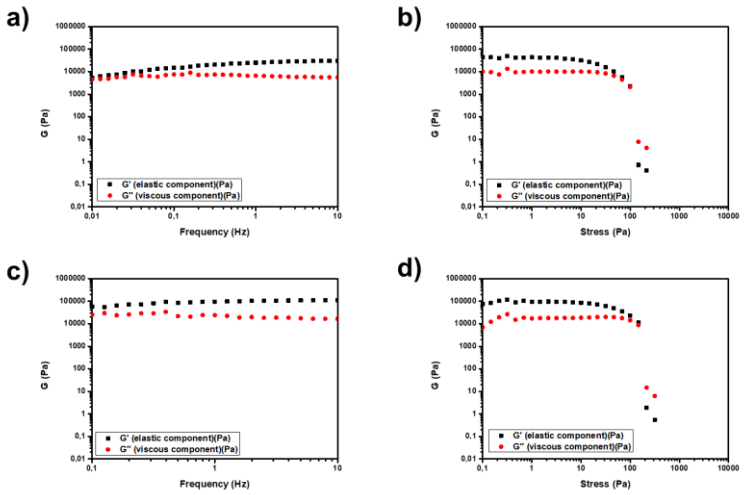

Figure 2.14: *Frequency and stress sweep tests of **3** at different concentrations. a), c), frequency sweep test at 40 and 50 mM, respectively. b), d) frequency sweep test at 40 and 50 mM, respectively.*

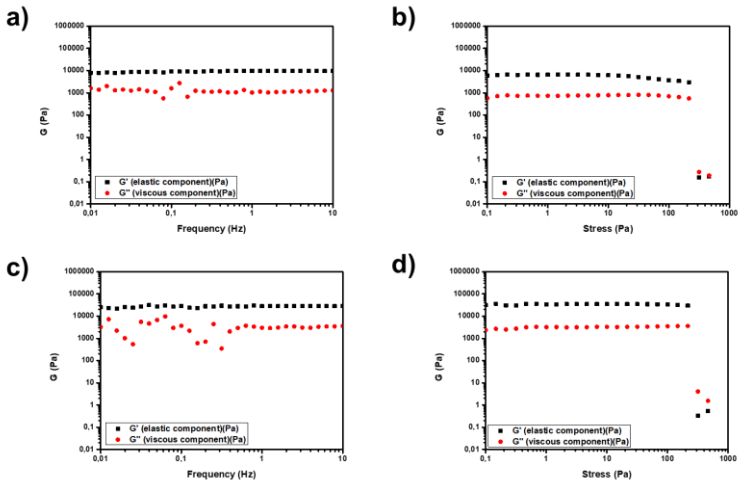

Figure 2.15: *Frequency and stress sweep tests of **4** at different concentrations. a), c), frequency sweep test at 15 and 20 mM, respectively. b), d) frequency sweep test at 15 and 20 mM, respectively.*

Peptide	Concentration (mM)	Elastic modulus (G') (kPa)	Viscous modulus (G'') (kPa)	Breaking point (kPa)
2	30	18.6 ± 2.5	1.8 ± 1.7	0.22
2	40	63.8 ± 8.1	8.3 ± 4.3	0.68
2	50	106.4 ± 7.4	14.1 ± 3.0	1.00
3	40	19.5 ± 8.4	6.4 ±1.0	0.10
3	50	73.9 ± 30.3	22.8 ±4.5	0.15
4	15	9.1 ± 0.6	1.3 ± 0.4	0.22
4	20	27.4 ± 0.6	3.4 ± 2.0	0.22

Table 2.2: *Elastic modulus (G'), viscous modulus (G'') and breaking points in kPa for all the organogels studied. [a]Data previously reported in literature.*[2]

In terms of nanomorphology, TEM images revealed that all peptides assembled into fibrils, with different behaviour in terms of rigidity, and level of bundling or branching. In particular, peptide **2** and **4** formed thin fibrils of an average diameter of ~ 16 nm (***Figure 2.16-18***) and ~ 20 nm (***Figure 2.21-22***), respectively, for all the concentrations tested. On the contrary, peptide **3** formed rigid, bundled fibrils with a diameter of 115.0 ± 38.9 nm (***Figure 2.19***), suggesting the influence of the branching of the side chain on the nano morphological behaviour. We inferred that the presence of side-chain branching closer to peptide backbone, as for **2** (peptide containing the D-Val) and **4** (peptide containing the D-Ile), promoted branching as opposed to bundling.[4]

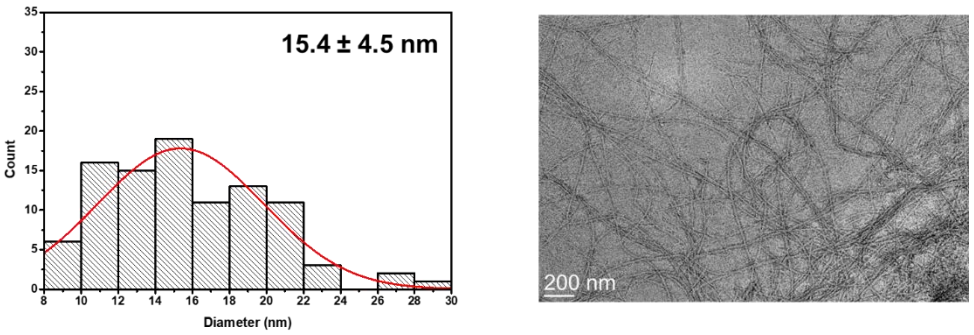

Figure 2.16: *Size distribution (nm) and TEM image of gel of peptide 2 at 30 mM.*

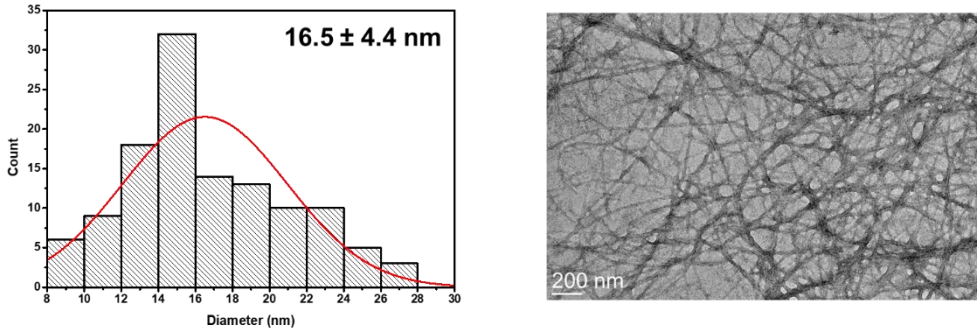

Figure 2.17: *Size distribution (nm) and TEM image of gel of peptide* ***2*** *at 40 mM.*

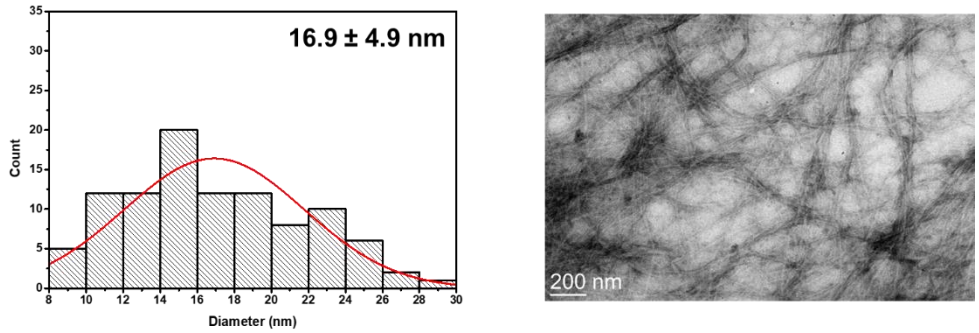

Figure 2.18: *Size distribution (nm) and TEM image of gel of peptide* ***2*** *at 50 mM.*

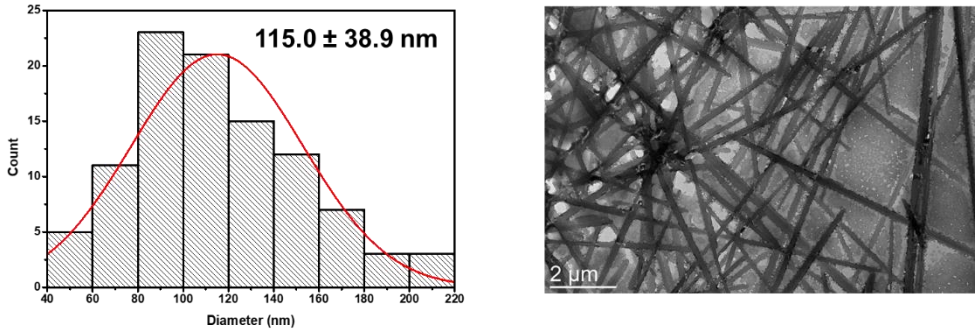

Figure 2.19: *Size distribution (nm) and TEM image of gel of peptide* ***3*** *at 50 mM.*

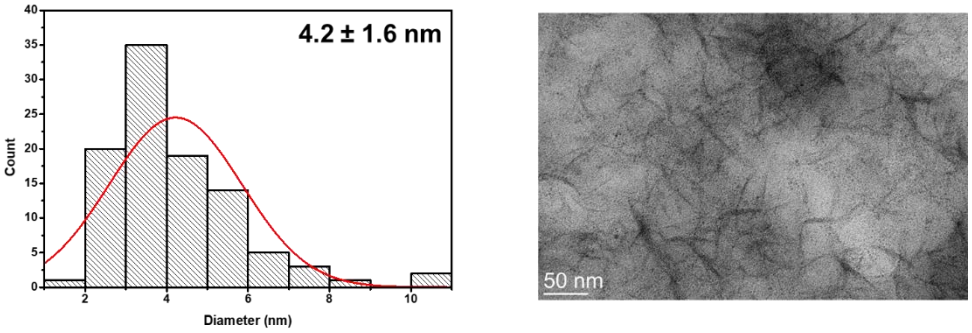

Figure 2.20: *Size distribution (nm) and TEM image of gel of peptide* ***3*** *at 40 mM.*

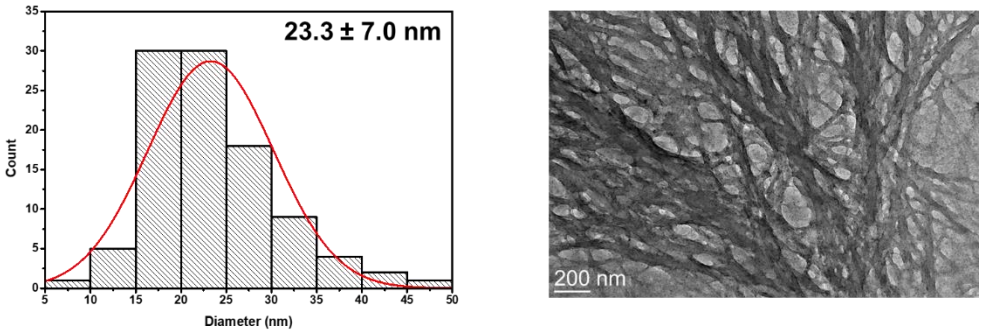

Figure 2.21: *Size distribution (nm) and TEM image of gel of peptide* ***4*** *at 15 mM.*

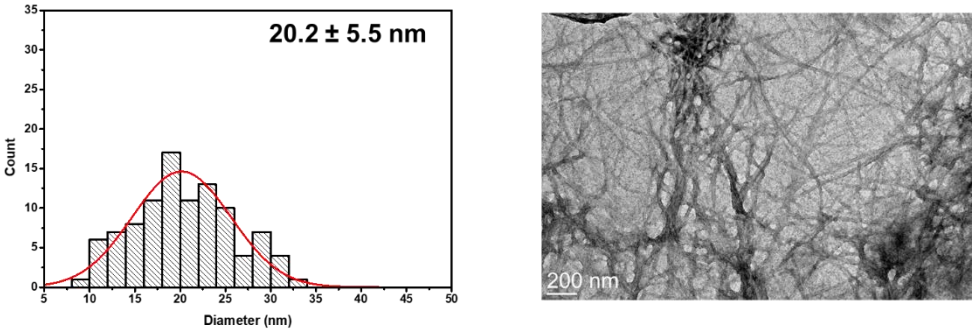

Figure 2.22: *Size distribution (nm) and TEM image of gel of peptide* ***4*** *at 20 mM.*

2.4.3. Synthesis of aldehydes

The 5,5',5"-(benzene-1,3,5-triyl)tripicolinaldehyde was synthesized in a two-step reaction, according to the literature.[8] The first steps involved the synthesis of the boronic ester, 1,3,5-tris(4, 4, 5, 5-tetramethyl-1,3,2-dioxaborolan-2-yl) benzene (**135TrBB**) through a Miyaura-borylation reaction. The main advantage of these

reaction is related to the possibility to easily synthesised a coupling partner for a Suzuki-Miyaura cross coupling in good yield for different aryl halide. The base chosen for this reaction is KOAc, a weak base that does not accelerate the reaction, but guarantees good yields and it is selective. Among the different palladium catalyst, the Pd(dppf)Cl_2 was chosen in this case, thanks to its air stability and its ease to handling. The bis(diphenylphosphino)ferrocene (dppf) ligand enhanced the stability of the complex, thanks to the chelating effect, facilitating the reductive elimination step over the β-hydrogen elimination. The reaction was performed at 90 °C in a polar solvent that was anhydrous DMF (***Figure 2.23***). The purity of the compound was confirmed by ^{1}H-NMR spectroscopy (***Figure 2.61***).

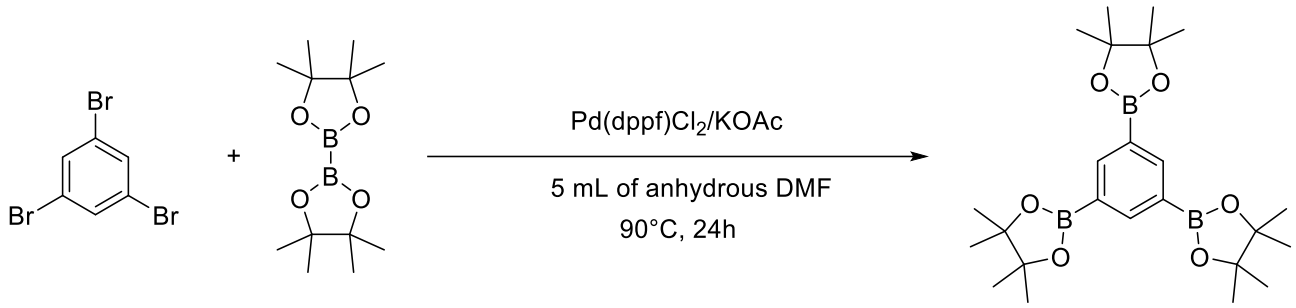

Figure 2.23: *Synthesis of 1,3,5-tris(4, 4, 5, 5-tetramethyl-1,3,2-dioxaborolan-2-yl) benzene (135TrBB).*

The second step concerned the synthesis of 5,5',5''-(benzene-1,3,5-triyl)tripicolinaldehyde, aldehyde **a**, through a Suzuki-Miyaura cross-coupling between 135TrBB previously synthesised and the commercially available 5-bromopicolinaldehyde (***Figure 2.24***). The chosen catalyst in this case is the classical Pd(PPh_3)$_4$ together with the weak base K_2CO_3 as reported in the literature procedure.[8] The successful reaction was confirmed by ^{1}H-NMR spectroscopy (***Figure 2.62***).

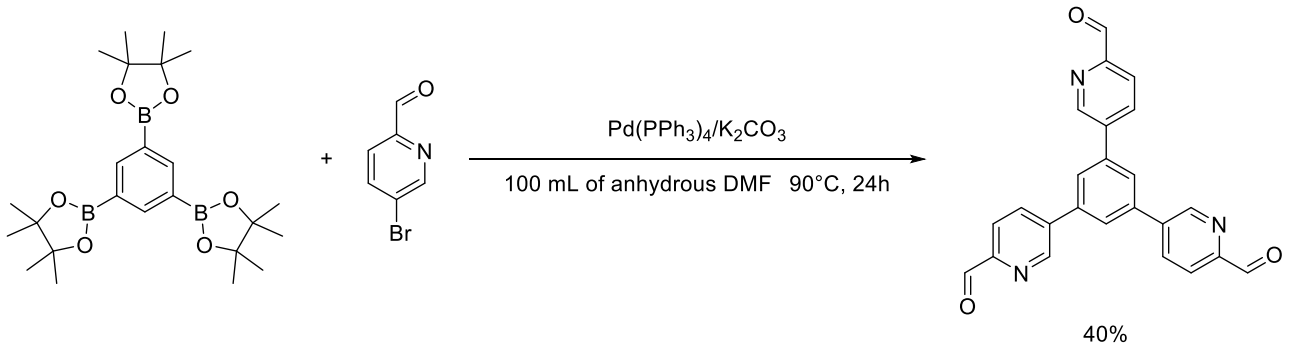

Figure 2.24: *Synthesis of 5,5',5''-(benzene-1,3,5-triyl)tripicolinaldehyde, aldehyde **a**.*

The porphyrin aldehyde has been synthesised using a procedure reported in the literature by the group of Prof. Nitschke.[8] In this case, the first step involved the synthesis of the meso-substituted porphyrin, tetrakis(4-bromomethylphenyl)porphyrin (T4BrP), using a synthetical approach developed in 1980s by Lindesy and co-workers (***Figure 2.25***). This approach entailed acid-catalysed condensation of an aldehyde and pyrrole to form a porphyrinogen, that will undergo to $6e^-/6H^+$ oxidative dehydrogenation mediated by an oxidant, as 2,3-dichloro-5,6-dicyanobenzoquinone (DDQ). The two main advantages of this procedure are the mild reaction conditions, the reaction was performed in anhydrous DCM at room temperature for 5 hours, and the good yield (>30%).

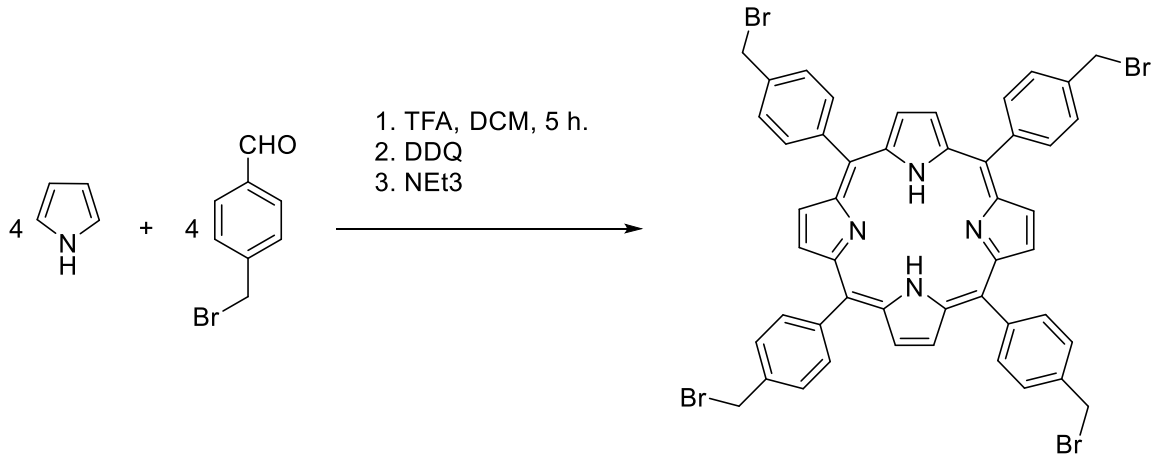

Figure 2.25: *Synthesis of tetrakis(4-bromomethylphenyl)porphyrin (T4BrP).*

The second step concerned the metalation of the porphyrin, for simple stirring of $Zn(OAc)_2$ in DCM at r.t. (***Figure 2.26***).[9] The mechanism of Zn^{2+} involves a weakly binding of Zn^{2+} ions forming a deformed "sitting-atop" (SAT) complex. SAT complex is then attached from to the back by another zinc (II) ion (***Figure 2.27***). Kinetic studies suggest the formation of bimetallic intermediate in which the r.d.s. is the incorporation of the zinc inside the porphyrin.[9]

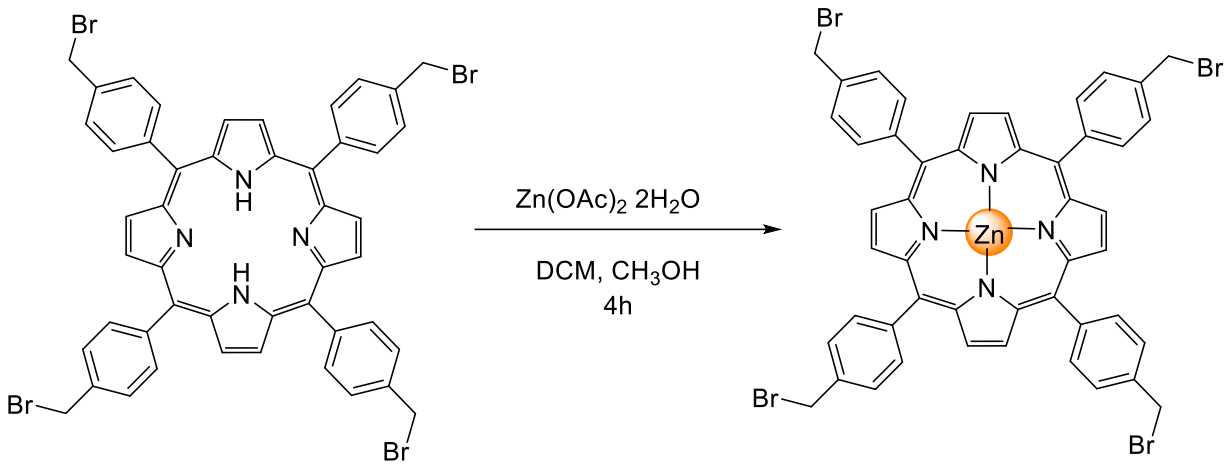

Figure 2.26: *Synthesis of Zn-T4BrP.*

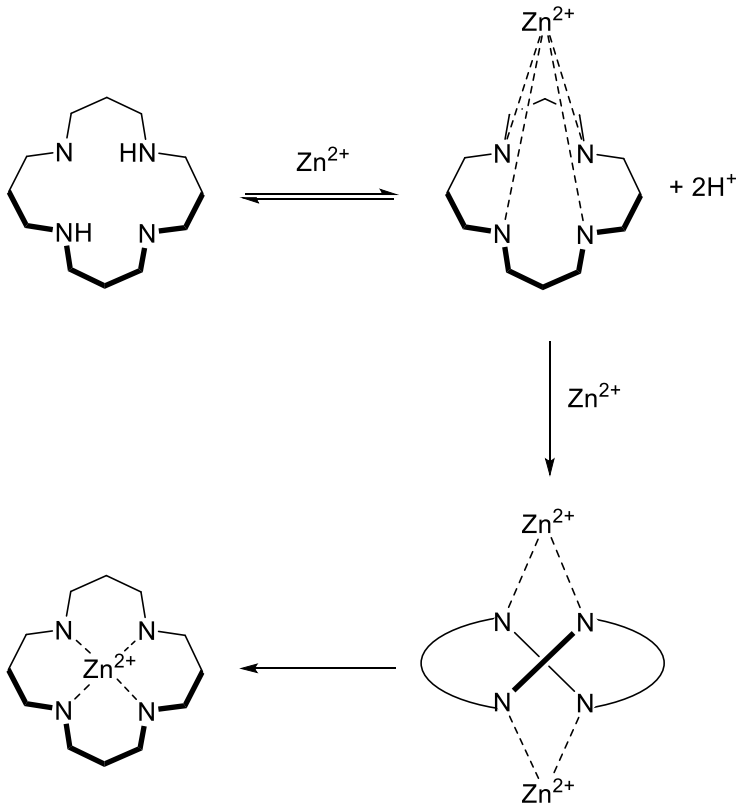

Figure 2.27: *Reaction mechanism of zincation of porphyrin.*[9]

The final step regards the synthesis of the porphyrin aldehyde, zinc(II) tetrakis(4-(((6-formylpyridin-3-yl)oxy)methyl)-phenyl)porphyrin **e**, through a Williamson ether reaction using K_2CO_3 as base and the commercially available (***Figure 2.28***).

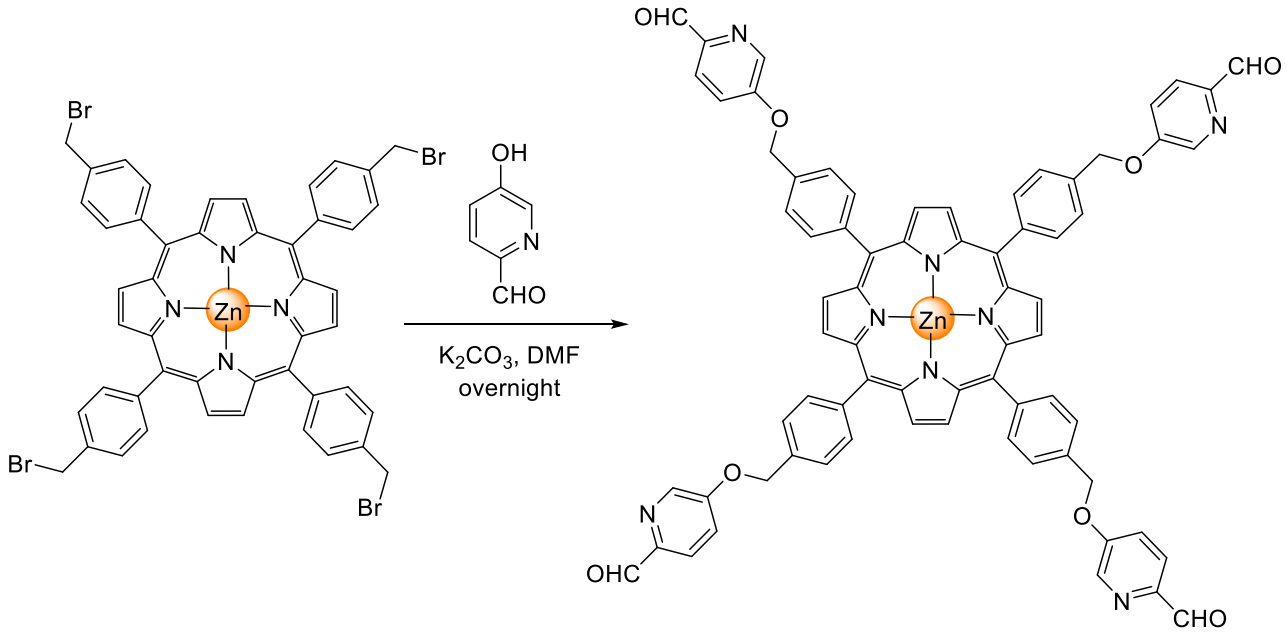

Figure 2.28: *Synthesis of zinc(II) tetrakis(4-(((6-formylpyridin-3-yl)oxy)methyl)-phenyl)porphyrin, aldehyde* ***e****.*

The intermediates and the final product have been characterised by ^{1}H-NMR spectroscopy (***Figure 2.63-65***) and the analytical data are in agreement with those previously published.[10]

Finally, aldehydes **b**, **c** and **d** have been synthesised by Dr. Andrew Heard at the University of Cambridge.

2.4.4. Cages synthesis and characterisation

The cages have been synthesised through a subcomponent self-assembly approach. This approach, originally investigated by Busch[11] and further developed by Hannon[12] and Nitschke[13], relies on the formation of both covalent bonds and metal-organic dative bonds through a metal-templation process. One of the main advantages of this approach is to avoid the synthesis of synthetically polydentate ligands, because of the organic subcomponents react separately around the template metal centre. This guarantees two benefits both for ligands thanks to stabilisation of the covalent bond led to the coordination, and for the metal, preventing its reduction or oxidation once coordinated. The second advantage is the use of dynamic covalent bond, as the imine bond. This bond is, generally, reversible through hydrolysis, however, once coordinated to a metal *via* nitrogen donor atoms, the complex formed renders the imine bond stable, even in water in selected cases.[14]

The peptides containing the aniline unit (**1-4**) were investigated to use them as subcomponents in self-assembly with aldehydes (**a-e**) and the metal salts. **Figure 2.29** showed the general reaction for the synthesis of a tetrahedral cage with aldehyde **a**.

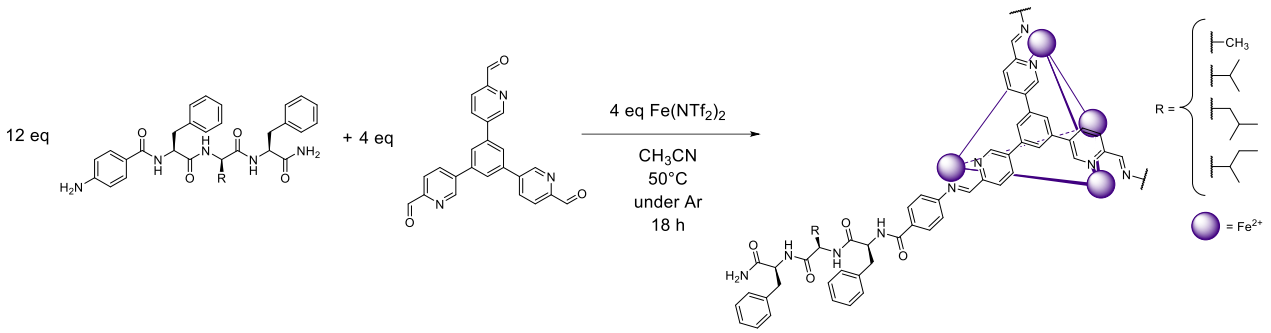

Figure 2.29: *General reaction scheme for cage synthesis using aldehyde* ***a****.*

The reaction of the peptide (12 eq) with 4 eq of piconiltrisaldehyde and $M(NTf_2)_2$ (4 eq) in CH_3CN at 50 °C for 18 h led to the formation of M_4L_4 assembly. The formation of all assemblies was confirmed by NMR and ESI-MS spectroscopy (***Figure 2.30-33***). The characterisation of the other cages $[M_4(\mathbf{Xa})_4](NTf_2)_8$ (X = **1-4**) was reported in **Experimental part 2.6.3** (***Figure 2.66-103***).

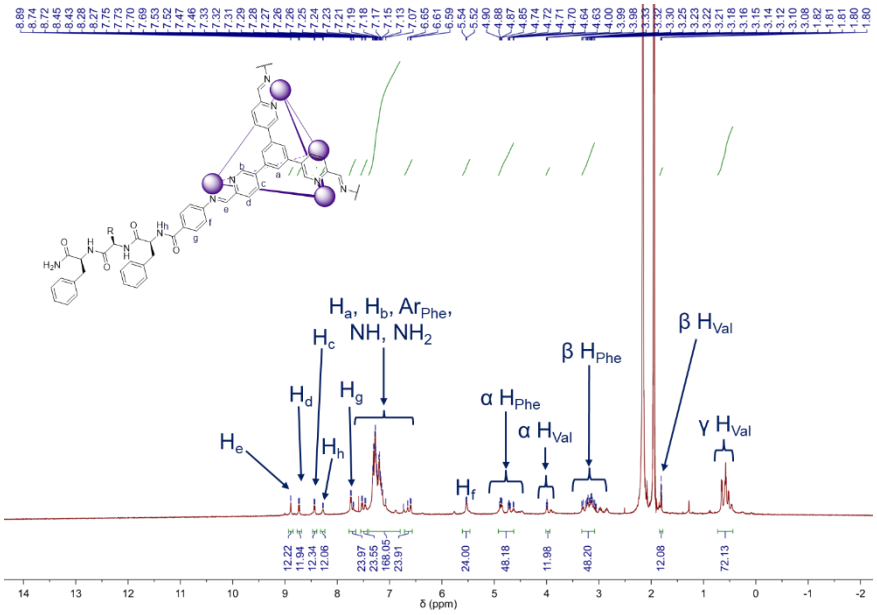

Figure 2.30: *^{1}H-NMR spectrum (CD_3CN, 500 MHz, T = 298 K) of cage $[Fe_4(\mathbf{2a})_4](NTf_2)_8$.*

Diffusion ordered spectroscopy (DOSY) NMR is a key analytic tool for the general characterisation of the cages. DOSY NMR, in this context, gives useful information about the number of species in solution and can be used to glean information on the effective shape of the cage.[15] In the DOSY NMR spectrum of $[Fe_4(\mathbf{2a})_4](NTf_2)_8$ is possible observed that signals assigned to the cage have the same diffusion coefficient and therefore, most likely belong to the same species (***Figure 2.31***).[15]

The other information that can be obtained regards the translational diffusion coefficient (*D*), describing the movement of molecules due to either concentration gradient or Brownian motion, in absence of any chemical gradient. The correlation between *D* and the hydrodynamic radius (*R*) is described by the Einstein-Smoluchwski equation (**Equation 2.4**):[15]

$$D = \frac{k_B T}{f} \quad (\mathbf{2.4})$$

This equation connects the diffusion coefficient and the so-called hydrodynamic friction factor (*f*) for infinitely diluted solutions. For *f* equal to $6\pi\eta R$ it was obtained the Stokes-Einstein equation (**Equation 2.5**) from which *R* is calculated.[15]

$$D = \frac{k_B T}{6\pi\eta R} \quad (\mathbf{2.5})$$

Equation 2.5 has been used to calculate the hydrodynamic radius of all the cages.

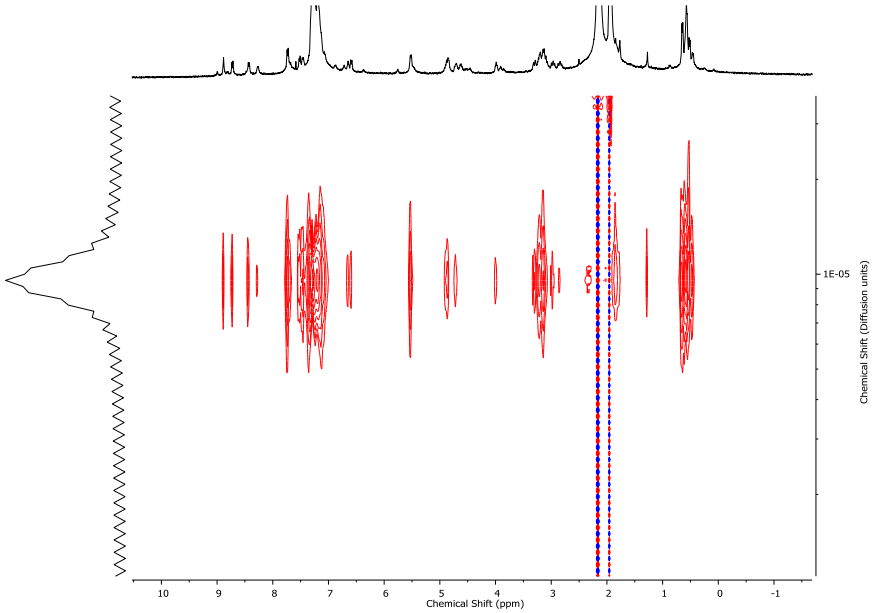

Figure 2.31: *^{1}H-DOSY NMR spectrum (CD_3CN, 400 MHz, T = 298 K) of cage $[Fe_4(\mathbf{2a})_4](NTf_2)_8$. The diffusion coefficient for $[Fe_4(\mathbf{3a})_4](NTf_2)_8$ in CD_3CN was measured to be 3.86 x 10^{-10} m^2 s^{-1} and the solvodynamic radius was calculated to be 16.9 Å.*

The synthesis of the desired tetrahedral cages has been confirmed by mass spectroscopy. ***Figure 2.32*** displayed a series of ion peaks at different for the different charged states of the cages.[16] In particular, all the synthesised cages, are obtained as host-guest complexes with TFA counterion that derives from SPPS. ***Table 2.3*** showed the m/z values for the cage $[Fe_4(\mathbf{2a})_4](NTf_2)_8$ chosen as examples.

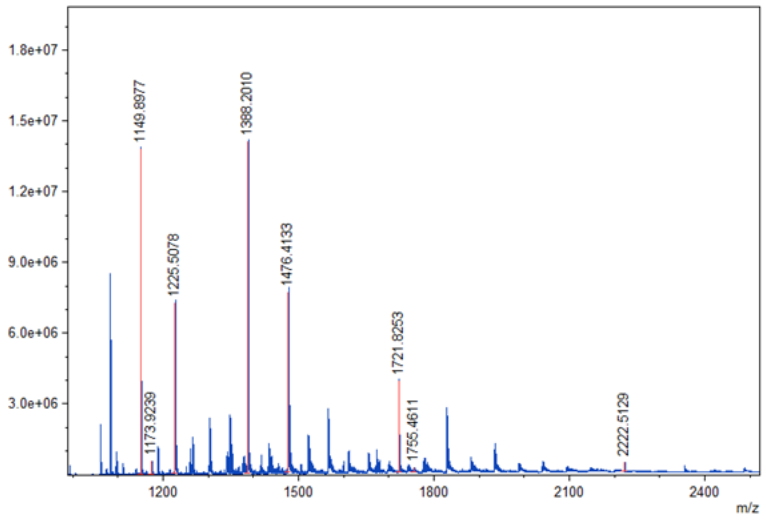

Figure 2.32: *ESI-MS of cage $[Fe_4(\mathbf{2a})_4](NTf_2)_8$.*

Species	Calculated m/z	Experimental m/z
$[Fe_4(C_{114}H_{114}N_{18}O_{12})_4(\mathbf{CF_3CO_2})]^{7+}$	1149.9094	1149.8977
$[Fe_4(C_{114}H_{114}N_{18}O_{12})_4(N(SO_2CF_3)_2)]^{7+}$	1173.7855	1173.9239
$[Fe_4(C_{114}H_{114}N_{18}O_{12})_4(N(SO_2CF_3)_2)(\mathbf{CF_3CO_2})]^{6+}$	1388.2525	1388.2010
$[Fe_4(C_{114}H_{114}N_{18}O_{12})_4(N(SO_2CF_3)_2)_2(\mathbf{CF_3CO_2})]^{5+}$	1721.9327	1721.8253
$[Fe_4(C_{114}H_{114}N_{18}O_{12})_4(N(SO_2CF_3)_2)_3]^{5+}$	1755.3593	1755.4611
$[Fe_4(C_{114}H_{114}N_{18}O_{12})_4(N(SO_2CF_3)_2)_3(\mathbf{CF_3CO_2})]^{4+}$	2222.4532	2222.5129

Table 2.3: *m/z values for $[Fe_4(\mathbf{2a})_4](NTf_2)_8$.*

The isotope pattern of a particular ion peak gives the information about the ratio of metal to ligand and of consequence about the geometry. The charge value was calculated from the reciprocal of the signals between signals in the peak series. From charge and the m/z it is possible to know exactly what the ratio of ligands to metal is, and after that take a guess at the geometry.[16]

In particular, from isotopic pattern distribution of the different ion peaks of $[Fe_4(\mathbf{2a})_4](NTf_2)_8$ (***Figure 2.32***) it is possible to have the definitive confirmation of the tetrahedral geometry.

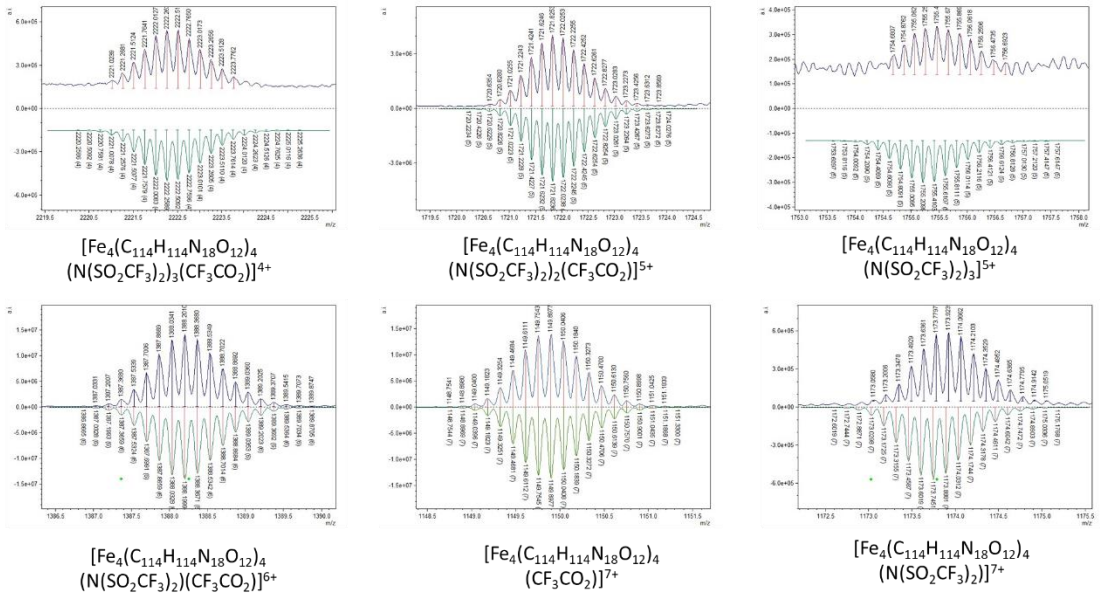

Figure 2.33: *Isotopic pattern distribution of $[Fe_4(\mathbf{2a})_4](NTf_2)_8$.*

Circular dichroism (CD) is an elite technique for the study of chiral molecules. The electromagnetic wave is composed of an orthogonal magnetic and electric field oscillating in a plane over the time. When these two

vibrations are confined to a single plane, light is defined as linearly polarized. Conversely, if the vibration plane rotates the light propagation, then the light is circularly polarized, and it consists of two components, left- and right-handed circularly polarized. The chiral molecules, interacting with light, absorb these two components differently, $\varepsilon_L \neq \varepsilon_R$, and the difference is measured in form of ellipticity.

Among its different possible applications, CD can be used to distinguish enantiomers. For this purpose, CD has been used to identify the major diastereomer of two possible for this type cages, the Λ_4 and the Δ_4, through comparison with reported literature. The positive Cotton effect at ~ 356 nm, followed by the negative one at 300 nm, due to π-π* transition localised on the imino pyridine chromophore, suggests that the Λ_4 is the major diastereoisomer for all the cages (***Figure 2.34***).[17]

The CD spectra of iron cages display also a first negative Cotton effect around 610 nm, followed by a second one at ~ 540 nm and a third one, less intense, just below 490 nm. The first one could be associated to a 3d-3d transition mixed with charge-transfer ones. While the second and third ones are probably due to two d-π* MLCT transitions (***Figure 2.34***).[17]

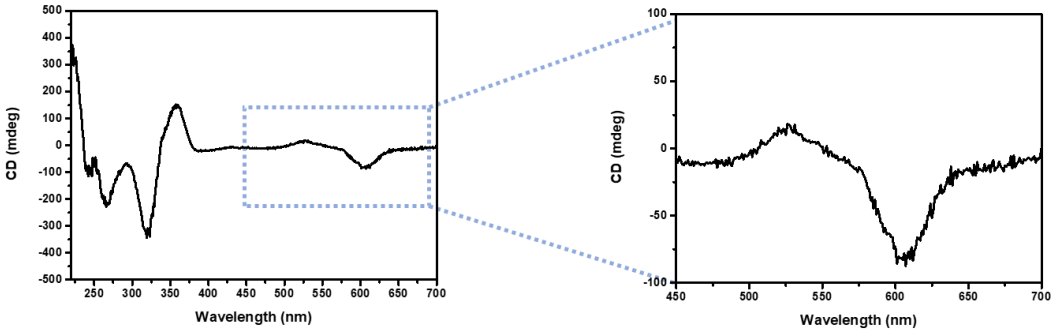

Figure 2.34: *CD spectrum of [Fe$_4$(**2a**)$_4$](NTf$_2$)$_8$, with zoom in region between 450-700 nm.*

The other tetrahedral cages with the other aldehydes, **b-d**, were synthesised using the same protocol reported in ***Figure 2.29***. No cage formation was observed for any aldehydes. In particular, using aldehydes **b** or **c**, it was observed the formation of a mixture of different supramolecular architectures as demonstrated by the integration of the aromatic signals in the NMR spectrum. In order to move the equilibrium toward the most thermodynamically stable species, an annealing reaction, consisting in heating the reaction mixture at 70°C for 1 day, was performed for the cage with aldehyde **c**, because of its similarity to **a** and generally higher

stability of cages with ligands on the faces. This attempt brought to the break of the cage, demonstrate by the appearance of the aldehyde proton signal in the ^{1}H-NMR spectrum (***Figure 2.35***).

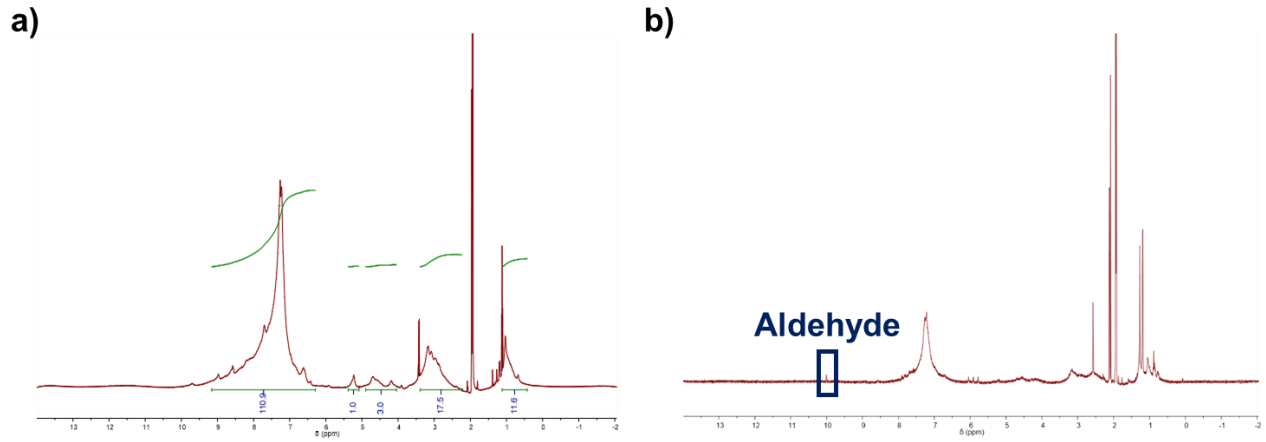

Figure 2.35: *a) ^{1}H-NMR spectrum (CD_3CN, 500 MHz, T = 298 K) of cage $[Fe_4(\mathbf{1b})_4](NTf_2)_8$; b)) ^{1}H-NMR spectrum (CD_3CN, 500 MHz, T = 298 K) of cage $[Fe_4(\mathbf{1b})_4](NTf_2)_8$ after annealing.*

Regarding aldehyde **d**, no cage formation was observed as confirmed by the value of the hydrodynamic radius similar to the one of a small molecule, 1.31 Å, (***Figure 2.105***).

The cubic cage, using aldehyde **e**, was synthetised using a literature procedure reported by group of Prof. Nitschke (***Figure 2.36***).[10] Two attempts with different solvents were performed. The first one using a mixture of DMF and CH_3CN and second one only in CH_3CN, where the aldehyde was partially insoluble and the cage, soluble in acetonitrile, formation should guide the reaction. Both attempts failed to yield the cage, despite the reactions were monitored for 15 days (***Figure 2.37***). Two reasons could explain these unsuccessful attempts, the first one is the high steric hindrance on the vertex of the cages and the second one is the tendency of the central zinc to coordinate peptides. The latter hypothesis derives by the fact that a similar cage, the difference is the type of amine used as peripherical ligand, was used to selectively encapsulate a protein through the zinc coordination.[10]

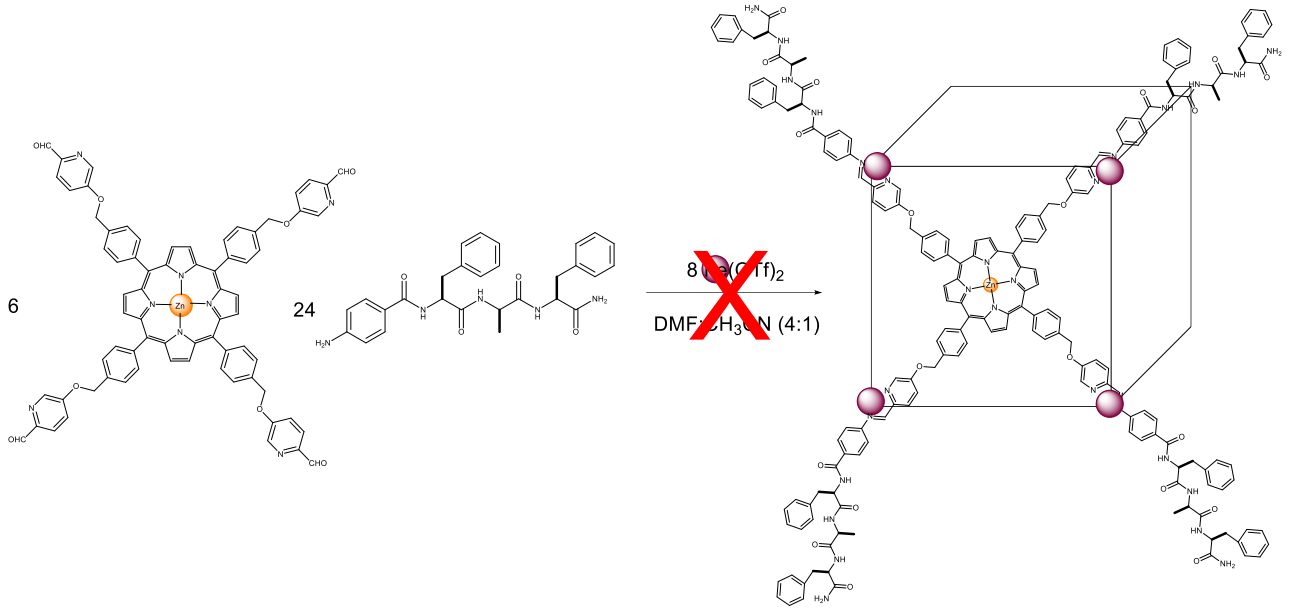

Figure 2.36: *Reaction scheme for synthesis of cage [Fe$_8$(**1e**)$_6$](OTf)$_{16}$.*

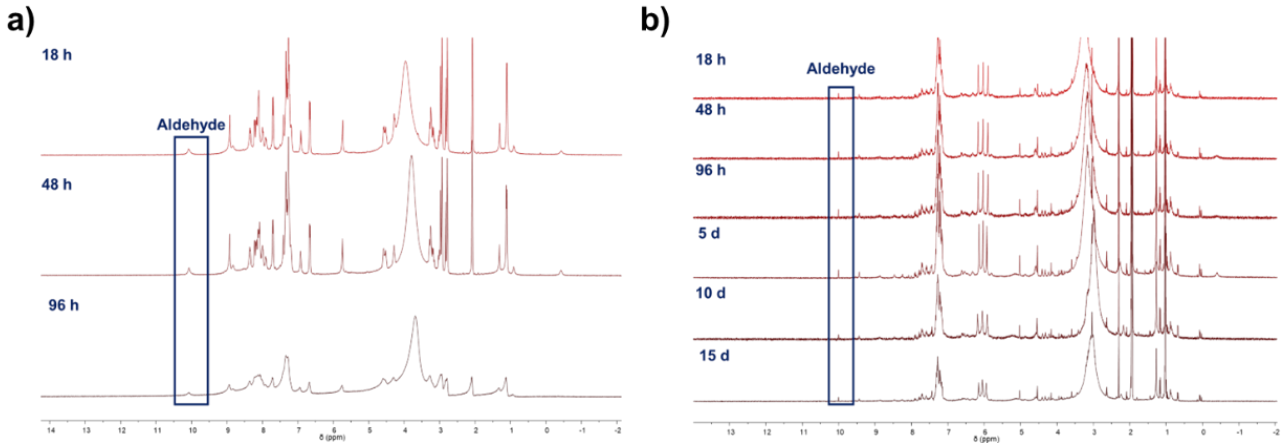

Figure 2.37: *a) ^{1}H-NMR spectrum (DMF-d$_7$, 500 MHz, T = 298 K) of cage [Fe$_8$(**1e**)$_6$](OTf)$_{16}$ over time; b)) ^{1}H-NMR spectrum (CD$_3$CN, 500 MHz, T = 298 K) of cage [Fe$_8$(**1e**)$_6$](OTf)$_{16}$ over time.*

2.4.5. Self-assembly of peptide-based cages

The self-assembly behaviour of the cages has been tested using the methodology previously reported in the Ph.D. thesis of Dr. Marion Kieffer.[3] The cages at concentration 5 mM were dissolved in CH_3CN heating at 50 °C and then sonicated for 1 h. Among all the cages $[M_4(\mathbf{Xa})_4](NTf_2)_8$ (M = Fe^{2+}, Zn^{2+}, and X = **1-4**), it was observed that only $[Fe_4(\mathbf{2a})](NTf_2)_8$ and $[Zn_4(\mathbf{1a})](NTf_2)_8$ are able to assemble in 18 hours and 3 weeks, respectively (***Figure 2.38***).

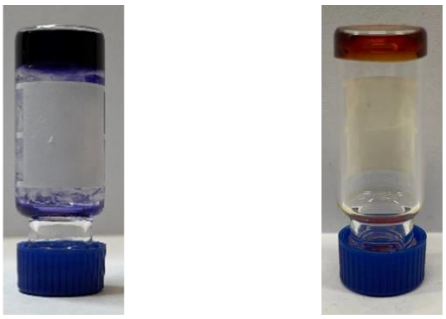

Figure 2.38: *Gels in CH_3CN of $[Fe_4(\mathbf{2a})](NTf_2)_8$ and $[Zn_4(\mathbf{1a})](NTf_2)_8$ at concentration 5 mM.*

All-atom Molecular dynamics (MD) analysis in explicit solvent of the gel of cage $[Fe_4(\mathbf{1a})_4](NTf_2)_8$ was carried out by Prof. A. V. Vargiu of the University of Cagliari and it showed that cages interacted with each other forming a 3D network (***Figure 2.39***) that encapsulated the solvent.

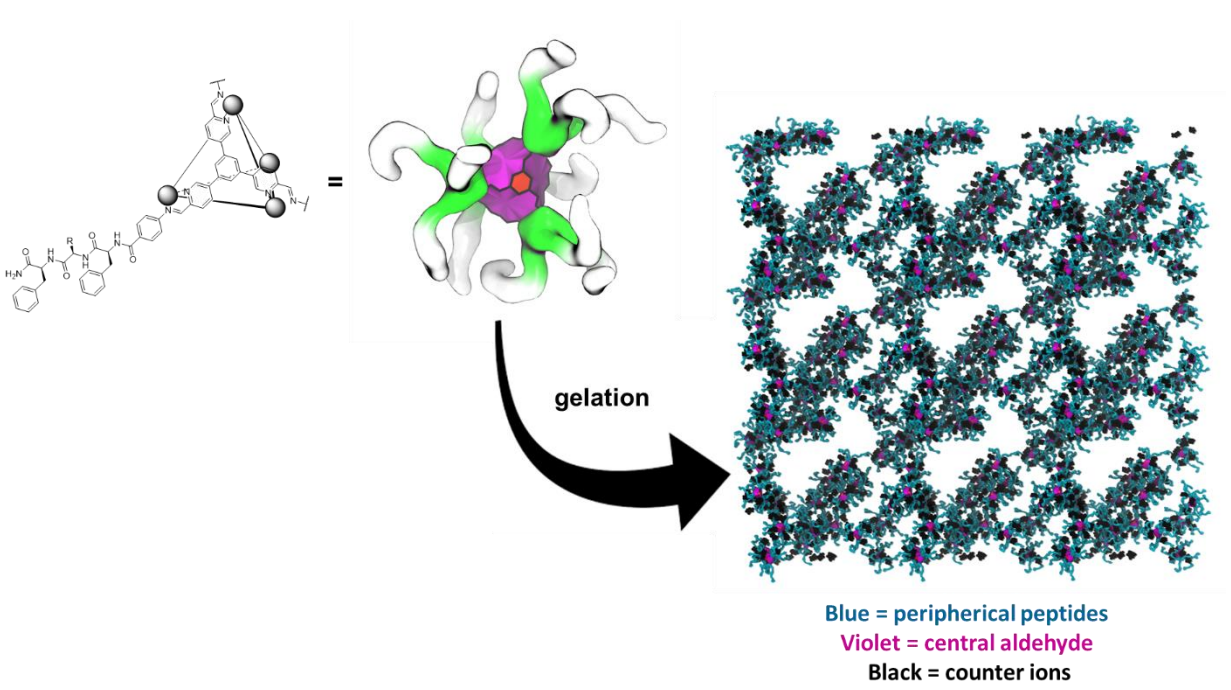

Figure 2.39: *All-atom molecular dynamics (MD) revealing the formation of stacks of cages forming fibrils that created the 3D lattice, responsible for the gel formation. Blue residues correspond to peripheral peptides; violet residues correspond to central aldehyde; black residues correspond to counter ions.*

A more detailed look of the MD study revealed the main interactions driving the self-assembly of the cage. The thickness of the bonds is correlated to the strength of the interactions, *i.e.*, the thicker they are, the stronger

is the interaction. In particular, the stronger intermolecular interaction was the aromatic interaction between the C-terminus Phe of a pendant peptide with the aromatic scaffold of the core aldehyde of a near cage (***Figure 2.40***). This is very interesting because it is a new type of interaction that is distinctive of this gel and obviously cannot be present in the gels formed solely by the peptides.

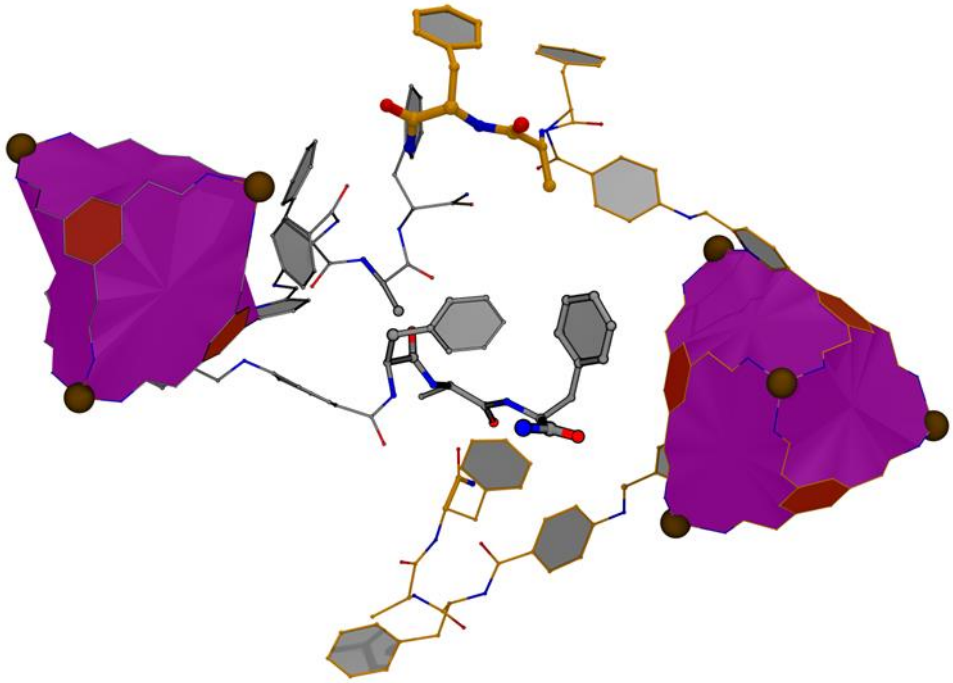

Figure 2.40: *Detailed of full-atom molecular dynamics (MD) revealing the strength of the interaction involved in the self-assembly. The thicker bonds are proportional to stronger interactions. The detailed look revealed the stronger aromatic interaction between C-terminus Phe of a pendant peptide with the aromatic scaffold of the aldehyde of a near cage.*

It is generally difficult find experimental evidence of aromatic interactions with common spectroscopic techniques. Ultraviolet Resonance Raman (UVRR) spectroscopy is a very valuable tool for collecting chemically specific information about a large variety of systems.[18] This technique was very useful especially for aromatic organic molecules exhibiting strong absorption in the UV range. It guarantees a selective strong enhancement in the UVRR spectra of solutions of the Raman cross-section of vibrations assigned to specific chromophores, making it an elite technique to study aromatic interactions.[18] UVRR spectra were acquired using synchrotron irradiation at Elettra synchrotron, IUVS beamline, with the assistance of Dr. Fatima Mahroudi.

In the first instance, the behaviour in solution of $[Fe_4(\mathbf{1a})_4](NTf_2)_8$ and the two subcomponents aldehyde **a** and peptide **1** were studied in solution. The spectrum of the cage in solution displayed two main features, a shoulder

at 1576 cm^{-1}, associated to ring vibrations of **a**, and a band at ~ 1608 cm^{-1}, derived from vibrational modes of **1** (**Figure 2.41**). The higher signal/noise ratio did not allow to identify some minor components showed in the spectrum.

The UVRR analysis of the peptide gel revealed that its spectrum was identical to the one of the peptide in solution (***Figure 2.41***, cyan and blue traces, respectively). The two main bands, at 1576 cm^{-1} 1608 cm^{-1}, were not influenced by the gelation.

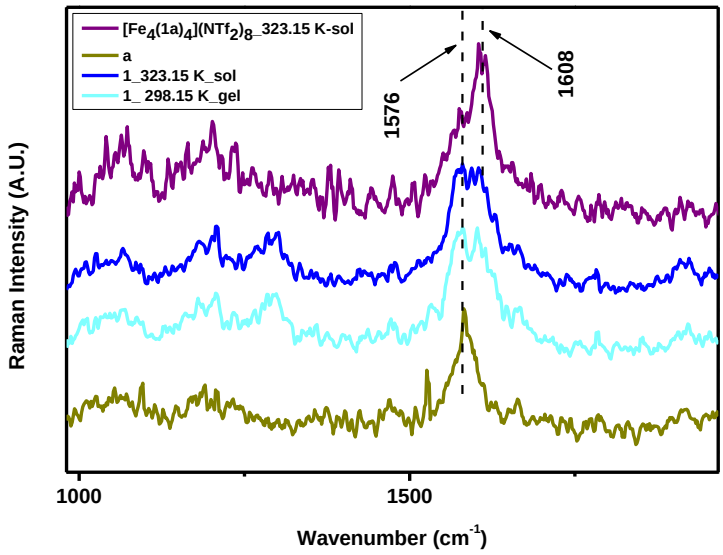

Figure 2.41: *UV Raman spectrum, in region 1000-2000 cm^{-1}, of solution state of cage $[Fe_4(\mathbf{1a})_4](NTf_2)_8$ compared with spectra of cage subcomponents peptide **1**, aldehyde **a**. Comparison between UV Raman spectrum of peptide **1** solution (T = 323.15 K) and gel (T = 298.15 K) at 30 mM.*

Despite the noise, it was possible to observe that the gelation decreased the intensity of the main features, at 1576 cm^{-1} and 1608 cm^{-1}, of the cage spectrum (***Figure 2.42***). This effect was consistent with the formation of aromatic interactions between the MOCs in the gel state, as confirmed by examples in literature regarding aromatic interactions in DNA native structure.[19] The similarity of the spectra of peptide **1** in solution and in gel state (***Figure 2.41***), suggested that these interactions were peculiar of the cage.

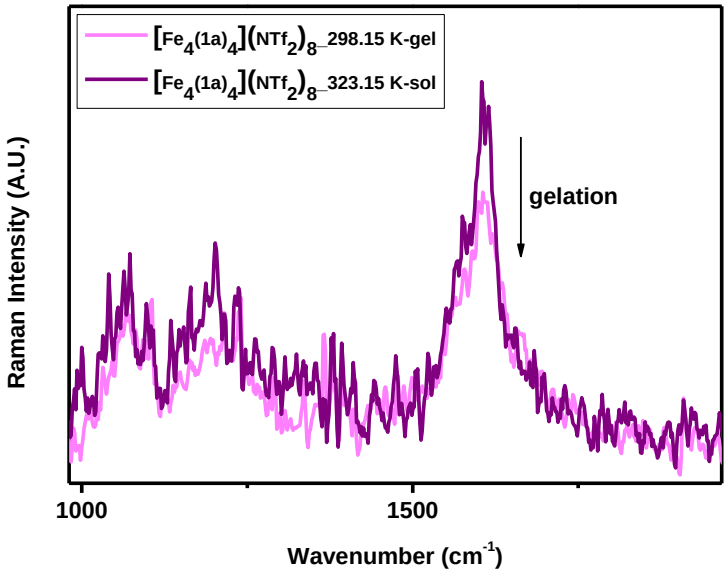

Figure 2.42: *UV Raman spectrum, in region 1000-2000 cm^{-1}, of solution state (T = 323.15 K) and gel (T = 298.15 K) of cage [Fe4(**1a**)4](NTf2)8.*

2.5. Conclusion and Future work

In this chapter, the gelation ability of different cages was investigated in CH_3CN, as a green solvent. Firstly, four different peptides were synthesized, purified, and thoroughly characterised both from a molecular and supramolecular point of view. All the peptides were capable to self-assemble in acetonitrile at different concentrations into gels with different mechanical properties and nanomorphology. In particular, it was observed the positive effect of the β-branching on the entanglement of nano-sized, thin fibrils, disfavouring their bundling into microscopic fibers, which leads to undesirable material properties, including opacity.

The four peptides were combined with the different aldehydes **a**-**e**. Only aldehyde **a** yielded the desired cages and their self-assembly behaviour were tested. Only $[Fe_4(\mathbf{2a})](NTf_2)_8$ and $[Zn_4(\mathbf{1a})](NTf_2)_8$ were able to form gels. This is probably related both to steric reasons related to the branching of the aliphatic sidechain of the amino-acids and to the higher dimension of zinc ions that could disfavour the aromatic interactions between the phenylalanine residues and the aromatic scaffold of the piconiltrisaldehyde. Full-atom molecular dynamics revealed that MOCs interact with each other forming the gel matrix. The main interaction that ruled the assembly was an aromatic interaction between the C-terminal Phe of one cage and the aromatic core of the aldehyde of another cage. This interaction was confirmed by UV Resonance Raman analysis. The intensity of

the main two signals relative to the cage decreased during the gel formation. This behaviour was generally related to the formation of aromatic interactions.

This project lays the foundation for the development of new soft materials with dual porosity for different applications from selective guest release to catalysis. One advantage of using very simple and minimalistic building blocks (such as tripeptides) is the low-cost and easy preparation on a large scale too. Minimalism is an elegant approach that includes only the essential, functional elements to attain the desired outcome. However, this approach is very challenging because the design has to be very accurate to enable the hierarchical assembly into gelling cages, and each fine detail of the supramolecular design has to be taken into account. More attempts will be also made to generalise this approach, testing new aldehydes and new metal salts. Given the importance of the aromatic interaction between pendant peptides and the aromatic core of the cage panel, aldehydes with flat aromatic panels will be preferred in the future.

2.6. Experimental part

2.6.1. Peptides characterisation

Peptide p-aminobenzoyl-L-Phe-D-Ala-L-Phe-NH_2 (1)

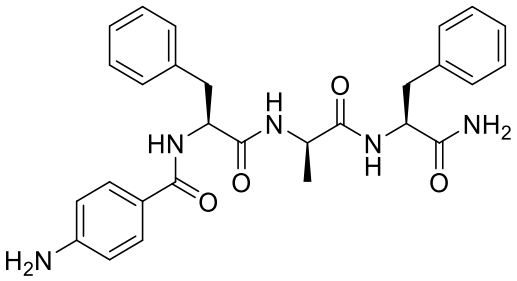

Chemical Formula: $C_{28}H_{31}N_5O_4$
Molecular Weight: 501,59

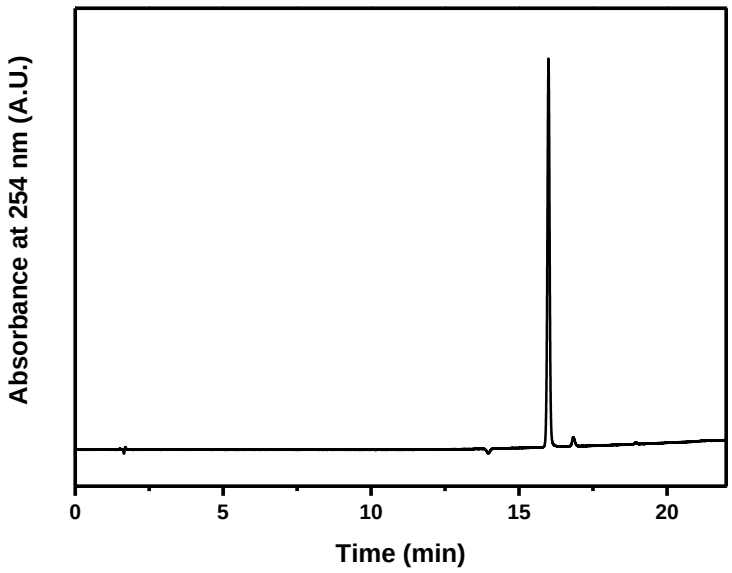

Figure 2.43: *LC-MS chromatogram at 254 nm of peptide **1**.*

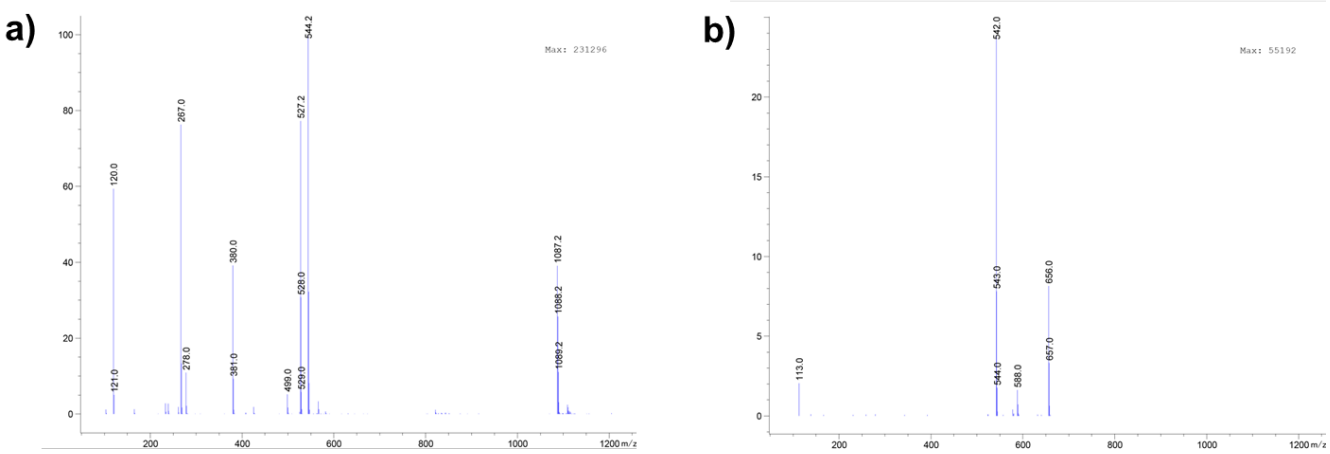

Figure 2.44: *ESI-MS of peptide **1**. a) positive spectrum, b) negative spectrum.*

Peptide p-aminobenzoyl-L-Phe-D-Val-L-Phe-NH_2 (2)

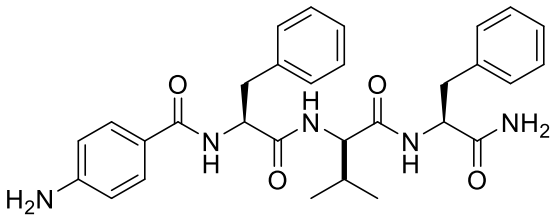

Chemical Formula: $C_{30}H_{35}N_5O_4$
Molecular Weight: 529,64

^{1}H NMR (500 MHz, DMSO-d_6) δ 8.26 (d, J = 8.7 Hz, 1H), 8.14 (d, J = 8.0 Hz, 1H), 7.97 (d, J = 8.6 Hz, 1H), 7.55 (d, J = 8.7 Hz, 2H), 7.39 (s, 1H), 7.34 – 7.30 (m, 2H), 7.26 – 7.10 (m, 9H), 6.58 (d, J = 8.6 Hz, 2H), 4.76 – 4.68 (m, 1H), 4.44 (ddd, J = 10.8, 8.8, 4.1 Hz, 1H), 4.09 (dd, J = 8.6, 6.0 Hz, 2H), 3.11 – 2.92 (m, 3H), 2.74 (dd, J = 13.7, 10.8 Hz, 1H), 1.79 – 1.76 (m, 1H), 0.49 (d, J = 6.8 Hz, 6H).

^{13}C NMR (126 MHz, DMSO-d_6) δ 173.12 (s), 171.95 (s), 170.58 (s), 166.25 (s), 138.19 (d, J = 3.8 Hz), 129.27 – 128.83 (m), 127.98 (d, J = 9.0 Hz), 126.13 (d, J = 8.0 Hz), 113.36 (s), 57.54 (s), 55.03 (s), 54.11 (s), 37.46 (s), 30.09 (s), 18.96 (s), 17.41 (s).

ESI-MS: m/z calculated for M = 529.64, observed positive mode $[M + H]^+$ = 530.2 and negative mode $[M-H]^-$ = 528.0

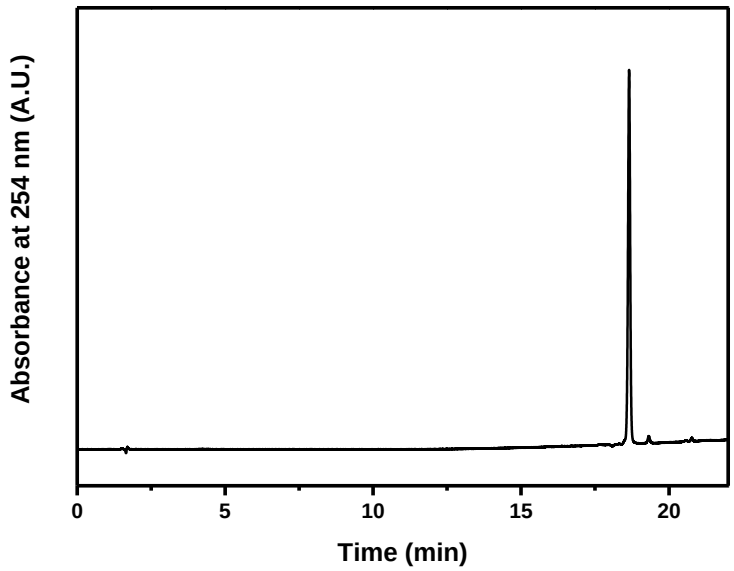

Figure 2.45: *LC-MS chromatogram at 254 nm of peptide* ***2****.*

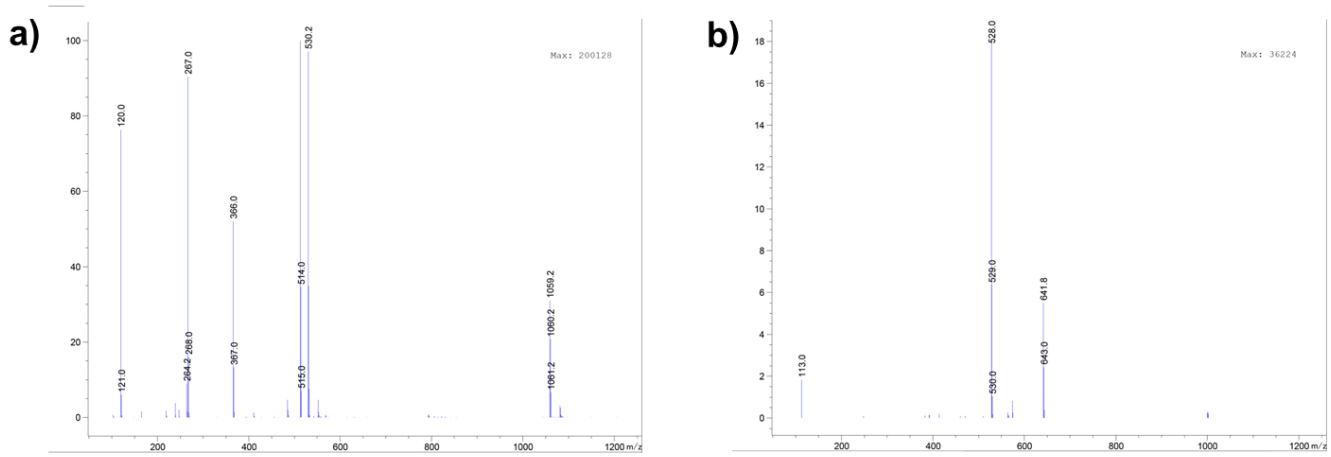

Figure 2.46: *ESI-MS of peptide* ***2****. a) positive spectrum, b) negative spectrum.*

Peptide p-aminobenzoyl-L-Phe-D-Leu-L-Phe-NH_2 (3)

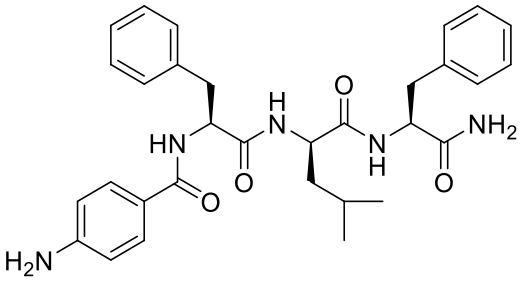

Chemical Formula: $C_{31}H_{37}N_5O_4$
Molecular Weight: 543,67

^{1}H NMR (500 MHz, DMSO-d_6) δ 8.21 (dd, J = 13.9, 8.1 Hz, 2H), 8.15 (d, J = 8.1 Hz, 1H), 7.58 (d, J = 8.7 Hz, 2H), 7.34 (s, 1H), 7.31 – 7.22 (m, 4H), 7.20 – 7.11 (m, 7H), 6.58 (d, J = 8.6 Hz, 2H), 4.59 (dd, J = 15.1, 7.5 Hz, 1H), 4.36 (ddd, J = 10.9, 8.9, 4.0 Hz, 1H), 4.11 (ddd, J = 9.5, 8.3, 5.4 Hz, 1H), 3.09 (dd, J = 13.6, 3.9 Hz, 1H), 3.01 (t, J = 7.0 Hz, 2H), 2.77 (dd, J = 13.6, 10.9 Hz, 1H), 1.25 – 1.10 (m, 2H), 1.04 – 0.94 (m, 1H), 0.67 (dd, J = 22.4, 6.5 Hz, 6H).

^{13}C NMR (126 MHz, DMSO-d_6) δ 173.12, 171.65, 166.49, 150.33, 138.29, 137.95, 129.33 – 128.87, 127.97, 126.12, 121.46, 113.35, 55.46, 54.24, 50.98, 40.36, 37.27, 23.62, 22.95, 21.53.

ESI-MS: m/z calculated for M = 543.67, observed positive mode $[M + H]^+$ = 544.2 and negative mode $[M-H]^-$ = 542.0

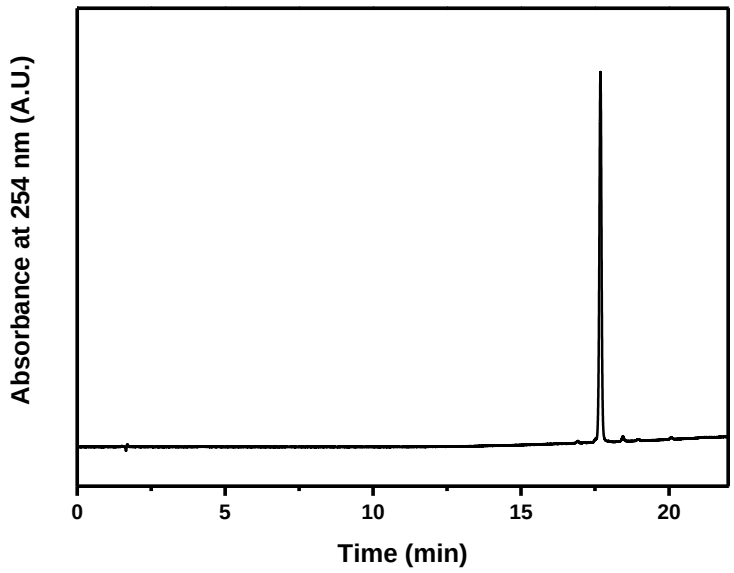

Figure 2.47: *LC-MS chromatogram at 254 nm of peptide **3**.*

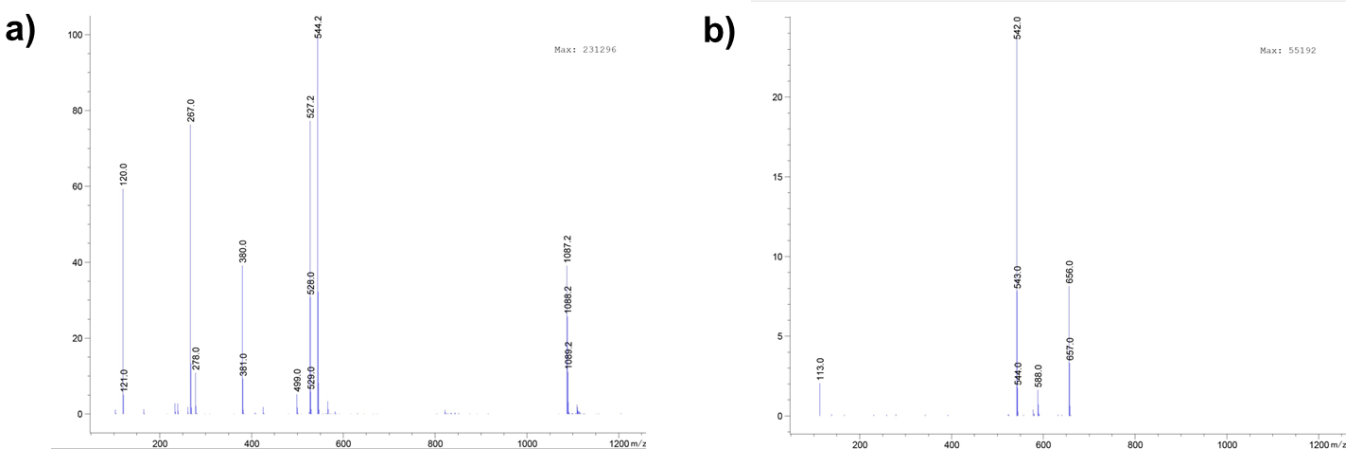

Figure 2.48: *ESI-MS of peptide **3**. a) positive spectrum, b) negative spectrum.*

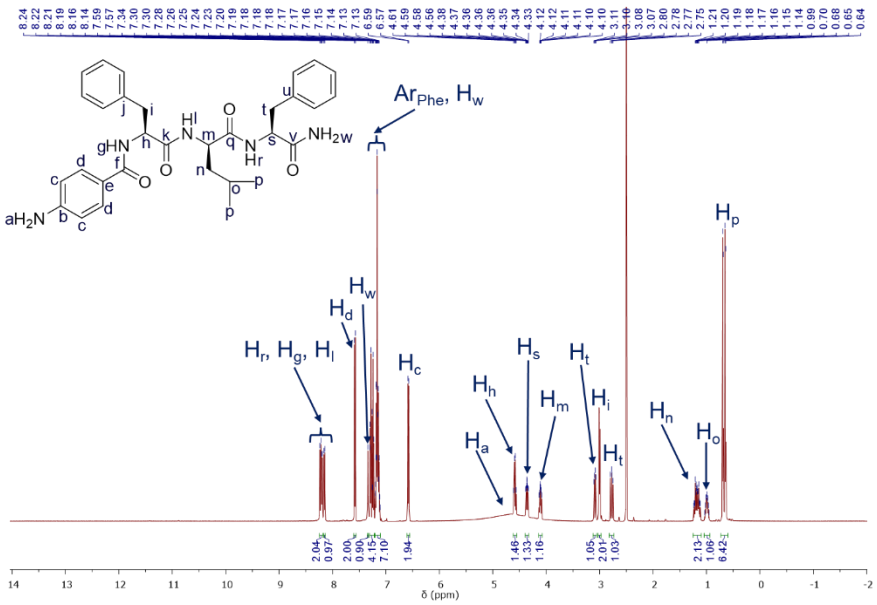

Figure 2.49: *^{1}H-NMR spectrum (DMSO-d_6, T = 298 K) of peptide* ***3****.*

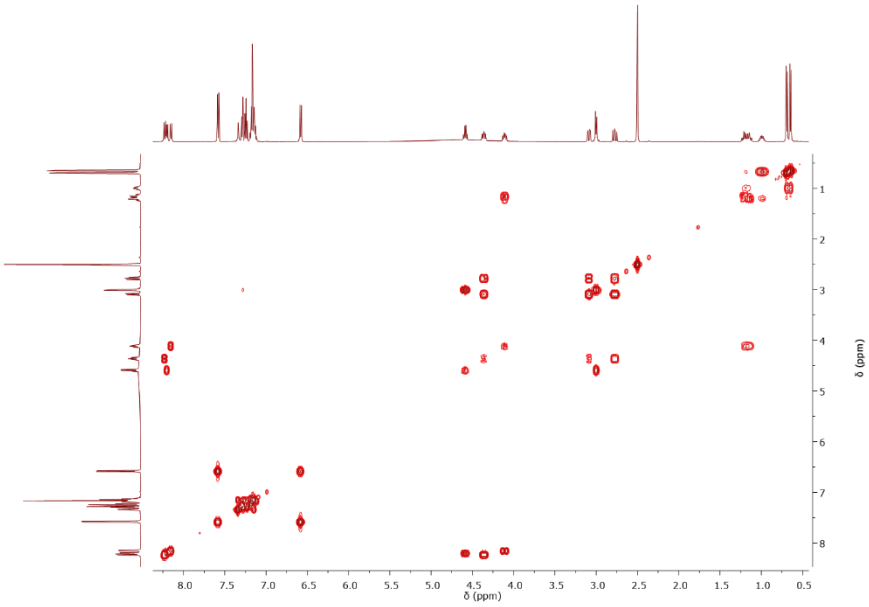

Figure 2.50: *^{1}H,^{1}H-COSY spectrum (DMSO-d_6, T = 298 K) of peptide* ***3****.*

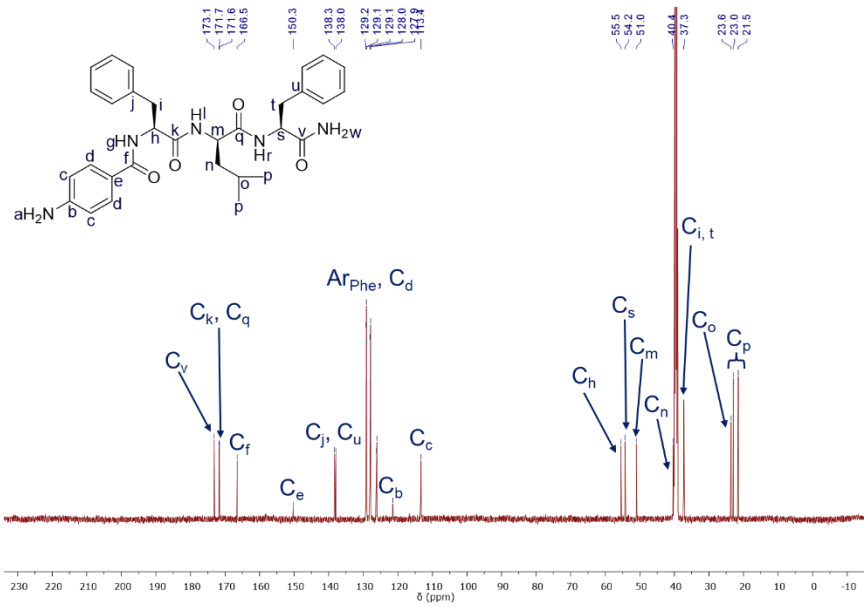

Figure 2.51: *^{13}C-NMR spectrum (DMSO-d_6, T = 298 K) of peptide **3**.*

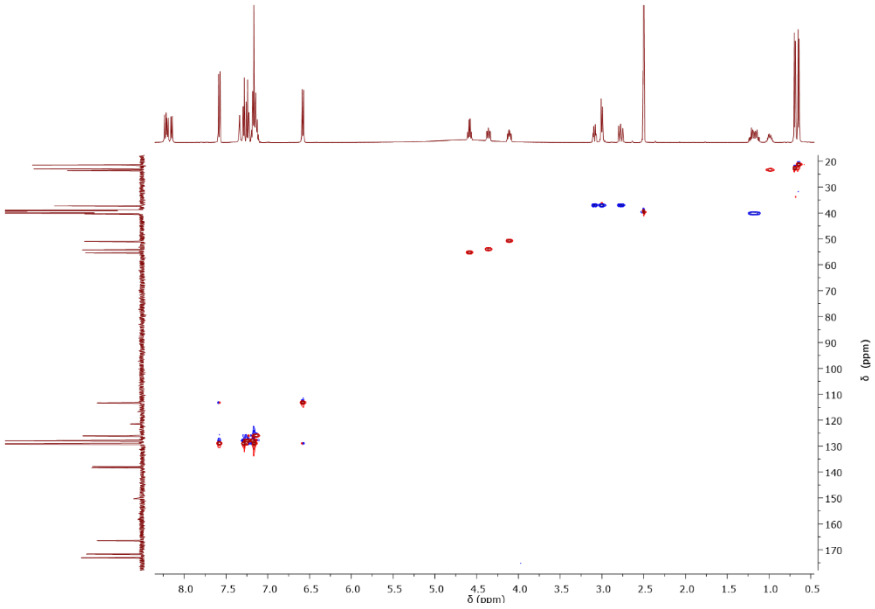

Figure 2.52: *^{1}H, ^{13}C-HSQC spectrum (DMSO-d_6, T = 298 K) of peptide **3**.*

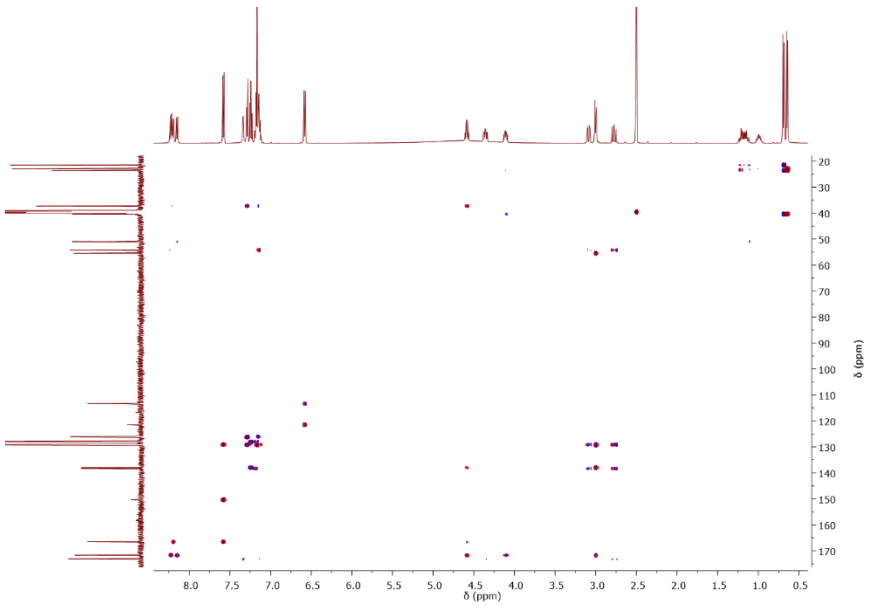

Figure 2.53: *$^{1}H,^{13}C$-HMBC spectrum (DMSO-d_6, T = 298 K) of peptide **3**.*

Peptide p-aminobenzoyl-L-Phe-D-Ile-L-Phe-NH_2 (4)

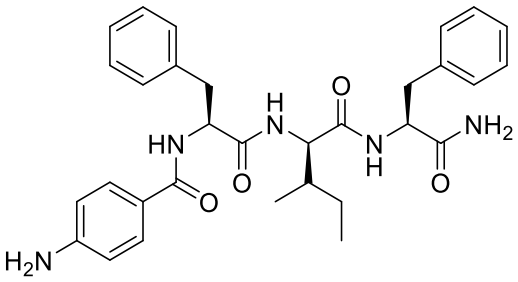

Chemical Formula: $C_{31}H_{37}N_5O_4$
Molecular Weight: 543,67

^{1}H NMR (499 MHz, DMSO-d_6) δ 8.28 (d, *J* = 8.7 Hz, 1H), 8.10 (d, *J* = 8.0 Hz, 1H), 7.99 (d, *J* = 8.5 Hz, 1H), 7.54 (d, *J* = 8.7 Hz, 2H), 7.37 (d, *J* = 0.9 Hz, 1H), 7.32 (d, *J* = 1.2 Hz, 2H), 7.26 – 7.09 (m, 9H), 6.55 (d, *J* = 8.6 Hz, 2H), 4.76 – 4.67 (m, 1H), 4.43 (ddd, *J* = 10.9, 8.7, 4.0 Hz, 1H), 4.09 (dd, *J* = 8.4, 6.5 Hz, 1H), 3.02 (dtd, *J* = 23.3, 13.7, 6.9 Hz, 3H), 2.75 (dd, *J* = 13.7, 10.9 Hz, 1H), 1.52 (tdd, *J* = 13.5, 8.5, 5.1 Hz, 1H), 1.11 – 1.01 (m, 1H), 0.77 (tt, *J* = 14.0, 7.2 Hz, 1H), 0.62 (d, *J* = 7.3 Hz, 3H), 0.44 (d, *J* = 6.8 Hz, 3H).

^{13}C NMR (126 MHz, DMSO-d_6) δ 173.14, 171.89, 170.64, 166.25, 150.71, 138.19, 129.53 – 128.43, 127.97, 126.14, 121.26, 113.05, 56.92, 54.94, 54.19, 37.40, 36.22, 23.81, 15.00, 11.04.

ESI-MS: m/z calculated for M = 543.67, observed positive mode $[M + H]^+$ = 544.2 and negative mode $[M-H]^-$ = 542.0

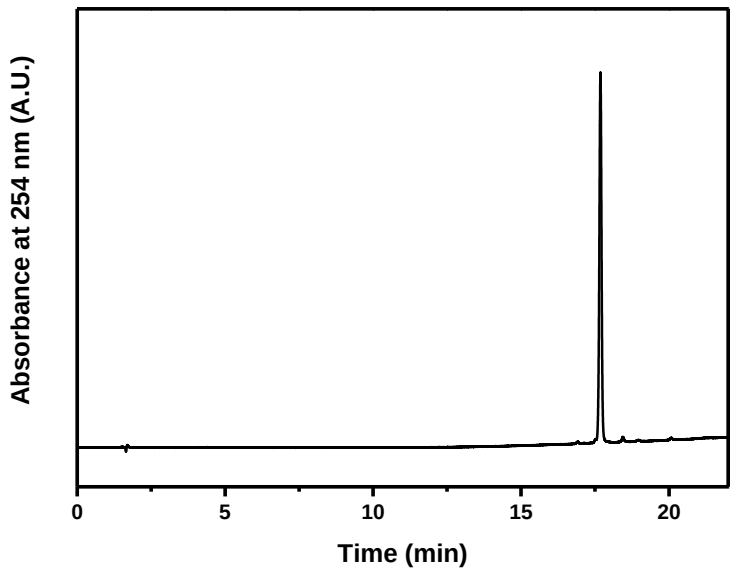

Figure 2.54: *LC-MS chromatogram at 254 nm of peptide* ***4****.*

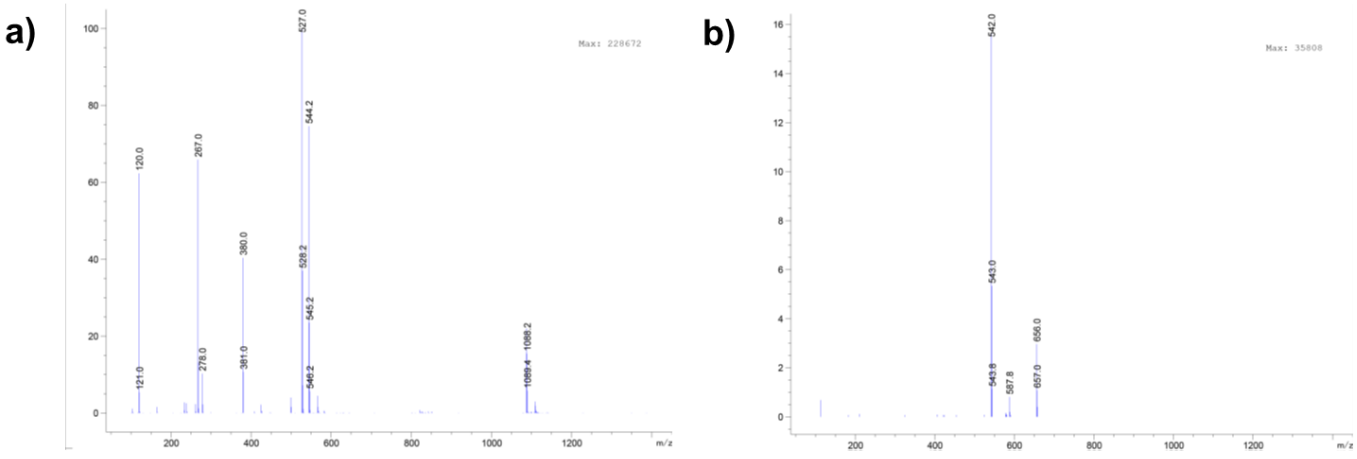

Figure 2.55: *ESI-MS of peptide* ***4****. a) positive spectrum, b) negative spectrum.*

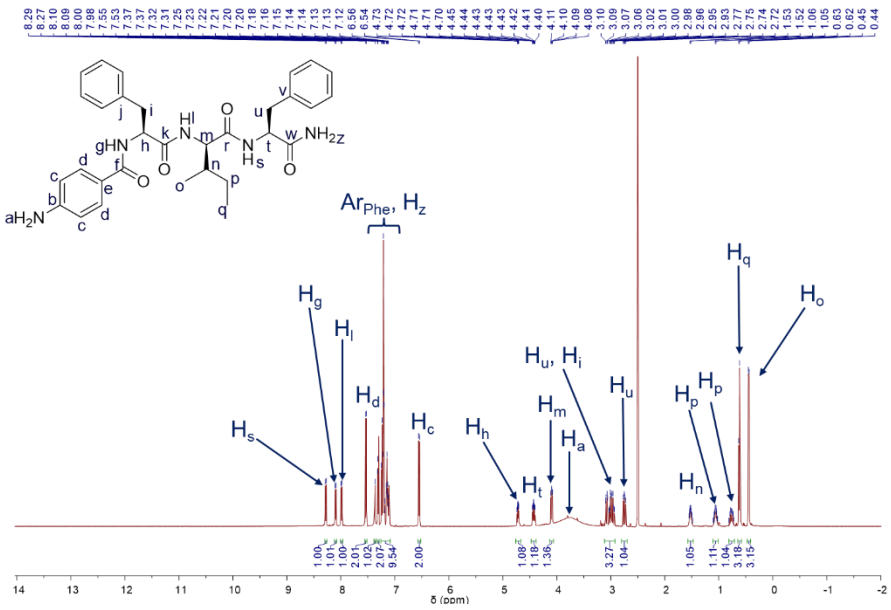

Figure 2.56: *^{1}H-NMR spectrum (DMSO-d_6, T = 298 K) of peptide **4**.*

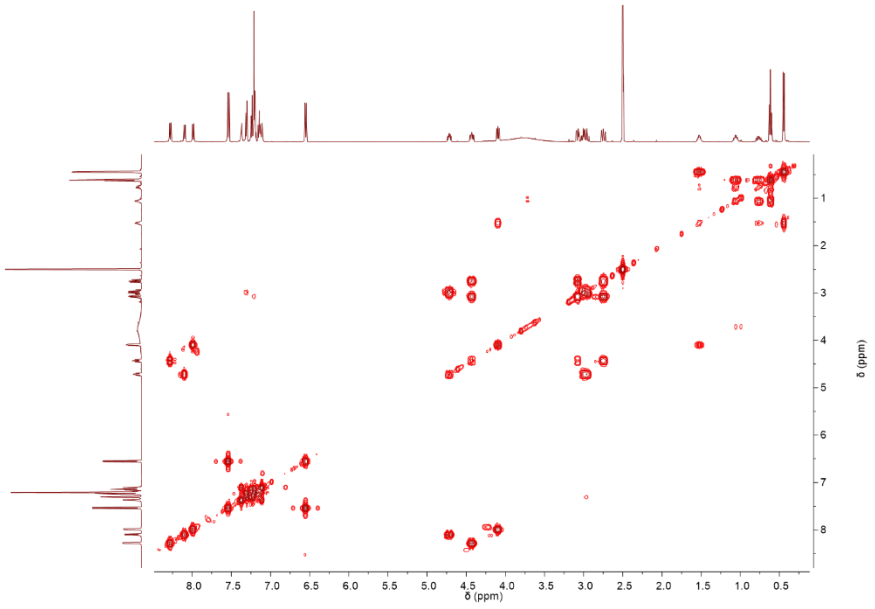

Figure 2.57: *^{1}H,^{1}H-COSY spectrum (DMSO-d_6, T = 298 K) of peptide **4**.*

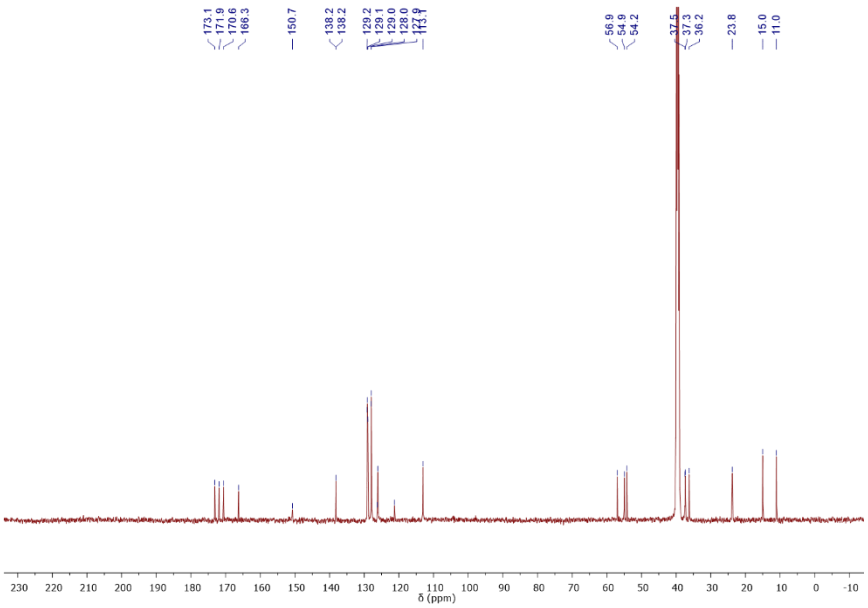

Figure 2.58: *^{13}C-NMR spectrum (DMSO-d_6, T = 298 K) of peptide **4**.*

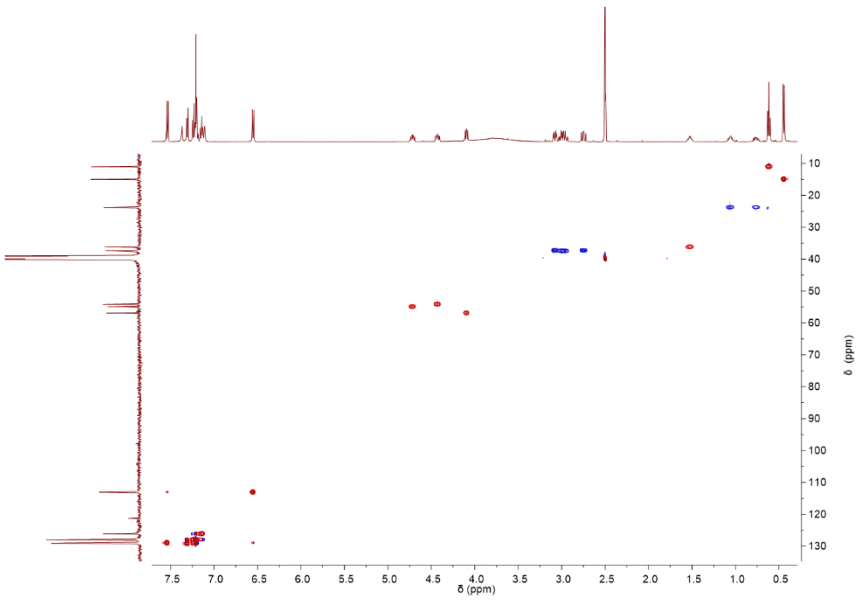

Figure 2.59: *^{1}H, ^{13}C-HSQC spectrum (DMSO-d_6, T = 298 K) of peptide **4**.*

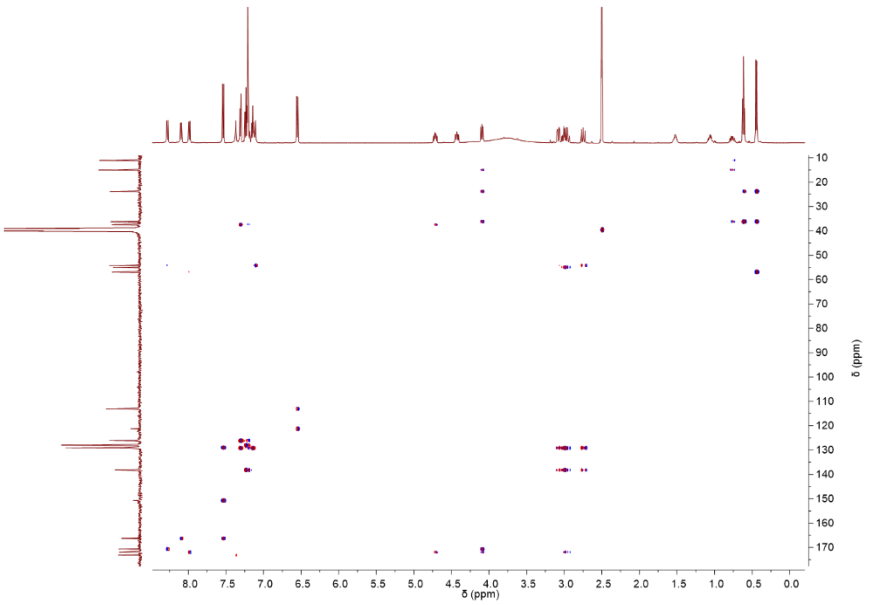

Figure 2.60: *$^{1}H,^{13}C$-HMBC spectrum (DMSO-d_6, T = 298 K) of peptide **4**.*

2.6.2. Aldehydes characterisation

135TrBB

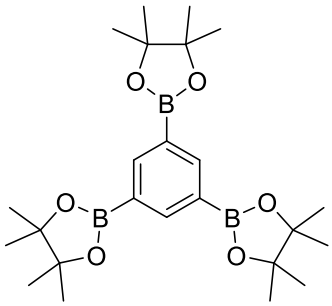

^{1}H NMR (400 MHz, $CDCl_3$) δ 8.36 (s, 3H), 1.33 (s, 36H).

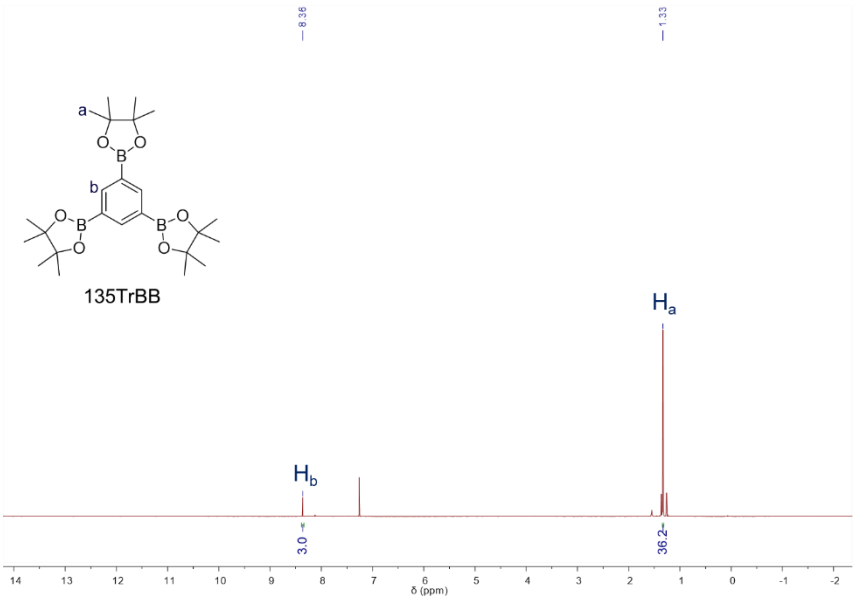

Figure 2.61: *^{1}H-NMR spectrum (CD_3CN, 400 MHz, T = 298 K) of 135TrBB.*

Aldehyde a

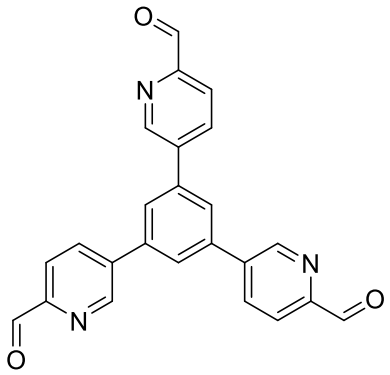

^{1}H NMR (400 MHz, $CDCl_3$) δ 10.18 (s, 3H), 9.12 (s, 3H), 8.19 (d, J = 8.1 Hz, 3H), 8.14 (d, J = 8.1 Hz, 3H), 7.95 (s, 3H).

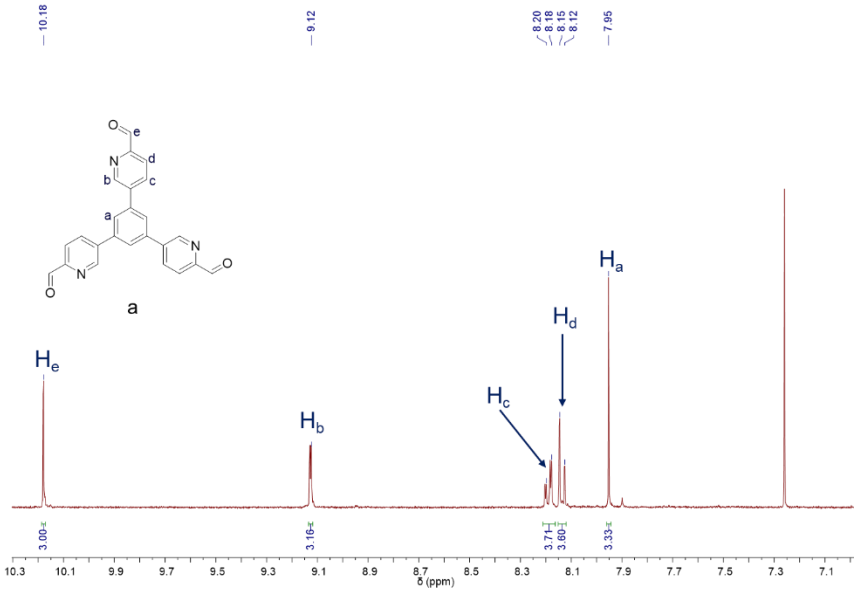

Figure 2.62: *^{1}H-NMR spectrum (CD_3CN, 400 MHz, T = 298 K) of aldehyde* ***a****.*

T4BrP

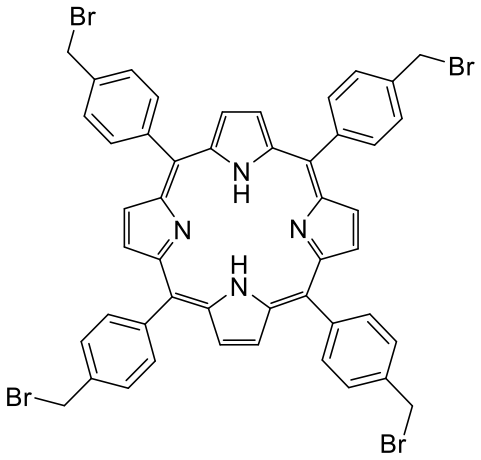

^{1}H NMR (400 MHz, $CDCl_3$) δ 8.84 (s, 8H), 8.19 (d, J = 7.9 Hz, 8H), 7.80 (d, J = 8.0 Hz, 8H), 4.86 (s, 8H).

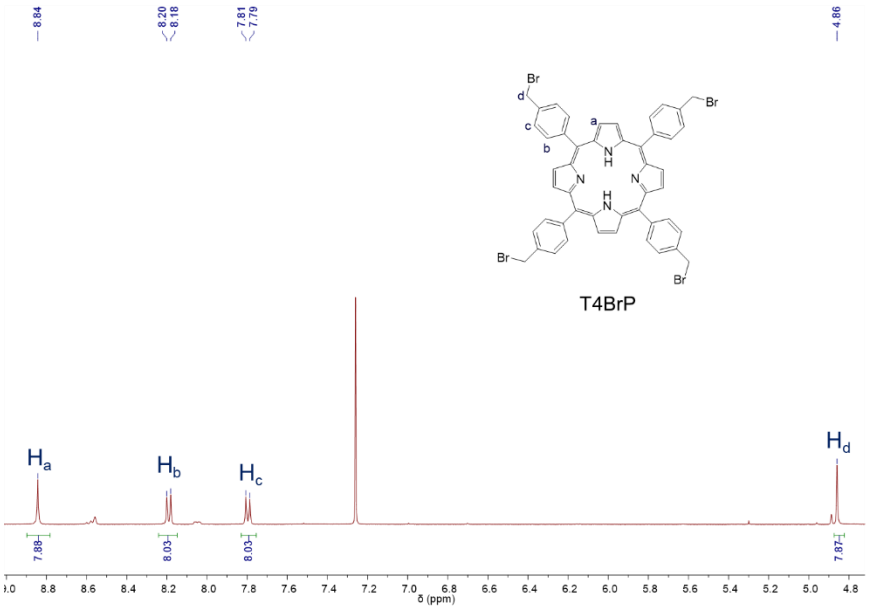

Figure 2.63: *^{1}H-NMR spectrum (CD_3CN, 400 MHz, T = 298 K) of T4BrP.*

Zn-T4BrP

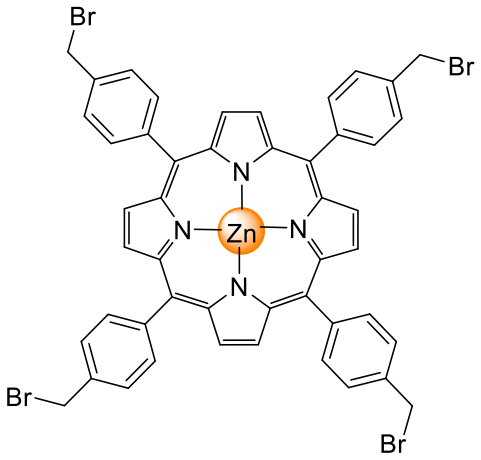

^{1}H NMR (400 MHz, $CDCl_3$) δ 8.95 (s, 8H), 8.19 (d, J = 8.0 Hz, 8H), 7.80 (s, 8H), 4.87 (s, 8H).

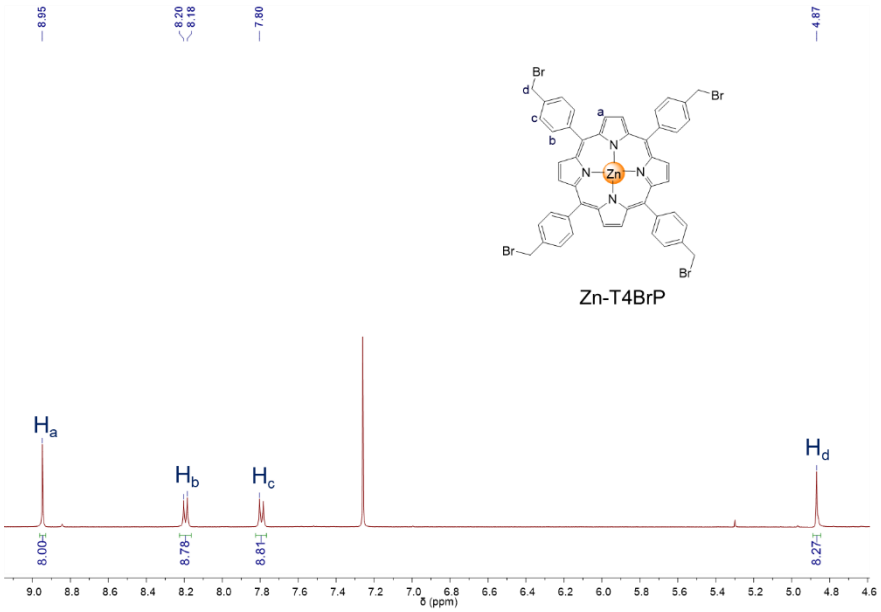

Figure 2.64: *^{1}H-NMR spectrum (CD_3CN, 400 MHz, T = 298 K) of Zn-T4BrP.*

Aldehyde e

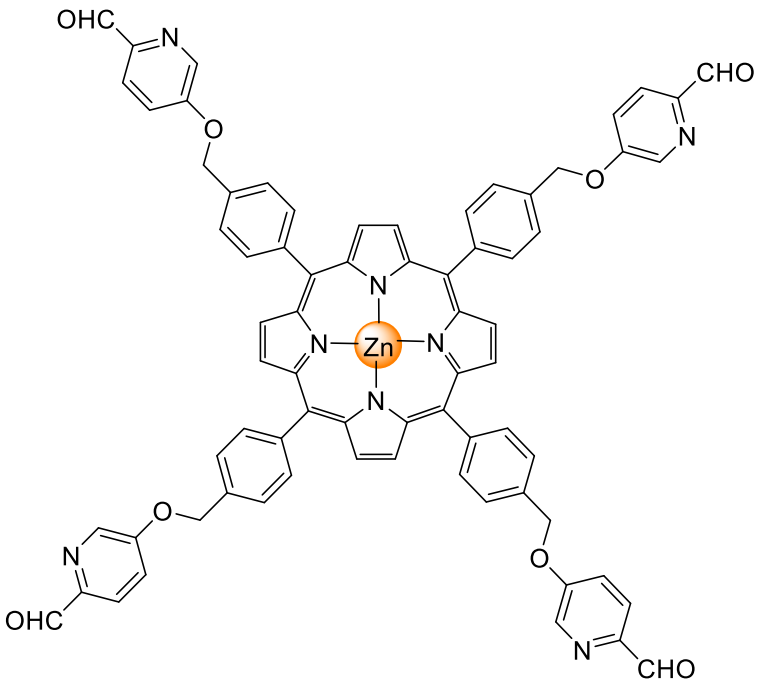

^{1}H NMR (400 MHz, DMF) δ 10.03 (s, 4H), 8.92 (s, 8H), 8.82 (s, 4H), 8.36 (d, J = 7.6 Hz, 8H), 8.12 (d, J = 8.6 Hz, 4H), 8.01 (s, 8H), 7.96 (d, J = 7.5 Hz, 4H), 5.78 (s, 8H).

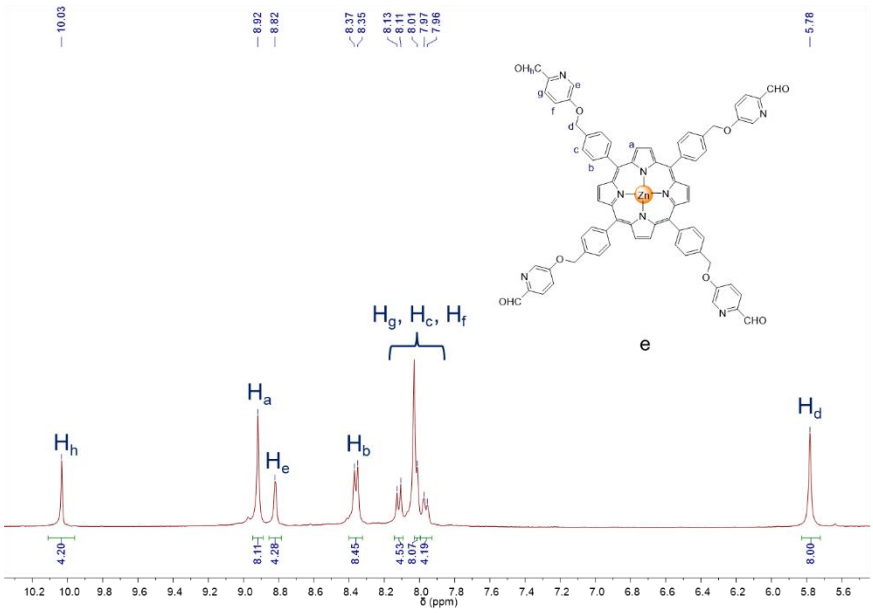

Figure 2.65: *[1]H-NMR spectrum (CD3CN, 400 MHz, T = 298 K) of aldehyde* ***e***

2.6.3. Cages characterisation

$[Fe_4(\mathbf{2a})_4](NTf_2)_8$

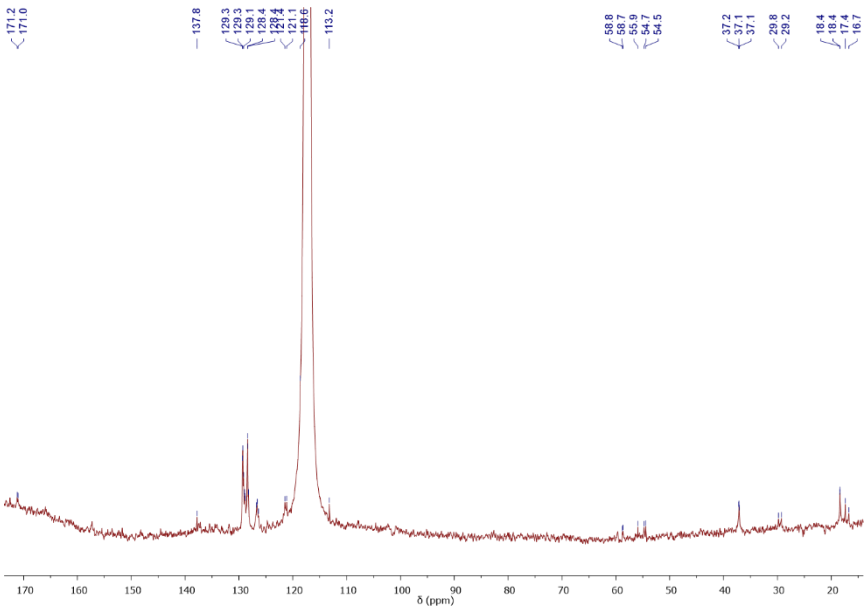

Figure 2.66: *[13]C-NMR spectrum (CD_3CN, 100 MHz, T = 298 K) of cage $[Fe_4(\mathbf{2a})_4](NTf_2)_8$.*

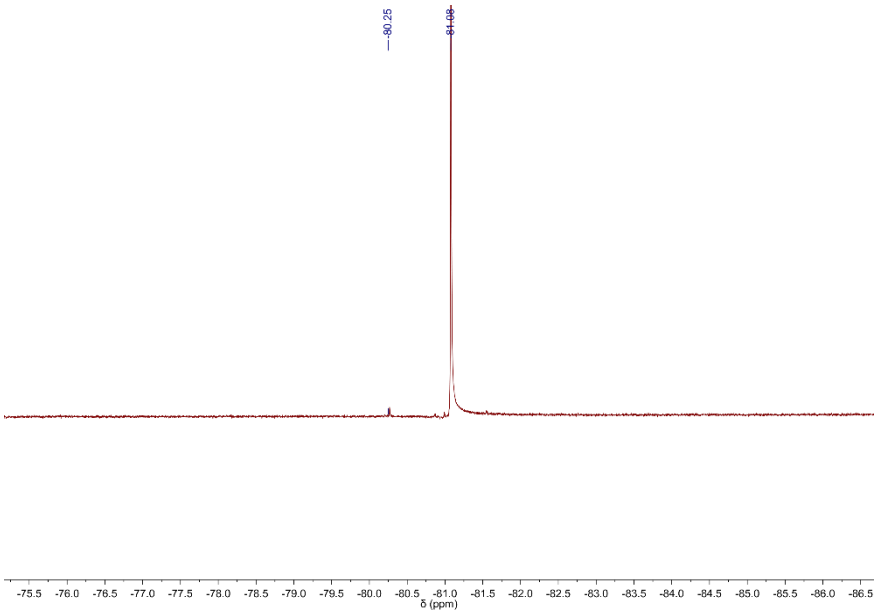

Figure 2.67: *^{19}F-NMR spectrum (CD_3CN, 471 MHz, T = 298 K) of cage $[Fe_4(\mathbf{2a})_4](NTf_2)_8$.*

$[Fe_4(\mathbf{3a})_4](NTf_2)_8$

Species	Calculated m/z	Experimental m/z
$[Fe_4(C_{117}H_{120}N_{18}O_{12})_4(N(SO_2CF_3)_2)_3(CF_3CO_2)]^{4+}$	2264.5330	2264.5436
$[Fe_4(C_{117}H_{120}N_{18}O_{12})_4(N(SO_2CF_3)_2)_2(CF_3CO_2)]^{5+}$	1755.5966	1755.4491
$[Fe_4(C_{117}H_{120}N_{18}O_{12})_4(N(SO_2CF_3)_2)(CF_3CO_2)_2]^{5+}$	1722.1700	1722.0494
$[Fe_4(C_{117}H_{120}N_{18}O_{12})_4(N(SO_2CF_3)_2)(CF_3CO_2)]^{6+}$	1416.3057	1416.2214
$[Fe_4(C_{117}H_{120}N_{18}O_{12})_4(CF_3CO_2)]^{7+}$	1173.9550	1173.9147

Table 2.4: *m/z values for $[Fe_4(\mathbf{3a})_4](NTf_2)_8$.*

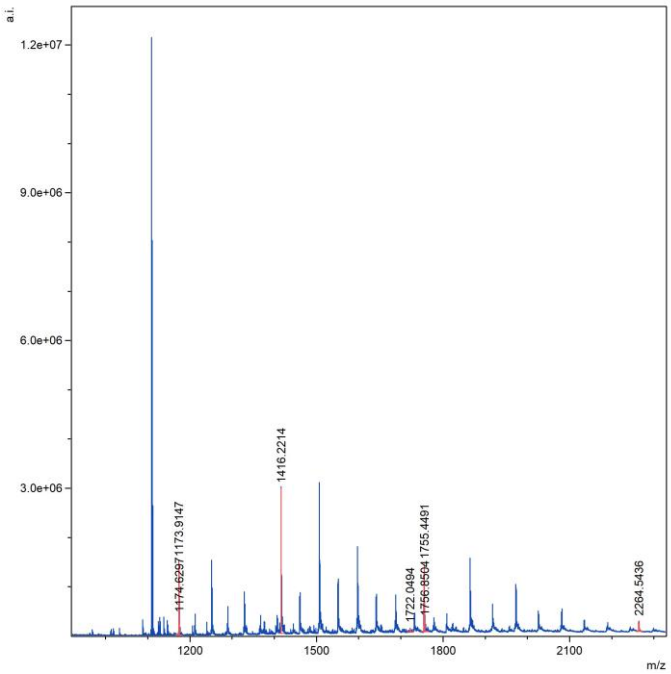

Figure 2.68: *ESI-MS of cage [Fe$_4$(**3a**)$_4$](NTf$_2$)$_8$.*

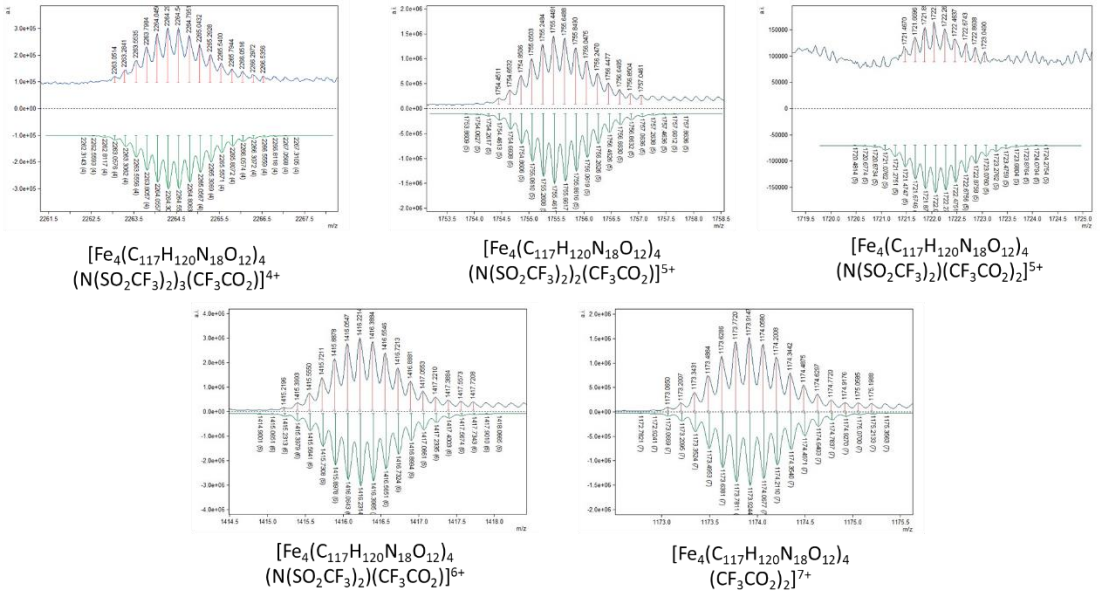

Figure 2.69: *Isotopic pattern distribution of [Fe$_4$(**3a**)$_4$](NTf$_2$)$_8$.*

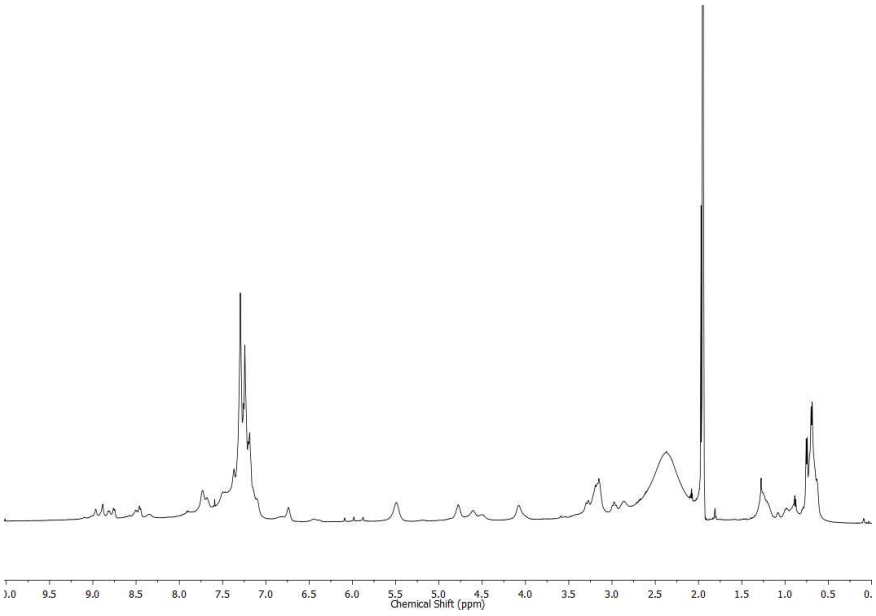

Figure 2.70: *^{1}H-NMR spectrum (CD_3CN, 500 MHz, T = 298 K) of cage $[Fe_4(\mathbf{3a})_4](NTf_2)_8$.*

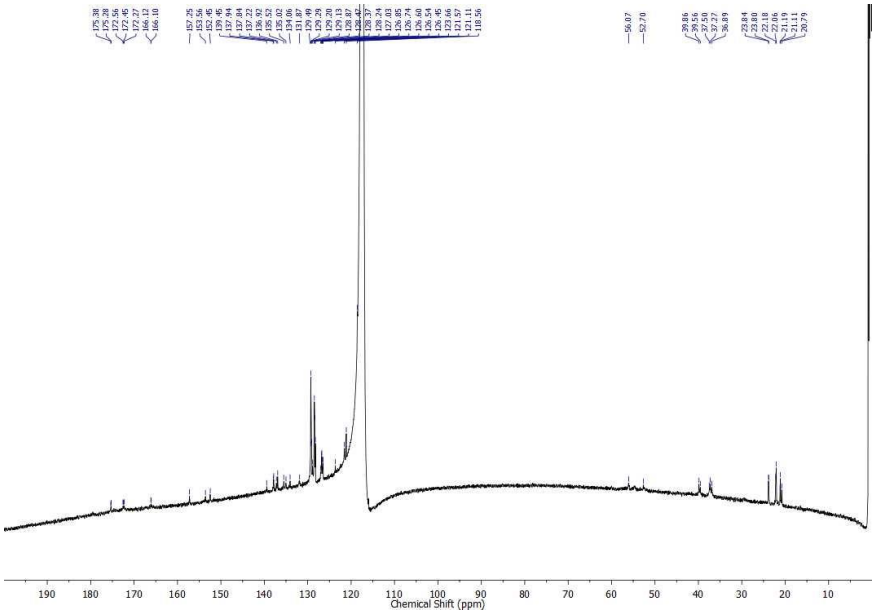

Figure 2.71: *^{13}C-NMR spectrum (CD_3CN, 125 MHz, T = 298 K) of cage $[Fe_4(\mathbf{3a})_4](NTf_2)_8$.*

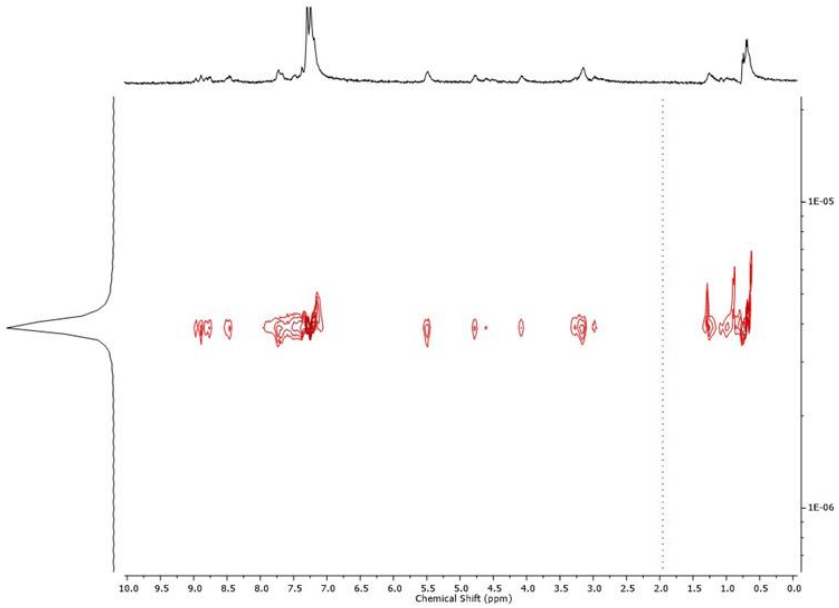

Figure 2.72: *^{1}H-DOSY NMR spectrum (CD_3CN, 400 MHz, T = 298 K) of cage $[Fe_4(\mathbf{3a})_4](NTf_2)_8$. The diffusion coefficient for $[Fe_4(\mathbf{3a})_4](NTf_2)_8$ in CD_3CN was measured to be 3.86 x 10^{-10} m^2 s^{-1} and the solvodynamic radius was calculated to be 16.9 Å.*

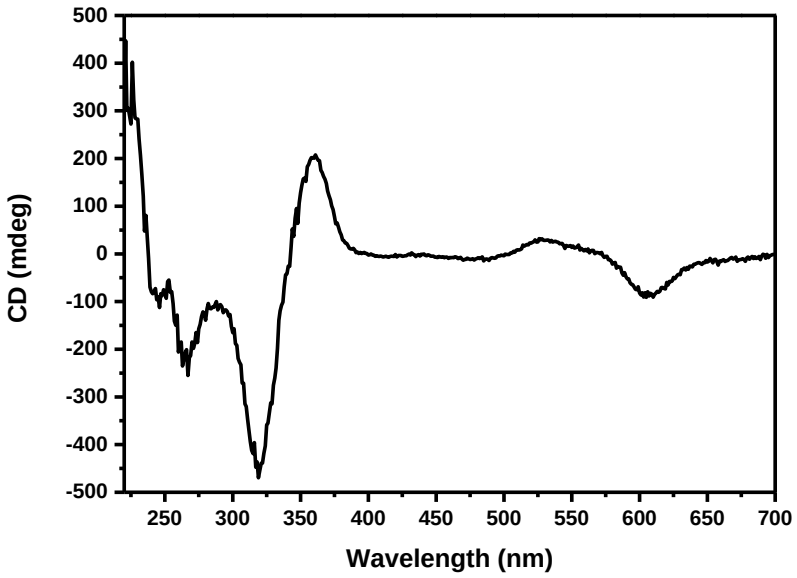

Figure 2.73: *CD spectrum of $[Fe_4(\mathbf{3a})_4](NTf_2)_8$.*

$[Fe_4(\mathbf{4a})_4](NTf_2)_8$

Species	Calculated m/z	Experimental m/z
$[Fe_4(C_{117}H_{120}N_{18}O_{12})_4(N(SO_2CF_3)_2)_3(CF_3CO_2)]^{4+}$	2264.5330	2264.5533
$[Fe_4(C_{117}H_{120}N_{18}O_{12})_4(N(SO_2CF_3)_2)_2(CF_3CO_2)]^{5+}$	1755.5966	1755.6584
$[Fe_4(C_{117}H_{120}N_{18}O_{12})_4(N(SO_2CF_3)_2)(CF_3CO_2)]^{6+}$	1416.3057	1416.3952
$[Fe_4(C_{117}H_{120}N_{18}O_{12})_4(CF_3CO_2)]^{7+}$	1173.9550	1173.9230

Table 2.5: *m/z values for* $[Fe_4(\mathbf{4a})_4](NTf_2)_8$.

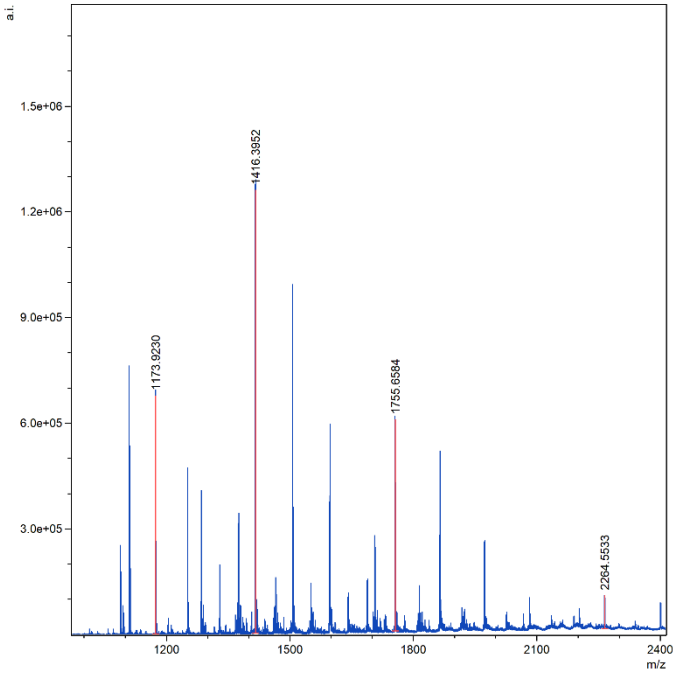

Figure 2.74: *ESI-MS of cage* $[Fe_4(\mathbf{4a})_4](NTf_2)_8$.

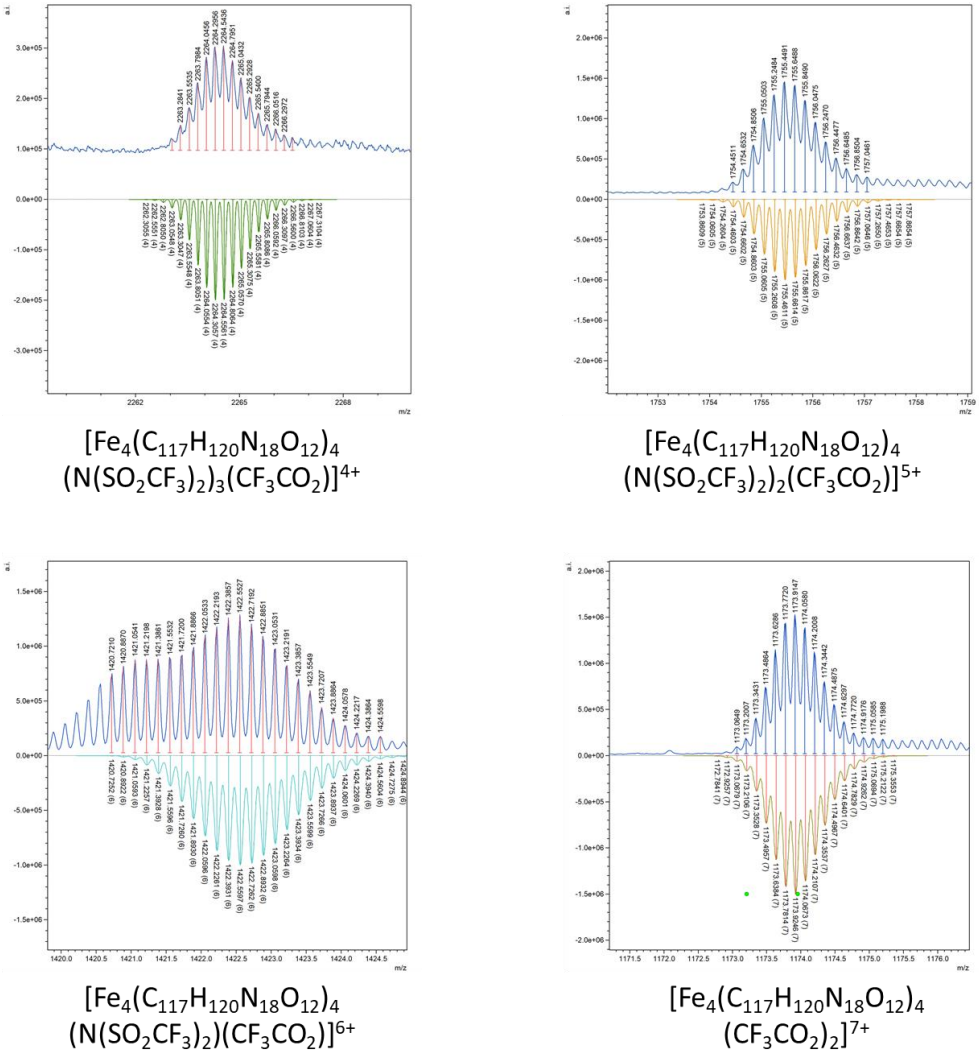

Figure 2.75: *Isotopic pattern distribution of [Fe₄(**4a**)₄](NTf₂)₈.*

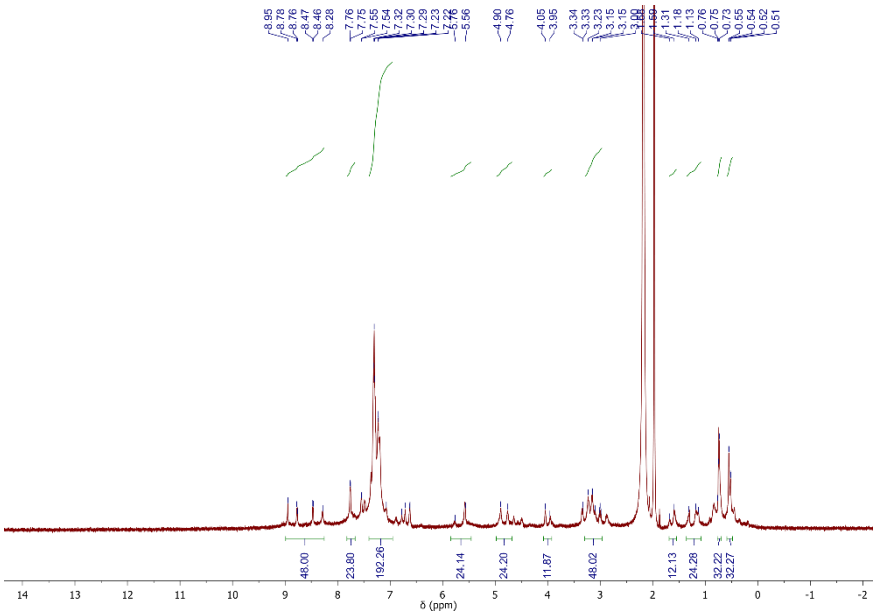

Figure 2.76: *^{1}H-NMR spectrum (CD_3CN, 500 MHz, T = 298 K) of cage [Fe₄(**4a**)₄](NTf₂)₈.*

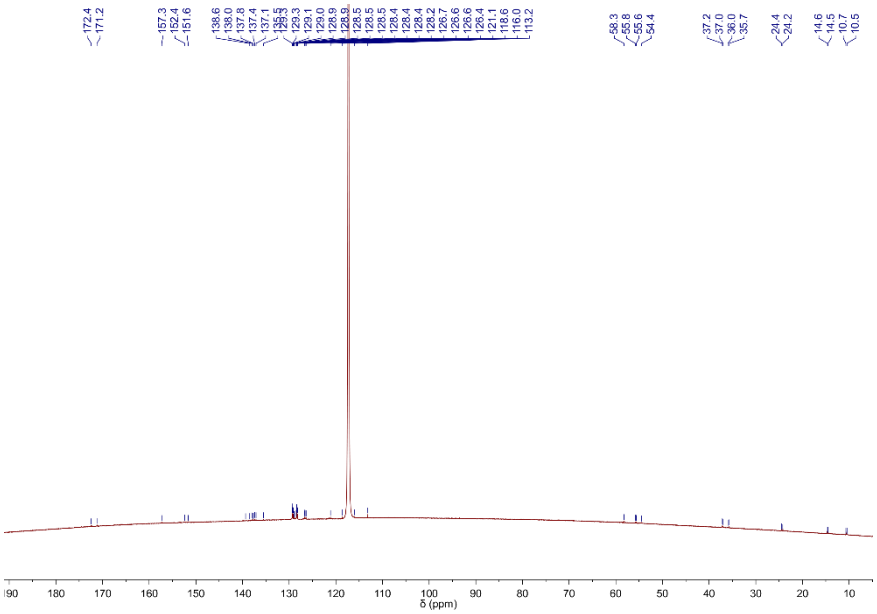

Figure 2.77: *^{13}C-NMR spectrum (CD_3CN, 125 MHz, T = 298 K) of cage $[Fe_4(\mathbf{4a})_4](NTf_2)_8$.*

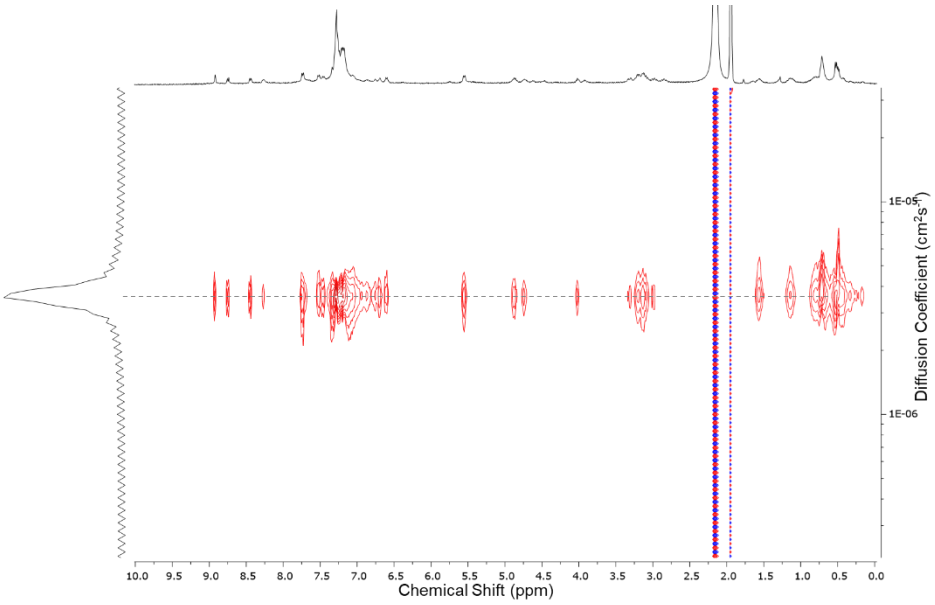

Figure 2.78: *^{1}H-DOSY NMR spectrum (CD_3CN, 400 MHz, T = 298 K) of cage $[Fe_4(\mathbf{4a})_4](NTf_2)_8$. The diffusion coefficient for $[Fe_4(\mathbf{4a})_4](NTf_2)_8$ in CD_3CN was measured to be 3.55 x 10^{-10} m^2 s^{-1} and the solvodynamic radius was calculated to be 18.4 Å.*

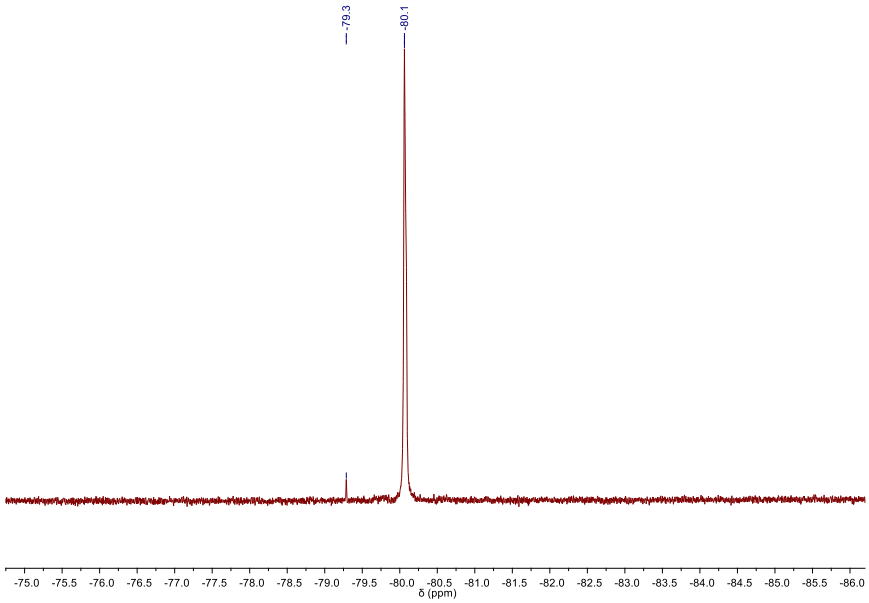

Figure 2.79: *^{19}F-NMR spectrum (CD_3CN, 471 MHz, T = 298 K) of cage $[Fe_4(\mathbf{4a})_4](NTf_2)_8$.*

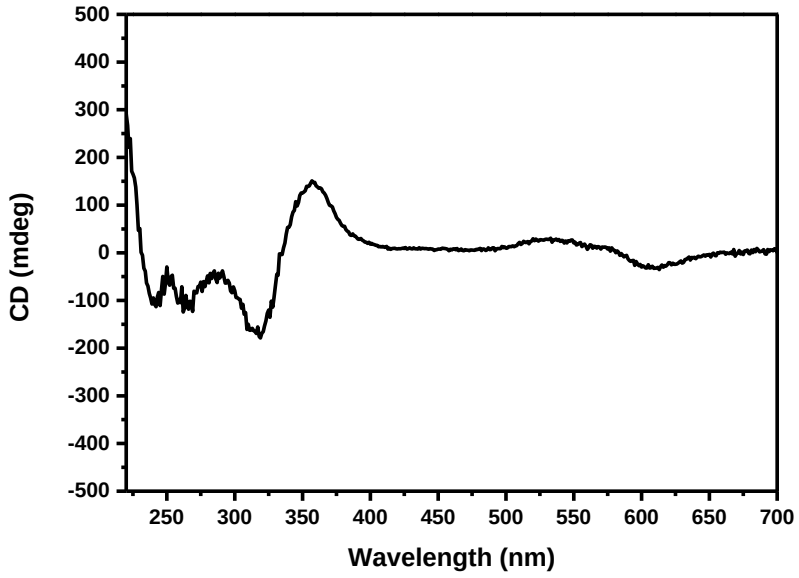

Figure 2.80: *CD spectrum of $[Fe_4(\mathbf{4a})_4](NTf_2)_8$.*

$[Zn_4(\mathbf{1a})_4](NTf_2)_8$

Species	Calculated m/z	Experimental m/z
$[Zn_4(C_{108}H_{102}N_{18}O_{12})_4(N(SO_2CF_3)_2)_3(\mathbf{CF_3CO_2})]^{4+}$	2147.6570	2147.4080

Table 2.6: *m/z values for $[Zn_4(\mathbf{1a})_4](NTf_2)_8$.*

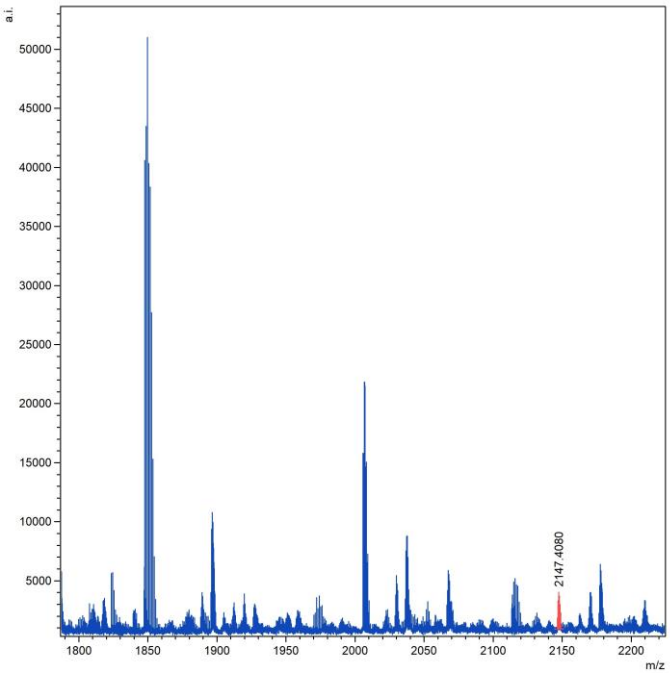

Figure 2.81: *ESI-MS of cage [Zn$_4$(**1a**)$_4$](NTf$_2$)$_8$.*

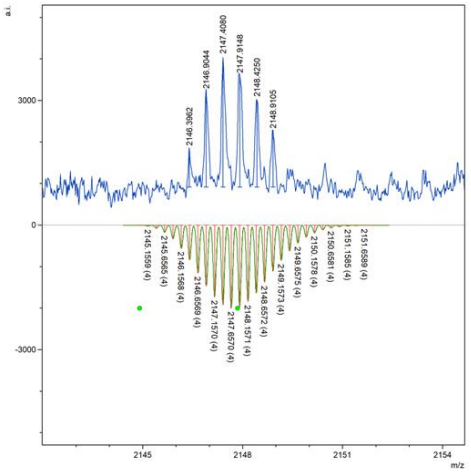

$[Zn_4(C_{108}H_{102}N_{18}O_{12})_4$
$(N(SO_2CF_3)_2)_3(CF_3CO_2)]^{4+}$

Figure 2.82: *Isotopic pattern distribution of [Zn$_4$(**1a**)$_4$](NTf$_2$)$_8$.*

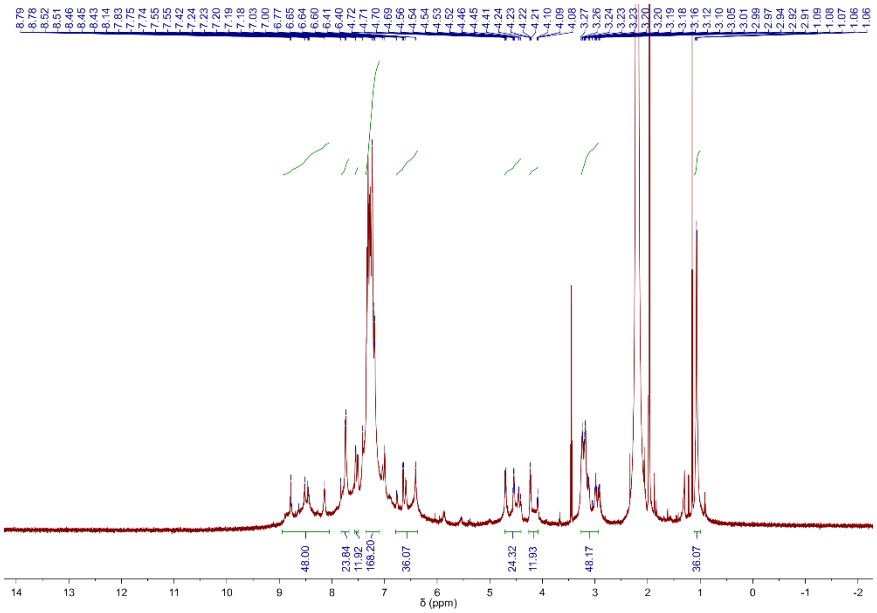

Figure 2.83: *^{1}H-NMR spectrum (CD_3CN, 500 MHz, T = 298 K) of cage $[Zn_4(\mathbf{1a})_4](NTf_2)_8$.*

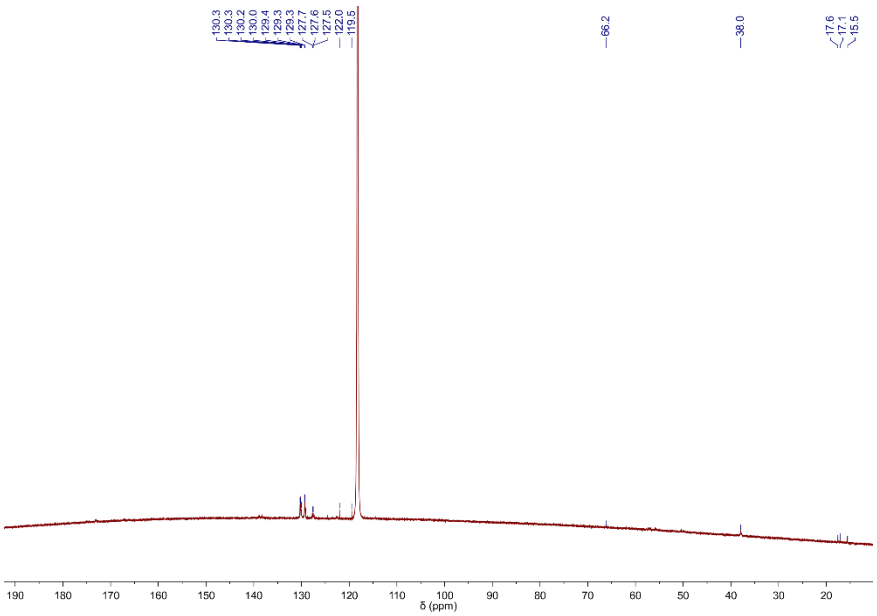

Figure 2.84: *^{13}C-NMR spectrum (CD_3CN, 125 MHz, T = 298 K) of cage $[Zn_4(\mathbf{1a})_4](NTf_2)_8$.*

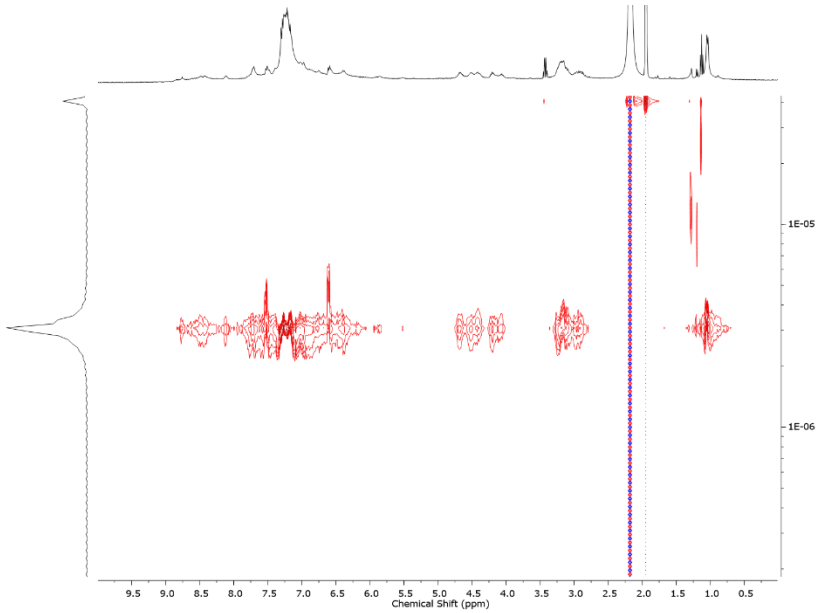

Figure 2.85: *^{1}H-DOSY NMR spectrum (CD_3CN, 400 MHz, T = 298 K) of cage $[Zn_4(\mathbf{1a})_4](NTf_2)_8$. The diffusion coefficient for $[Fe_4(\mathbf{4a})_4](NTf_2)_8$ in CD_3CN was measured to be 3.06 x 10^{-10} m^2 s^{-1} and the solvodynamic radius was calculated to be 21.4 Å.*

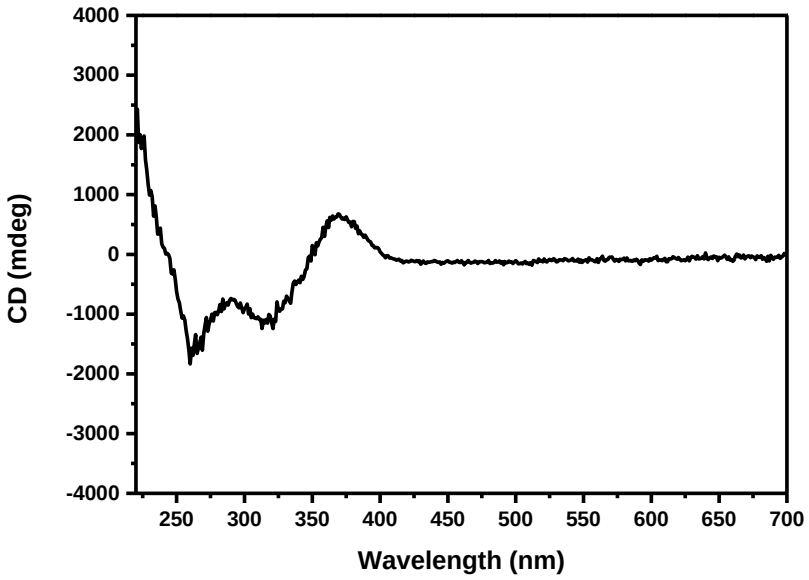

Figure 2.86: *ESI-MS of cage $[Zn_4(\mathbf{1a})_4](NTf_2)_8$.*

$[Zn_4(\mathbf{2a})_4](NTf_2)_8$

Species	Calculated m/z	Experimental m/z
$[Zn_4(C_{114}H_{114}N_{18}O_{12})_4(N(SO_2CF_3)_2)_2(\mathbf{CF_3CO_2})]^{5+}$	1729.5731	1729.6132
$[Zn_4(C_{114}H_{114}N_{18}O_{12})_4(N(SO_2CF_3)_2)(\mathbf{CF_3CO_2})]^{6+}$	1394.6194	1394.5239
$[Zn_4(C_{114}H_{114}N_{18}O_{12})_4(\mathbf{CF_3CO_2})]^{7+}$	1155.3668	1155.4576

Table 2.7: *m/z values for* $[Zn_4(\mathbf{2a})_4](NTf_2)_8$.

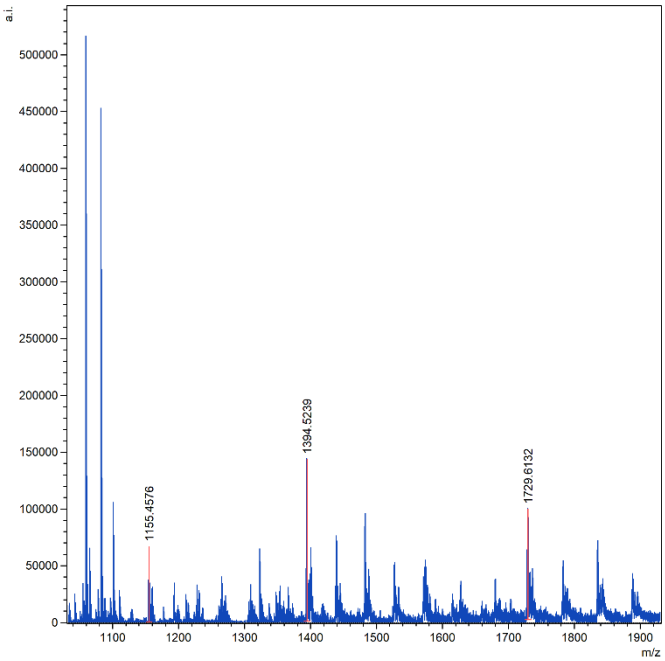

Figure 2.87: *ESI-MS of cage* $[Zn_4(\mathbf{2a})_4](NTf_2)_8$.

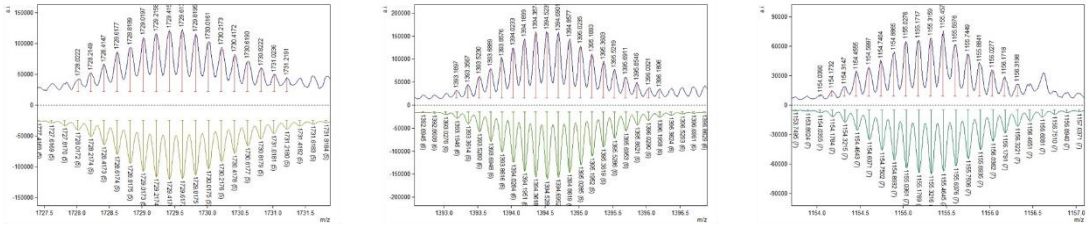

Figure 2.88: *Isotopic pattern distribution of* $[Zn_4(\mathbf{2a})_4](NTf_2)_8$.

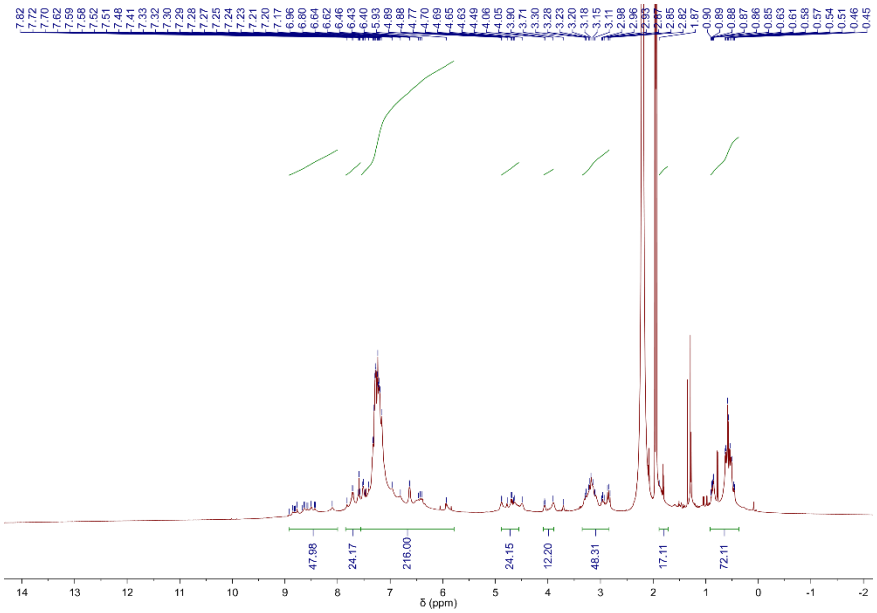

Figure 2.89: *^{1}H-NMR spectrum (CD_3CN, 400 MHz, T = 298 K) of cage $[Zn_4(\mathbf{2a})_4](NTf_2)_8$.*

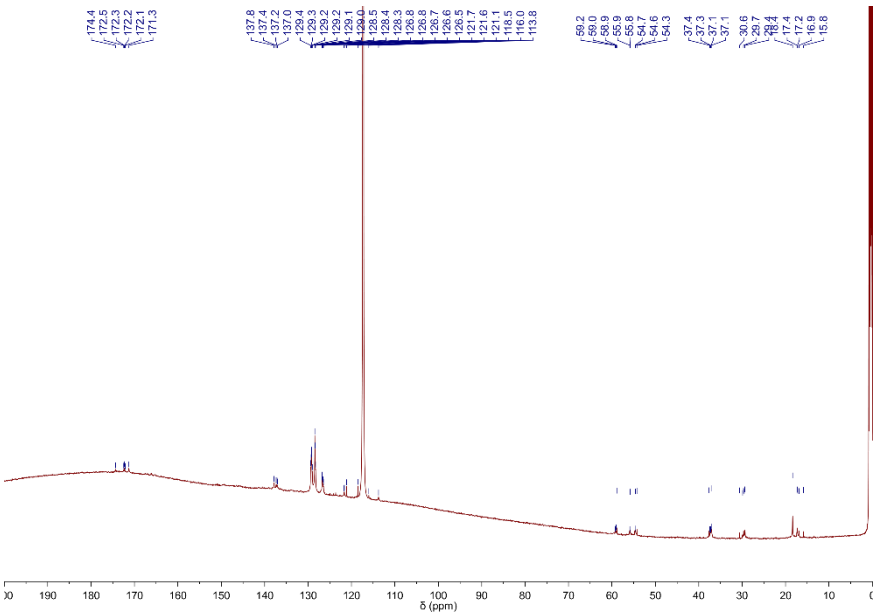

Figure 2.90: *^{13}C-NMR spectrum (CD_3CN, 100 MHz, T = 298 K) of cage $[Zn_4(\mathbf{2a})_4](NTf_2)_8$.*

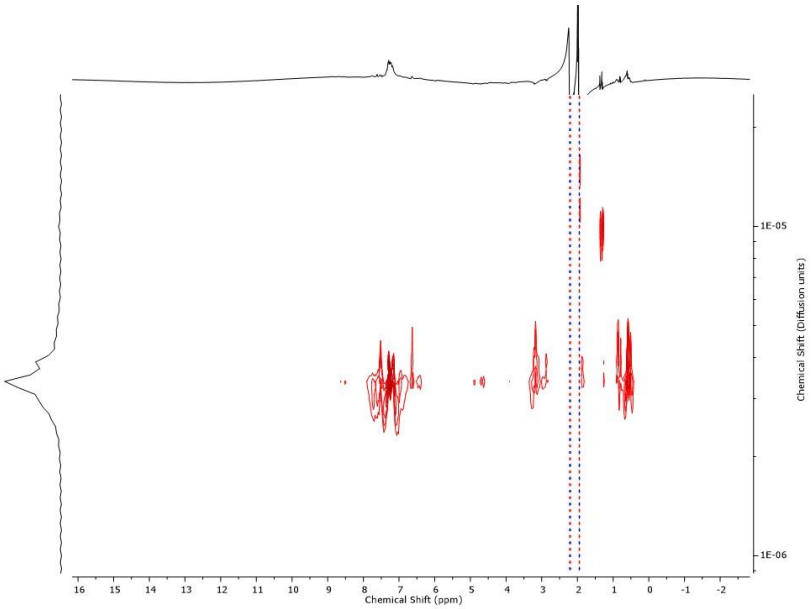

Figure 2.91: *^{1}H-DOSY NMR spectrum (CD_3CN, 400 MHz, T = 298 K) of cage $[Zn_4(\mathbf{2a})_4](NTf_2)_8$. The diffusion coefficient for $[Zn_4(\mathbf{2a})_4](NTf_2)_8$ in CD_3CN was measured to be 3.39 x 10^{-10} m^2 s^{-1} and the solvodynamic radius was calculated to be 19.3 Å.*

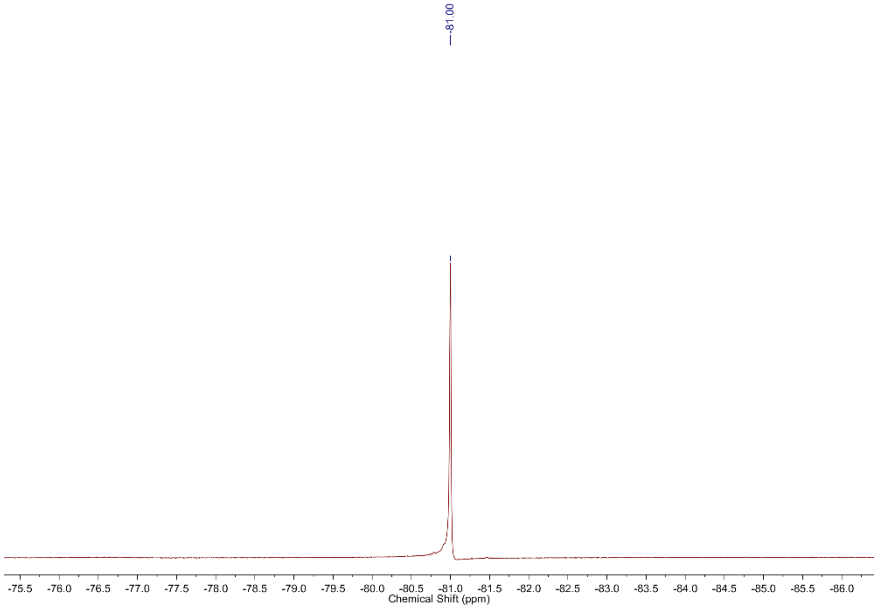

Figure 2.92: *^{19}F-NMR spectrum (CD_3CN, 471 MHz, T = 298 K) of cage $[Zn_4(\mathbf{2a})_4](NTf_2)_8$.*

$[Zn_4(\mathbf{3a})_4](NTf_2)_8$

It was not possible to perform ESI-MS due to problem with mass spectrometer.

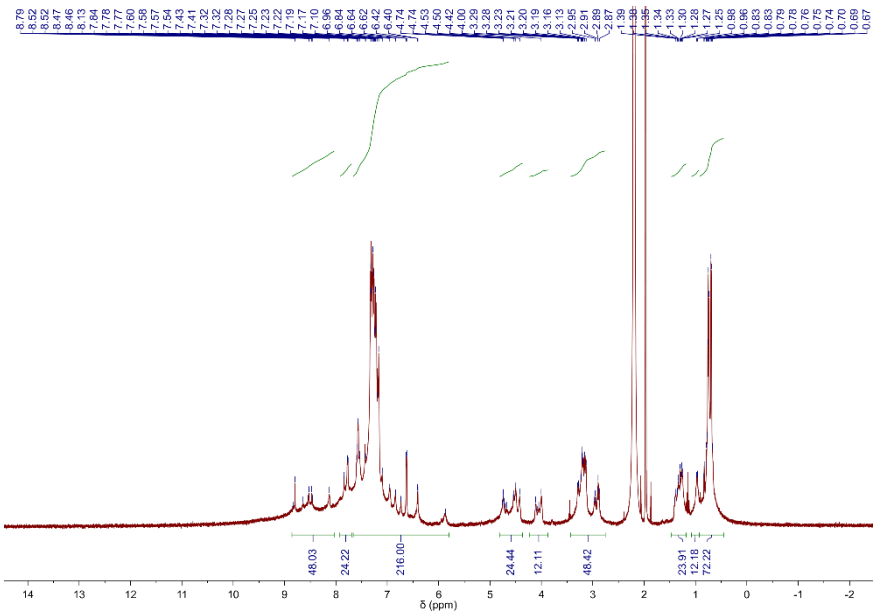

Figure 2.93: *^{1}H-NMR spectrum (CD_3CN, 500 MHz, T = 298 K) of cage $[Zn_4(\mathbf{3a})_4](NTf_2)_8$.*

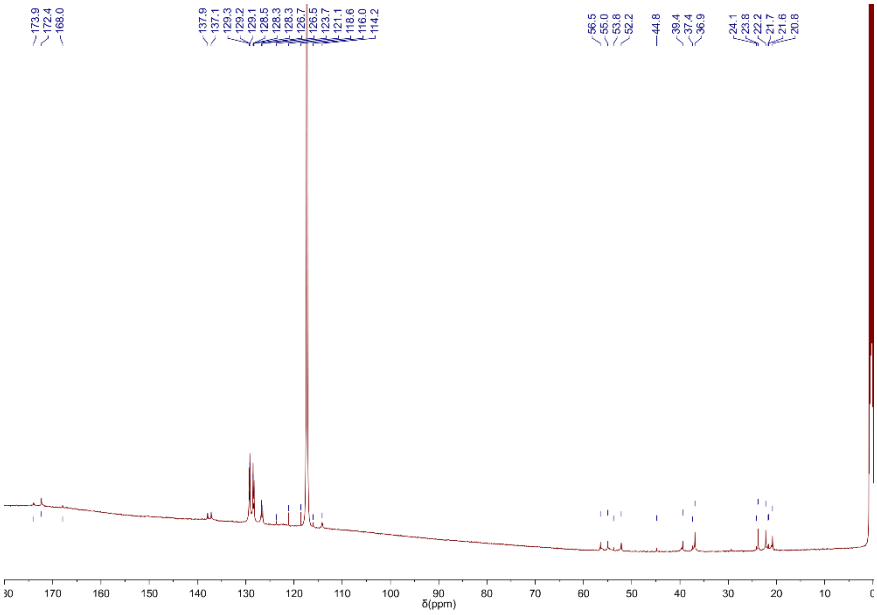

Figure 2.94: *^{13}C-NMR spectrum (CD_3CN, 125 MHz, T = 298 K) of cage $[Zn_4(\mathbf{3a})_4](NTf_2)_8$.*

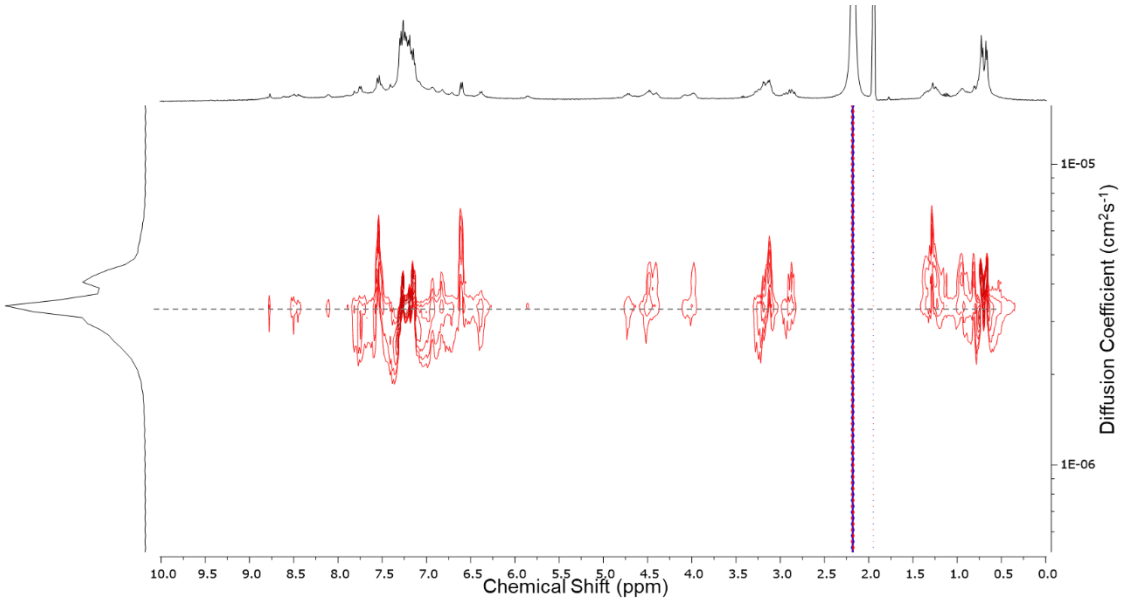

Figure 2.95: *^{1}H-DOSY NMR spectrum (CD_3CN, 400 MHz, T = 298 K) of cage $[Zn_4(\mathbf{3a})_4](NTf_2)_8$. The diffusion coefficient for $[Zn_4(\mathbf{3a})_4](NTf_2)_8$ in CD_3CN was measured to be 3.36 x 10^{-10} m^2 s^{-1} and the solvodynamic radius was calculated to be 19.5 Å.*

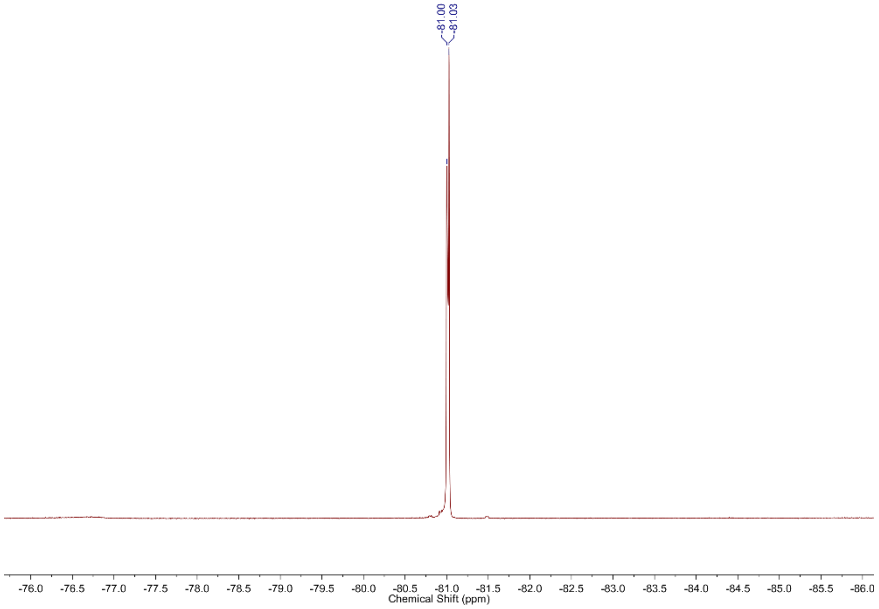

Figure 2.96: *^{19}F-NMR spectrum (CD_3CN, 471 MHz, T = 298 K) of cage $[Zn_4(\mathbf{3a})_4](NTf_2)_8$.*

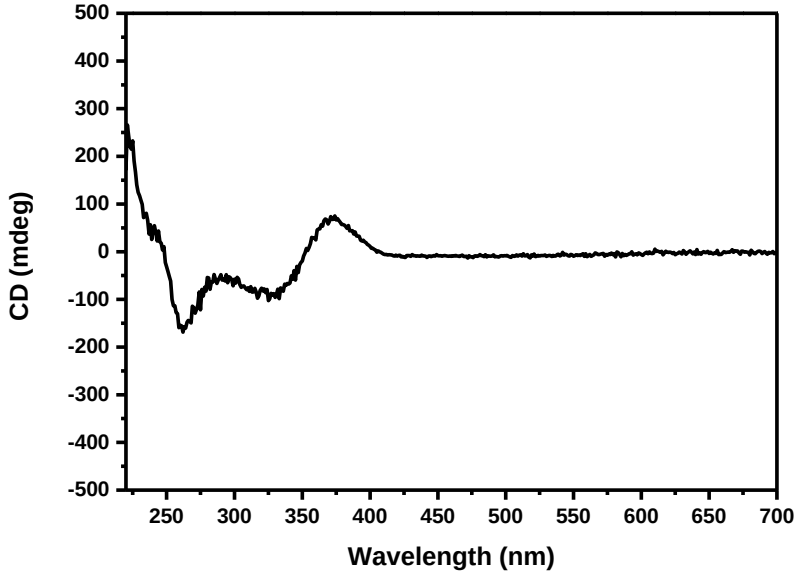

Figure 2.97: *CD spectrum of [Zn$_4$(**3a**)$_4$](NTf$_2$)$_8$.*

[Zn$_4$(**4a**)$_4$](NTf$_2$)$_8$

Species	Calculated m/z	Experimental m/z
[Zn$_4$($C_{117}H_{120}N_{18}O_{12}$)$_4$(N($SO_2CF_3$)$_2$)$_3$(**$CF_3CO_2$**)]$^{4+}$	2274.0834	2274.0401
[Zn$_4$($C_{117}H_{120}N_{18}O_{12}$)$_4$(N($SO_2CF_3$)$_2$)$_2$(**$CF_3CO_2$**)]$^{5+}$	1763.2370	1763.0474
[Zn$_4$($C_{117}H_{120}N_{18}O_{12}$)$_4$(N($SO_2CF_3$)$_2$)(**$CF_3CO_2$**)]$^{6+}$	1422.6726	1422.5527
[Zn$_4$($C_{117}H_{120}N_{18}O_{12}$)$_4$(**$CF_3CO_2$**)]$^{7+}$	1179.4124	1179.2002

Table 2.8: *m/z values for [Zn$_4$(**4a**)$_4$](NTf$_2$)$_8$.*

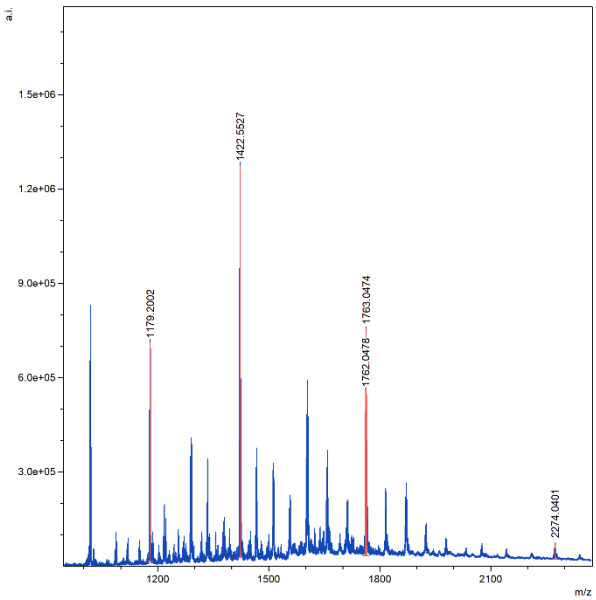

Figure 2.98: *ESI-MS of cage [Zn₄(**4a**)₄](NTf₂)₈.*

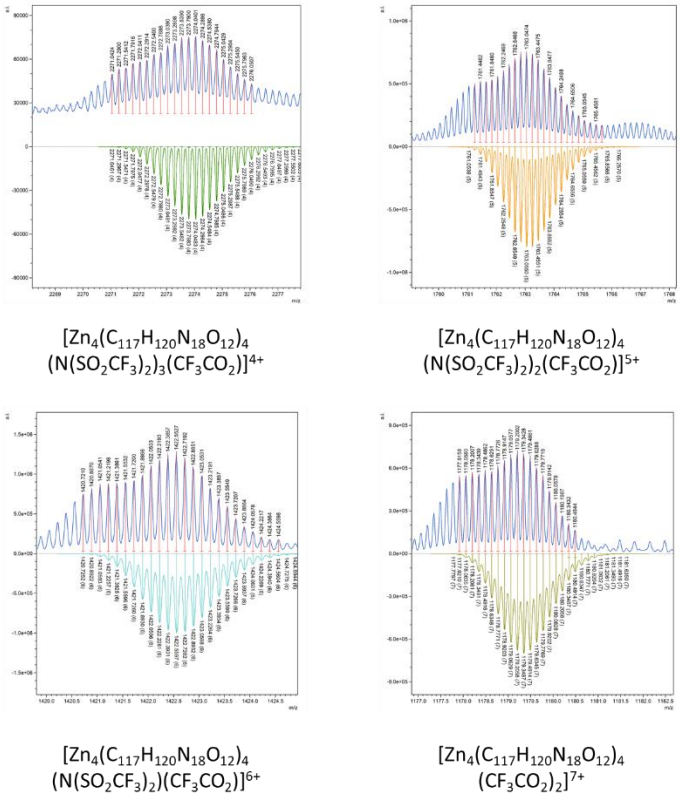

Figure 2.99: *Isotopic pattern distribution of [Zn₄(**4a**)₄](NTf₂)₈.*

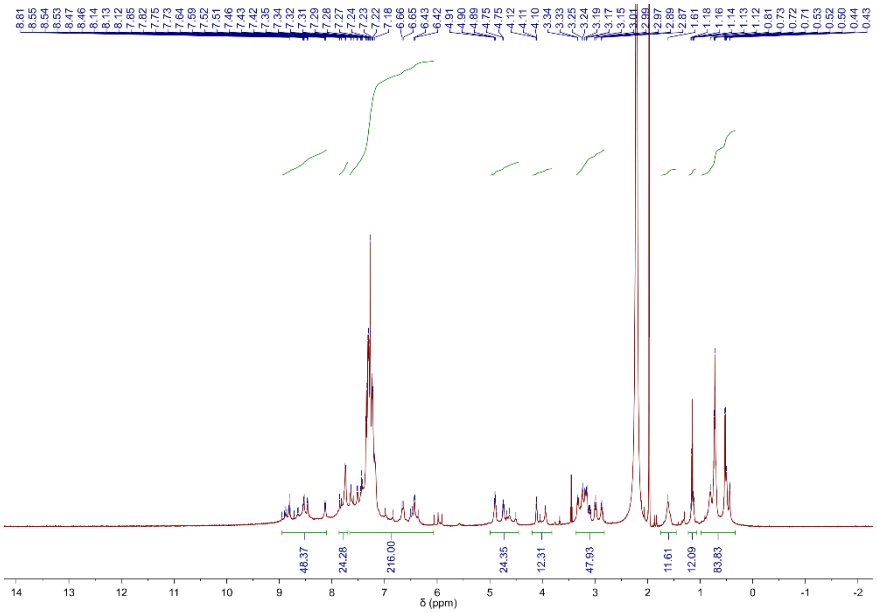

Figure 2.100: *^{1}H-NMR spectrum (CD_3CN, 500 MHz, T = 298 K) of cage $[Zn_4(\mathbf{4a})_4](NTf_2)_8$.*

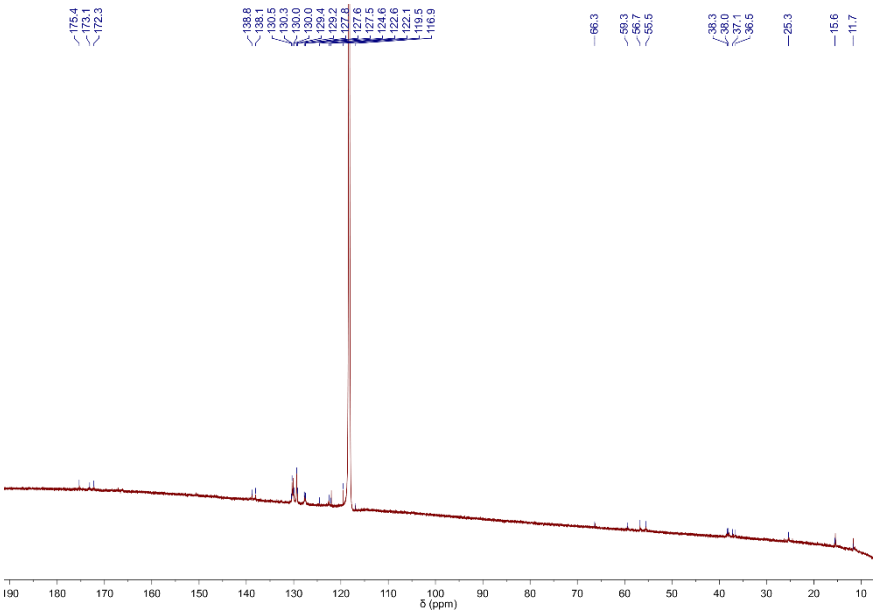

Figure 2.101: *^{13}C-NMR spectrum (CD_3CN, 125 MHz, T = 298 K) of cage $[Zn_4(\mathbf{4a})_4](NTf_2)_8$.*

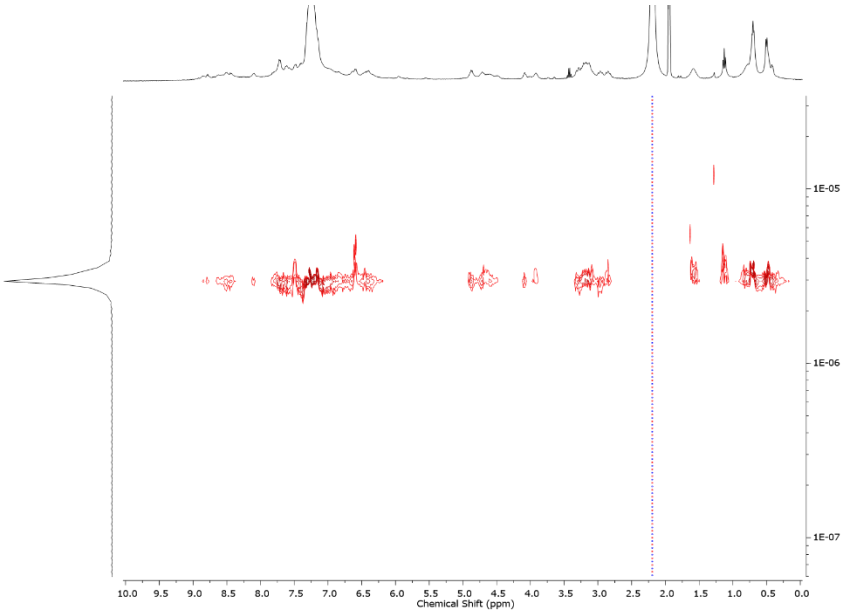

Figure 2.102: *^{1}H-DOSY NMR spectrum (CD_3CN, 400 MHz, T = 298 K) of cage $[Zn_4(\mathbf{4a})_4](NTf_2)_8$. The diffusion coefficient for $[Zn_4(\mathbf{4a})_4](NTf_2)_8$ in CD_3CN was measured to be 2.93 x 10^{-10} m^2 s^{-1} and the solvodynamic radius was calculated to be 22.3 Å.*

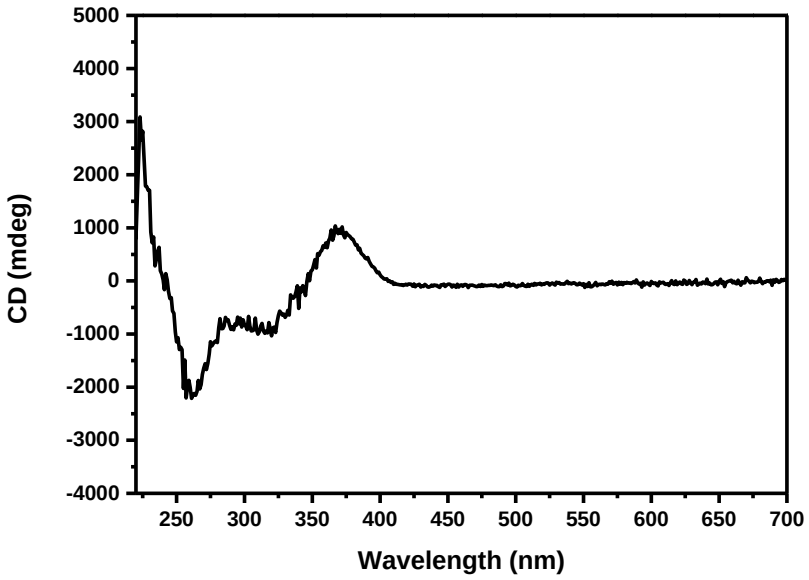

Figure 2.103: *CD spectrum of $[Zn_4(\mathbf{4a})_4](NTf_2)_8$.*

$[Fe_4(\mathbf{1c})_6](NTf_2)_8$

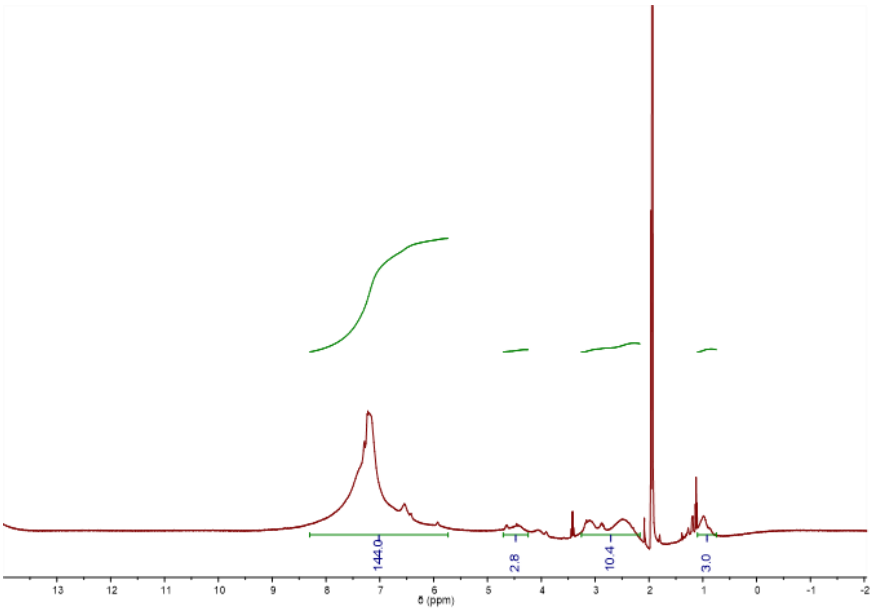

Figure 2.104: *^{1}H-NMR spectrum (CD_3CN, 400 MHz, T = 298 K) of cage $[Fe_4(\mathbf{1c})_6](NTf_2)_8$.*

$[Fe_4(\mathbf{1d})_6](NTf_2)_8$

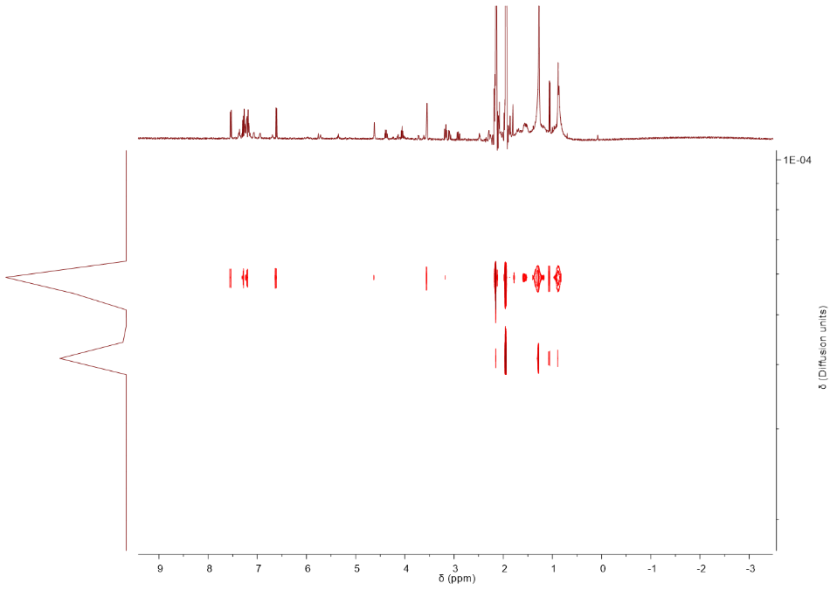

Figure 2.105: *^{1}H-DOSY NMR spectrum (CD_3CN, 400 MHz, T = 298 K) of cage $[Fe_4(\mathbf{1d})_4](NTf2)_8$. The diffusion coefficient for $[Fe_4(\mathbf{1d})_4](NTf2)8$ in CD_3CN was measured to be 5.01 x 10^{-9} m^2 s^{-1} and the solvodynamic radius was calculated to be 1.31 Å.*

2.7. Bibliography

(1) Jahović, I.; Zou, Y.-Q.; Adorinni, S.; Nitschke, J. R.; Marchesan, S. Cages meet gels: Smart materials with dual porosity. *Matter* **2021**, *4* (7), 2123-2140.

(2) Kieffer, M.; Garcia, A. M.; Haynes, C. J. E.; Kralj, S.; Iglesias, D.; Nitschke, J. R.; Marchesan, S. Embedding and Positioning of Two FeII4L4 Cages in Supramolecular Tripeptide Gels for Selective Chemical Segregation. *Angew. Chem. Int. Ed.***2019**, *58* (24), 7982-7986.

(3) Kieffer, M. Biofunctionalised Coordination Cages and Quantified Speciation in Supramolecular Mixtures. Doctoral, University of Cambridge, 2019.

(4) Garcia, A. M.; Iglesias, D.; Parisi, E.; Styan, K. E.; Waddington, L. J.; Deganutti, C.; De Zorzi, R.; Grassi, M.; Melchionna, M.; Vargiu, A. V.; et al. Chirality Effects on Peptide Self-Assembly Unraveled from Molecules to Materials. *Chem* **2018**, *4* (8), 1862-1876.

(5) Zhang, D.; Ronson, T. K.; Güryel, S.; Thoburn, J. D.; Wales, D. J.; Nitschke, J. R. Temperature Controls Guest Uptake and Release from Zn4L4 Tetrahedra. *J. Am. Chem. Soc.* **2019**, *141* (37), 14534-14538.

(6) Maity, S.; Kumar, P.; Haldar, D. Sonication-induced instant amyloid-like fibril formation and organogelation by a tripeptide. *Soft Matter* **2011**, *7* (11), 5239-5245.

(7) Bardelang, D. Ultrasound induced gelation: a paradigm shift. *Soft Matter* **2009**, *5* (10), 1969-1971.

(8) Castilla, A. M.; Ousaka, N.; Bilbeisi, R. A.; Valeri, E.; Ronson, T. K.; Nitschke, J. R. High-Fidelity Stereochemical Memory in a FeII4L4 Tetrahedral Capsule. *J. Am. Chem. Soc.* **2013**, *135* (47), 17999-18006.

(9) Sanders, J.; Kampos, N.; Clyde-Watson, Z. Axial Coordination Chemistry of Metalloporphyrins, The Porphyrin Handbook. by KM Kadish, KM Smith, and R. Guieard (Academic Press, San Diego, San …: 2000.

(10) Mosquera, J.; Szyszko, B.; Ho, S. K. Y.; Nitschke, J. R. Sequence-selective encapsulation and protection of long peptides by a self-assembled FeII8L6 cubic cage. *Nat. Commun.* **2017**, *8* (1), 14882.

(11) Busch, D. H. Distinctive coordination chemistry and biological significance of complexes with macrocyclic ligands. *Acc. Chem. Res.* **1978**, *11* (10), 392-400.

(12) Hamblin, J.; Childs, L. J.; Alcock, N. W.; Hannon, M. J. Directed one-pot syntheses of enantiopure dinuclear silver(i) and copper(i) metallo-supramolecular double helicates. *J. Chem. Soc., Dalton trans.* **2002**, (2), 164-169, 10.1039/B106987J.

(13) Schultz, D.; Nitschke, J. R. Dynamic covalent and supramolecular direction of the synthesis and reassembly of copper(I) complexes. *Proc. Natl. Acad. Sci. U.S.A.* **2005**, *102* (32), 11191-11195.

(14) Nitschke, J. R. Mutual Stabilization between Imine Ligands and Copper(i) Ions in Aqueous Solution. *Angew. Chem. Int. Ed.***2004**, *43* (23), 3073-3075.

(15) Avram, L.; Cohen, Y. Diffusion NMR of molecular cages and capsules. *Chem. Soc. Rev.* **2015**, *44* (2), 586-602.

(16) McConnell, A. J. Metallosupramolecular cages: from design principles and characterisation techniques to applications. *Chem. Soc. Rev.* **2022**, *51* (8), 2957-2971.

(17) Dragna, J. M.; Pescitelli, G.; Tran, L.; Lynch, V. M.; Anslyn, E. V.; Di Bari, L. In Situ Assembly of Octahedral Fe(II) Complexes for the Enantiomeric Excess Determination of Chiral Amines Using Circular Dichroism Spectroscopy. *J. Am. Chem. Soc.* **2012**, *134* (9), 4398-4407.
(18) Rossi, B.; Bottari, C.; Catalini, S.; D'Amico, F.; Gessini, A.; Masciovecchio, C. Chapter 13 - Synchrotron-based ultraviolet resonance Raman scattering for material science. In *Molecular and Laser Spectroscopy*, Gupta, V. P., Ozaki, Y. Eds.; Elsevier, 2020; pp 447-482.
(19) Rossi, B.; Tortora, M.; Catalini, S.; Vigna, J.; Mancini, I.; Gessini, A.; Masciovecchio, C.; Mele, A. Insight into the thermal stability of DNA in hydrated ionic liquids from multi-wavelength UV resonance Raman experiments. *Phys. Chem. Chem. Phys.* **2021**, *23* (30), 15980-15988.

CHAPTER 3

Metal ions trigger the gelation of peptide-appended coordination cages

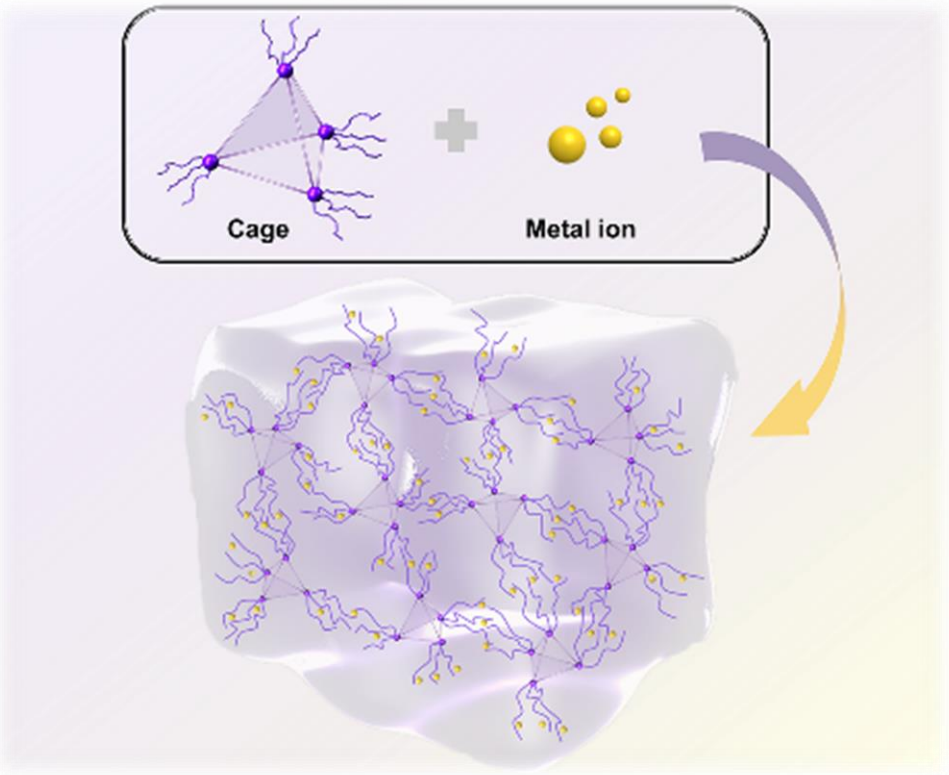

3.1. Introduction

Metal-coordination is an excellent tool, not only for the synthesis of self-assembled discrete materials, but also to link together different molecules for the creation of multifunctional supramolecular materials. Recently, different examples of metal coordination have appeared in the scientific literature, for the synthesis of peptide-based metal organic frameworks[1] and of knotted frameworks, such as nona-foil knots or deca-foil supercoils.[2] Peptides can be incorporated into synthetic ligands or used without any further functionalisation, thanks to the presence of different natural amino acids (*e.g.*, histidine, cysteine, methionine) containing functional groups that are excellent metal ligands.[3, 4]

3.2. Aim of the project

This work will present a strategy for the design of cage gel materials that form upon metal-triggered crosslinking of the peripheral peptide arms of metal organic cages. Three different peptides containing a sulfur functional group will be studied (***Figure 3.1***). The peptide ligands bear also an aminobenzoyl unit necessary for the formation of the imine bond coordinating ligand. The first two peptides (**5** and **6**) contain a cysteine residue (Cys), in the central or C-terminal position, respectively. The third one (**7**) contains a methionine moiety (Met). All these three peptides will used for the synthesis of three different cages, all having the 5,5',5''–(benzene–1,3,5–triyl)tripicolinaldehyde (**a**), as internal ligand (***Figure 3.1***). The self-assembly behaviour of the three MOCs alone and in presence of three environmentally toxic metal salts (Ag(Otf), $Hg(OAc)_2$, $Zn(OTf)_2$) will be explored.

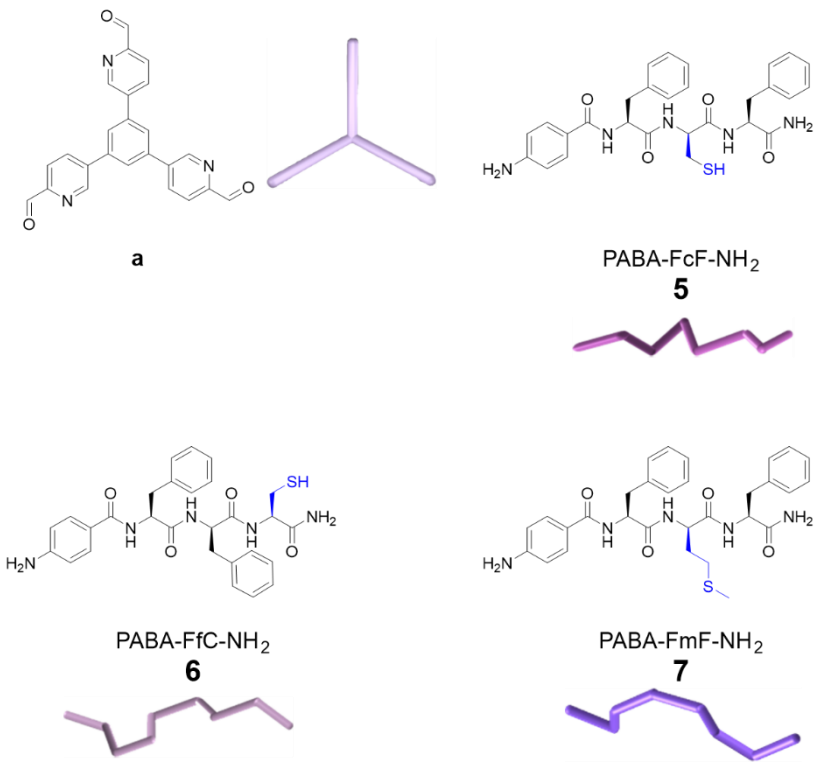

Figure 3.1: *Peptides and aldehyde studied for the synthesis of iron tetrahedral cages.*

3.3. Results and discussion

3.3.1. Synthesis and characterisation of peptides and aldehydes

The three peptides have been synthesized using Fmoc-solid phase peptide synthesis using 2-chlorotrityl resin and HOAt and HOBT as coupling agents. The procedure followed was the same reported in the previous chapter, **Chapter 2-Section 2.4.1**. The first step involves the swelling of the resin followed by its activation with $SOCl_2$. The second step is the loading of the Rink amide linker, necessary to protect the C-terminus with an amide group. Afterward the protocol consists of coupling of desired amino-acids and their deprotection in basic conditions. Finally, the peptide was cleaved by the resin in acidic conditions and the crude purified through HPLC. The peptides were characterised by NMR and ESI-MS spectroscopy.

The ^{1}H-NMR spectra (***Figure 3.2, 15, 18***) confirmed the purity of the compounds and displayed the typical signals of peptides in DMSO-d_6. In the region between 8.0 and 8.5 ppm the amide signals, followed by aromatic peaks around 7.5 ppm. In the aliphatic region, there are the α-protons around 4.5 ppm and the β-ones between 2.5 and 3.5 ppm. Finally, at 2.0 ppm there is the doublet of doublet relative to thiol proton.

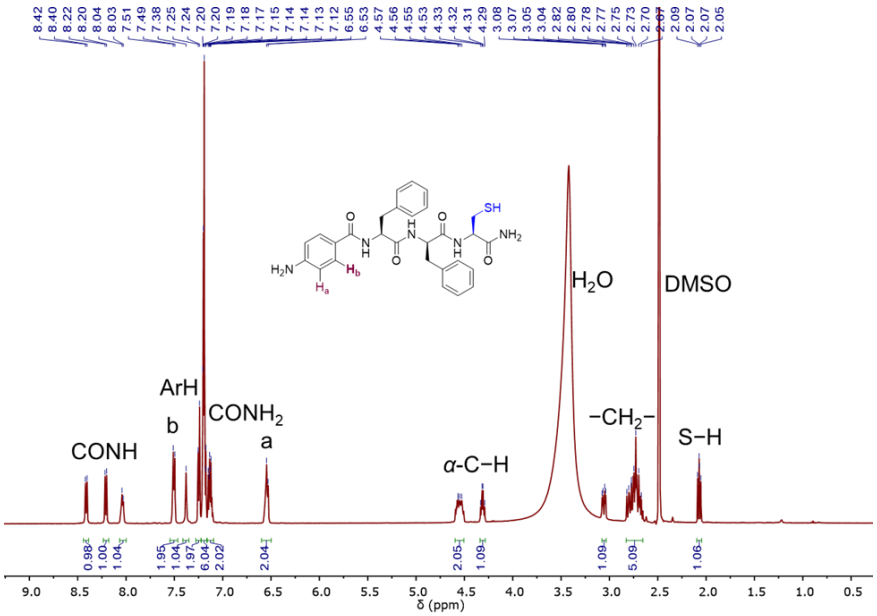

Figure 3.2: *[1]H-NMR spectrum (DMSO-d6, T = 298 K) of peptide* ***5****.*

The aldehyde **a** was synthesised followed in **Chapter 2-Section 2.4.3**, concerning a two-steps synthesis, before the boronic ester and after the aldehyde. The ^{1}H-NMR confirms the purity and the successfully synthesis.

3.3.2. Synthesis and characterisation of the cages

The three cages were synthesised using the same sub-component approach, reported in previous chapter. The general scheme reaction is reported in ***Figure 3.3***. It consists of mixing together the three sub-components in the right stoichiometric ration 3:1:1 aniline peptide: aldehyde:metal in CH_3CH and then stirred the reaction at 70°C for 18 hours. The cages were obtained in quantitative yield and simply purified through precipitation in Et_2O.

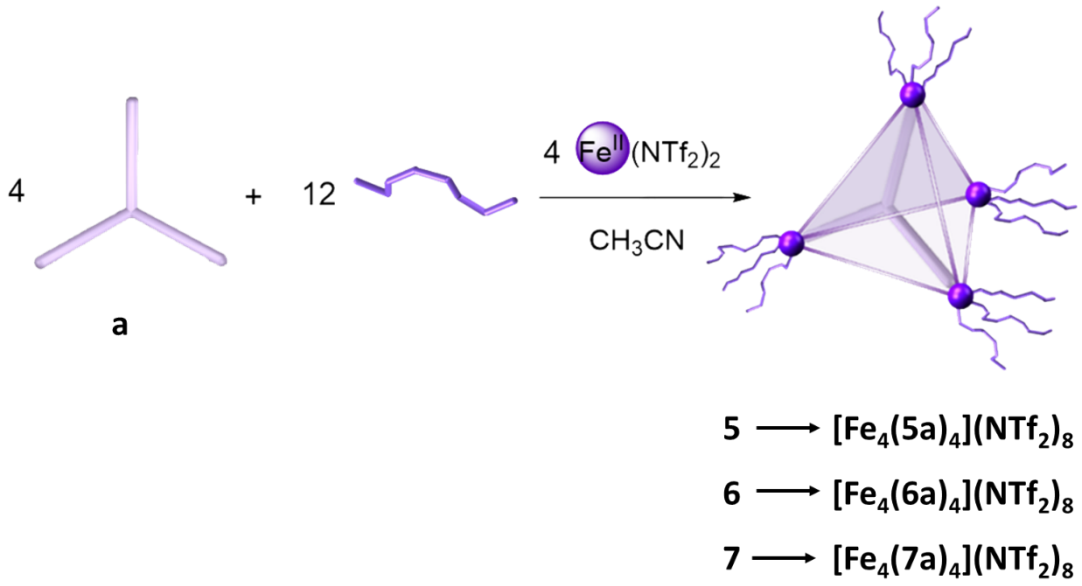

Figure 3.3: *General reaction scheme for cage synthesis.*

The structural characterisation was based on cage $[Fe_4(\mathbf{7a})_4](NTf_2)_8$ because of the longer alkyl chains that guarantee a better solubility in acetonitrile. For these cages, the ^{1}H NMR spectrum (***Figure 3.4***) displayed two sets of proton signals in a ratio of 2.5:1 (diastereomeric excess of 40%), with the same diffusion coefficient observed for both sets of peaks in the diffusion-ordered spectroscopy (DOSY) spectrum (***Figure 3.5***). This observation indicates that $[Fe_4(\mathbf{7a})_4](NTf_2)_8$ exists as a pair of diastereomers with opposite handedness at its Fe^{II} vertices: Δ_4 and Λ_4.[5] This diastereomeric enrichment was connected to the transfer of stereochemical information from the enantiopure peptide side chains to the metal vertices during self-assembly.[6, 7]

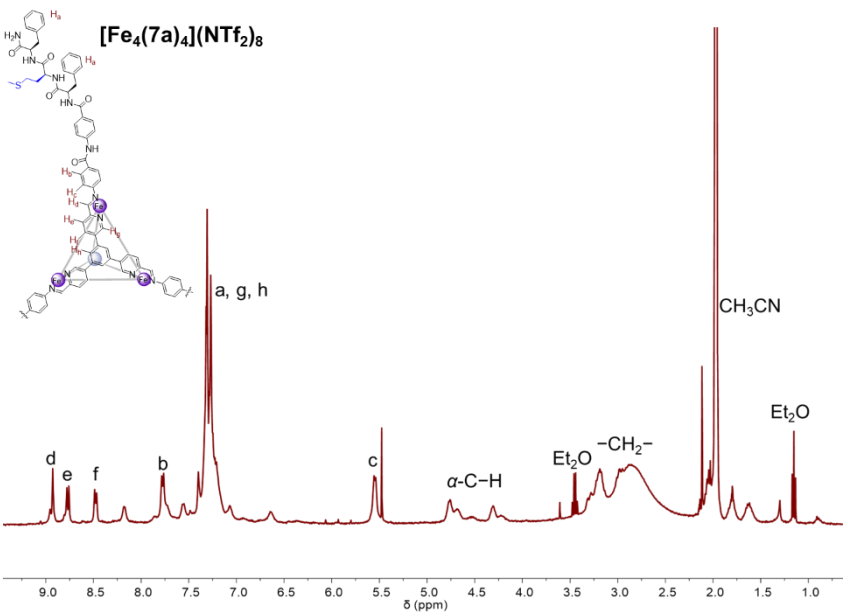

Figure 3.4: *^{1}H-NMR spectrum (CD_3CN, 500 MHz, T = 298 K) of cage [Fe_4(**7a**)$_4$](NTf_2)$_8$.*

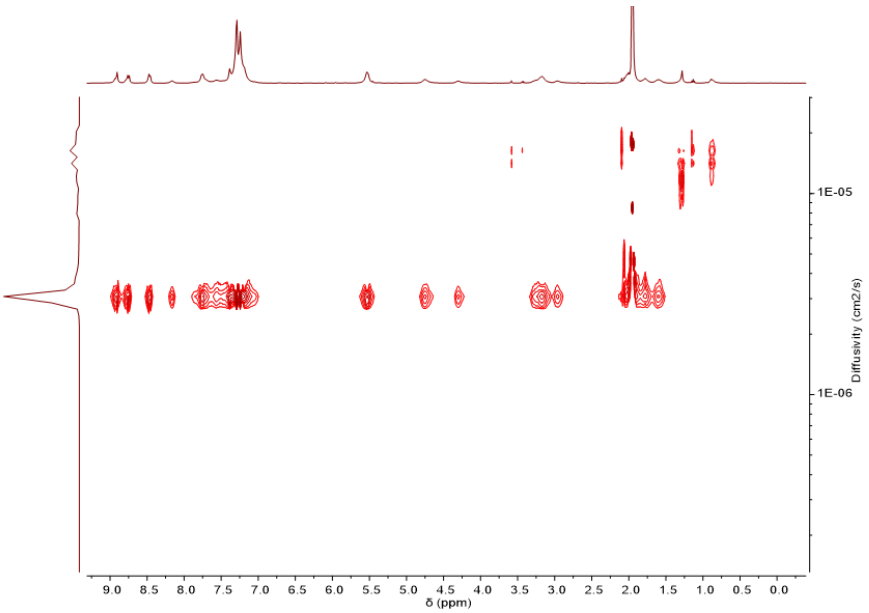

Figure 3.5: *^{1}H-DOSY NMR spectrum (CD_3CN, 400 MHz, T = 298 K) of cage [Fe_4(**7a**)$_4$](NTf_2)$_8$. The diffusion coefficient for [Fe_4(**7a**)$_4$](NTf_2)$_8$ in CD_3CN was measured to be 3.07 x 10^{-10} m^2 s^{-1} and the solvodynamic radius was calculated to be 21.3 Å.*

The major diastereomer was determined through CD analysis. The CD spectra (***Figure 3.6***) displayed the same behaviour of the iron cages synthesised and described in **Chapter 2**. In particular, clear Cotton effects were evident at 210–410 nm and 490–630 nm, corresponding to π–π* and metal-to-ligand charge transfer (MLCT) transitions, respectively. The observed sign of the MLCT bands corresponds to Λ–handedness of the metal

vertices, suggesting that Λ_4 was the major diastereomer.[8] Cages $[Fe_4(\mathbf{5a})_4](NTf_2)_8$ and $[Fe_4(\mathbf{6a})_4](NTf_2)_8$ also formed with predominantly Λ_4 stereochemistry but with lower diastereoselectivity.

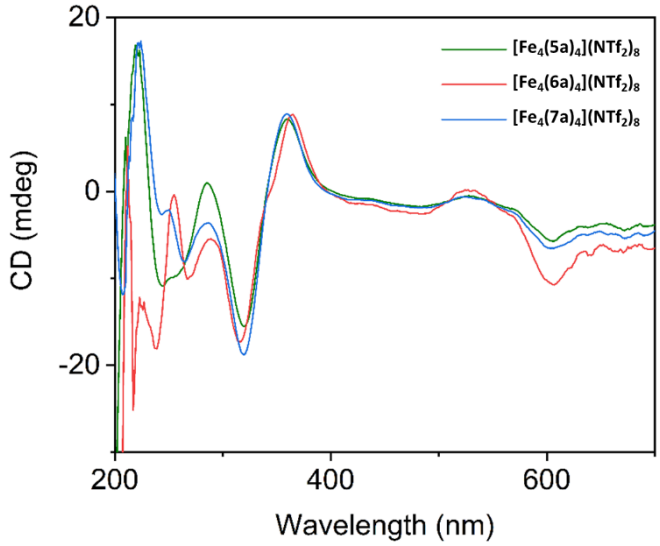

Figure 3.6: *CD spectrum of $[Fe_4(\mathbf{5a})_4](NTf_2)_8$ (green line), $[Fe_4(\mathbf{6a})_4](NTf_2)_8$ (red line), $[Fe_4(\mathbf{7a})_4](NTf_2)_8$ (blue line).*

3.3.3. Gelation process

We then examined the gelation of the resulting cages. Tube inversion tests were conducted to gauge gel formation. No gels were observed to form from saturated cage solutions (ca. 5 mM) or through the oxidation of the Cys residues to form disulfide crosslinks, which can induce peptide assembly and gelation (**Table 3.1**).[9-11]

Cage	Concentration (mM)	Gel	Time for gelation
$[Fe_4(5\mathbf{a})_4](NTf_2)_8$	1.27	NO	Solution even after 24 hours
	2.5	NO	Solution even after 24 hours
	5	NO	Solution even after 24 hours
$[Fe_4(6\mathbf{a})_4](NTf_2)_8$	1.27	NO	Solution even after 24 hours
	2.5	NO	Solution even after 24 hours
	5	NO	Solution even after 24 hours
$[Fe_4(7\mathbf{a})_4](NTf_2)_8$	1.27	NO	Solution even after 24 hours
	2.5	NO	Solution even after 24 hours
	5	NO	Solution even after 24 hours

Table 3.1: *Attempts for the preparation of the cage gel.*

The cysteine residues can also coordinate metal ions and so, cages $[Fe_4(5\mathbf{a})_4](NTf_2)_8$ and $[Fe_4(6\mathbf{a})_4](NTf_2)_8$ were tested for metal-coordination-driven gelation (**Table 3.2**). Upon the addition of an acetonitrile solution of AgOTf to the solution of $[Fe_4(5\mathbf{a})_4](NTf_2)_8$, gels were not observed even at $[Ag^+]$ = 90 mM; nor were Zn^{2+} or Hg^{2+} observed to induce gel formation at these concentrations. This is probably related to position of the thiol groups, too close to the hindered cage vertices to allow for metal-ion-induced cage crosslinking to form gels.

Cage	Metals	Concentration (mM)	Gelation	Observations
$[Fe_4(5\mathbf{a})_4](NTf_2)_8$	Ag^+	30 mM	NO	-
		60 mM	NO	-
		90 mM	NO	-
	Zn^{2+}	30 mM	NO	-
		60 mM	NO	-
		90 mM	NO	-
	Hg^{2+}	30 mM	NO	-
		60 mM	NO	-
		90 mM	YES	Leave for 2 days
$[Fe_4(6\mathbf{a})_4](NTf_2)_8$	Ag^+	30 mM	YES	Minimum Gelation Concentration
		60 mM	YES	Sonication 30 seconds[a]
		90 mM	YES	Sonication 30 seconds[a]
	Zn^{2+}	30 mM	YES	Sonication 30 seconds[a]
		60 mM	YES	Sonication 30 seconds[a]
		90 mM	YES	Sonication 30 seconds[a]
	Hg^{2+}	30 mM	YES	Sonication 30 seconds[a]
		60 mM	YES	Sonication 30 seconds[a]
		90 mM	YES	Sonication 30 seconds[a]

Table 3.2: *Attempts for the preparation of cage gel triggered by different metal ions at different concentrations. [a]The cage was dissolved in acetonitrile by heating. Then the metal ions were added to get a final concentration of 5 mM cage with different concentrations of metal ions and it was sonicated for the indicated time to get the gel.*

In contrast, the thiol group on $[Fe_4(6\mathbf{a})_4](NTf_2)_8$ is located farther from the cage core, in a potentially more accessible position (**Figure 3.1**). Upon treatment of a solution of cage $[Fe_4(6\mathbf{a})_4](NTf_2)_8$ with AgOTf in

acetonitrile, followed by two minutes of sonication, the transformation of the purple solution of cage $[Fe_4(6\mathbf{a})_4](NTf_2)_8$ into a purple metallogel was observed. Zn^{2+} and Hg^{2+} were likewise observed to trigger gel formation, as demonstrated by tube inversion tests (**Figure 3.7**).

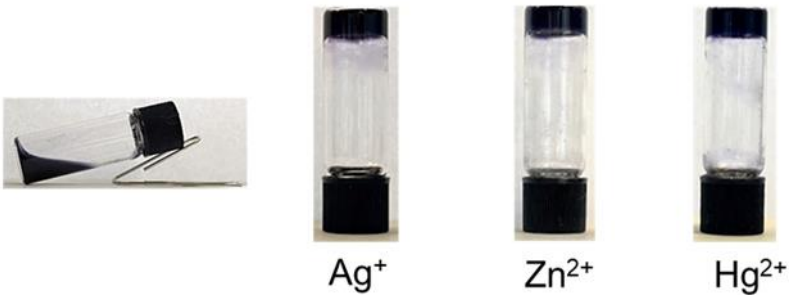

Figure 3.7: *Tube inversion test of metallogels from* ***$[Fe_4(6a)_4](NTf_2)_8$*** *triggered by these metal ions.*

The viscoelastic properties of the cage-gel materials were studied by oscillatory rheology (**Figure 3.8**).[12] Frequency sweeps indicated that both the elastic (G') and the viscous (G") moduli were independent of the applied frequency, and G' > G", confirming the presence of weak gels (G' ≤ 10 G''). Gelation kinetics revealed a two-stage process with a lag phase, suggesting a longer nucleation phase relative to gel matrix formation, especially for Ag^+. Calculation of gel stiffness (**Table 3.3**) yielded shear moduli of 1.6 kPa, 3.2 kPa and 3.9 kPa for Ag^+, Zn^{2+}, Hg^{2+}, respectively. Stress sweeps confirmed gel breaking just above 20 Pa in the case of Ag^+, and at nearly 70 Pa for Hg^{2+} and Zn^{2+}.

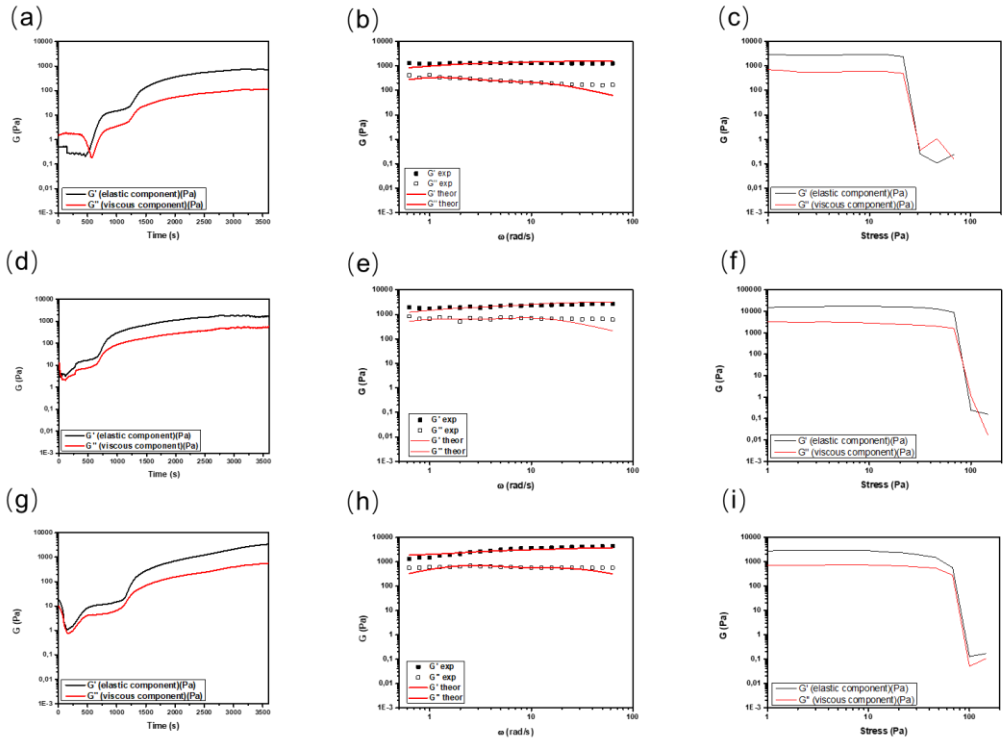

Figure 3.8: *Time sweeps, frequency sweep and stress sweep tests of (a-c) Ag^{+}-triggered gels of cage $[Fe_4(\mathbf{6a})_4](NTf_2)_8$; (d-f) Zn^{2+}-triggered gels of cage $[Fe_4(\mathbf{6a})_4](NTf_2)_8$; (g-i) Hg^{2+}-triggered gels of cage $[Fe_4(\mathbf{6a})_4](NTf_2)_8$.*

	G' (Pa)	G" (Pa)	Shear modulus (Pa)	Broken stress (Pa)	γ_c (%)
Ag	1297±34	255±83	1626	22	2.78
Zn	2225±312	683±67	3209	68	1.67
Hg	3507±708	591±39	3867	68	1.03

Table 3.3: *Elastic (G') and viscous (G") moduli for the different gels described here. The values shown in the table are calculated as the average (standard deviation included) of 3 independent experiments performed using 3 different samples. The cage concentration was kept at 5 mM and metal ions at 30 mM for the different hybrid gels.*

These results suggest that the cations Hg^{2+} and Zn^{2+} coordinate more strongly to the thiol groups of the terminal Cys residues than Ag^{+},[13] thus providing more crosslinks. Scanning electron microscopy (SEM) and transmission electron microscopy (TEM) provided insights into the observed rheological differences from a morphological point of view. Contrary to gels arising from tripeptide stacks that yield a fibrillar network,[14] also in the presence of embedded cages,[15] the three gels displayed spherical nuclei interconnected in the gel matrix (**Figures 3.9b-c, e-f, i-h**). The nuclei displayed an average diameter of 84 ± 29 nm in the case of Ag^{+}, whereas the gels triggered by Zn^{2+} and Hg^{2+} exhibited smaller average diameters of 45 ± 13 nm and 31 ± 18

nm, respectively (**Figures 3.9a, d, g**). This observation may help explain the longer lag phase prior to gelation in the case of Ag^{+}, which incorporates larger nuclei.

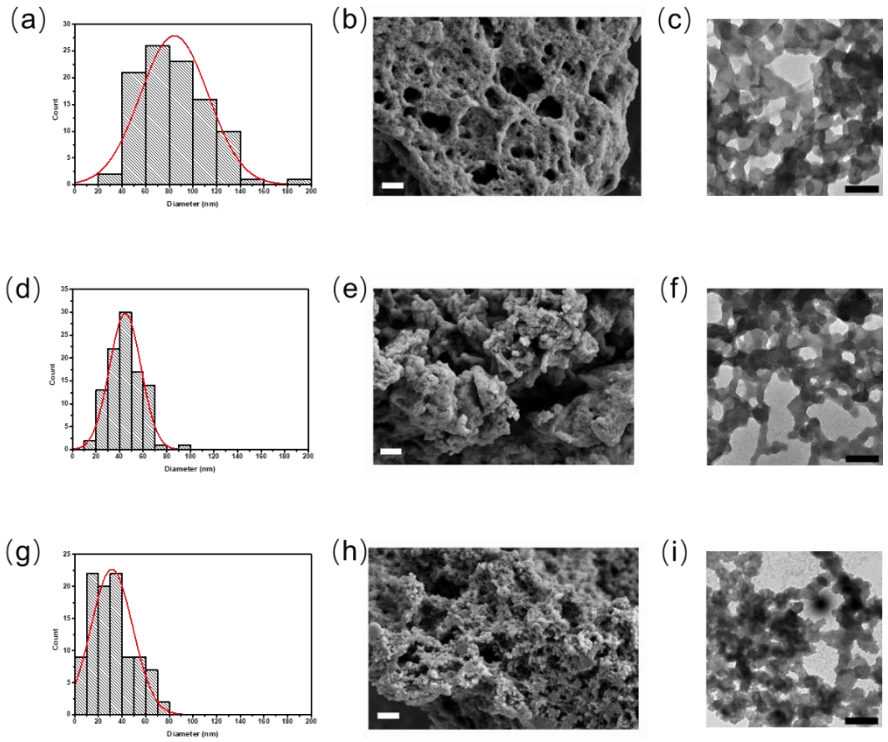

Figure 3.9: *Nanomorphological size distribution analysis of TEM micrographs of gels prepared by $[Fe_4(\mathbf{6a})_4](NTf_2)_8$, SEM and TEM images of (a-c) Ag^{+}-triggered gels of cage $[Fe_4(\mathbf{6a})_4](NTf_2)_8$; (d-f) Zn^{2+}-triggered gels of cage $[Fe_4(\mathbf{6a})_4](NTf_2)_8$; (g-i) Hg^{2+}-triggered gels of cage $[Fe_4(\mathbf{6a})_4](NTf_2)_8$.*

The stability of the cage after the gelation was studied by Raman spectroscopy. Raman is a vibrational spectroscopy technique discovered in 1928 by C. V. Raman, who gave his name to the technique being awarded with Nobel Prize in 1930. In Raman, instead, the laser brings molecules from the vibrational ground state to a transient virtual state, and from this level they can scatter the light back in three different ways:

- To the ground state: this is Rayleigh scatter that has the same energy of the laser and no changes in energy are noticed (elastic scattering);
- To an excited vibrational state, taking out to the ground state: in this case Stokes scattering is observed (inelastic scattering); from an even higher virtual state to the ground state: anti-Stokes photons with higher energy than laser energy are scattered (inelastic scattering) and they are related to fluorescence phenomena.

Stokes scattering is the most common phenomenon studied by Raman instruments, since the different frequency returning from the sample corresponds to the vibrational frequency of the molecule bonds and it is measured in Raman shift that is the shift in wavenumbers with respect to the exciting laser. The overall intensity of Raman bands depends on the laser colour (*i.e.* laser frequency).

Raman spectra of the gels and of the cage alone (**Figure 3.10**) confirmed that the cage framework remained intact after gelation. The medium intensity bands with four peaks in the region 3030-3200 cm^{-1} are relative to overlapping of aromatic C-H stretching vibrations and much broader N-H stretching vibrations. Intense bands between 1493 and 1600 cm^{-1}, which were attributed to C=N and N-Fe stretching. The weak signals in the region are due to aromatic =C-H in-plane deformation vibrations.

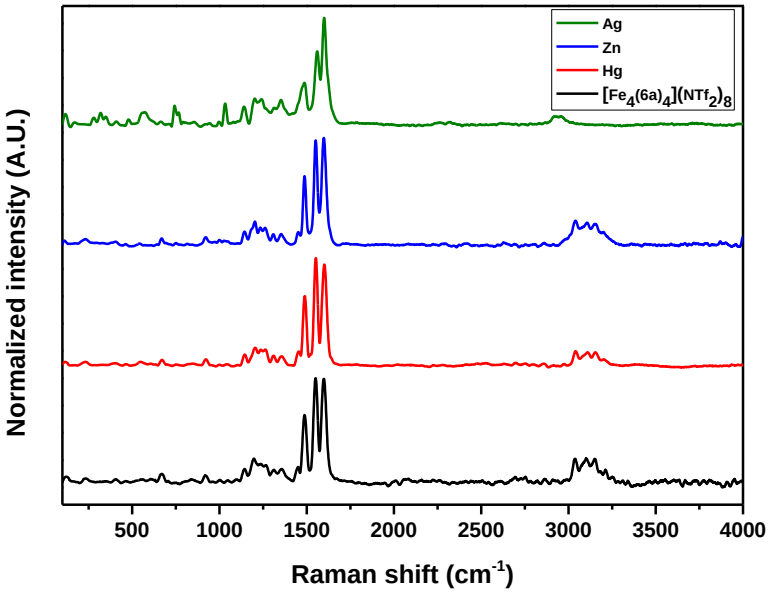

Figure 3.10 *Raman characterization including Raman spectra of cage [Fe₄(6**a**)₄](NTf₂)₈ and the gels triggered by different metal ions.*

XPS analysis was used to confirm metal coordination in the gels. For all three gels, the Fe 2p peak at 709.01–710.07 eV supported the presence of Fe–N coordination linkages within the cages.[16] The peak at 717.54 eV was attributed to Fe^{3+}, indicating trace oxidization (***Figure 3.34***).[17] The Ag^{+}-triggered gel displayed an Ag $3d_{3/2}$ peak at 373.53 eV and an Ag $3d_{5/2}$ peak at 367.50 eV, matching the Ag^{I} signal in Ag_2S (**Figure 3.11a**).[18] The S $2p_{1/2}$ peak at 162.78 eV and S $2p_{3/2}$ peak at 161.50 eV match the reported S^{2-} values in Ag_2S. The peaks at 167.18 and 168.08 eV, assigned to S $2p_{1/2}$, both match the sulfur(VI) signals in Tf_2N^{-} (**Figure 3.11b**).[19] Both Zn^{2+}-triggered and Hg^{2+}-triggered gel shows similar characteristics, confirming the existence of Zn and Hg

(***Figure 3.11c-f, Figure 3.35***).[20, 21] All XPS data were consistent with the metal ions interacting with the thiol groups of the Cys residues incorporated into the peripheries of cages in gels.

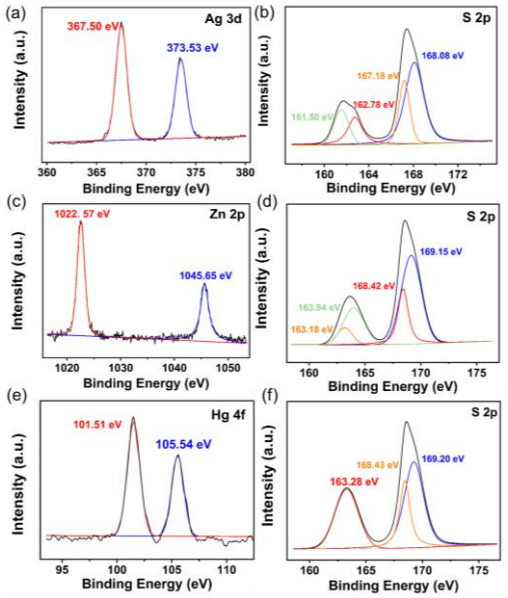

Figure 3.11: *XPS analysis of three cage-peptide gels prepared from 2. (a), (c) and (e) are XPS spectra corresponding to Ag 3d, Zn 2p, and Hg 4f, respectively, and (b) (d) and (f) are the S 2p XPS spectra for the same samples shown in (a), (c) and (e), confirming the presence of Tf2N- in each case.*

XPS analyses were performed by Nitschke Group of University of Cambridge.

3.4. Conclusion and Future work

Although the stereochemical information transfer observed here is moderate, our work may provide an insight into using homochiral peptides, which contain chiral directing groups far from the coordination sites, to control cage stereochemistry.[22, 23]

The metal-organic cages we report here thus incorporate peptide subcomponents for the first time, the Cys residues of which are demonstrated to bind peripheral metal ions, bringing about gelation. The observed diastereoselectivity in cage formation reveals stereochemical information transfer from the peripheral arms to the metal vertices. This phenomenon showcases the ability to control the stereochemistry of the resulting cages by manipulating the stereochemistry of the peripheral arms, thereby opening up a new pathway for the design of cages with controlled stereochemistry. The spherical nuclei formed during gelation interconnect to form a

gel matrix, as opposed to the fibrillar networks observed for peptide gels. This gelation in the presence of heavy metals holds promise for the removal of toxic metal ions from the environment. Future efforts will focus upon the extension of this chemical platform to the formation of biocompatible materials able to perform catalysis and chemical purification by taking advantage of the two distinct spaces present within these gels – the voids within the cages, and the larger regions of trapped solvent immobilized by matrix formation.

3.5. Experimental part

3.5.1. Peptides characterisation

Peptide *p*-aminobenzoyl-L-Phe-D-Cys-L-Phe-NH_2 (5)

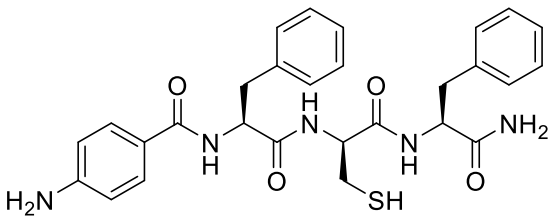

Chemical Formula: $C_{28}H_{31}N_5O_4S$
Molecular Weight: 533,65

^{1}H NMR (500 MHz, DMSO-d_6, 298 K) δ 8.34 – 8.18 (m, 3H, CONH), 7.56 (d, J = 8.2 Hz, 2H, ArH), 7.39 (s, 1H, $CONH_2$), 7.31 (d, J = 7.3 Hz, 2H, ArH), 7.24 (dd, J = 7.6 Hz, 2H, ArH), 7.23 – 7.07 (m, 7H, ArH), 6.55 (d, J = 8.5 Hz, 2H, ArH), 4.61 – 4.55 (m, 1H, αCH), 4.42 – 4.37 (m, 1H, αCH), 4.30 (ddd, J = 7.9, 4.7 Hz, 1H, αCH), 3.10 – 2.99 (m, 3H, βCH), 2.77 (dd, J = 13.7, 10.5 Hz, 1H, βCH), 2.56 (dd, J = 4.4 Hz, 1H, βCH), 2.47 – 2.41 (m, 1H, βCH), 1.54 (dd, J = 9.2, 7.9 Hz, 1H, SH).

^{13}C NMR (126 MHz, DMSO-d_6, 298 K) δ 172.9, 172.0, 169.2, 166.8 (4x CO); 138.3, 138.1, 129.3, 129.2, 129.2, 128.2, 128.1, 126.3, 126.3, 113.3, (Ar); 55.6, 54.7, 54.3, (αC); 37.6, 37.1, 26.2 (βC).

ESI-MS: m/z $[M + H]^+$ 534.2161, $[M + Na]^+$ 556.1990.

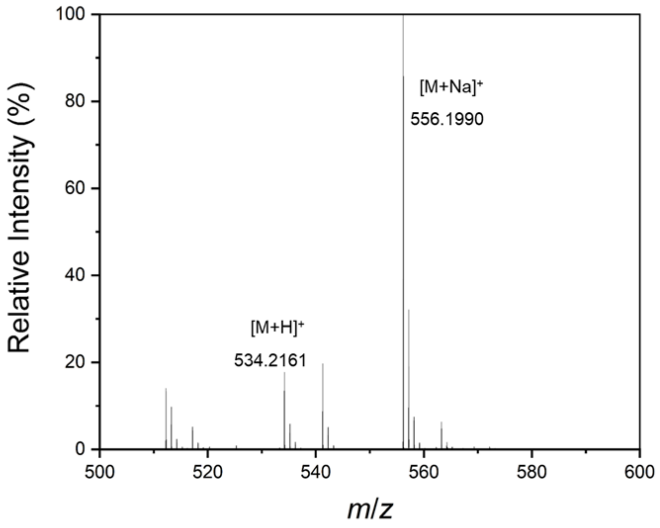

Figure 3.12: *ESI-MS of peptide* ***5****.*

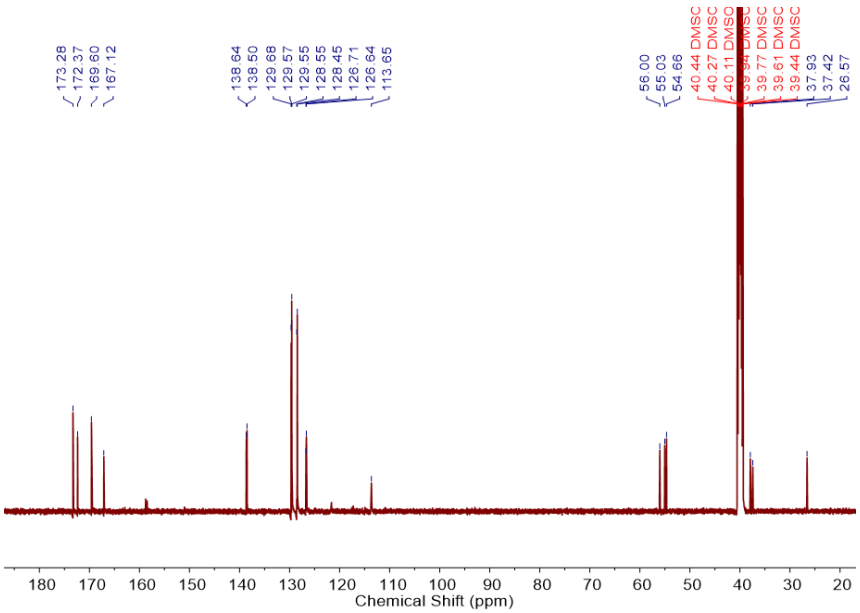

Figure 3.13: *^{13}C-NMR spectrum (DMSO-d$_6$, T = 298 K) of peptide* ***5****.*

Peptide *p*-aminobenzoyl-L-Phe-D-Phe-L-Cys-NH_2 (6)

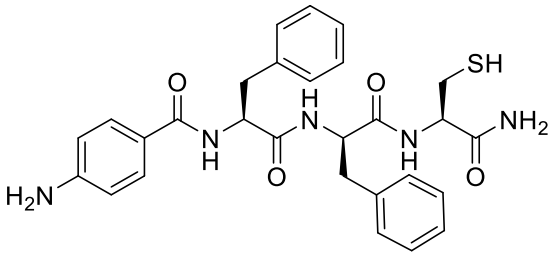

Chemical Formula: $C_{28}H_{31}N_5O_4S$
Molecular Weight: 533,65

^{1}H NMR (500 MHz, DMSO-d_6, 298 K) δ 8.41 (d, J = 8.2 Hz, 1H, CONH), 8.21 (d, J = 8.4 Hz, 1H, CONH), 8.03 (d, J = 7.4 Hz, 1H, CONH), 7.50 (d, J = 8.6 Hz, 2H, ArH), 7.38 (s, 1H, $CONH_2$), 7.25 (d, J = 7.1 Hz, 2H, ArH), 7.22 – 7.17 (m, 6H, ArH), 7.16 – 7.09 (m, 2H, ArH), 6.54 (d, J = 8.5 Hz, 2H, ArH), 4.60 – 4.50 (m, 2H, αCH), 4.34 – 4.28 (m, 1H, αCH), 3.06 (dd, J = 13.6, 4.7 Hz, 1H, βCH), 2.83 – 2.65 (m, 5H, βCH), 2.07 (dd, J = 9.2, 7.9 Hz, 1H, SH).

^{13}C NMR (126 MHz, DMSO-d_6, 298 K) δ 172.0, 171.5, 171.1, 166.5, (4 x CO); 138.5, 137.8, 129.4, 129.2, 129.1, 128.1, 126.4, 126.2, 113.12, (Ar); 55.2, 55.00, 54.1, (3x αC); 37.8, 37.0, 26.2 (3x βC).

ESI-MS: m/z calculated for M = 533.2097, observed positive mode $[M + H]^+$ = 534.2171 and $[M + Na]^+$ = 556.2000.

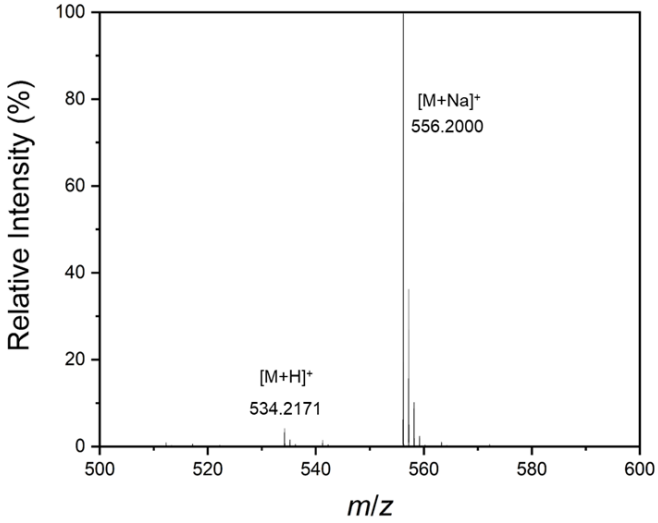

Figure 3.14: *ESI-MS of peptide* ***6****.*

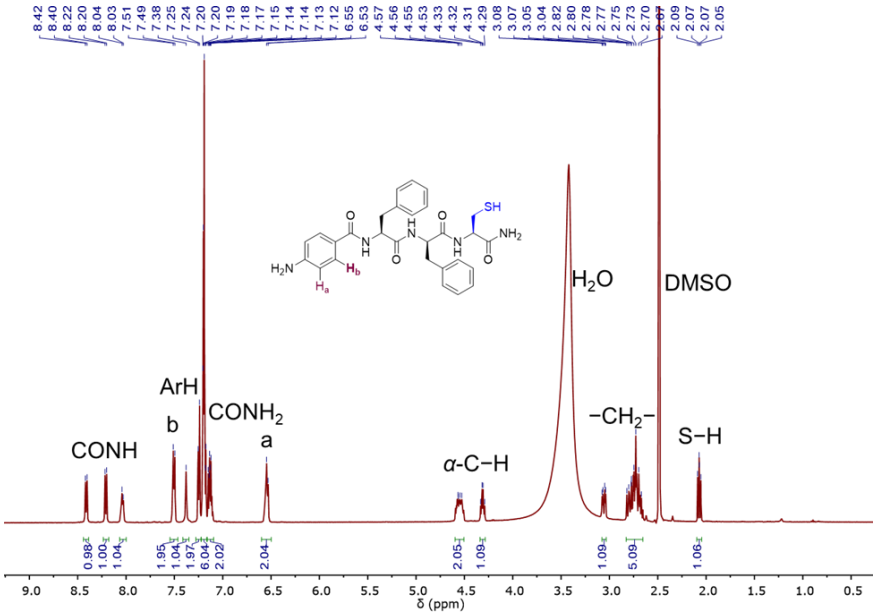

Figure 3.15: *[1]H-NMR spectrum (DMSO-d6, T = 298 K) of peptide* ***6****.*

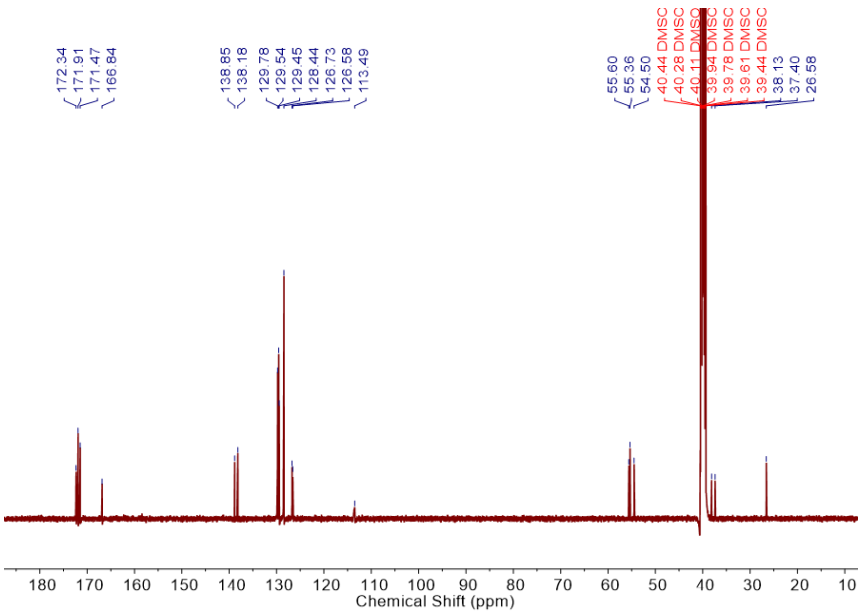

Figure 3.16: *^{13}C-NMR spectrum (DMSO-d_6, T = 298 K) of peptide* ***6****.*

Peptide *p*-aminobenzoyl-L-Phe-D-Met-L-Phe-NH_2 (7)

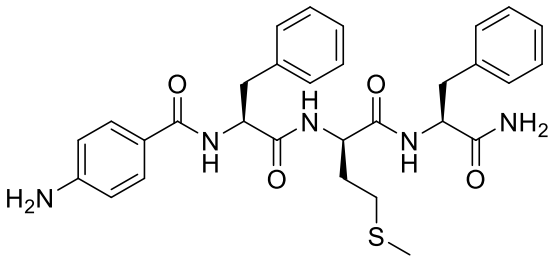

Chemical Formula: $C_{30}H_{35}N_5O_4S$
Molecular Weight: 561,70

^{1}H NMR (500 MHz, DMSO-d_6, 298 K) δ 8.24 (d, J = 7.1 Hz, 1H, CONH), 8.19 (dd, J = 8.5, 2.6 Hz, 2H, CONH), 7.57 (d, J = 8.7 Hz, 2H, ArH), 7.36 (s, 1H, $CONH_2$), 7.30 – 7.26 (m, 2H, ArH), 7.23 (dd, J = 7.6 Hz, 2H, ArH), 7.20 – 7.09 (m, 7H, ArH), 6.56 (d, J = 8.7 Hz, 2H, ArH), 4.53 (dd, J = 7.5 Hz, 1H, αCH), 4.39 – 4.34 (m, 1H, αCH), 4.18 (ddd, J = 8.6, 4.3 Hz, 1H, αCH), 3.09 – 3.05 (m, 1H, βCH), 3.00 (d, J = 8.5 Hz, 2H, βCH), 2.78 – 2.72 (m, 1H, βCH), 1.91 (dd, J = 8.6, 6.9 Hz, 2H, δCH_2), 1.88 (s, 3H, SCH_3), 1.71 – 1.65 (m, 1H, γCH), 1.46 (ddd, J = 14.2, 6.7, 1.7 Hz, 1H, γCH).

^{13}C NMR (126 MHz, DMSO-d_6, 298 K) δ 173.1, 171.9, 170.7, 166.7, (4x CO); 138.3, 138.0, 129.3, 129.2, 129.1, 128.2, 128.0, 126.4, 126.2, 121.4, 113.4, (Ar); 55.7, 54.3, 51.7, (3x αC); 37.4, 37.2, 31.3, (3x βC); 29.1 (γC); 14.5 (δC).

ESI-MS: m/z calculated for M = 561.2410, observed positive mode $[M + Na]^+$ = 584.2266.

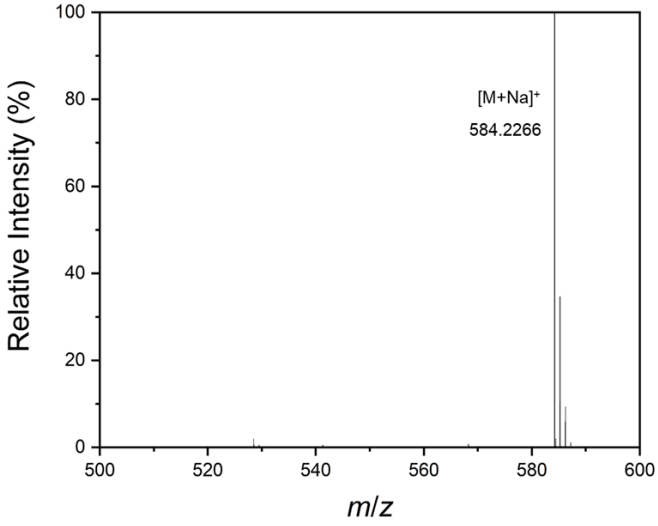

Figure 3.17: *ESI-MS of peptide 7.*

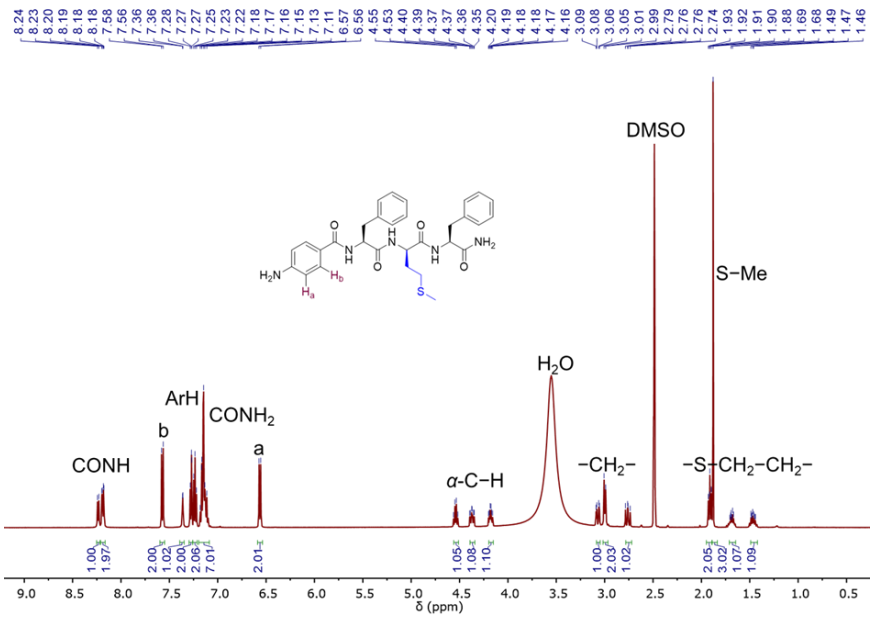

Figure 3.18: *^{1}H-NMR spectrum (DMSO-d_6, T = 298 K) of peptide 7.*

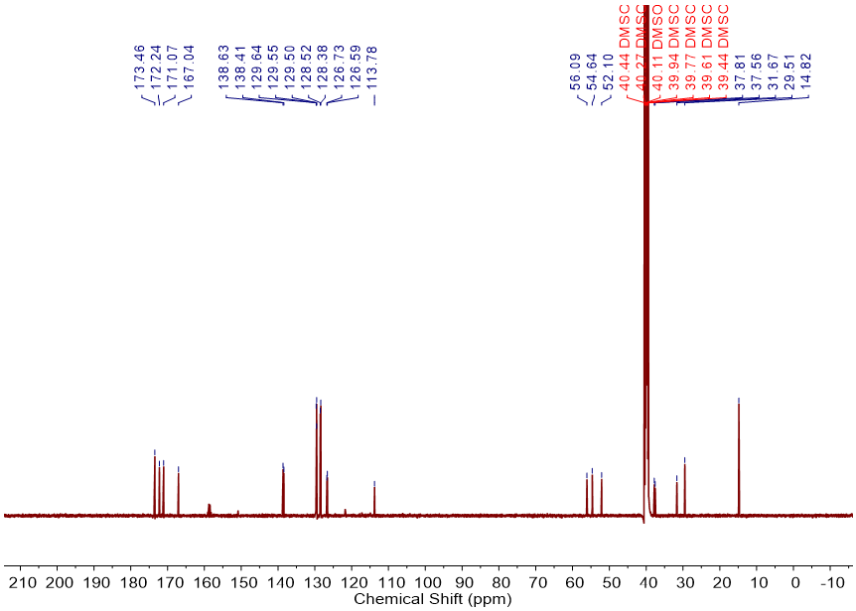

Figure 3.19: *^{13}C-NMR spectrum (DMSO-d_6, T = 298 K) of peptide* ***6****.*

3.5.2. Cages characterisation

$[Fe_4(\mathbf{5a})_4](NTf_2)_8$

This compound has a poor solubility in CD_3CN that is not sufficient for ^{13}C NMR spectrum. Only ^{1}H and ^{19}F NMR spectra are presented.

^{19}F NMR (471 MHz, 298 K, CD_3CN) δ –79.29 (encapsulated TFA^-), –80.02 (free NTf_2^-).

Species	Calculated m/z	Experimental m/z
$[Fe_4(C_{108}H_{102}N_{18}O_{12}S_3)_4(N(SO_2CF_3)_2)_3(CF_3CO_2)]^{4+}$	2234.4917	2234.3305
$[Fe_4(C_{108}H_{102}N_{18}O_{12}S_3)_4(N(SO_2CF_3)_2)_2(CF_3CO_2)]^{5+}$	1731.5636	1731.4757
$[Fe_4(C_{108}H_{102}N_{18}O_{12}S_3)_4(N(SO_2CF_3)_2)\ (CF_3CO_2)]^{6+}$	1396.2782	1396.2436
$[Fe_4(C_{108}H_{102}N_{18}O_{12}S_3)_4(CF_3CO_2)]^{7+}$	1156.7886	1156.7886

Table 3.4: *m/z values for $[Fe_4(\mathbf{5a})_4](NTf_2)_8$.*

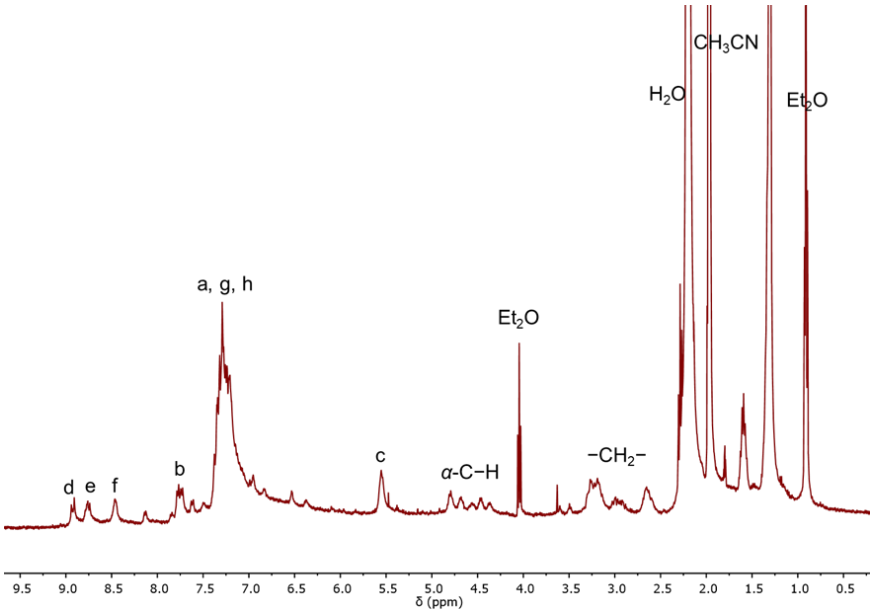

Figure 3.20: *^{1}H-NMR spectrum (CD_3CN, 500 MHz, T = 298 K) of cage $[Fe_4(\mathbf{5a})_4](NTf_2)_8$.*

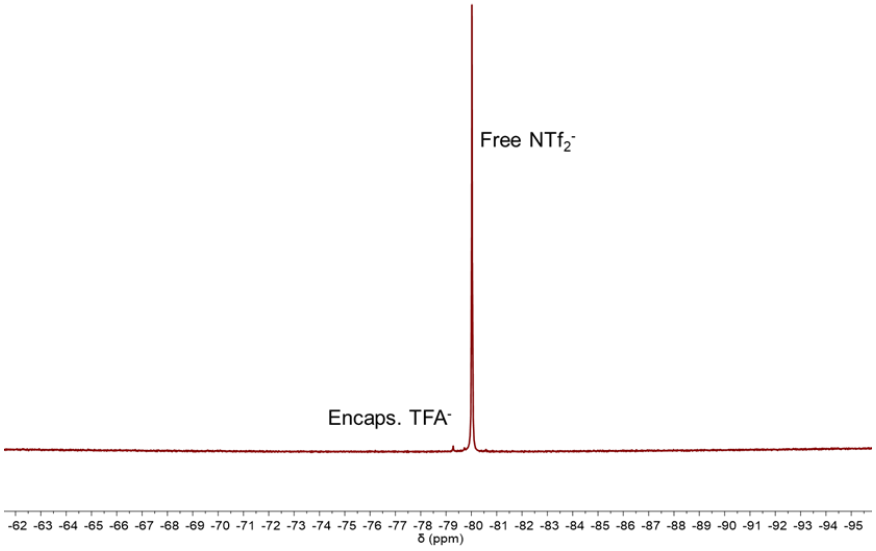

Figure 3.21: *^{19}F-NMR spectrum (CD_3CN, 471 MHz, T = 298 K) of cage $[Fe_4(\mathbf{5a})_4](NTf_2)_8$.*

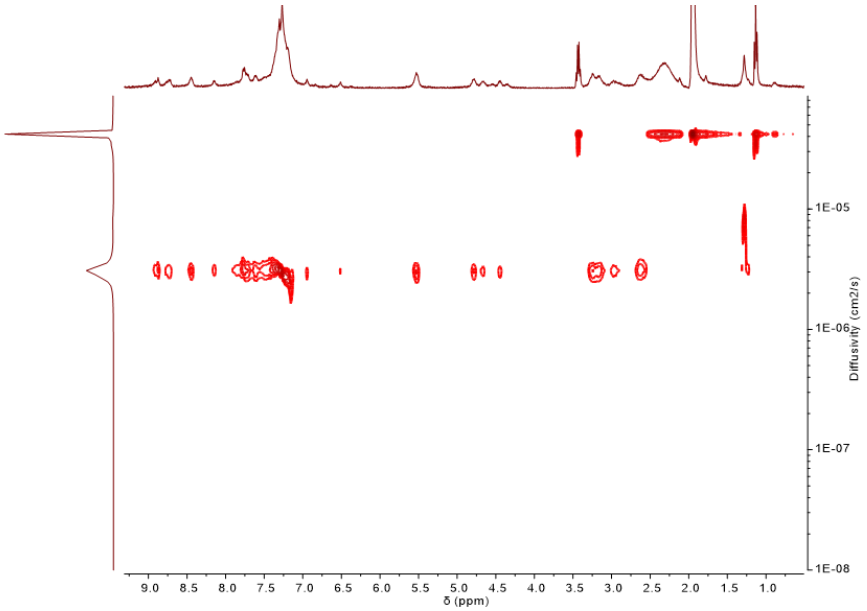

Figure 3.22: *^{1}H-DOSY NMR spectrum (CD_3CN, 400 MHz, T = 298 K) of cage $[Fe_4(\mathbf{5a})_4](NTf_2)_8$. The diffusion coefficient for $[Fe_4(\mathbf{5a})_4](NTf_2)_8$ in CD_3CN was measured to be 3.01 x 10^{-10} m^2 s^{-1} and the solvodynamic radius was calculated to be 21.71 Å.*

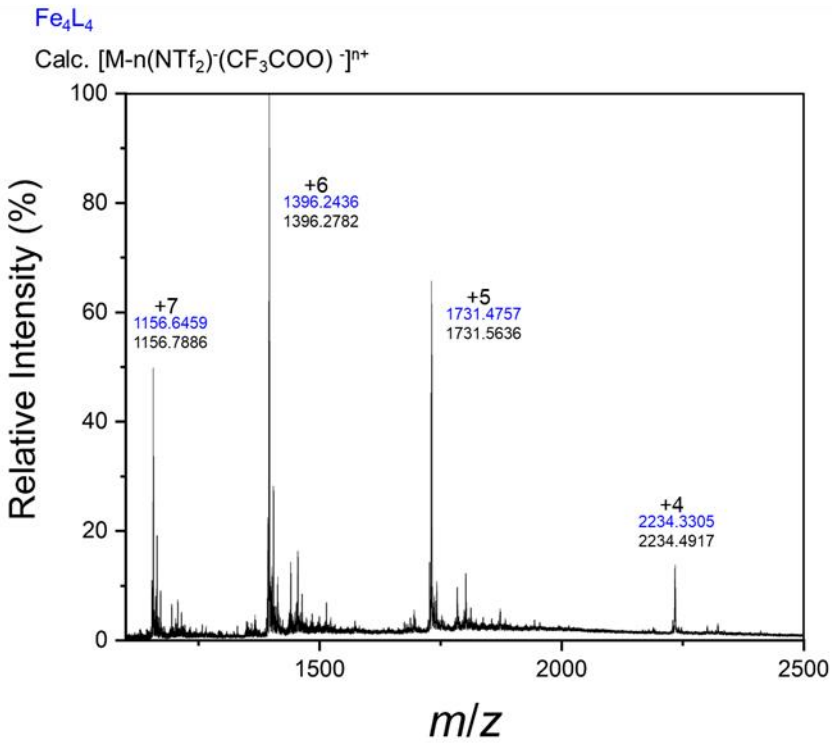

Figure 3.23: *ESI-MS of cage $[Fe_4(\mathbf{5a})_4](NTf_2)_8$.*

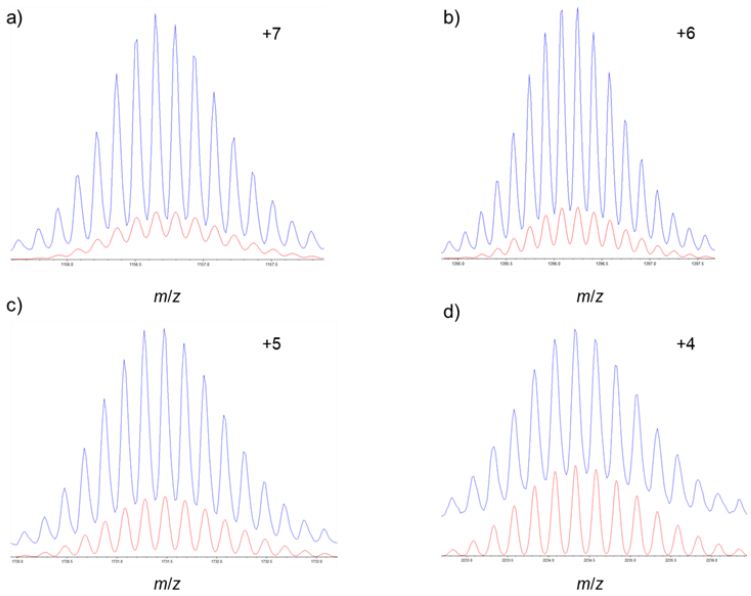

Figure 3.24: *Isotopic pattern distribution of [Fe$_4$(**5a**)$_4$](NTf$_2$)$_8$.*

[Fe$_4$(6**a**)$_4$](NTf$_2$)$_8$

This compound has a poor solubility in CD_3CN that is not sufficient for ^{13}C NMR spectrum. Only ^{1}H and ^{19}F NMR spectra are presented.

^{19}F NMR (471 MHz, acetonitrile-d_3) δ –76.24 (free TFA^-), –79.29 (encapsulated TFA^-), –80.06 (NTf_2^-).

Species	Calculated m/z	Experimental m/z
$[Fe_4(C_{108}H_{102}N_{18}O_{12}S_3)_4(N(SO_2CF_3)_2)_3(CF_3CO_2)]^{4+}$	2234.4917	2234.3234
$[Fe_4(C_{108}H_{102}N_{18}O_{12}S_3)_4(N(SO_2CF_3)_2)_2(CF_3CO_2)]^{5+}$	1731.5636	1731.4730
$[Fe_4(C_{108}H_{102}N_{18}O_{12}S_3)_4(N(SO_2CF_3)_2)\ (CF_3CO_2)]^{6+}$	1396.2782	1396.2428
$[Fe_4(C_{108}H_{102}N_{18}O_{12}S_3)_4(CF_3CO_2)]^{7+}$	1156.7926	1156.7926

Table 3.5: *m/z values for [Fe$_4$(**6a**)$_4$](NTf$_2$)$_8$.*

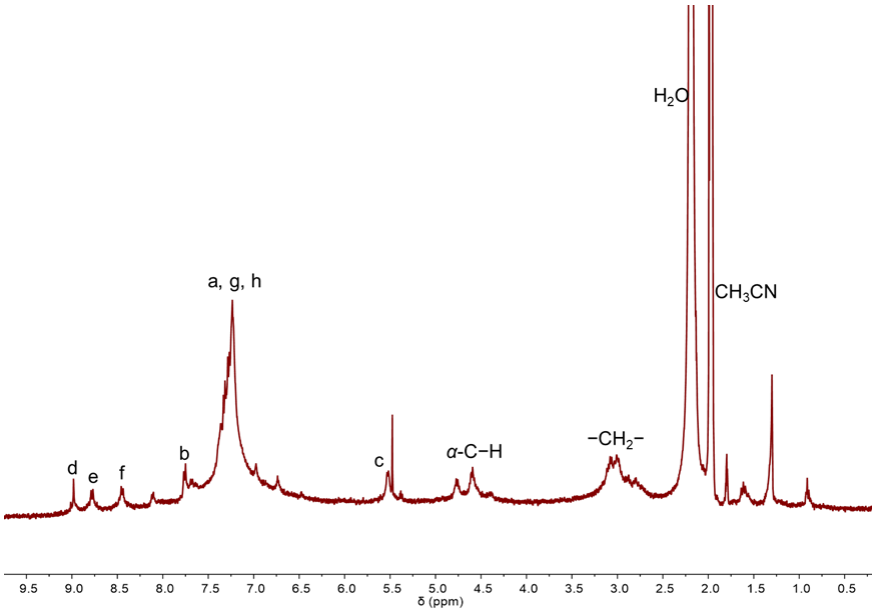

Figure 3.25: *[1]H-NMR spectrum (CD_3CN, 500 MHz, T = 298 K) of cage $[Fe_4(\mathbf{6a})_4](NTf_2)_8$.*

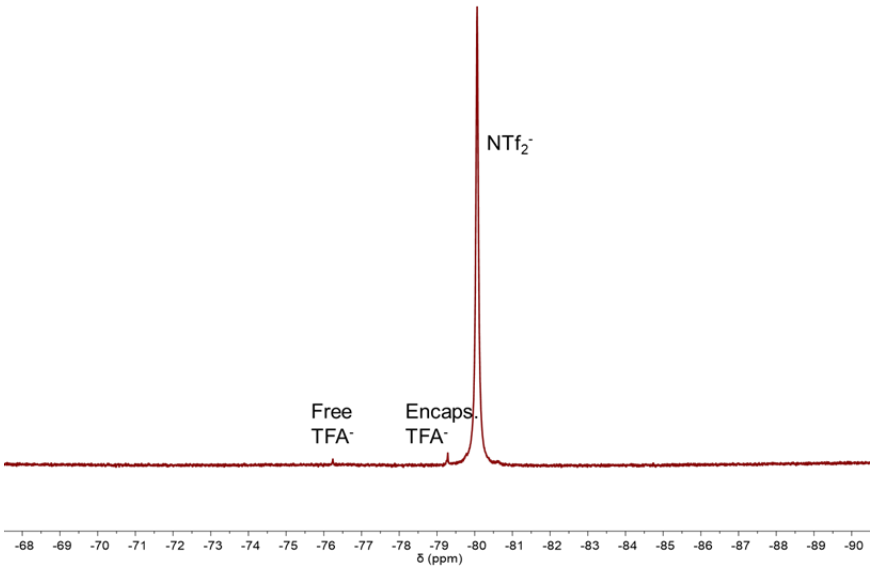

Figure 3.26: *[19]F-NMR spectrum (CD_3CN, 471 MHz, T = 298 K) of cage $[Fe_4(\mathbf{6a})_4](NTf_2)_8$.*

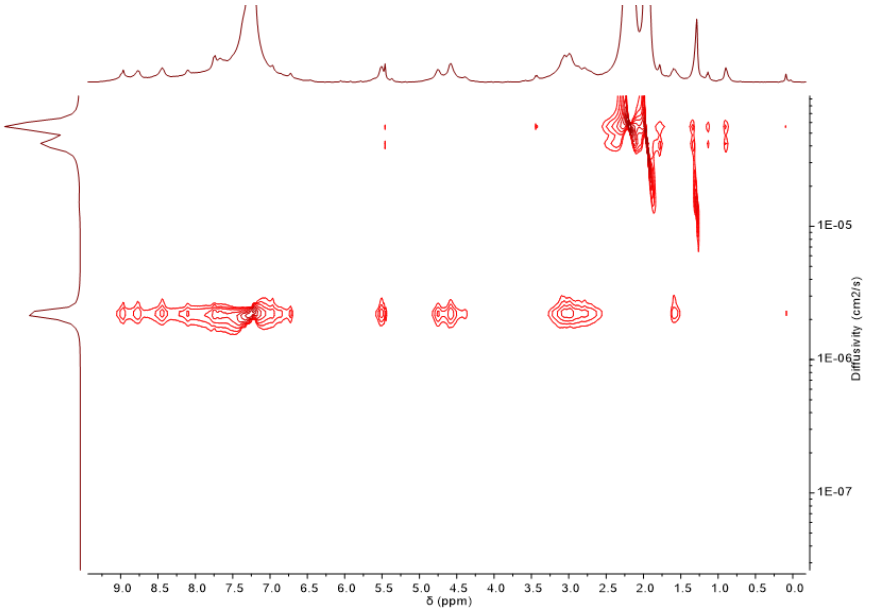

Figure 3.27: *^{1}H-DOSY NMR spectrum (CD_3CN, 400 MHz, T = 298 K) of cage $[Fe_4(\mathbf{6a})_4](NTf_2)_8$. The diffusion coefficient for $[Fe_4(\mathbf{6a})_4](NTf_2)_8$ in CD_3CN was measured to be 2.14 x 10^{-10} m^2 s^{-1} and the solvodynamic radius was calculated to be 30.54 Å.*

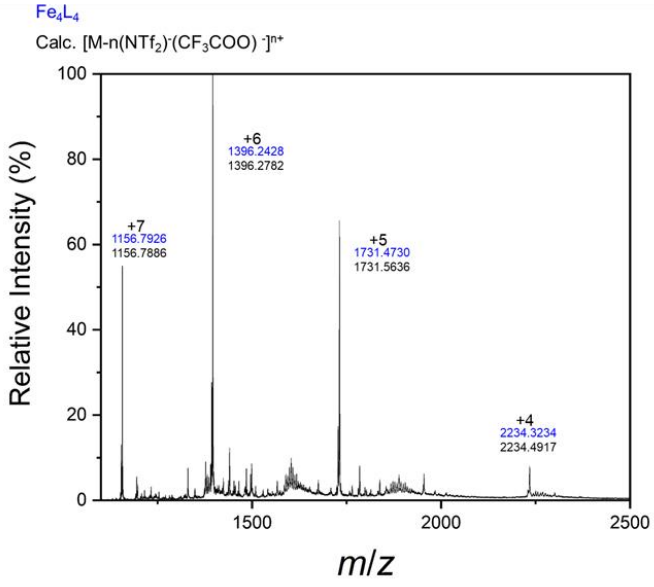

Figure 3.28: *ESI-MS of cage $[Fe_4(\mathbf{6a})_4](NTf_2)_8$.*

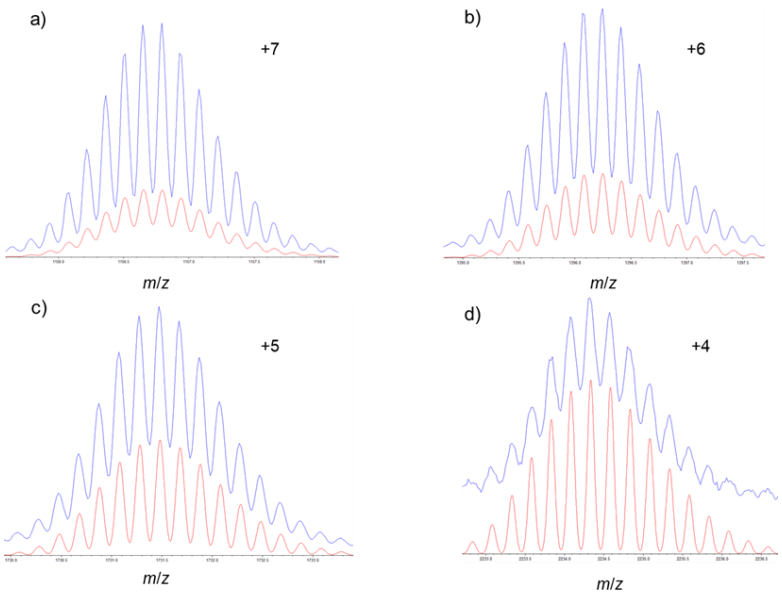

Figure 3.29: *Isotopic pattern distribution of* $[Fe_4(\mathbf{6a})_4](NTf_2)_8$.

$[Fe_4(\mathbf{7a})_4](NTf_2)_8$

^{19}F NMR (471 MHz, acetonitrile-d_3) δ –76.22 (free TFA^-), –79.27 (encapsulated TFA^-), –80.05 (NTf_2^-).

Species	Calculated m/z	Experimental m/z
$[Fe_4(C_{114}H_{114}N_{18}O_{12}S_3)_4(N(SO_2CF_3)_2)_3(CF_3CO_2)]^{4+}$	2318.6514	2318.6884
$[Fe_4(C_{114}H_{114}N_{18}O_{12}S_3)_4(N(SO_2CF_3)_2)_2(CF_3CO_2)]^{5+}$	1798.8913	1798.7642
$[Fe_4(C_{114}H_{114}N_{18}O_{12}S_3)_4(N(SO_2CF_3)_2)\ (CF_3CO_2)]^{6+}$	1452.3846	1452.3153
$[Fe_4(C_{114}H_{114}N_{18}O_{12}S_3)_4(CF_3CO_2)]^{7+}$	1204.8798	1204.8519

Table 3.6: *m/z values for* $[Fe_4(\mathbf{7a})_4](NTf_2)_8$.

HR-MS [charge, calculated mass]: *m/z* = 2318.6884 [$\mathbf{3}(NTf_2)_3(CF_3COO)^{4+}$, 2318.6514], 1798.7642 [$\mathbf{3}(NTf_2)_2(CF_3COO)^{5+}$, 1798.8913], 1452.3153 [$\mathbf{3}(NTf_2)(CF_3COO)^{6+}$, 1452.3846], 1204.8519 [$\mathbf{3}(CF_3COO)^{7+}$, 1204.8798].

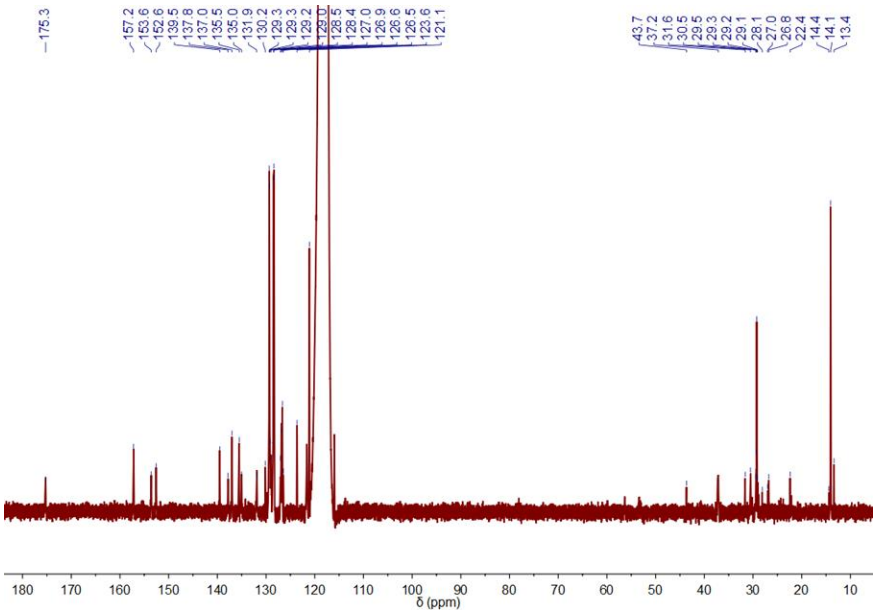

Figure 3.30: *^{13}C-NMR spectrum (CD_3CN, 125 MHz, T = 298 K) of cage $[Fe_4(\mathbf{7a})_4](NTf_2)_8$.*

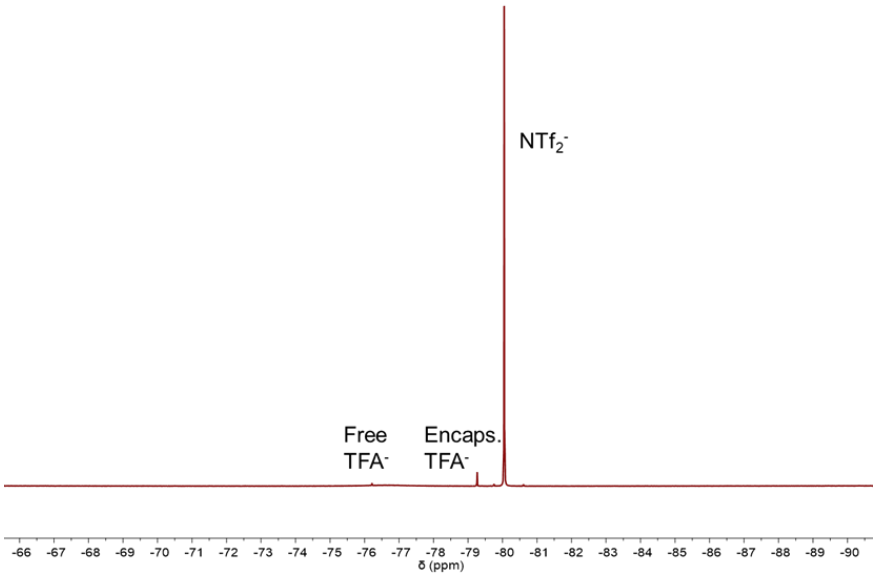

Figure 3.31: *^{19}F-NMR spectrum (CD_3CN, 471 MHz, T = 298 K) of cage $[Fe_4(\mathbf{7a})_4](NTf_2)_8$.*

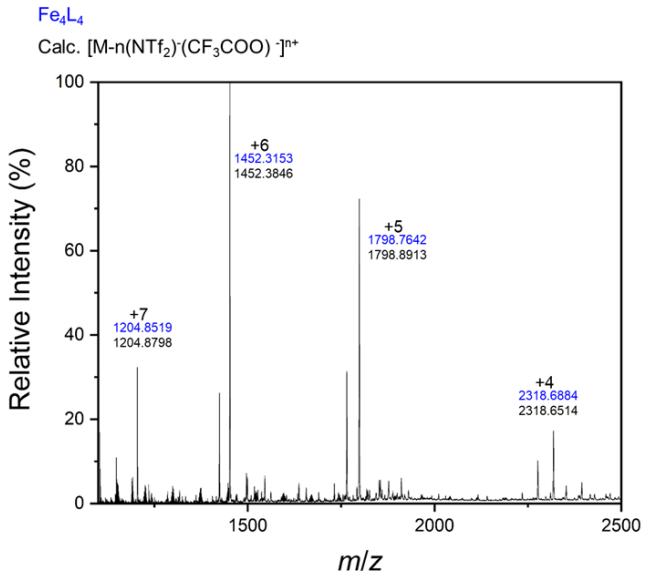

Figure 3.32: *ESI-MS of cage [Fe4(**7a**)4](NTf2)8.*

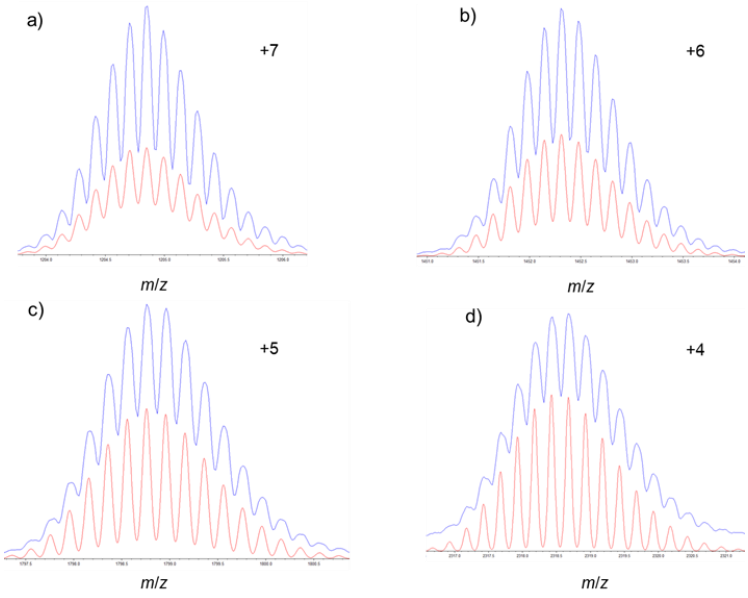

Figure 3.33: *Isotopic pattern distribution of [Fe4(**7a**)4](NTf2)8.*

3.5.3. XPS analysis

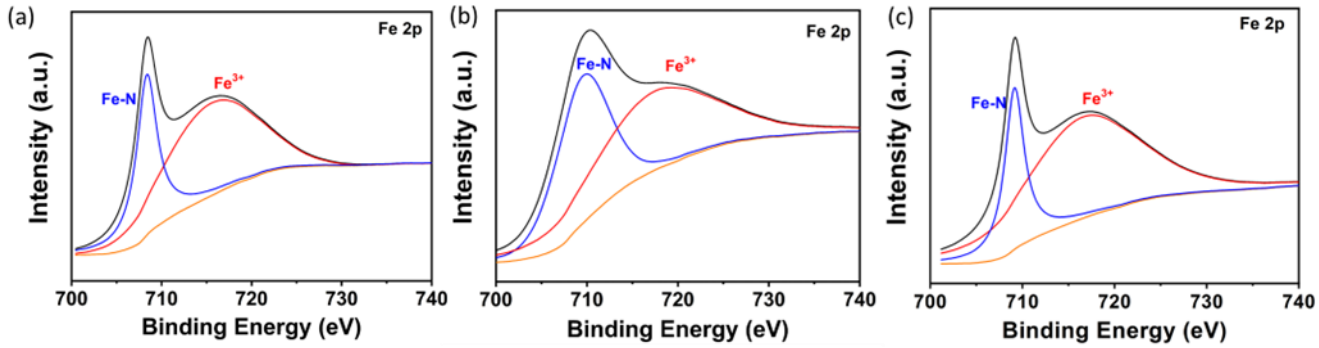

Figure 3.34: *XPS characterizations of three gels with Fe 2p XPS spectra of Ag^{+} regulated gel (a); Zn^{2+} regulated gel (b); Hg^{2+} regulated gel (c).*

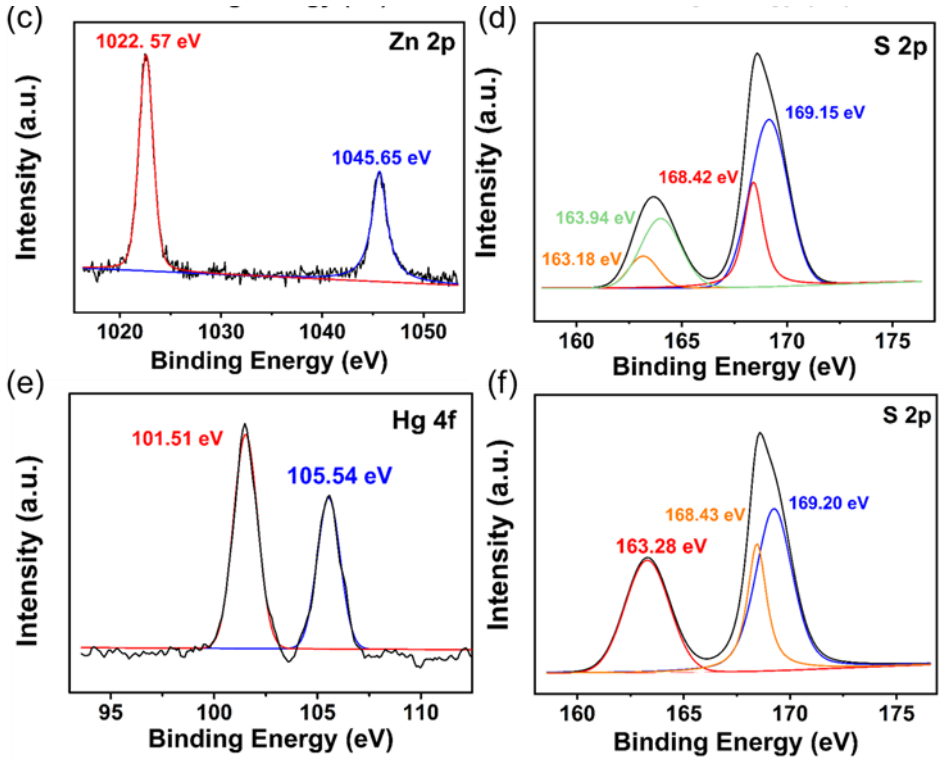

Figure 3.35: *XPS analysis of three cage-peptide gels prepared from $[Fe_4(\mathbf{6a})_4](NTf_2)_8$. (c) and (e) are XPS spectra corresponding to Zn 2p, and Hg 4f, respectively, and (d) and (f) are the S 2p XPS spectra for the same samples shown in (c) and (e), confirming the presence of Tf_2N- in each case.*

3.6. Bibliography

(1) Dong, J.; Liu, Y.; Cui, Y. Artificial Metal–Peptide Assemblies: Bioinspired Assembly of Peptides and Metals through Space and across Length Scales. *J. Am. Chem. Soc.* **2021**, *143* (42), 17316-17336.

(2) Inomata, Y.; Sawada, T.; Fujita, M. Metal–Peptide Nonafoil Knots and Decafoil Supercoils. *J. Am. Chem. Soc.* **2021**, *143* (40), 16734-16739.

(3) Dey, S.; Misra, R.; Saseendran, A.; Pahan, S.; Gopi, H. N. Metal-Coordinated Supramolecular Polymers from the Minimalistic Hybrid Peptide Foldamers. *Angew. Chem. Int. Ed.***2021**, *60* (18), 9863-9868.

(4) Zou, R.; Wang, Q.; Wu, J.; Wu, J.; Schmuck, C.; Tian, H. Peptide self-assembly triggered by metal ions. *Chem. Soc. Rev.* **2015**, *44* (15), 5200-5219.

(5) Castilla, A. M.; Ousaka, N.; Bilbeisi, R. A.; Valeri, E.; Ronson, T. K.; Nitschke, J. R. High-Fidelity Stereochemical Memory in a FeII4L4 Tetrahedral Capsule. *J. Am. Chem. Soc.* **2013**, *135* (47), 17999-18006.

(6) Castilla, A. M.; Ramsay, W. J.; Nitschke, J. R. Stereochemical communication within tetrahedral capsules. *Chem. Lett.* **2014**, *43* (3), 256-263.

(7) Ousaka, N.; Clegg, J. K.; Nitschke, J. R. Nonlinear Enhancement of Chiroptical Response through Subcomponent Substitution in M4L6 Cages. *Angew. Chem. Int. Ed.***2012**, *51* (6), 1464-1468.

(8) Dragna, J. M.; Pescitelli, G.; Tran, L.; Lynch, V. M.; Anslyn, E. V.; Di Bari, L. In Situ Assembly of Octahedral Fe(II) Complexes for the Enantiomeric Excess Determination of Chiral Amines Using Circular Dichroism Spectroscopy. *J. Am. Chem. Soc.* **2012**, *134* (9), 4398-4407.

(9) Sequeira, M. A.; Herrera, M. G.; Dodero, V. I. Modulating amyloid fibrillation in a minimalist model peptide by intermolecular disulfide chemical reduction. *Phys. Chem. Chem. Phys.* **2019**, *21* (22), 11916-11923.

(10) Kanti Das, B.; Samanta, R.; Ahmed, S.; Pramanik, B. Disulphide Cross-Linked Ultrashort Peptide Hydrogelator for Water Remediation. *Chem. Eur. J.* **2023**, *29* (37), e202300312.

(11) Diaferia, C.; Rosa, E.; Balasco, N.; Sibillano, T.; Morelli, G.; Giannini, C.; Vitagliano, L.; Accardo, A. The Introduction of a Cysteine Residue Modulates The Mechanical Properties of Aromatic-Based Solid Aggregates and Self-Supporting Hydrogels. *Chem. Eur. J.* **2021**, *27* (60), 14886-14898.

(12) Wang, Y.; Gu, Y.; Keeler, E. G.; Park, J. V.; Griffin, R. G.; Johnson, J. A. Star PolyMOCs with Diverse Structures, Dynamics, and Functions by Three-Component Assembly. *Angew. Chem. Int. Ed.***2017**, *56* (1), 188-192.

(13) Shannon, R. Revised effective ionic radii and systematic studies of interatomic distances in halides and chalcogenides. *Acta Crystallographica Section A* **1976**, *32* (5), 751-767.

(14) Garcia, A. M.; Iglesias, D.; Parisi, E.; Styan, K. E.; Waddington, L. J.; Deganutti, C.; De Zorzi, R.; Grassi, M.; Melchionna, M.; Vargiu, A. V.; et al. Chirality Effects on Peptide Self-Assembly Unraveled from Molecules to Materials. *Chem* **2018**, *4* (8), 1862-1876.

(15) Makam, P.; Gazit, E. Minimalistic peptide supramolecular co-assembly: expanding the conformational space for nanotechnology. *Chem. Soc. Rev.* **2018**, *47* (10), 3406-3420.

(16) Wu, Z.-Y.; Xu, X.-X.; Hu, B.-C.; Liang, H.-W.; Lin, Y.; Chen, L.-F.; Yu, S.-H. Iron Carbide Nanoparticles Encapsulated in Mesoporous Fe-N-Doped Carbon Nanofibers for Efficient Electrocatalysis. *Angew. Chem. Int. Ed.***2015**, *54* (28), 8179-8183.

(17) Jia, Y.; Zhang, W.; Yeon Do, J.; Kang, M.; Liu, C. Z-scheme SnFe2O4/α-Fe2O3 micro-octahedron with intimated interface for photocatalytic CO2 reduction. *Chem. Eng. J.* **2020**, *402*, 126193.

(18) Liang, T.-Y.; Chan, S.-J.; Patra, A. S.; Hsieh, P.-L.; Chen, Y.-A.; Ma, H.-H.; Huang, M. H. Inactive Cu2O Cubes Become Highly Photocatalytically Active with Ag2S Deposition. *ACS Appl. Mater. Interfaces* **2021**, *13* (9), 11515-11523.

(19) Fogarty, Richard M.; Rowe, R.; Matthews, R. P.; Clough, M. T.; Ashworth, C. R.; Brandt, A.; Corbett, P. J.; Palgrave, R. G.; Smith, E. F.; Bourne, R. A.; et al. Atomic charges of sulfur in ionic liquids: experiments and calculations. *Faraday Discuss.* **2018**, *206* (0), 183-201.

(20) Madkour, M.; Abdelmonem, Y.; Qazi, U. Y.; Javaid, R.; Vadivel, S. Efficient Cr(vi) photoreduction under natural solar irradiation using a novel step-scheme ZnS/SnIn4S8 nanoheterostructured photocatalysts. *RSC Advances* **2021**, *11* (47), 29433-29440.

(21) Jia, F.; Liu, C.; Yang, B.; Zhang, X.; Yi, H.; Ni, J.; Song, S. Thermal Modification of the Molybdenum Disulfide Surface for Tremendous Improvement of Hg2+ Adsorption from Aqueous Solution. *ACS Sustain. Chem. Eng.* **2018**, *6* (7), 9065-9073.

(22) Xue, W.; Ronson, T. K.; Lu, Z.; Nitschke, J. R. Solvent Drives Switching between Λ and Δ Metal Center Stereochemistry of M8L6 Cubic Cages. *J. Am. Chem. Soc.* **2022**, *144* (14), 6136-6142.

(23) Domoto, Y.; Yamamoto, K.; Horie, S.; Yu, Z.; Fujita, M. Amplification of weak chiral inductions for excellent control over the helical orientation of discrete topologically chiral (M3L2)n polyhedra. *Chem. Sci.* **2022**, *13* (15), 4372-4376.

Chapter 4

Metal organic cages

on carbon nanotubes

4.1. Introduction

The mechanical,[1] electrical,[2] and optical[3, 4] properties of CNTs are heavily influenced by their size and structure. Generally, after the synthesis, the batches contain a mixture of CNTs with different sizes and properties. The sorting of them is, as consequence, a key problem in their production.[5] During the years, many approaches have been established to solve this problem.[5] These approaches can be both physical and chemical. The first one generally involves chromatography,[6, 7] centrifugation,[8] or electrophoresis.[9] The chemical approaches are based on covalent and non-covalent functionalisation of the tubes. The covalent functionalisation, however, affects the integrity of the materials disrupting the π-conjugated network. The non-covalent route is thus preferable to preserve the intrinsic properties of the materials, whilst allowing to introduce new features depending on the nature of the molecules chosen for the functionalisation. An intriguing technique based on non-covalent functionalisation is the biphasic extraction, thanks to its simplicity, offering high levels of resolution, and not requiring a sophisticated apparatus.[10-15]

This last point and the research work of Pérez and co-workers on MINTs (see **Section 1.2.2** of the **Introduction**) that described a simple method to calculate the affinity of organic aromatic molecules on SWCNTs through thermogravimetric analysis (TGA), inspired Marchesan and Nitschke groups to study the affinity of MOCs for CNTs.[16]

The preliminary experiment regarded a very well-known cage, developed in the Nitschke group.[17] This iron tetrahedral possesses a melamine core that could establish weak interactions with the surface of SWCNTs. The titration through TGA analysis revealed a good affinity for this cage towards SWCNTs. The value of the K_a of 5.26 ± 1.28 mM^{-1}, was also comparable to the ones reported by Pérez, that may change from 4.5 M^{-1} to 2.6 mM^{-1} depending on the solvent.[16]

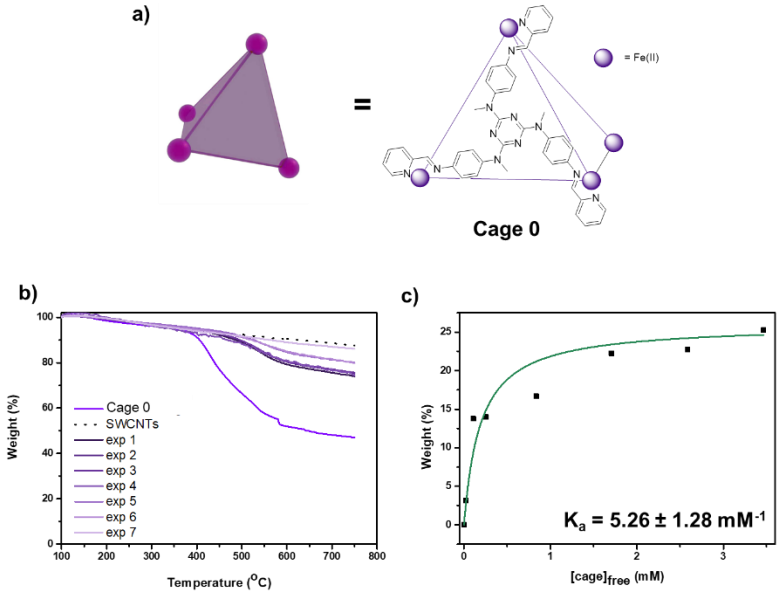

Figure 4.1 *a) MOCs used to functionalise the SWCNTs,* ***Cage 0****;*[17] *b) TGA analysis under* N_2 *of titration of* ***Cage 0*** *vs SWCNTs; c) titration of* ***Cage 0*** *vs SWCNTs.*

4.2. Aim of the project

The goal of this project is to further explore the interaction between CNTs and MOCs developed by the Nitschke group. This zinc tetrahedral cage (**1**) was chosen for this study, instead of cage **0**, because of its ability to be soluble and stable both in aqueous and organic solvents only changing the counter ion, the sulfate and the triflate, respectively.[18]

In the first instance, the association constant between this MOC and SWCNTs will be calculated, and the possibility to transport CNTs across aqueous and organic phases will be tested by changing the counterion of the cage.

The second part of the project regards the possibility of sorting tubes with different dimensions, thanks to their non-covalent functionalisation with cage **1**, and using a biphasic extraction method.

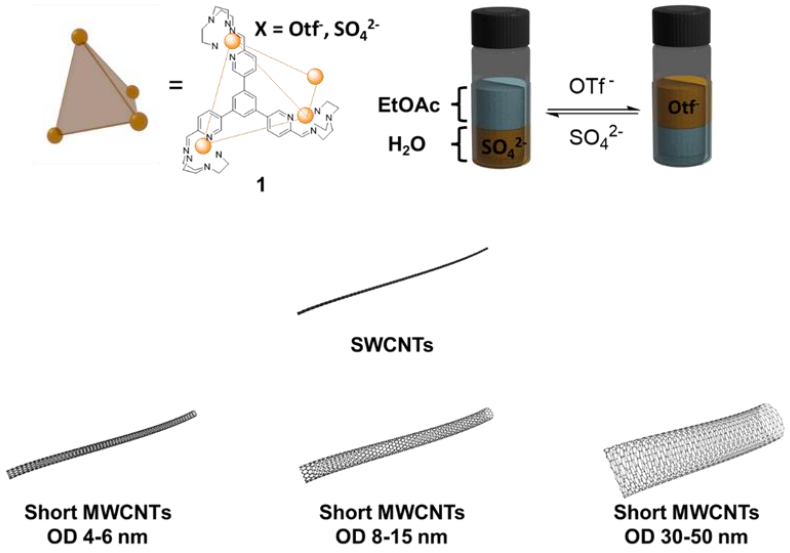

Figure 4.2 *Zinc cages, cage* ***1****, and CNTs used in the project.*

4.3. Results and discussion

4.3.1. Synthesis and characterisation of the cage

The cage was synthesised following the literature protocol reported by Nitschke and co-workers. As for the synthesised MOCs of the previous chapters, all the sub-components were mixed together and the solution heated at 70 °C for 24 h.[18] The successful synthesis was confirmed by MS analysis.

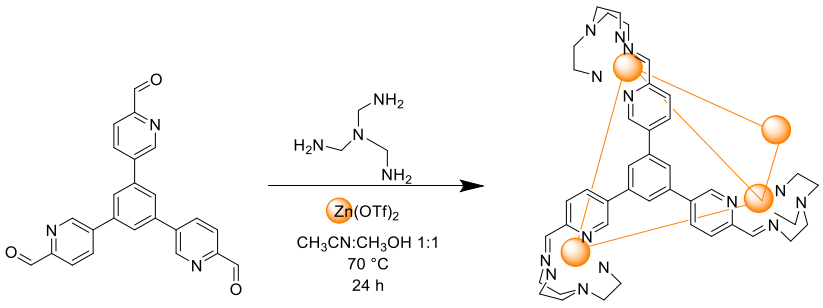

Figure 4.3: *Synthetical procedure of* ***1****.*

4.3.2. Characterisation of pristine CNTs

Pristine CNTs were characterised, before their usage, through three different types of techniques, calorimetric, spectroscopic, and microscopic. The typical calorimetric technique used for the study of the CNM is the thermogravimetric analysis (TGA). In this analysis the sample is heated with an increasing temperature and the weight loss percentage is measured. The analysis can be carried out under inert atmosphere (generally N_2) or in air. Both are extremely useful because they give different information. Under inert atmosphere, most pristine CNMs are stable until higher temperatures. Once functionalised with an organic moiety, they are less stable at higher temperatures, resulting in higher weight loss than the pristine material. The degree of functionalization can be estimated by comparison of the pristine and the functionalised sample thermograms. The analysis in air is related to the thermal stability of the sample or the amount of metal present in the sample (*i.e.* inorganic residue at high temperature).

The TGA analysis of SWCNTs (***Figure 4.4***) and MWCNTs with different diameters (***Figure 4.5***) revealed a higher quality for the latter relative to the former. SWCNTs displayed a higher amount of amorphous carbon ~ 10 wt % at 700 °C, and in air the CNT degradation over a wide range of temperatures suggested a rather heterogeneous sample. The MWCNTs showed a sharper transition at 485 °C, which was sharper with increasing CNT diameter. Under nitrogen gas, MWCNTs displayed only about 6 % wt. of amorphous carbon at 700 °C. The better quality of the MWCNTs was further confirmed by an inorganic residue of 1-2 % wt. at 700 °C, instead of the 5 % wt. for the SWCNTs.

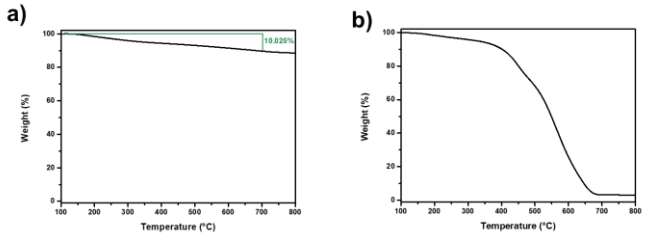

Figure 4.4: *Thermogravimetric analysis (TGA) of pristine SWCNTs of different diameters* ***a)*** *in nitrogen and* ***b)*** *in air.*

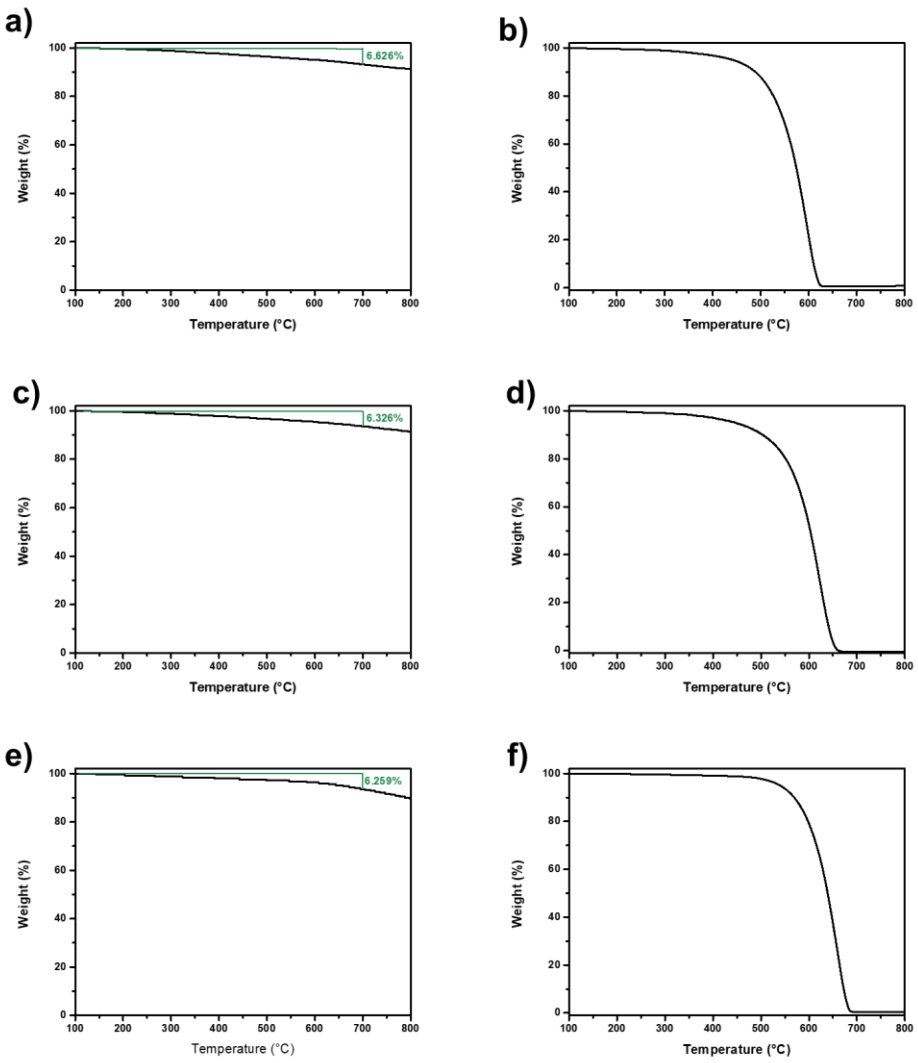

Figure 4.5: *Thermogravimetric analysis (TGA) of pristine short MWCNTs of different diameters* ***a), c), d)*** *in nitrogen and* ***b), d), f)*** *in air.* ***a)*** *and* ***b) OD-4-6*** *nm;* ***c)*** *and* ***d) OD-8-15*** *nm;* ***e)*** *and* ***f) OD-30-50*** *nm.*

Raman analysis is one of the most powerful tools to studying properties of CNTs, in general for all the carbon nanomaterials (CNMs). Raman spectroscopy can give information about doping, defects, crystallite size, diameter of tubes, chirality, curvature, and metallic-semiconducting behaviour.

The main feature in CNTs spectra is the G band, around 1582 cm^{-1}, (***Figure 4.6*** and ***Figure 4.7***) common to all sp^2 carbon forms. This first order mode is relative to stretching of the C-C bond in sp^2 systems. This band is also highly effective to strain effects, as curvature in CNTs. The latter effect is the reason for the multiple peaks displayed by SWCNTs spectra (***Figure 4.6***). The other first order mode, present only in single- and double-wall carbon nanotubes, is the radial breathing mode (RBM), in the range between 100-500 cm^{-1}, (***Figure 4.6***) relative to an out of plane stretching phonon mode for which all the carbon atoms move coherently

in the radial direction. The RBM frequency is inversely proportional to tube diameter established by the following equation (**4.1**):

$$\omega = \frac{A}{d} + B \ (\mathbf{4.1})$$

With A = 234 cm^{-1}, value related to vibrational force constant of the sp^2 C-C bond, and B = 10 cm^{-1}, related to environmental effect.[19] In particular, regarding this batch of p-SWCNTs, the average value of the diameter was 1.0 ± 0.1 nm, and it was previously calculated and reported by Marchesan and co-workers.[20]

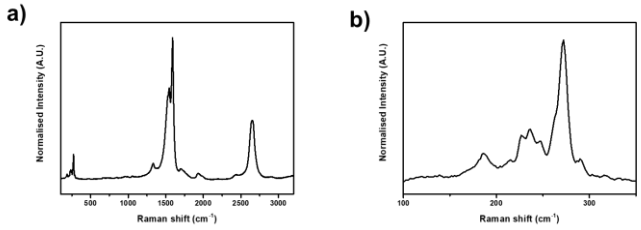

Figure 4.6: *Raman spectra of pristine SWCNTs.* ***a)*** *all spectra,* ***b)*** *zoom in RBM region.*

Another key feature of Raman spectra of CNTs is a second order mode band, called the D-band, at 1350 cm^{-1}, (***Figure 4.7***) and associated to the introduction of defects in the carbon lattice. The introduction of defects is generally related to the covalent functionalisation of carbon nanomaterials, due to the introduction of sp^3 atoms in the sp^2-hybridezed carbon system. The increasing of the ratio between the intensity of the D-band and the intensity of the G one, I_D/I_G, is an excellent tool to the evaluate the level of functionalisation of the material after the desired reaction, but can be used quantitatively for SWCNTs, and not MWCNTs, which have too many walls contributing to the signal.

In particular, p-SWCNT showed an I_D/I_G value of 0.16 ± 0.05 (***Table 4.1***), suggesting the absence of defects in the sp^2 carbon lattice. The p-MWCNTs shows a higher presence of defects, decreasing with increasing of the size of tubes' diameter (***Table 4.1***).

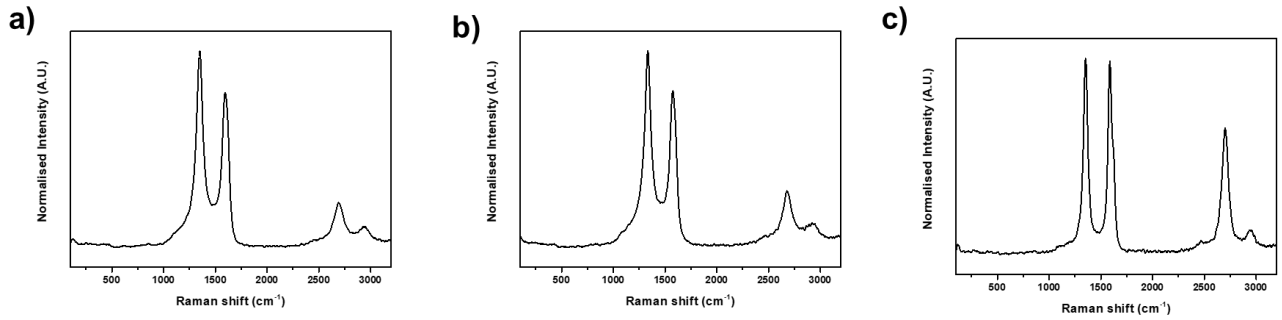

Figure 4.7: *Raman spectra of pristine MWCNTs* ***a) OD-4-6*** *nm, scalebar 50 nm;* ***b) OD-8-15*** *nm, scalebar 50 nm;* ***c) OD-30-50*** *nm, scalebar 200 nm.*

Finally, the dimension of tubes was evaluated through transmission electric microscopy (TEM). A statistical analysis of 100 samples were performed to calculate the average diameter of the pristine materials. In this way, it was possible observe a narrow distribution for the p-MWCNTs with diameter of 4-6 nm (***Figure 4.8***). While for larger CNTs the distribution became wider, especially for **OD 30-50** nm, where it was observed the presence of smaller tubes until 15-20 nm (***Figure 4.8***).

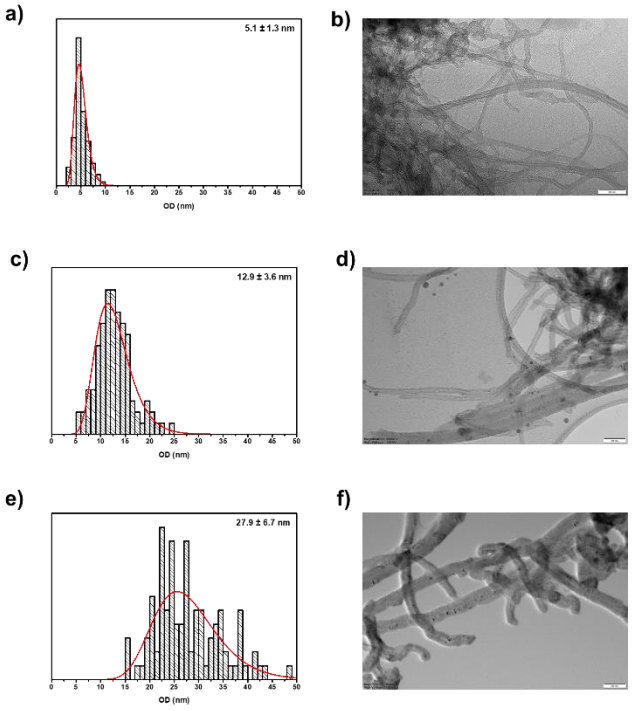

Figure 4.8: *TEM side distribution and images of p-MWCNTs* ***a),b) OD-4-****6 nm;* ***c),d) OD-8-15*** *nm;* ***e),f) OD-30-50*** *nm, scalebar size 50 nm.*

4.3.3. Determination of association constant K_a

Aiming to get more information about the interaction between cages and MWCNTs, the association constant between the CNTs and MOC **1** was derived. The experiment was performed following the procedure reported by Pérez and co-worker.[16] The CNTs (1 mg/mL) were dispersed in solutions with 7 different concentrations of the cages and sonicated at 40 °C overnight (***Figure 4.9***). Then tubes were filtered and dried under vacuum.

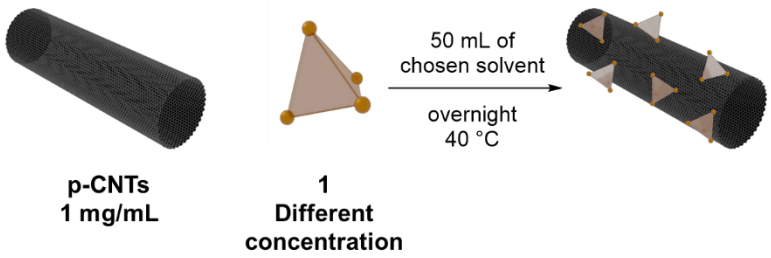

Figure 4.9: *Scheme of reaction for determination of association constant, K_a.*

The functionalised tubes were analysed through TGA analysis under N_2, obtaining the value of weight loss at 700 °C. This value, in first instance, was corrected for the weight loss of the tubes alone in order to obtain only the weight loss of the cage. However, not all the cage decomposed under the analysis conditions and so the latter value was also corrected for the cage. This final value was used to obtain the millimolar concentration of free cage. The binding isotherm was obtained by plotting the weight percentage, corresponding to degree of functionalisation, against the latter value calculated.

The fitting was performed through the standard 1:1 isotherm, 4.2, used also by Pérez:[16]

$$\theta = \frac{S \times K_a \times [H]_{free}}{1 + K_a + [H]_{free}} \quad (\mathbf{4.2})$$

S represents the maximum functionalisation at saturation and it was calculated by iteration through *Origin Lab Software*. The values of K_a obtained for all the tubes are lower than one calculated for the Jeanne's cage with SWCNTs (***Figure 4.10***). This could be related to its melamine scaffold, instead of the benzene one of cage **1**, that favoured the stacking on CNTs' surface.

It was also possible to observe that tubes with smaller diameter, SWCNTs and MWCNT **OD-4-6**, displayed a similar association constant and higher than the other two (***Figure 4.10***). Also, MWCNTs **OD-8-15** and **OD-30-50**, showed a similar association, despite the big difference in terms of diameter size (***Figure 4.10***). This result was probably connected to the fact that **OD-30-50** had a diameter distribution more centred around ~ 30 nm and very broad, with also CNTs with a size similar to **OD-8-15** (***Figure 4.8***). Despite the small differences in terms of absolute value of K_a between **OD-4-6** and **OD-30-50**, it was intriguing to use the cage functionalisation to separate a mixture of the two.

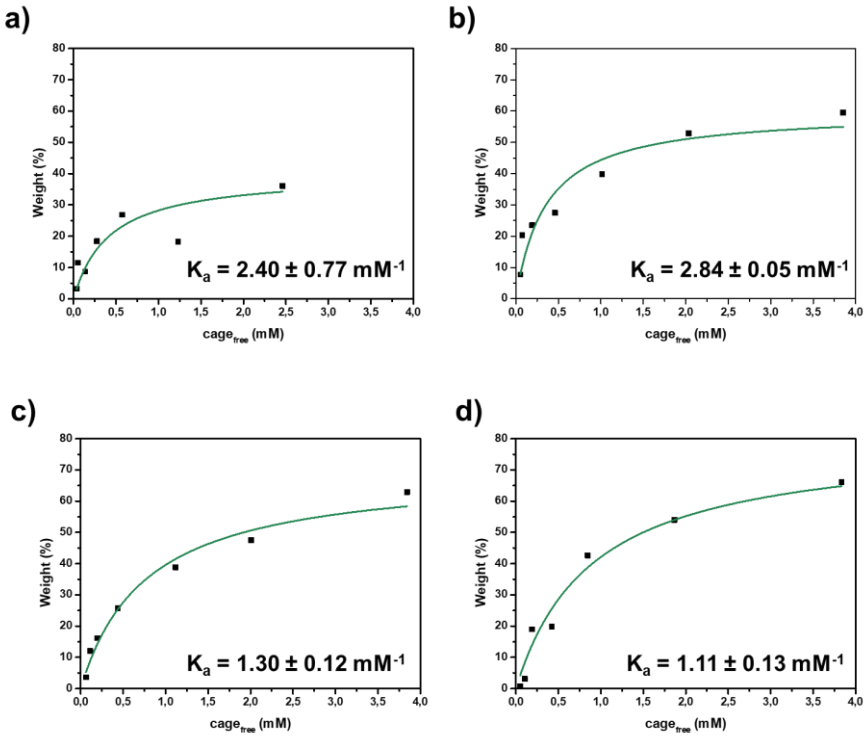

Figure 4.10: *Titration of **1** with a) SWCNTs, b) MWCNTs OD-4-6 nm, c) MWCNTs OD-8-15 nm, d) MWCNTs OD-30-50 nm.*

4.3.4. Exchange phase experiments

Cage **1** was stable both in H_2O and in organic solvents thanks to a simple change of the counter-ion.[18] This feature enabled the study of the possibility to transfer this ability from cages to tubes, through their functionalisation.

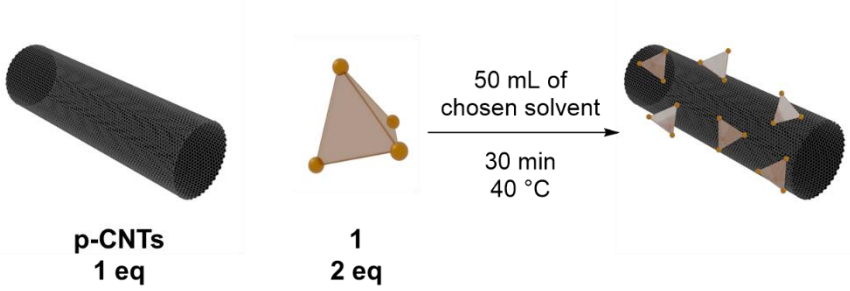

Figure 4.11: *General scheme of reaction for exchange phase experiments.*

In the first instance, we explored the possibility of move the functionalised SWCNTs from an aqueous phase to an organic one (ethyl acetate was chosen as organic phase for the study) and *viceversa*. ***Figure 4.12*** shows that the cage functionalisation allowed to disperse CNTs in the desired solvent, simply changing its counter ion.

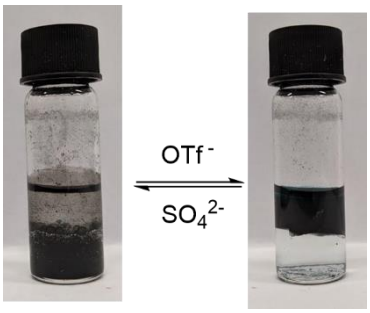

Figure 4.12: *Exchange phase experiment for* ***1****-SWCNTs.*

Figure 4.13 showed that this behaviour was also extended to other type of functionalised MWCNTs. The control experiments with pristine carbon nanotubes displayed negative results, and the CNTs remained dispersed in the organic phase (***Figure 4.17***).

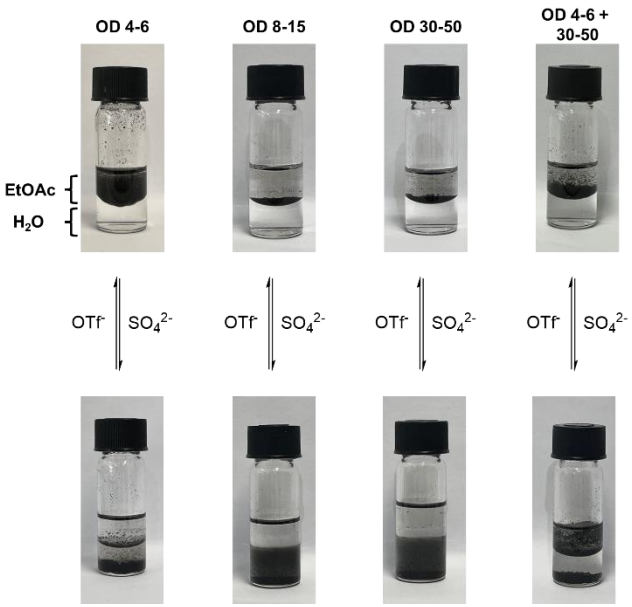

Figure 4.13: *Exchange phase experiment for* ***1****-OD-4-6,* ***1****-OD-8-15,* ***1****-OD-30-50,* ***1****-OD-4-6+OD-30-50.*

Once the experiment was performed with a mixture of functionalised-MWCNTs with different diameters, **OD-4-6** and **OD-30-50** nm, it was observed the presence of CNTs in both the phases, accordingly with the aim of the experiment to try to separate them exploiting their different affinity with the cage.

TEM statistical analysis revealed that in the aqueous phase there was a large presence of smaller CNTs, centred around 4-6 nm (***Figure 4.14***), and a smaller presence of bigger tubes. This result was in accordance with expectations, because **OD-4-6** has a higher K_a than **OD-30-50** nm (***Figure 4.10***).

On the other hand, in the organic phase a broader CNT diameter distribution was found that fitted well with a bimodal distribution centred around tubes of ~ 5 nm and ~ 20 nm (***Figure 4.14***). The broader distribution was related to the smaller difference in terms of association constant between the two types of tubes. On the other hand, the wider distribution of **p-OD-30-50** (***Figure 4.8***) is reflected also in the distribution of the functionalised ones.

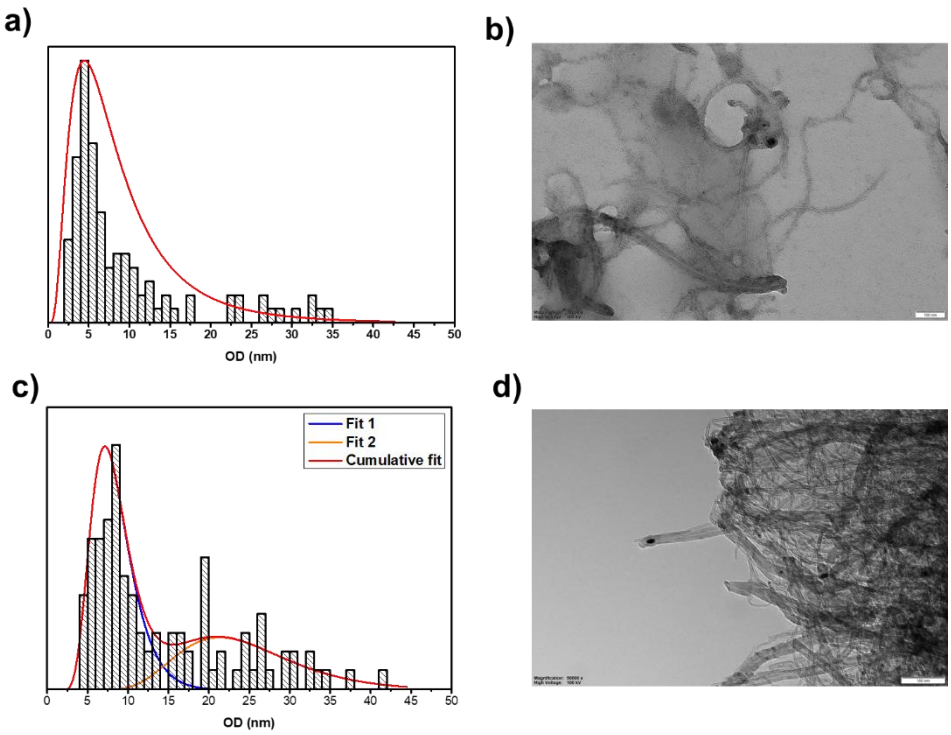

Figure 4.14: *a) TEM statistical analysis of aqueous phase; b) TEM image of aqueous phase, scalebar 100 nm; c) TEM statistical analysis of organic phase; c) TEM image of organic phase, scalebar 100 nm.*

4.4. Conclusion and Future work

This work reported the non-covalent functionalisation of four types of CNTs, one SWCNTs and three short-MWCNTs with different diameters, **OD-4-6**, **OD-8-15**, **OD-30-50** nm. First of all, the association constant value of a zinc (II) tetrahedral cage with CNTs was derived using a titration method based on TGA analysis, previously reported by Pérez and co-workers.[16] The K_a values are between 1.1 and 2.8 mM^{-1}, and in particular smaller tubes, SWCNTs and **OD-4-6** nm, displayed the higher and similar constants, 2.40 ± 0.77 and 2.85 ± 0.05 mM^{-1}, respectively. Cage **1** is able to transfer between aqueous and organic phases, though exchange of its counterion.[18] It was observed that the cage was able to induce its ability to CNTs that became able to move themselves from the phases by ion exchanging.

Furthermore, the difference between K_a values of MWCNTs **OD-4-6** and **OD-30-50** nm gave the opportunity to perform a sorting of the two CNTs through a biphasic system. **OD-4-6** nm, the tubes with higher K_a, should be selectively transferred to the aqueous phase after ion exchange, while **OD-30-50** nm should remain in the organic one. TEM images revealed that in aqueous phase the distribution was centred around tubes of ~ 5 nm,

with a small number of tubes of higher dimensions, according to the fact that the difference between the two association constants is not very large. On the other hand, the organic phase displayed a much broader bimodal distribution, centred around ~ 5 nm and ~ 20 nm. The broader distribution was related to the non-functionalisation of the CNTs, possibly because higher amounts of cages were needed for a better separation. On the other hand, the presence of tubes with size smaller than 30 nm was explained looking the statistical distribution of **p-OD-30-50,** that showed a lower amount of bigger tubes with diameter between 40 and 50 nm. The following steps of this study will regard the use tubes with higher size or **OD-30-50** nm, but with a narrow distribution to better visualise CNT phase separation based on diameter, as well optimisation of the experimental protocol. Further advanced analysis such as EDS-mapping with nanoscale resolution or XPS will be attempted to quantify the amount of MOC present on the CNTs. In addition, the interaction with other cages will be studied. In particular, a cubic cage M_8L_6 with a porphyrin scaffold seems very promising in terms of interaction with the tubes.[21] This Fe (II) cubic cage, reported by Nitschke group, is also able to become alternatively water-soluble or -insoluble by changing the sulfate anion with the triflate one.[21]

Furthermore, all the MOCs used in this work are able to entrap different types of guests (including toxic gases and small molecules) and thus, combined with CNTs, can be used to develop new high-performance composites with sensing properties.

4.5 Experimental part

4.5.1. Cage 1 characterisation

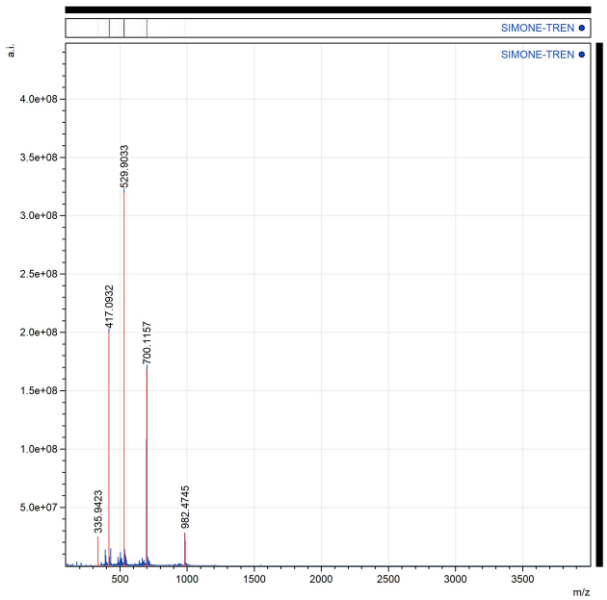

Figure 4.15: *ESI-MS of cage* ***1****.*

4.5.2. TEM image of SWCNTs

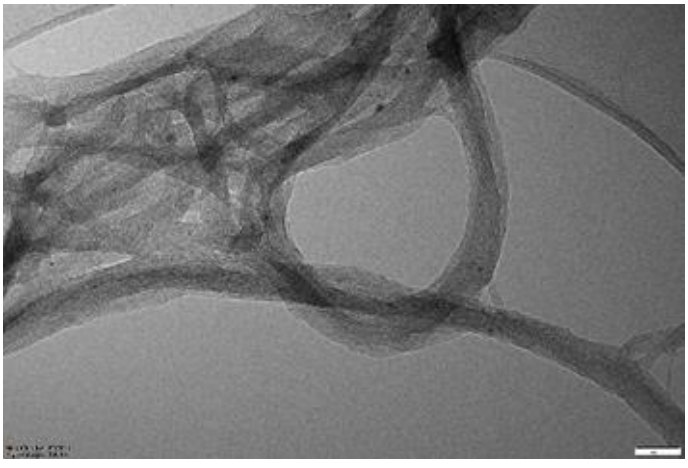

Figure 4.16: *TEM image of p-SWCNTs.*

4.5.3. Raman of CNTs

CNTs	I_D/I_G
SWCNT	0.16 ± 0.05
OD-4-6	1.42 ± 0.16
OD-8-15	1.21 ± 0.06
OD-30-50	0.94 ± 0.05

Table 4.1: *I_D/I_G value for the CNTs studied.*

4.5.4. Exchange phase experiment

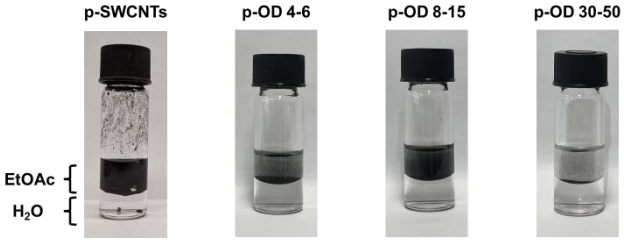

Figure 4.17: *Exchange phase experiments for p-CNTs.*

4.6. Bibliography

(1) Cao, G.; Chen, X. The effects of chirality and boundary conditions on the mechanical properties of single-walled carbon nanotubes. *Int J of Solids Struct* **2007**, *44* (17), 5447-5465.

(2) Zhang, X.; Lu, W.; Zhou, G.; Li, Q. Understanding the Mechanical and Conductive Properties of Carbon Nanotube Fibers for Smart Electronics. *Adv. Mat.* **2020**, *32* (5), 1902028.

(3) Brozena, A. H.; Kim, M.; Powell, L. R.; Wang, Y. Controlling the optical properties of carbon nanotubes with organic colour-centre quantum defects. *Nat. Rev. Chem.* **2019**, *3* (6), 375-392.

(4) Bachilo, S. M.; Strano, M. S.; Kittrell, C.; Hauge, R. H.; Smalley, R. E.; Weisman, R. B. Structure-Assigned Optical Spectra of Single-Walled Carbon Nanotubes. *Science* **2002**, *298* (5602), 2361-2366.

(5) Hou, P.-X.; Liu, C.; Cheng, H.-M. Purification of carbon nanotubes. *Carbon* **2008**, *46* (15), 2003-2025.

(6) Liu, H.; Nishide, D.; Tanaka, T.; Kataura, H. Large-scale single-chirality separation of single-wall carbon nanotubes by simple gel chromatography. *Nature Commun.* **2011**, *2* (1), 309.

(7) Liu, H.; Tanaka, T.; Kataura, H. Optical Isomer Separation of Single-Chirality Carbon Nanotubes Using Gel Column Chromatography. *Nano Lett.* **2014**, *14* (11), 6237-6243.

(8) Arnold, M. S.; Green, A. A.; Hulvat, J. F.; Stupp, S. I.; Hersam, M. C. Sorting carbon nanotubes by electronic structure using density differentiation. *Nat. Nanotechol.* **2006**, *1* (1), 60-65.
(9) Tanaka, T.; Jin, H.; Miyata, Y.; Kataura, H. High-Yield Separation of Metallic and Semiconducting Single-Wall Carbon Nanotubes by Agarose Gel Electrophoresis. *Appl. Phys. Express* **2008**, *1*, 114001.
(10) Tu, X.; Hight Walker, A. R.; Khripin, C. Y.; Zheng, M. Evolution of DNA Sequences Toward Recognition of Metallic Armchair Carbon Nanotubes. *J. Am. Chem. Soc.* **2011**, *133* (33), 12998-13001.
(11) Fagan, J. A.; Khripin, C. Y.; Silvera Batista, C. A.; Simpson, J. R.; Hároz, E. H.; Hight Walker, A. R.; Zheng, M. Isolation of Specific Small-Diameter Single-Wall Carbon Nanotube Species via Aqueous Two-Phase Extraction. *Adv. Mat.* **2014**, *26* (18), 2800-2804.
(12) Subbaiyan, N. K.; Cambré, S.; Parra-Vasquez, A. N. G.; Hároz, E. H.; Doorn, S. K.; Duque, J. G. Role of Surfactants and Salt in Aqueous Two-Phase Separation of Carbon Nanotubes toward Simple Chirality Isolation. *ACS Nano* **2014**, *8* (2), 1619-1628.
(13) Ao, G.; Khripin, C. Y.; Zheng, M. DNA-Controlled Partition of Carbon Nanotubes in Polymer Aqueous Two-Phase Systems. *J. Am. Chem. Soc.* **2014**, *136* (29), 10383-10392.
(14) Gui, H.; Streit, J. K.; Fagan, J. A.; Hight Walker, A. R.; Zhou, C.; Zheng, M. Redox Sorting of Carbon Nanotubes. *Nano Lett.* **2015**, *15* (3), 1642-1646.
(15) Podlesny, B.; Shiraki, T.; Janas, D. One-step sorting of single-walled carbon nanotubes using aqueous two-phase extraction in the presence of basic salts. *Sci. Rep.* **2020**, *10* (1), 9250.
(16) de Juan, A.; López-Moreno, A.; Calbo, J.; Ortí, E.; Pérez, E. M. Determination of association constants towards carbon nanotubes. *Chem. Sci.* **2015**, *6* (12), 7008-7014.
(17) Bolliger, J. L.; Ronson, T. K.; Ogawa, M.; Nitschke, J. R. Solvent Effects upon Guest Binding and Dynamics of a FeII4L4 Cage. *J. Am. Chem. Soc.***2014**, *136* (41), 14545-14553.
(18) Grommet, A. B.; Hoffman, J. B.; Percástegui, E. G.; Mosquera, J.; Howe, D. J.; Bolliger, J. L.; Nitschke, J. R. Anion Exchange Drives Reversible Phase Transfer of Coordination Cages and Their Cargoes. *J. Am.Chem. Soc.* **2018**, *140* (44), 14770-14776.
(19) Costa, S.; Borowiak-Palen, E.; Kruszynska, M.; Bachmatiuk, A.; Kalenczuk, R. Characterization of carbon nanotubes by Raman spectroscopy. *Materials Science-Poland* **2008**, *26* (2), 433-441.
(20) Rozhin, P.; Kralj, S.; Soula, B.; Marchesan, S.; Flahaut, E. Hydrogels from a Self-Assembling Tripeptide and Carbon Nanotubes (CNTs): Comparison between Single-Walled and Double-Walled CNTs. *Nanomaterials* **2023**, *13*, 847.
(21) Percástegui, E. G.; Mosquera, J.; Nitschke, J. R. Anion Exchange Renders Hydrophobic Capsules and Cargoes Water-Soluble. *Angew. Chem. Int. Ed.* **2017**, *56* (31), 9136-9140.

CHAPTER 5

Conclusions

5. Conclusions

In conclusion, this Ph.D. research work focussed on the design on new functional materials based on MOCs with two different types of functional materials, *i.e.*, peptide-based gels or CNTs. In particular, **Chapter 2** and **3** focussed mainly on the synthesis and the self-assembly of new MOCs with pending peptide gelators, while **Chapter 4** on the functionalisation of different CNTs (SWCNTs, MWCNTs OD-4-6 nm, OD-8-15 nm, OD-30-50 nm) with MOCs.

In particular, **Chapter 2** reported the synthesis of four heterochiral tripeptides PABA-L-Phe-D-Xaa-L-Phe-NH_2 (Xaa = Ala, Val, Leu, Ile) derivatised at the N-terminus with a *p*-amino benzoyl unit and amidated at the C-terminus, the preparation of aldehydes, and of the corresponding MOCs through sub-component self-assembly. The peptides chosen as peripherical ligands of the cages were able to self-assemble at different concentrations in acetonitrile. Therefore, it was interesting to study if the peptides were able to induce the self-assembling ability to the correspondent cages. Only three cages, including one previously reported in a previous Ph.D. thesis, were able to gel acetonitrile. Two cages containing iron, $[Fe_4(\mathbf{1a})_4](NTf_2)_8$ (previously reported) and $[Fe_4(\mathbf{2a})_4](NTf_2)_8$, and one containing zinc, $[Zn_4(\mathbf{1a})_4](NTf_2)_8$. The higher steric hindrance due to the longer alkyl chain of the other aliphatic amino acids and the higher size of zinc ions relative to iron prevented the interaction between the different cages and, thus, their assembly. Molecular dynamics suggested that the self-assembly of these cages was mainly driven by the aromatic interactions between the C-terminal phenylalanine of the pendant peptide of one cage and the aromatic core of the central aldehyde of another. This hypothesis was confirmed by UV Resonance Raman Spectroscopy, where the signal corresponding signal intensity decreased from the solution to the gel phase, as a result of with aromatic interactions. This project laid the foundation for the synthesis of materials able to perform double functions by taking advantage of the two distinct spaces present within these gels, the cavity of cages, and the meshes of the gel. It showed that it is possible to change metal ion and peptide sequence, while the aldehydic structure plays a more critical role and only the melaminic sub-component effectively worked out to yield gelling cages.

In **Chapter 3** similar cages were synthesised, *i.e.* tetrahedral iron (II) M_4L_4 cages. The differences regarded the peripherical peptides used and the self-assembly process. Three different peptides were tested, all containing a sulfur functionality on the amino acidic sidechain. Two peptides contained cysteine, either in the

central position (PABA-L-Phe-D-Cys-L-Phe-NH_2, peptide **5**) or at the C-terminus (PABA-L-Phe-D-Phe-L-Cys-NH_2, peptide **6**), while the third one contained methionine (PABA-L-Phe-D-Met-L-Phe-NH_2, peptide **7**). All the MOCs formed, providing further examples of this type of design through subcomponent assembly to obtain MOCs with pendant tripeptides. However, in contrast with the MOCs described in **Chapter 2**, in this case no MOCs were able to self-assemble into gels, not even after oxidation of the cysteine residues and formation of disulfide bridges. A metal-coordination driven gelation was also studied thanks the ability of cysteine to coordinate metal ions. Only $[Fe_4(\mathbf{6a})_4](NTf_2)_8$ gelled in the presence of different metal ions (Ag^+, Zn^{2+}, Hg^{2+}). Rheological data revealed that the Cys preferred coordination to the two divalent cations instead of the monovalent one, provided more cross-links that stabilised the gels. Moreover, TEM images showed that gel-containing Ag^+ formed larger spherical aggregates (84 ± 29 nm) than those containing Zn^{2+} (45 ± 13 nm) and Hg^{2+} (31 ± 18 nm). The coordination of metal ions by cysteine was also confirmed by XPS analysis. This work opens the way for the design of new functional materials able to remove toxic metal salts in aqueous environment thanks to their coordination.

Chapter 4 presented the first example of MWCNTs non-covalently functionalised with a zinc (II) M_4L_4. Four different types of CNTs were studied, *i.e.*, one SWCNTs and three MWCNTs with different outer diameters, 4-6 nm, 8-15 nm, 30-50 nm. The association constants (K_a) of the cages on the CNTs were calculated using a thermogravimetric protocol, previously reported in the literature by the group of Prof. Pérez on MINTs. SWCNTs and MWCNTs OD-4-6 nm had similar $K_a \sim 2.5\ mM^{-1}$, and MWCNTs OD-8-15 nm and 30-50 nm showed also similar association constant of $\sim 1.2\ mM^{-1}$. The latter result can be explained looking the size distribution of MWCNTs calculated from TEM images, where MWCNTs OD-30-50 showed a distribution centred around ~ 30 nm with a significant amount of smaller CNTs, therefore leading to similar constant values for the MWCNTs with the two different OD ranges. The zinc cage used for this study was soluble both in organic and aqueous phase by simple anion exchange, OTf^- and SO_4^{2-}, respectively. It was observed that this ability was transferred to functionalised CNTs that became dispersible in both the phases depending on the counter ion of the cage, although over time they precipitated as it can be seen from the photographs shown in the Chapter. This intriguing property was exploited to test the possibility of sort CNTs with different diameters using a non-covalent functionalisation with MOCs and a biphasic system. MWCNTs with OD-4-6 and 30-50 nm are chosen for this experiment because of the higher difference of K_a values. The narrower tubes should be

transferred in the aqueous phase, after the ion exchange from triflate to sulfate, while the wider ones should remain dispersed in the organic solvent. TEM images of the aqueous phase revealed a prevalence of narrow tubes of ~ 5 nm OD. In the organic phase, however, a wider bimodal distribution was found, that could be explained by the fact that there is not a big difference in the values of the association constants, and that the experimental setup needs further optimisation of the conditions used. Nevertheless, this project showed the effect of the MOCs on CNT behaviour and it was very promising both in terms of preparation of new functional materials for sensing, and also as a new way to sort CNTs and enable their phase transfer. In the future, exploitation of MOC properties, such as luminescence or catalysis, and how they are affected by the CNT binding, could pave the way to innovative materials for various uses in sensing and catalysis.

CHAPTER 6

General materials and methods

6.1. Solid phase peptide synthesis

The peptides were synthesized according to Fmoc-based solid-phase peptide synthesis (SPPS) method with Oxyma B and DIC (peptides **Chapter 2**) or HBTU, HOAt and DIPEA (peptides **Chapter 3**) activation, using 2-chlorotrityl chloride resin as solid support.

6.1.1. Loading of the first amino acid on the resin

1 g of 2-chlorotrityl chloride resin was swelled in DCM for 30 minutes in a plastic vessel. Once the swelling was completed, the resin was activated by treating it with a mixture of 0.1 mL of $SOCl_2$ (0.1 mL/g of resin) in of DCM for 1 hour, at room temperature. After that time, the resin was washed three times with DMF and DCM. The first Fmoc-Rink amide linker was dissolved (1.6 mmol per gram of resin) in a mixture 2:3 of DCM/DMF and added to the activated resin, followed by addition of 0.9 mL of concentrated DIPEA (0.9 mL/g of resin). The reaction was stirred at room temperature for 3 hours. Then, 2.0 ml of methanol, to cap the free non-reactive site of the resin, were added to the reaction vessel and stirred at room temperature for 10 minutes. After that time, the resin was filtered and washed alternately with DMF and DCM, three times. The N-protecting Fmoc group was, finally, removed from the resin by treating it with 20% piperidine in DMF. In this case, two consecutive deprotection steps of 5 minutes each were performed. After that, the resin was filtered again and washed with DMF and DCM.

6.1.2. Calculation of the loading

Three samples of 5 to 10 mg of loaded resin were weighted in Eppendorf tubes.

1.0 mL of a solution of piperidine 20% in DMF was added to each sample.

Samples were shaken (at 700 r.p.m.) for 20 minutes and then centrifuged for 5 minutes (at 12000 r.p.m.).

100 µl of the above solutions were transferred into 3 vials each containing 10 mL of DMF.

The absorbance at λ=301 nm of each sample was measured using 1 cm cuvette and DMF for baseline.

The average substitution for Fmoc-amino acid loaded resin for each sample was calculated, using the formula following below:

$$\text{Substitution(mmol/g)} = (101 \times A\_301)/(7.8 \times w)$$

Where:

A_{301} = Absorption of the sample solution at 301 nm

w = Weight of the resin in mg

The formula is based on the Lambert-Beer law:

$Abs = C \times l \times \varepsilon$

Where:

C= Concentration of the solution (mol/L)

l= Optical path length in the cell in cm (1 cm)

ε= Molar absorption coefficient of the adduct at 301 nm = 7800 $M^{-1}cm^{-1}$

6.1.3. Colorimetric test

To monitor both the Fmoc-cleavage and the coupling of each amino acid on the resin, two different colorimetric tests were performed before and after each deprotection step.

6.1.3.1. Chloranil test

A few resin beads were placed in a Eppendorf and 100 µL of two test solutions were added to the tube, respectively:

Solution 1: 2% acetaldehyde in DMF (stored at 4 °C for one month maximum)

Solution 2: 2% chloranil in DMF (stored at 4 °C for one month maximum)

After mixing, the solution was left at room temperature for 5 minutes. The test will give these two possible results shown in ***Figure 6.1***:

Negative Result	Positive Result (free amino groups)
Colourless to yellowish beads	Brown beads

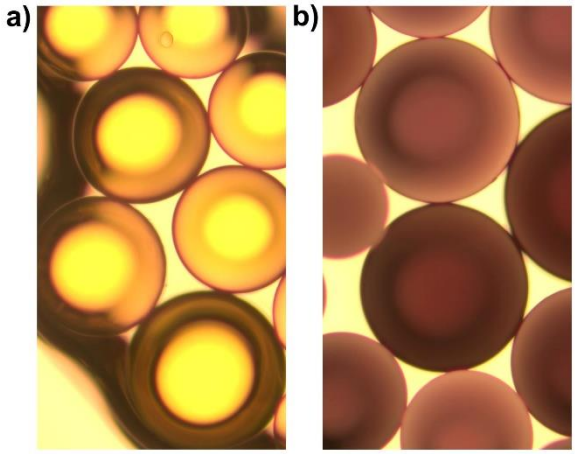

Figure 6.1: *Chloranil test results; a) negative result b) positive result.*

6.1.3.2. Bromophenol Blue test

A few resin beads were placed in a glass test tube and 100 µL of test solution were added to the tube. Test solution was made of 0.05% bromophenol blue in DMF (stored at 4 °C for one month maximum). After mixing, the solution was left at room temperature and the colour of the resin beads was immediately inspected (***Figure 6.2***).

Negative Result	Positive Result (free amino groups)
Colourless to yellowish beads	Dark blue-purple beads

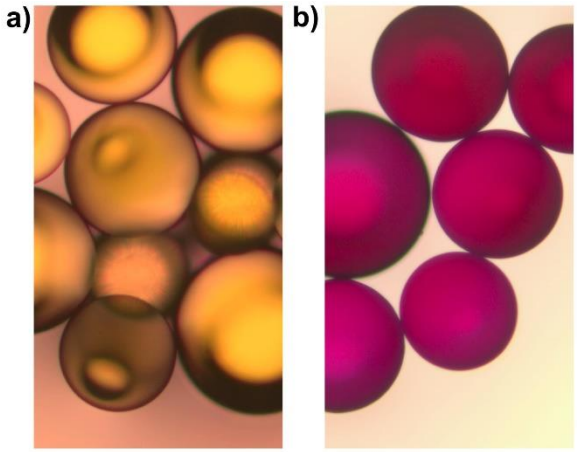

Figure 6.2: *Bromophenol blue test results; a) negative result b) positive result.*

6.1.4. Coupling of the amino acids

The Fmoc-amino acid (4 equivalents) was dissolved in DMF with 4 equivalents of Oxyma B. Once the two powder was solved, 4 eq of DIC was added and the solution was sonicated for 2 minutes. The purple solution was added to the resin and the reaction was stirred at room temperature for 1.5 hour (in the case of the coupling of Fmoc-PABA, the reaction was left for 3 hour). Negative colorimetric test showed complete coupling. After that time, the resin was filtered and washed alternately with DCM and DMF (x 3).

The Fmoc-group was removed by treating the resin with 20% piperidine in DMF. Two consecutive deprotection steps of 5 minutes each were performed. After that, the resin was filtered again and finally washed with DMF and DCM (x 3). The same protocol was used for the coupling of the others amino acids.

6.1.5. Cleavage of the peptide from the resin

The resin was treated with a cleavage solution, which was freshly prepared using a mixture of 47.5% trifluoroacetic acid (TFA), 47.5% DCM with 3% triisopropylsilane (TIPS) and 2% H_2O. The resin with the cleavage solution was stirred for 2 hours. After that time, the resin was filtered in a glass tube and washed twice with fresh cleavage cocktail. TFA was removed by evaporation under compressed air.

6.2. Peptide purification

The peptide was purified dissolving the reaction's crude into a mixture of CH_3CN:H_2O 30:70, both with 0.1% of TFA, and then the mixture was spinned to remove the precipitate. The supernatant was filtered and then purified using HPLC.

The methods used for the purification is the following one:

- t = 0-2 min 30 % CH_3CN
- t = 16 min 72 % CH_3CN
- t = 17 min 95 % CH_3CN
- t = 19 min 95 % CH_3CN

6.3. Peptide characterisation

Each synthesised peptide was characterised by Electron Ionisation-Mass Spectroscopy (ESI-MS) and by Nuclear Magnetic Resonance Spectroscopy (^{1}H-NMR and ^{13}C-NMR).

The ^{1}H-NMR and ^{13}C-NMR spectra were recorded in deuterated dimethyl sulfoxide (DMSO-d_6), using tetramethylsilane (TMS) as internal standard, with a Varian Innova spectrometer at the frequency of 400 and 100 MHz, respectively.

6.4. Aldehydes synthesis

6.4.1. Synthesis of aldehyde a (Chapter 2-4)

1,3,5-tris(4,4,5,5-tetramethyl-1,3,2-dioxaborolan-2-yl)benzene (135TrBB)

A 25 mL R.B.F. was charged with 1,3,5-tribromobenzene (0.0016 mmol), bis(pinacolato)diboron (0.0050 mmol), KOAc (0.0095 mmol), $Pd(dppf)Cl_2$ (0.0000615 mmol). The R.B.F. was purged with N_2 for a couple of minutes and then 5 mL of anhydrous DMF were added. The reaction was stirred at 90°C for 24 h. After this time, the solution was cooled down at r.t. and 120 mL of deionized water was added. The black precipitate formed was centrifuged and washed 3 times with deionized water. The solid was collected in a 250 mL R.B.F. with CH_3CN and the solvent removed under reduced pressure. Finally, the solid was dried under N_2. (yield 76 %)

Aldehyde a

A flask was charged with 1.5 mmol of 135(TrBB), 6.7 mmol of 5-bromo-2-pyridinecarboxaldehyde, 22 mmol of K_2CO_3, 0.44 mmol of $Pd(PPh_3)_4$ in 100 mL of anhydrous DMF. The flask was degassed and stirred under N_2 atmosphere at 90 ºC for 24h. The solvent was removed under reduced pressure and the solid residue triturated with water, collected by filtration and washed three times with water, two times with hot diethyl ether and two times with hot hexane. The dried solid was another time triturated with DCM and collected again. The resulting product was redissolved in hot $CHCl_3$, the insoluble materials filtered off and the pure product was precipitated, as pale yellow solid, in Et_2O. (yield 40 %)

6.4.2. Synthesis of aldehyde e (Chapter 2)

tetrakis(4-bromomethylphenyl)porphyrin (T4BrP)

3.52 mmol of 4-(bromomethyl)benzaldehyde and 3.36 mmol of pyrrole was dissolved in 250 of DCM in a 500 mL R.B.F. The flask was purged for 15 minutes, covered with alumina foil and 210 uL of TFA were added, turning the solution colour to pink-orange. The solution was stirred for 5 h at r.t., after 20 minutes its colour turned to dark-red. 2.5 mmol of DDQ were added to the solution and the reaction was stirred for 30 minutes. TFA was quenched with 370 μL of TEA. The crude was passed through silica and the purple-red solution was collected. The solution was evaporated and the solid was dried under N_2. Purple microcrystalline was obtained (yield 31 %)

Zn-tetrakis(4-bromomethylphenyl)porphyrin (Zn-T4BrP)

A 100 mL R.B.F. was charged with T4Br (0.19 mmol) and Zn(acetate)$_2$•2 H_2O (2.33 mmol) and dissolved in a solution of 30 mL of CH_2Cl_2 and 10 mL of CH_3OH.The reaction was stirred for 4 hours at r.t. The crude was washed three times with H_2O and one time with brine. The organic phase was dried with anhydrous Na_2SO_4, filtered and the removed by reduced pressure. (yield 69 %)

Aldehyde e

0.1594 mmol of 5-hydroxypicolinaldehyde, 0.1943 mmol of K_2CO_3, 0.0286 Zn-T4Br, were added to a 2 mL R.B.F. The flask was purged under nitrogen atmosphere for 30 minutes and then 0.5 mL of anhydrous DMF were added. The reaction was stirred at 70°C for 12 h. The solution was cooled down, diluted with water and it was observed the precipitation of a purple solid. The suspension was centrifuged, the supernatant removed, and the powder washed 3 times with water. The solid was finally dried under N_2. (yield 72 %).

6.5. Cages synthesis

6.5.1. Synthesis of cage M_4L_4 (Chapter 2)

The peptides (**1**-**4**, 0.02285 mmol, 3.0 eq.) and aldehyde (**a**, **b**, **d**, 0.007616 mmol, 1.0 eq.) were dissolved in 1.65 mL of CH_3CN in a sealed 5 mL glass tube. The solution was degassed with N_2 for 10 min after which $M_4(NTf_2)_2$ (0.007616 mmol, 1.0 eq.) was added. The solution was degassed for an additional 10 min. The solution was heated at 50 °C for 18 h. The solution was then cooled and concentrated under a flow of nitrogen. Addition of 10 mL of diethyl ether precipitated the compound. The solid was separated by centrifugation and washed with diethyl ether (2 × 10 mL). The solid was then dried under a flow of nitrogen with yield of 90%. Regarding the cages with aldehydes **b** and **d** the reactions were monitored with ^{1}H-NMR spectroscopy.

6.5.2. Synthesis of cage M_4L_6 (Chapter 2)

The peptide **1** (0.01420 mmol, 6.0 eq.) and aldehyde **c** (0.007097 mmol, 3.0 eq.) were dissolved in 1.54 mL of CH_3CN in a sealed 5 mL glass tube. The solution was degassed with N_2 for 10 min after which $M_4(NTf_2)_2$ (0.004732 mmol, 2.0 eq.) was added. The solution was degassed for an additional 10 min. The solution was heated at 50 °C for 18 h. The solution was then cooled and concentrated under a flow of nitrogen. Addition of 10 mL of diethyl ether precipitated the compound. The solid was separated by centrifugation and washed with diethyl ether (2 × 10 mL). The reaction was monitored through NMR spectroscopy.

6.5.3. Synthesis of cage M_8L_6 (Chapter 2)

In a J-Young NMR tube aldehyde **e** (3.4 μmol, 6 eq.), Fe(OTf)2 (4.9 μmol, 8 eq.). and peptide **1** (13 μmol, 24 eq.) were suspended in 400 μL of DMF-d_7 and 100 μL of CH_3CN-d3 (or 500 μL of CH_3CN-d_3). The solution was deoxygenated by three freeze-pump-thaw cycles and heated in the oil bath for 8 h at 70°C. The reaction was monitored through NMR spectroscopy.

6.5.4. Synthesis of cage-Chapter 3

Peptides **5**-**7** (12.8 mg, 0.0229 mmol, 3.0 equiv.) and aldehyde **a** (3.0 mg, 0.0076 mmol, 1.0 equiv.) were dissolved in 3.0 mL of CH_3CN in a sealed 10 mL round bottom flask. The solution was degassed with N_2 for 10 min after which $Fe(NTf_2)_2$ (5.31 mg, 0.0076 mmol, 1.0 equiv.) was added. The solution was degassed for an additional 10 min. The solution was heated at 70 °C for 18 h. The dark purple solution was then cooled and concentrated under a flow of nitrogen. Addition of 10 mL of diethyl ether precipitated the compound into a dark purple solid. The solid was separated by centrifugation and washed with diethyl ether (2 × 10 mL). The solid was then dried under a flow of nitrogen with yield of 90%.

6.6. Cages characterisation

The characterisation of the cages was performed using facilities of the Yusuf-Hamied Department of University of Cambridge.

6.6.1. Nuclear Magnetic Resonance (NMR)

NMR spectra were recorded on a Bruker DRX-400, Bruker Avance 500 Cryo, Bruker 500 TCI-ATM Cryo and Bruker 700 TCI-ATM Cryo. All NMR data was recorded at 298 K. Proton chemical shift (δ) values are reported in parts per million (ppm) relative to the residual protons from $CDCl_3$ (δ = 7.26 ppm), CD_3CN (δ = 1.94 ppm), or $(CD_3)_2SO$ (δ = 2.50 ppm). DOSY NMR experiments were performed on a Bruker Avance III HD Smart Probe 400 Hz spectrometer using the standard Bruker pulse program ledbpgp2s. The DOSY NMR spectra were processed on MestReNova using the Bayesian DOSY transform. The diffusion coefficients obtained from the DOSY experiments were used to calculate the hydrodynamic radius of products according to the Stokes-Einstein equation, with a CD_3CN viscosity of 3.41×10^{-4} Pa.s.[3]

6.6.2. Mass Spectrometry (MS)

Low-resolution electrospray ionization (ESI) mass spectra were obtained on a Micromass Quattro LC mass spectrometer (cone voltage 10-30 eV; source temperature 313 K) infused from a Harvard Syringe Pump at a rate of 10 μL min^{-1}. High resolution (HR) mass spectra were obtained on a ThermoFinnigan Orbitrap Classic mass spectrometer.

6.7. Self-assembly protocols

6.7.1. Self-assembly of peptides 1-4 (Chapter 2)

The peptides were dissolved in CH_3CN at the desired concentration and heated at 50°C until its dissolution. The solution was sonicated until the gel formation.

6.7.2. Self-assembly of cages (Chapter 2)

The cages were dissolved in CH_3CN at 5 mM and heated at 50°C for 1 hour. The solution was then sonicated for 1 hour at 40°C. The solution was cooled down at room temperature until the gel formation.

6.7.3. Self-assembly of cages (Chapter 3)

A stock solution of 5 mM cage, and **2** were prepared in acetonitrile, respectively. Then, different metal ions were added to the required volume of the cage solution to get the desired final concentrations of metal ions of 30, 60, 90 mM, respectively and cage of 5 mM. The sample was ultrasonicated for 3 minutes.

6.8. Oscillatory rheology

6.8.1. Peptides' gel of Chapter 2

Dynamic time sweep rheological analyses were performed on a Malvern Kinexus Ultra Plus Rheometer (Alfatest, Milan, Italy) with a 20 mm stainless steel parallel plate geometry. The system was kept at 25 °C using a Peltier temperature controller. Each gel was prepared in situ and immediately analysed with a gap of 0.8 mm. Frequency sweeps were recorded from 0.1 to 100 Hz using a controlled stress of 1 Pa. Finally, stress sweeps were recorded using a frequency of 1 Hz until the breaking point for every gel, recognizable by the inversion of G' and G'' values.

6.8.2. Cages' gel of Chapter 3

Dynamic time sweep rheological analyses were performed on a Malvern Kinexus Ultra Plus Rheometer (Alfatest, Milan, Italy) with a 20 mm stainless steel parallel plate geometry. The system was kept at 25 °C using a Peltier temperature controller. Each gel was prepared in situ and immediately analysed with a gap of 0.8 mm. Time sweeps were recorded for 1 hour, using a frequency of 2 Hz and a controlled stress of 2 Pa. After 1 hour, frequency sweeps were recorded from 0.1 to 20 Hz using a controlled stress of 2 Pa. Finally, stress sweeps were recorded using a frequency of 2 Hz until the breaking point for every gel, recognizable by the inversion of G' and G'' values.

6.9. Circular Dichroism analysis (CD)

6.9.1. Cages of Chapter 2

The CD spectra of cages at concentration 0.1 mM were analysed using a 1 mm quartz cell on a Jasco J815 Spectropolarimeter, with 1 s integrations, one accumulation and a step size of 1 nm with a bandwidth of 1 nm over a range of wavelengths from 220 to 700 nm at 25°C.

6.9.2. Cages of Chapter 3

Circular Dichroism was performed on an Applied-Photophysics Chirascan CD spectrometer using a 1 mm path-length cuvette. Experiments were recorded at 298 K, maintained with a Peltier temperature control. Measurements were background subtracted from blank solvent in an identical cuvette. The sample concentrations were adjusted to maintain a HV below 800 V.

6.10. Transmission Electron Microscopy (TEM)

6.10.1. TEM analysis of Chapter 2 and 3

Samples were prepared settling the gels on copper-lacey carbon film grids, using uranyl acetate as negative stain. The grids were previously treated exposing them to UV-Ozone cleaner (UV-Ozone Procleaner Plus) for 5 minutes to increase surface hydrophilicity. TEM images were acquired using Jeol JEM 2100 (Japan) instrument at 100 kV. Average diameter of the nanostructures was derived considering at least 100 objects from various micrographs using FIJI2 software.

6.10.2. TEM analysis of Chapter 4

Samples were prepared settling the gels on copper-lacey carbon film grids. The grids were previously treated exposing them to UV-Ozone cleaner (UV-Ozone Procleaner Plus) for 5 minutes to increase surface hydrophilicity. TEM images were acquired using FEI EM208 (Philips) instrument at 100 kV. Average diameter of the nanostructures was derived considering at least 100 objects from various micrographs using FIJI2 software.

6.11. Scanning Electron Microscopy (SEM)

SEM analyses were performed on Gemini 300, ZEISS (Germany) equipped with an Oxford Instruments INCS X-Act energy-dispersive X-ray spectroscopy (EDXS) detector. SEM grids (copper-grid-supported lacey carbon film) were first exposed to the UV-ozone cleaner (UV-Ozone Procleaner Plus) for 10 mins to make the grid surface more hydrophilic. Seven days aged gels were precisely deposited on a SEM grid, dried for 15 mins at room temperature.

6.12. Raman spectroscopy

Raman analysis was acquired in an Invia Renishaw microspectrometer (50) equipped with He-Ne laser at 532 nm. The laser was focused using a 50x microscope and the power of the laser was set as required for the sample. At least 10 spectra per sample were acquired to assure the homogeneity of the samples. For the characterization of the gels, a small piece of gel was deposited on a glass microscope slide and open air dried before the analysis. For the characterisation of the CNTs, a small amount of powder was deposited on the glass slide.

6.13. UV Resonance Raman (UVRR)

UV Raman spectra of cages in solution were collected at the BL10.2-IUVS beamline of Elettra Sincrotrone Trieste using 226 nm as the excitation wavelength. The vertically polarized VV Raman spectra were recorded in a back-scattered geometry and analysed by using a single pass of a Czerny-Turner spectrometer (Trivista 557, Princeton Instruments, 750 mm of focal length) equipped with holographic grating at 1800 g/mm and a UV-optimized CCD camera. The calibration of the spectrometer was standardized using cyclohexane (spectroscopic grade, Sigma Aldrich). The resolution was set at 1.2 cm^{-1}/pixel. The final radiation power on the samples was kept at about 0.2 mW. Comparison between individual spectra acquired repeatedly for each sample showed no gradual changes to the spectra during accumulation, indicating a lack of sample photodegradation due to UV radiation.

6.14. Thermogravimetric analysis (TGA)

6.14.1. TGA analysis of pristine materials

TGA of approximately 1 mg of each compound was recorded on a TGA 5500 (TA Instruments) under nitrogen, by equilibrating at 100 °C for 20 min, and following a ramp of 10 °C min^{-1} up to 800 °C.

6.14.2. TGA analysis for determination of association constant (K_a)

TGA of approximately 0.6-0.8 mg of each compound was recorded on a TGA 5500 (TA Instruments) under nitrogen, by equilibrating at 100 °C for 20 min, and following a ramp of 50 °C min^{-1} up to 800 °C.

6.15. Determination of association constant (K_a)

The experimental protocol to calculate the K_a was recently described by De Juan *et al.* Briefly, 2 mg of CNTs were ultrasonicated overnight at 40°C in a solution of cage. Then, the samples were filtrated through a Millipore membrane (JHWP 0.45 μm) and the solid is dry under vacuum. The recovered solid was analysed by TGA.

6.16 Exchange phase experiment

3 mg of CNTs and 6 mg of cage were dispersed in the desired solvent (water or acetonitrile) and sonicated at 40°C for 30 minutes. Then, the samples were filtrated through a Millipore membrane (JHWP 0.45 μm) and dried under vacuum.

1 mg of functionalised CNTs with zinc cage with triflate anion were dispersed in mixture 1:1 of Et_2OAc: H2O. The substitution of H_2O sonicating the functionalised CNTs in 0.5 mL of a tetrabutylammonium sulfate solution (50 wt. % in H_2O). The successful anion exchange, from triflate to sulfate, was confirmed by the correspondent phase exchange of tubes.

ABBREVIATIONS

AIBN 2,2′-azobisisobutyronitrile

AMPs Antimicrobial peptides

CD Circular Dichroism spectroscopy

CNMs Carbon nanomaterials

CNOs Carbon nano-onions

CNTs Carbon nanotubes

DCM Dichloromethane

DDQ 2,3-Dichloro-5,6-dicyano-1,4-benzoquinone

DIC *N*,*N*′-Diisopropylcarbodiimide

DHPM 2,3-dihydroxypropylmethacrylate

DME Ethylene dimethacrylate

DMF *N*,*N*-Dimethylformamide

dppf 1,1'-Bis(diphenylphosphino)ferrocene

ESI-MS Electron Ionisation-Mass Spectroscopy

Fmoc 9-fluorenylmethyloxycarbonyl

HPLC High-performance liquid chromatography

IR Infrared spectroscopy

LCST lower critical solution temperature

LMWG Low molecular weight gelators

MD All-atom molecular dynamics

MEH (E)-3-(2-(2-Hydroxystyryl)-3,3-dimethyl-3H-indol-1-ium-1-yl)propane-1-sulfonate

mgc Minimum gel concentration

MIMs Mechanically interlocked molecules

MINTs Mechanically interlocked derivatives of carbon nanotubes

MOCs Metal Organic Cages

MWCNTs Multi-wall carbon nanotubes

NDs Nanodiamonds

NMR Nuclear Magnetic Resonance Spectroscopy

NTf_2 Bis(trifluoromethylsulfonyl)imide

OTf Trifluoromethanesulfonate

Oxyma B 5-(hydroxyimino)-1,3-dimethylpyrimidine-2,4,6(1H,3H,5H)-trione

PABA 4-Aminobenzoic acid

PAG Photoacid generator

pHEMA Poly(2-hydroxyethylmethacrylate)

PVA Poly(vinyl acetate)

RCM Ring-closing metathesis

SWCNTs single-wall carbon nanotubes

TEA Triethylamine

TEM Transmission Electron Microscopy

TFA Trifluoroacetic acid

TGA Thermogravimetric Analysis

TIPS 3% triisopropylsilane

TMS Tetramethylsilane

T4BrP Tetrakis(4-bromomethylphenyl)porphyrin

UCST Upper critical solution temperature

UV Ultraviolet irradiation

UV-Vis Ultraviolet-Visible irradiation

UV-RR Ultaviolet Resonance Raman

XPS X-Ray Photoelectron Microscopy

135TrBB 1,3,5-tris(4,4,5,5-tetramethyl-1,3,2-dioxaborolan-2-yl)benzene

5-FU 5-fluorouracil

ADDITIONAL WORKS PERFROMED DURING PhD

Scientific Publications

Rozhin, P., Adorinni, S., Iglesias, D., Mackiol, T., Kralj, S., Bisetto, M., Abrami, M., Grassi, M., Bevilacqua, M., Fornasiero, P., Marchesan, S. Nanocomposite Hydrogels with Self-Assembling Peptide-Functionalized Carbon Nanostructures, *Chem. Eur. J.* **2023**, e202301708.

Adorinni, S.; Goti, G.; Rizzo, L.; Grassi, F.; Kralj, S.; Matroodi, F.; Natali, M.; De Zorzi, R.; Marchesan, S.; Dell'Amico, L. Self-assembly of benzophenone-diphenylalanine conjugate into a nanostructured photocatalyst. *Chem. Commun.* **2023**, 59 (49), 7619.

Parisi, E.; Adorinni, S.; Garcia, A. M.; Kralj, S.; De Zorzi, R.; Marchesan, S. Self-assembling tripeptide forming water-bound channels and hydrogels. *J. Pept. Sci.* **2023**, e3524.

Marin, D.; Bartkowski, M.; Kralj, S.; Rosetti, B.; D'Andrea, P.; Adorinni, S.; Marchesan, S.; Giordani, S. Supramolecular Hydrogels from a Tripeptide and Carbon Nano-Onions for Biological Applications. *Nanomaterials* **2023**, 13 (1), 172.

Scarel, E.; Pierri, G.; Rozhin, P.; Adorinni, S.; Polentarutti, M.; Tedesco, C.; Marchesan, S. Self-Assembly and Gelation Study of Dipeptide Isomers with Norvaline and Phenylalanine. *Chemistry* **2022**, 4 (4), 1417-1428.

Rosetti, B.; Scarel, E.; Colomina-Alfaro, L.; Adorinni, S.; Pierri, G.; Bellotto, O.; Mamprin, K.; Polentarutti, M.; Bandiera, A.; Tedesco, C.; et al. Self-Assembly of Homo- and Hetero-Chiral Cyclodipeptides into Supramolecular Polymers towards Antimicrobial Gels. *Polymers* **2022**, 14 (21), 4554.

Melchionna, M.; Moro, M.; Adorinni, S.; Nasi, L.; Colussi, S.; Poggini, L.; Marchesan, S.; Valenti, G.; Paolucci, F.; Prato, M.; et al. Driving up the Electrocatalytic Performance for Carbon Dioxide Conversion through Interface Tuning in Graphene Oxide–Bismuth Oxide Nanocomposites. *ACS Appl. Energy Mater.* **2022**, 5 (11), 13356.

Mosetti, V.; Rosetti, B.; Pierri, G.; Bellotto, O.; Adorinni, S.; Bandiera, A.; Adami, G.; Tedesco, C.; Crosera, M.; Magnano, G. C.; et al. Cyclodipeptides: From Their Green Synthesis to Anti-Age Activity. *Biomedicines* **2022**, 10 (10), 2342.

Jahović, I.; Zou, Y.-Q.; Adorinni, S.; Nitschke, J. R.; Marchesan, S. Cages meet gels: Smart materials with dual porosity. *Matter* **2021**, 4 (7), 2123.

Adorinni, S.; Rozhin, P.; Marchesan, S. Smart Hydrogels Meet Carbon Nanomaterials for New Frontiers in Medicine. *Biomedicines* **2021**, 9 (5), 570.

Adorinni, S.; Cringoli, M. C.; Perathoner, S.; Fornasiero, P.; Marchesan, S. Green Approaches to Carbon Nanostructure-Based Biomaterials. *Appl. Sci.* **2021**, 11 (6), 2490.

Caporale, A.; Adorinni, S.; Lamba, D.; Saviano, M. Peptide–Protein Interactions: From Drug Design to Supramolecular Biomaterials. *Molecules* **2021**, 26 (5), 1219.

Schools

"Catalysis Fundamentals and Practice" University of Liverpool, 18-21 July 2022, 33 hours (Poster session)

"International oligonucleotides and peptides conference", IOPC 2023, Milan, Italy on 5-7 June, 2023 (oral+poster)

Internationally awarded scholarships

- RSC SURCAT bursary - Catalysis: Fundamentals and Practice. Liverpool July 2022
- E-COST Eutopia Grant (CA17139) - STSM: University of Cambridge from 01/09/2022 to 16/09/2022, project: Supramolecular gels from metal coordination cages with peptides
- E-COST Essence Grant (CA19118) – STSM: University of Cambridge from 17/09/2022 to 29/09/2022, project: Nanocarbons and MOCs for sensing

Institutional courses

"Scientific writing, PARTE 1+ PARTE 2", Prof. Scarso (UniVe)

tirocinio di formazione per osservazione e acquisizione di immagini al TEM in modalità autonoma su TEM FEI EM 208 camera QUEMESA software RADIUS, Paolo Bertoncin (UniTs)

"Electron microscopy: an introduction to TEM, SEM and AFM part. 1 and part. 2", Federica Rigoni (UniVe).

Seminars

- *"Un detective in azione: materiali catalitici sotto indagine*" Silvia Bordiga, Università di Torino- venerdì 13 novembre 2020, ore 15-Società Chimica Italiana.
- *"Sintesi organica e biologia sintetica: "thinking outside the box" in opto-elettronica"* Gianluca Farinola, Università di Bari- venerdì 20 novembre 2020, ore 15-Società Chimica Italiana.
- *"Ogni cosa è illuminata…": Un "turista per caso" nella catalisi fotoredox"*, Piergiorgio Cozzi, Università di Bari- venerdì 27 novembre 2020, ore 15-Società Chimica Italiana.
- *"Dallo spazio interstellare alla terra e ritorno: l'affascinante viaggio dell'astrochimica prebiotica"*, Vincenzo Barone, Scuola Normale Superiore di Pisa- venerdì 11 dicembre 2020, ore 15-Società Chimica Italiana.
- *"Sonochemistry and sonoprocessing, from research lab to industrial applicactions"*, Giancarlo Cravotto, Università di Torino- venerdì 18 dicembre 2020, ore 15-Società Chimica Italiana.
- *"Fotovoltaico e combustibili solari: guardare oltre silicio e idrogeno"*, Federico Bella, Università di Torino- venerdì 15 gennaio 2021, ore 15-Società Chimica Italiana.
- *"Mechanically chiral molecules: synthesis and applications"*, Steve Goldup, University of Southampton, venerdì 22 gennaio 2021, ore 14:30-Università degli Studi di Milano.
- *"I poliioduri nella chimica supramolecolare: dalle origini verso nuove architetture allo stato solido"*, Matteo Savastano, Università degli Studi di Firenze, mercoledì 21 aprile 2021, ore 15:00-Seminari Virtuali di Chimica Supramolecolare.
- *"Self-assembling heterochiral peptides: playing the Mirror Game"*, Silvia Marchesan, Università degli Studi di Trieste, martedì 25 maggio 2021, ore 15:00-Seminari Virtuali di Chimica Supramolecolare.
- *"Eutecto- e Ionogel: una Panoramica dalle Proprietà alle Applicazioni"*, Francesca D'Anna, Università degli Studi di Palermo, mercoledì 23 giugno 2021, ore 15:00-Seminari Virtuali di Chimica Supramolecolare.
- *"Sviluppo di formulazioni liposomiche per la veicolazione di principi attivi al Sistema Nervoso Centrale"*, Beatrice Simonis, Università di Roma La Sapienza, giovedì 22 luglio 2021, ore 15:00-Seminari Virtuali di Chimica Supramolecolare.
- *1st EPS Peptide Highlights Virtual Symposium Peptide design and engineering*, martedì 13 luglio 2021, ore 14:00.
- *"FINAL EVENT OF CATHENA PROJECT - CAncer THErapy by NAnomedicine", venerdì 29 marzo 2022, ore 15.*

- *"Metal-Catalyzed Oxidations Enabled by Designer Ligands" Martin Albrecht, 12 giugno 2022, ore 16:30.*
- *"Microwaves and Ball Milling in Organic Synthesis and Material Chemistry", Ester Vazquez, 13-16 giugno 2022.*
- *"Smart materials for real-world (bio)sensing" Prof. Stefano Cinti, University of Naples Federico, January 11th, 2023.*
- *"Ruthenium-based photoactivated chemotherapy for hypoxic tumors treatment progresses and challenges", Prof. Sylvestre Bonnet, University of Leiden, April 5th, 2023.*
- *"Chirality in Plasmonic Nanoparticles and Nanostructures", Prof. Luis M. Liz-Marzan, CIC biomaGUNE, May 8th, 2023.*
- *"The Impact of Mesoionic and N-Heterocyclic Carbene Ligands in Manganese Catalysis", Prof. Beatriz Royo, ITQB NOVA, May 11th, 2023.*
- *"Homogeneous catalysis as a powerful tool for sustainability", round table with Prof. Beatriz Royo, May 15th, 2023.*
- *"Gold nanoparticles for the development of cancer vaccines", Prof. Roberto Fiammengo, University of Verona, May 18th, 2023.*
- *BOTTOM-UP DESIGN AND SYNTHETIC CONSTRUCTION OF LIFE-LIKE TECHNOLOGIES-SYMPOSIUM SERIES - 1ST SYMPOSIUM "INTEGRATING SELF-ASSEMBLED NANOSTRUCTURES IN PROTOCELL DESIGN", June 14th, 2023.*
- *"DNA nanotechnology as a platform to build synthetic cells and programmable materials", Prof. Elisa Franco, UCLA, June 21th, 2023.*
- *"Construction of Metal-Organic Supramolecular Containers Based on BINOL Backbone", Prof. You-Quan Zou, July 13th, 2023.*
- *"Stimuli-responsive bipyridinium salts: expanding the playground of aqueous supramolecular chemistry", Prof. Marcos D. Garcia, July 14th, 2023.*